

**SHEET FLOW AND SUSPENDED SEDIMENT TRANSPORT
PROCESSES ON A SURF ZONE SANDBAR**

by

Ryan S. Mieras

A dissertation submitted to the Faculty of the University of Delaware in partial fulfillment of the requirements for the degree of Doctor of Philosophy in Civil Engineering

Fall 2017

© 2017 Ryan S. Mieras
All Rights Reserved

**SHEET FLOW AND SUSPENDED SEDIMENT TRANSPORT
PROCESSES ON A SURF ZONE SANDBAR**

by

Ryan S. Mieras

Approved: _____
Sue McNeil, Ph.D.
Chair of the Department of Civil and Environmental Engineering

Approved: _____
Babatunde A. Ogunnaike, Ph.D.
Dean of the College of Engineering

Approved: _____
Ann L. Ardis, Ph.D.
Senior Vice Provost for Graduate and Professional Education

I certify that I have read this dissertation and that in my opinion it meets the academic and professional standard required by the University as a dissertation for the degree of Doctor of Philosophy.

Signed:

Jack A. Puleo, Ph.D.
Professor in charge of dissertation

I certify that I have read this dissertation and that in my opinion it meets the academic and professional standard required by the University as a dissertation for the degree of Doctor of Philosophy.

Signed:

Daniel T. Cox, Ph.D.
Member of dissertation committee

I certify that I have read this dissertation and that in my opinion it meets the academic and professional standard required by the University as a dissertation for the degree of Doctor of Philosophy.

Signed:

Tian-Jian Hsu, Ph.D.
Member of dissertation committee

I certify that I have read this dissertation and that in my opinion it meets the academic and professional standard required by the University as a dissertation for the degree of Doctor of Philosophy.

Signed:

James T. Kirby, Ph.D.
Member of dissertation committee

ACKNOWLEDGMENTS

I could not have completed my graduate studies without the everlasting, unconditional support – in all aspects – from my Mom and Dad in the nearly 24 years of my academic studies. You were always pushing me to be better, and the two of you were the perfect balance between “Great work son, keep it up!” and “You can do better than that.” And Mom, you somehow pretended to “understand” my research, and were always willing to listen, even when I would go off on tangents about bed shear stress and pressure gradients. Nevertheless, having to explain complicated things in simple terms was very useful and taught me how to communicate my research to a broader audience.

I must thank my committee members for participating on my Ph.D. committee. Thank you for your time and always thoughtful comments. Ya’ll always helped to steer me in a better direction. I especially must thank my Ph.D. advisor, Jack. Your door was always open and you never (well, maybe once or twice?) complained when students would flood your office, even sometimes forming a line out the door, with questions related to our research. Your uncanny ability to always make time for your students is unmatched. I am particularly grateful for your willingness to give me the freedom to pursue my passions in research and knowing when to take a hands-off approach, even if it involved me taking a chance/risks. I have learned more than I ever would have imagined as a result. (But also, thank you for putting up with my many antics ☺). I will also miss your dogs: Maiden (maidy cakes) and Lindy (lindy cakes) [something tells me they will miss me too].

The most important aspect of surviving the gauntlet of completing a Ph.D. is an awesome friend group. You will rely on them A LOT. So thanks to the following friends I made during my time at UD: Tobias, Babak, Mike, Mikey “3 for 3” Beeee, Patricia, Nick, Demi, Doug, Matt, Andy, Thijs, Aline, Yaroo and many others I cannot mention here. Thanks also to all the people (students, visitors, etc.) who came and went during my six years at CACR. Your curiosity drove my curiosity, and I think we are all better as a result. I’m am appreciative for such a stimulating environment.

The two FOBS sensors were generously loaned to us by the U.S. Army Corps of Engineers. A special thanks also goes to Pedro Lomonaco, Tim Maddux and Cooper “Coopa-doopa-ding-dong” Pearson at the O.H. Hinsdale Wave Research Laboratory for their tireless contribution to this project, including weekends, in addition to the following researchers/visitors for their help during the BARSED experiment: Patricia “Patria” Chardón-Maldonado, Yeulwoo “Yarinskies” Kim, Douglas “Dougie Blue/Balinskies/SnippSnapps” Krafft, Jose “YaAay-sEee” Pintado-Patiño, William “Willy” Pringle, Taka Suzuki, and Zheyu “Kung-Fu Nancy” Zhou.

I would be remiss not to acknowledge the influence of podcasts in getting me through the six years of my graduate studies, including Above & Beyond Group Therapy, Shane 54, Oliver Heldens, Aly & Fila, Markus Schulz, Spinnin’ Sessions, Morgan Page, Nicole Moudaber, Roger Sanchez, the Radiotopia family and, of course, Hello Internet. Through podcasts, I was introduced to entirely new ideas, musical genres, and stimulating topics, helping me to maintain my life-long learner aspirations with a dose of sanity.

Finally, while composing this Dissertation, three of the most vicious hurricanes ever recorded in the North Atlantic/Gulf of Mexico (Harvey, Irma & Maria) caused

catastrophic devastation to the states of Texas (Harvey) and Florida (Irma); U.S. territories of Puerto Rico and the Virgin Islands (Irma and Maria); most of the Leeward Caribbean Islands (Irma and Maria); the Dominican Republic (Maria); Cuba (Irma); and the Turks and Caicos (Irma and Maria). Being the “weatherphile” I am, I spent many days and nights tracking these hurricanes that directly impacted so many of my friends. My heart goes out to all those who were affected and I wish for a full and speedy recovery in the long road ahead. My hope is for the future of Ocean and Earth Sciences as a whole to continue receiving the adequate support from our governments and people required to continue groundbreaking research that undoubtedly saved lives during hurricanes like those witnessed during the 2017 season.

TABLE OF CONTENTS

LIST OF TABLES	xi
LIST OF FIGURES	xii
ABSTRACT	xxii

Chapter

1	INTRODUCTION	1
1.1	Surf Zone Sandbar Migration	1
1.2	Outline	3
2	QUASI-STEADY SHEET FLOW MEASUREMENT PERFORMANCES OF HIGH-RESOLUTION ACOUSTIC AND CONDUCTIVITY PROFILERS	6
2.1	Introduction	6
2.2	PARROT Experiment.....	8
2.2.1	Experimental Facility and Flow Conditions.....	8
2.2.2	Instrumentation Setup.....	10
2.2.3	Experiment Protocol.....	11
2.3	High-resolution Measurement Systems.....	13
2.3.1	Conductivity Concentration Profiler (CCP)	13
2.3.1.1	Concentration Measurements	13
2.3.1.2	Bed Interface Detection and Sheet Layer Thickness....	14
2.3.1.3	Sheet Layer Thickness Correction Formula and Measurement Volume for CCP2mm	15
2.3.2	Acoustic Concentration and Velocity Profiler (ACVP)	20
2.3.2.1	Velocity Measurements	20
2.3.2.2	Concentration Measurements	21
2.3.2.3	Bed Interface Detection	24

2.3.3	Validation of Acoustic Transport Rate Measurements	24
2.3.3.1	Topographic Estimation of Transported Particle Volume	25
2.3.3.2	Acoustic Inversion Parameters	26
2.3.3.3	Comparison between Topographic and Acoustic Estimations	27
2.4	Results	29
2.4.1	Instantaneous Velocity and Concentration Measurements.....	30
2.4.2	Instantaneous Detection of the Bed Interface.....	33
2.4.3	Averaged Flow Quantities	33
2.4.3.1	Velocity, Concentration and Sediment Volume Flux Profiles.....	33
2.4.3.2	Sheet Flow Layer Thickness	38
2.5	Conclusions	40
3	LARGE-SCALE EXPERIMENTAL OBSERVATIONS OF SHEET FLOW ON A SANDBAR UNDER SKEWED-ASYMMETRIC WAVES.....	42
3.1	Introduction	42
3.2	Methodology.....	44
3.2.1	Experimental Setup	44
3.2.2	Near-bed Instrumentation.....	50
3.2.3	Test Conditions.....	52
3.3	Data Analysis.....	55
3.4	Results	61
3.4.1	Phase-averaged Sediment Concentration Profiles.....	61
3.4.2	Bed Shear Stress and Sheet Thickness	62
3.5	Discussion.....	72
3.5.1	Grain Roughness and Friction Factor.....	72
3.5.2	Quantification of Bed Shear Stress.....	79
3.5.3	Free Stream Horizontal Advective Acceleration.....	82
3.6	Conclusions	88

4	RELATIVE CONTRIBUTIONS OF WAVE-INDUCED SHEET FLOW AND SUSPENDED SEDIMENT TRANSPORT ON A SANDBAR.....	91
4.1	Introduction	91
4.2	Laboratory Experiment.....	96
4.2.1	Facilities and Test Conditions	96
4.2.2	Instrumentation and Calibration	99
4.3	Data Treatment	103
4.3.1	Merging Concentration and Velocity Profiles.....	104
4.3.2	Definitions	105
4.3.2.1	Averaging Operators	105
4.3.2.2	Sheet Flow Layer.....	106
4.3.2.3	Vertical Coordinate Systems, z^* and z'	107
4.3.3	Velocity Profiles in the Sheet Flow Layer	109
4.4	Results	113
4.4.1	Velocity, Concentration and Sediment Flux	113
4.4.1.1	Phase-averaged Profiles.....	113
4.4.1.2	Wave-averaged Profiles.....	116
4.4.2	Suspended Sediment and Sheet Flow Transport Rates	118
4.4.3	Net Sediment Transport Rates.....	121
4.4.3.1	Suspended Sediment and Sheet Flow.....	121
4.4.3.2	Positive and Negative Half-Cycles.....	124
4.4.4	Net Sheet Flow Transport Rate and Velocity Skewness	130
4.5	Discussion.....	132
4.5.1	Net Sediment Transport Rate Estimates.....	133
4.5.1.1	Sheet Flow Sediment Transport Rates	134
4.5.1.2	Suspended Sediment Transport Rates	138
4.6	Conclusions	147
5	SUMMARY AND CONCLUSIONS.....	150

5.1	PARROT Experiment.....	150
5.1.1	Quasi-steady Sheet Flow High-Resolution Measurement Technologies.....	150
5.2	BARSED Experiment.....	151
5.2.1	Oscillatory Sheet Flow Dynamics under Skewed-asymmetric Surface Waves	151
5.2.2	Relative Contributions of Suspended Load and Sheet Flow	152
	REFERENCES	154
Appendix		
A	SUPPLEMENTAL FIGURES FOR PARROT EXPERIMENTS	172
B	COPYRIGHT NOTES	180

LIST OF TABLES

Table 2.1: Summary of experiments, particle sizes, and flow parameters.	10
Table 2.2: CCP calibration parameters.....	14
Table 2.3: Root-mean-square differences between different instruments for different ranges of the ensemble-time-averaged concentration profiles.	36
Table 2.4: Ensemble-time-averaged sheet flow layer thickness, δs , comparison between instruments.	38
Table 3.1: Summary of wave cases with select wave conditions, skewness and asymmetry parameters. (Note: the numbers in parentheses correspond to the equation number used to compute each parameter. Data from the Case IDs marked with asterisks are plotted in Figure 3.15.).....	54
Table 3.2: Summary of friction parameters and flow parameters, where N is the number of ensembles used during phase-averaging for each wave case and sediment size. All values are reported for $z^* = 15$ mm, unless otherwise noted.....	64
Table 3.3: Summary of values for Λ obtained using three different expressions for grain roughness, ks	75
Table 3.4: Summary of Λ values and respective coefficients of determination (R^2) for 4 different combinations of expressions for ks and fw . ^a	78
Table 4.1: Summary of wave cases, trials and number of ensembles.	98
Table 4.2: Ensemble-averaged net transport rates and half-cycle periods.	126
Table 4.3: Effect of the profile shape parameter on net sheet flow transport rates and corresponding adjustment factors, $\mathbb{F}sf$	137
Table 4.4: Summary of nonlinear regression analysis for all three wave periods.....	143
Table 4.5: Summary of net transport rate adjustment factors.	145

LIST OF FIGURES

Figure 1.1: Flow chart outlining several distinct time scales for sandbar evolution.....	2
Figure 2.1: (a) Sketch of the experiment under active flow and location of the instruments. A and B delineate the upstream and downstream edges of the sediment pit, at $x = 0$ m and $x = 3$ m, respectively. (b) Picture of the CCP probes deployed before an S3 run. (c) Picture of the ACVP.	9
Figure 2.2: Normalized current density field results from the numerical simulations of the electric field around <i>CCP2mm</i> . The region inside the white curve (0.01 contour) contains 86% of the total current.	17
Figure 2.3: Prescribed transition thicknesses versus sheet thickness determined from prescribed concentration profiles (dotted line) and from concentration profiles measured by a simulated 2 mm CCP probe (circles). Solid squares represent corrected sheet thickness values using equation (2.4), while the red markers indicate corrected sheet thickness values using the correction formula for a 1 mm probe (Lanckriet et al., 2014).	18
Figure 2.4: (a) Nonlinear least squares regression of the form given by equation (2.3), where the solid line is the best fit to the solid dots. The open circles were excluded from the fit. (b) Relative error between corrected (δs) and actual ($\delta s, real$) sheet thickness computed using equation (2.5) for the 2 mm CCP probe, with the 10% error cutoff at $\delta s, sens = 6.3$ mm (dotted line).	20
Figure 2.5: Example time-space color plots of (a, c) streamwise velocity and (b, d) logarithm base-10 of the acoustic intensity measurements during a topographic survey conducted (a, b) before and (c, d) after an experimental run. The black lines represent instantaneous profiles at intervals of approximately 3 s, where the time range on the x -axis (i.e., $t = 0 \sim 37$ s) is the duration of time over which the trolley traversed the 3-m long particle pit.....	26

Figure 2.6: Time evolution of (a-b) the cumulative transported particle volume derived from ACVP measurements (Equation (2.15)), and (c-d) particle transport rate (filtered at 1 Hz), for all N runs of the S3 (left column) and S1 (right column) conditions..... 28

Figure 2.7: Comparison between the total transported particle volume estimates for all runs during the S3 and S1 conditions, from the topographic surveys (V_{Topo} ; Equation (2.13)) and from ACVP measurements (V_{ACVP} ; Equation (2.15)). The solid line represents a 1:1 match, and the dashed lines correspond to an uncertainty of $\pm 30\%$ 29

Figure 2.8: Time-space plots of (a, b) streamwise ACVP velocity, (c, d) ACVP-derived concentration, (e, f) $CCP1mm$ -derived concentration, (g, h) $CCP2mm$ -derived concentration; and (i, j) bed interfaces derived from ACVP (blue line), $CCP1mm$ (red line) and $CCP2mm$ (black line) bed interfaces for trials S3b (left panel) and S1b (right panel) experiments. The black lines in (a, b) represent the instantaneous free-surface. The white lines are the bed interfaces estimated from ACVP and CCP data. The vertical dashed black lines denote the quasi-steady time interval over which the data are time-averaged..... 32

Figure 2.9: Time-space plots of ensemble-averaged (a, g) ACVP-derived concentration, (b, h) $CCP1mm$ -derived concentration, (c, i) $CCP2mm$ -derived concentration; and time-averaged (light blue) and ensemble-time-averaged (dark blue) concentration profiles from (d, j) ACVP, (e, k) $CCP1mm$, (f, l) $CCP2mm$ for S3 (a-f) and S1 (g-l) conditions. Only the time-span over which time-averages were computed is shown. The white lines outline the bed interfaces estimated from ACVP and CCPs data..... 35

Figure 2.10: Ensemble-time-averaged (a, d) velocity profiles, (b, e) concentration profiles, and (c, f) particle volume flux profiles for S3 (a – c, top row) and S1 (d – f, bottom row). In panels (b, e), the concentration was measured by the ACVP (+, plus), $CCP1mm$ (o, circles) and $CCP2mm$ (diamonds). The same concentration data are plotted in semi-logarithmic scale (insets) to highlight the suspension layer (i.e., $\phi < 0.08$). The blue lines in panels (c, f) are normalized, cumulatively integrated volume flux..... 37

Figure 2.11: (a, c) Time series of ensemble-averaged sheet flow thickness, δst , normalized by particle diameter, and (b, d) time-averages of the ensemble-averaged sheet flow thickness, δs , for the ACVP (blue), *CCP1mm* (red) and *CCP2mm* (black), with error bars of +/- one standard deviation shown in plots (b) and (d). The top row (a-b) corresponds to the S3 conditions while the bottom row (c-d) corresponds to the S1 condition. 39

Figure 3.1: (a) Barred beach profile and sediment pit, where the vertical dashed line (---) on the sandbar crest denotes the instrument frame location shown in panel (d). Surface piercing wave gauges are plotted as vertical lines with open squares, and ultrasonic wave gauges are plotted as solid squares. Two wave gauges in particular are labeled for use in Table 3.1 (*Hi*: $x = 17.7$ m; *Hbar*: $x = 43.3$ m). (b) Sediment pit installed on the sandbar crest, prior to being filled with sand. (c) Sediment pit filled with sand. (d) Instrumentation deployed on/over the sandbar, viewed from above. 46

Figure 3.2: Images of samples of the two sediments, (a) S1 and (b) S2, used during the BARSED experiments. 47

Figure 3.3: Statistics from sieve analysis for the two sediment types used during BARSED: S1 [top row] and S2 [bottom row]. Grain size is presented in phi-scale, where $\phi = -\log_2 D$ and D being grain diameter in units of mm. 48

Figure 3.4: Schematic of the near-bed instrumentation outlined by the dashed white box ($x = 45.1$ m) in Fig. 3.1d, viewed looking in the spanwise and onshore directions. 51

Figure 3.5: Example time series of data from one trial for case S1T7H60. (a) free surface elevation; (b) free stream velocity from *ADV1*; (c) Pressure head from the horizontal row of transducers 2 – 5 in the PPTA; (d) Horizontal pressure gradient, where negative is onshore directed; (e) volumetric sediment concentration from the CCP, where the solid white line is the top of the sheet layer, z_{top} , and the solid black line is the bottom of the sheet layer, z_{bott} ; (f) inset showing cross-shore variation in pressure head, where *P2* (blue), *P3* (red), *P4* (yellow) and *P5* (purple), where the subscript corresponds to the transducer # in Fig. 3.4. The grey rectangles in (a) – (d) and the dashed white lines in (e) denote the span of data plotted in the panels on the right. The concentration profile marked by the dashed-dot white line in (e) is plotted in Fig. 3.6. 56

- Figure 3.6: Example measured sheet flow concentration profile (Fig. 3.5e; dashed-dot white line) showing the best fit to equation (3.4) (blue curve), with free parameters: $\alpha = 3.68$, $\beta = 0.0087$ m, $cb = 0.624$ m³/m³ and $z_1 = -8.6$ mm. The vertical dashed line represents the upper sheet layer cutoff value of 0.08 m³/m³. 59
- Figure 3.7: Phase-averaged (a) – (c) streamwise near-bed velocity at $z^* = 15$ mm, and (d) – (l) time-space diagrams of sediment concentration, for nine different wave cases with S1 ($d_{50} = 0.17$ mm). The bottom of the sheet layer is marked (solid-dotted black line) in (d) – (l), where the solid black line signifies when phase-averaged sheet thickness was strictly resolvable by the CCP. Columns denote constant T , and the y-axis colors correspond to the line colors in (a) – (c). 62
- Figure 3.8: Slope of the least-square-error regression, Λ , versus number of iterations, for $z^* = 15$ mm. 66
- Figure 3.9: Maximum Shields parameter versus maximum non-dimensional sheet thickness. Empirical relationships are given for oscillatory flow tunnel data (Ribberink et al. (2008), solid line) and wave flume data (Schretlen (2012), dashed and dotted lines). Experimental data are provided for a range of oscillatory flow tunnel experiments (with and without a superimposed current) for fine to coarse sand (Δ) (Ribberink et al., 2008), as well as for large wave flume experiments with a flat sediment bed (fine to medium sand) (+) (Schretlen, 2012) and over a mobile sandbar (\times) (Van der Zanden, 2016). 68
- Figure 3.10: Phase-averaged results for case T7H60 with sediments S1 (blue) and S2 (red). (a) streamwise velocity at $z^* = 15$ mm and (b) free stream velocity; (c) – (d) sheet thickness; (e) – (f) Shields parameter; and (g) – (h) Sleath parameter using equations (3.12) (grey) and (3.19) (black). The dashed lines in (b – c) are the minimum reliable δs , which was only exceeded under the crest for S2. The standard deviation from the phase-averaged quantities are shown in grey envelopes in (a – b) and (g – h). 71
- Figure 3.11: Comparison of three different empirical expressions for grain roughness (normalized by median grain diameter) as a function of Shields parameter. Grain roughness values were computed using equation (3.11) (dots, \bullet) and equation (3.14) (triangles, \blacktriangle). 73

Figure 3.12: Comparison between least-squares-fits to data for both sediment sizes using a constant ks value as nominal grain roughness ($= 2.5d_{50}$), and mobile grain roughness based on observed sheet thickness and iteration for Λ (Equation (3.11)). Overall fits, Λ , are shown for both methods (grey lines), as well as separately for each grain size, $\Lambda S1$ (dashed blue lines) and $\Lambda S2$ (dotted red lines). The Shields parameter for all data points is computed using (3.6) and (3.7)..... 75

Figure 3.13: Wave friction factor as a function of ks/A , computed with equations (3.8) and (3.15), using data from BARSED and Schretlen (2012). 77

Figure 3.14: (a) Sheet thickness, (b) Shields parameter and (c) cross-shore momentum balance from equation (3.20), for wave case S1T7H60..... 85

Figure 3.15: Non-dimensional momentum terms ($I - III$) from (3.20) and Shields parameter versus non-dimensional sheet thickness for seven wave cases with sediment S1 (marked with an asterisk, *, in Table 3.1). (a) Local free stream acceleration (II), (b) pressure gradient (III), (c) free stream horizontal advective acceleration (I), (d) Shields parameter. The dot colors denote the magnitude of wave asymmetry, As , for each case (Table 3.1) and the dotted lines are the minimum resolvable sheet thickness by the CCP. The solid lines are a least-square fit with 100% error outlined with the two dashed lines. Note the x -axis limits are different for panel (d). 86

Figure 4.1: (a) Beach profile, sediment pit and two wave gauges, where the vertical dashed line on the sandbar crest indicates the cross-shore deployment location of the sensors. (b) Photo of instrumentation deployed on/over the sandbar. (c) Close-up view of the lower 5 of 6 ADVs ($ADV1 - ADV5$), with $ADV6$ labeled in (b). (d) Expanded view of the near-bed instrumentation at Site 4..... 97

Figure 4.2: Schematic of velocity and concentration measurement bin locations in the (a) entire still water column, and (b) lower 0.10 m of the water column. The shaded regions represent the general range over which measurements were obtained, where the colors correspond to the sensor color scheme in Fig. 4.1. The symbols within the shaded areas represent actual measurement bin locations. Different markers are used to distinguish FOBS probeA (white circles) from probeB (black circles). 102

Figure 4.3: Ensembles of sheet flow layer quantities in different vertical coordinate systems for case S1T7H60: Trial 14 (dashed lines), Trial 51 (dotted lines), and Trial 80 (solid lines) in the first three columns. Phase-averaged quantities are shown in the fourth column. (a – d) flume coordinates as in Fig. 4.1, (e – h) z^* -coordinate system, and (i – l) z' -coordinate system. Phase-averaged sediment concentrations are shown in pseudo-color plots in plots (h) and (l). 107

Figure 4.4: (a) Phase-averaged near-bed velocities for S1T5H50. (b) One ensemble of near-bed velocities measured between $0.01 < z^* < 0.03$ m for S2T5H50 (Trial 118, $n_{trial} = 8$). The level of lowest measured velocities by the ADPV for S2T5H50 is shown in (a) and (b) at $z^* = 0.011$ m (dashed black line). (c) Difference between velocities shown in (a) and (b) above the dashed line. Velocity profiles between the bottom (z_{bott}^* , thick black line) and top (z_{top}^* , thin black line) of the sheet flow layer were extrapolated using equation (4.6). The sheet flow layer bounds are phase-averaged in (a) and instantaneous in (b) and (c). 111

Figure 4.5: Cumulative frequency (%) of the average differences (for all eight S2 cases, 455,294 data points) between measured near-bed ($z^* < 0.04$ m) velocities for each ensemble in an S2 wave case and phase-averaged near-bed velocities for the corresponding S1 wave case (circles, \circ). The shaded areas highlight the percentage of data points contained within one (light grey) and two (dark grey) standard deviations of the sample mean. 112

Figure 4.6: Phase-averaged quantities ($N = 40$) for S1T7H50: (a) free-stream velocity, (b) profile of the root-mean-square cross-shore velocity, and boundary layer thickness, δ . Phase-averaged profiles of fluid velocity, sediment concentration, and sediment flux are shown for: (c) – (e) the entire measurement range, and (f) – (h) the lower 0.10 m of the water column. The colors of the curves in (c) – (h) correspond to the wave phase of the marker with the same color in panel (a), where squares (\blacksquare) denote the phases of maximum, minimum, zero up- and zero down-crossings in the free-stream velocity, while circles (\bullet) denote temporal midpoints between the squares. The elevation of the highest FOBS measurement is shown as a dashed line at $z' = 0.45$ m in plots (c) – (e). 114

Figure 4.7: Wave-averaged near-bed horizontal sediment flux profiles and sheet flow layer properties for the (a) – (c) S1 and (d) – (e) S2 wave cases. Columns are constant wave period, 5.0, 7.0 and 9.0 s, from left to right. The curves are colored based on the wave maker input signal wave height, given in the Case ID in Table 4.1. Markers represent wave-averaged elevations of the top, inflection point, and bottom of the sheet flow layer for each case..... 117

Figure 4.8: Phase-averaged suspended (blue) and sheet flow (red) sediment transport rates for six different wave cases: (a) S1T5H40, (b) S1T7H45, (c) S1T9H50, (d) S2T5H40, (e) S2T7H45 and (f) S2T9H50. The shaded areas represent one standard deviation. The fractional contributions of each component (q_{sss} versus q_{ssf}) to the total transport rate, q_s , given by equations (4.10) and (4.11), are provided in the lower panel of each plot (solid black curves). Equal contribution by both q_{sss} and q_{ssf} is represented with a dotted black line. 119

Figure 4.9: Ensemble-averaged net sheet flow versus suspended sediment transport rate. Grey error bars represent one standard deviation from the mean. Positive (negative) values indicate net onshore (offshore) sediment transport..... 122

Figure 4.10: Ensemble-averaged net sediment transport rate versus the percentage of the net transport contained within the sheet flow layer, φ_{sf} . Positive (negative) values indicate net onshore (offshore) sediment transport..... 124

Figure 4.11: Ensemble-averaged net sediment transport rate in the crest and trough half-cycles versus the percentage of the net transport contained within the sheet flow layer for each respective half-cycle. Positive (negative) values indicate net onshore (offshore) sediment transport..... 127

Figure 4.12: Ensemble-averaged net sheet flow versus suspended sediment transport rate within the crest and trough half-cycles. Grey error bars represent one standard deviation from the mean. Positive (negative) values indicate net onshore (offshore) sediment transport..... 128

Figure 4.13: Ensemble-averaged net sheet flow sediment transport rates versus the third moment of phase-averaged free-stream velocity (dimensional velocity skewness). Cases with sediment S1 ($d_{50} = 0.17$ mm) are shown with green circles, and S2 cases ($d_{50} = 0.27$ mm) are plotted as gold circles, with grey error bars representing one standard deviation from the mean. Also plotted are the linear regression (forced through origin) best fit to the data points (thick black line), and best fits to the data points plus/minus one standard deviation (dotted lines), along with a factor of two deviation from the best fit (thick grey lines). 132

Figure 4.14: [Top row] Gross suspended sediment transport rates for all NT ensembles (grey lines); phase-averaged gross suspended sediment transport rates (thick black lines), and corresponding peak values under the wave crests (right-triangles) and troughs (left-triangles). [Middle row] Color plots of phase-averaged normalized cumulatively integrated gross suspended sediment transport rates, $Q_{ssgross}$, as a function of relative water depth, z^*/h . The time-varying elevation of $z_{FOBS}, 20^*/h$ is shown with dashed lines. [Bottom row] (dots) Wave-averaged profiles of the phase-averaged color plots in (d) – (f). (dotted lines) exponential fits to the profiles of $Q_{ssgross}$, corresponding to the phases of maximum $q_{ssgross}$ in the crests and troughs; the right- and left-facing triangles are the phase-averaged data to which the crest and trough fits were performed, respectively. (solid lines) ensemble-average of all the exponential fits to $Q_{ssgross}$ from $0 \leq t/T \leq 1$. The intersection between the fitted curves labeled ‘a’, ‘b’ and ‘c’ in (g) – (i) and $z^*/h = 1$ are the baseline (\mathbb{F}_{ss}), upper (\mathbb{F}_{Uss}), and lower (\mathbb{F}_{Lss}) suspended sediment transport rate adjustment factors, respectively (see Table 4.4, footnotes)..... 140

Figure 4.15: Shaded patches represent the range of expected values considering: (i) multiple shapes of the velocity profile in the sheet flow layer ($0.25 \leq \alpha \leq 1$), and (ii) the upper and lower bounds of the suspended sediment transport adjustment factor, \mathbb{F}_{Uss} and \mathbb{F}_{Lss} , respectively (see Table 4.5). The black dots inside each patch are the baseline results using: (i) $\alpha = 0.50$, and (ii) the baseline suspended sediment transport adjustment factor, \mathbb{F}_{Bss} , for the corresponding wave period. The black lines connected to the colored markers show the changes from (a) Fig. 4.9 and (b) Fig. 4.10..... 146

Figure A.1: Time-space plots of (a) streamwise velocity, (b) ACVP-derived concentration, (c) *CCP1mm*-derived concentration, (d) *CCP2mm*-derived concentration; and (e) bed interfaces derived from ACVP (blue line), *CCP1mm* (red line) and *CCP2mm* (black line) bed interfaces for experiment S3a. The black dashed lines represent the instantaneous free-surface. The white lines outline the bed interfaces estimated from ACVP and CCP data. The vertical dashed black lines signify the time spans over which time-averages were computed. 173

Figure A.2: Time-space plots of (a) streamwise velocity, (b) ACVP-derived concentration, (c) *CCP1mm*-derived concentration, (d) *CCP2mm*-derived concentration; and (e) bed interfaces derived from ACVP (blue line), *CCP1mm* (red line) and *CCP2mm* (black line) bed interfaces for experiment S3c. The black dashed lines represent the instantaneous free-surface. The white lines outline the bed interfaces estimated from ACVP and CCP data. The vertical dashed black lines signify the time spans over which time-averages were computed. 174

Figure A.3: Time-space plots of (a) streamwise velocity, (b) ACVP-derived concentration, (c) *CCP1mm*-derived concentration, (d) *CCP2mm*-derived concentration; and (e) bed interfaces derived from ACVP (blue line), *CCP1mm* (red line) and *CCP2mm* (black line) bed interfaces for experiment S3d. The black dashed lines represent the instantaneous free-surface. The white lines outline the bed interfaces estimated from ACVP and CCP data. The vertical dashed black lines signify the time spans over which time-averages were computed. 175

Figure A.4: Time-space plots of (a) streamwise velocity, (b) ACVP-derived concentration, (c) *CCP1mm*-derived concentration, (d) *CCP2mm*-derived concentration; and (e) bed interfaces derived from ACVP (blue line), *CCP1mm* (red line) and *CCP2mm* (black line) bed interfaces for experiment S3e. The black dashed lines represent the instantaneous free-surface. The white lines outline the bed interfaces estimated from ACVP and CCP data. The vertical dashed black lines signify the time spans over which time-averages were computed. 176

Figure A.5: Time-space plots of (a) streamwise velocity, (b) ACVP-derived concentration, (c) *CCP1mm*-derived concentration, (d) *CCP2mm*-derived concentration; and (e) bed interfaces derived from ACVP (blue line), *CCP1mm* (red line) and *CCP2mm* (black line) bed interfaces for experiment S3f. The black dashed lines represent the instantaneous free-surface. The white lines outline the bed interfaces estimated from ACVP and CCP data. The vertical dashed black lines signify the time spans over which time-averages were computed. 177

Figure A.6: Time-space plots of (a) streamwise velocity, (b) ACVP-derived concentration, (c) *CCP1mm*-derived concentration, (d) *CCP2mm*-derived concentration; and (e) bed interfaces derived from ACVP (blue line), *CCP1mm* (red line) and *CCP2mm* (black line) bed interfaces for experiment S1a. The black dashed lines represent the instantaneous free-surface. The white lines outline the bed interfaces estimated from ACVP and CCP data. The vertical dashed black lines signify the time spans over which time-averages were computed. 178

Figure A.7: Time-space plots of (a) streamwise velocity, (b) ACVP-derived concentration, (c) *CCP1mm*-derived concentration, (d) *CCP2mm*-derived concentration; and (e) bed interfaces derived from ACVP (blue line), *CCP1mm* (red line) and *CCP2mm* (black line) bed interfaces for experiment S1c. The black dashed lines represent the instantaneous free-surface. The white lines outline the bed interfaces estimated from ACVP and CCP data. The vertical dashed black lines signify the time spans over which time-averages were computed. 179

ABSTRACT

A novel large wave flume experiment was conducted on a fixed, barred beach with a sediment pit on the sandbar, allowing for the isolation of small-scale bed response to large-scale wave forcing. Concurrent measurements of instantaneous sheet flow layer and suspended sediment concentration profiles, pore-pressure gradients, near-bed velocity profiles, and velocity profiles spanning the whole water column were obtained on a sandbar. Two sediment distributions were used with median grain diameters, d_{50} , of 0.17 and 0.27 mm. Sheet flow occurred primarily under wave crests, where sheet thickness increased with increasing wave height. A proportionality constant, Λ , was used to relate maximum Shields parameter to maximum sheet thickness (normalized by d_{50}), with bed shear stress computed using the quadratic drag law. An enhanced sheet layer thickness was apparent for the smaller sediment experiments ($\Lambda = 18.7$), when directly compared to closed-conduit oscillatory flow tunnel data ($\Lambda = 10.6$). However, Λ varied significantly ($5 < \Lambda < 31$) depending on the procedure used to estimate grain roughness, k_s , and wave friction factor, f_w . Three models for k_s were compared (keeping the model for f_w fixed): constant $k_s = 2.5d_{50}$, and two expressions dependent on flow intensity, derived from steady and oscillatory sheet flow experiments. Values of k_s/d_{50} varied by two orders of magnitude and exhibited an inverse relationship with Λ , where $\Lambda \sim 30$ for k_s/d_{50} of $O(1)$ while $\Lambda \sim 5$ for k_s/d_{50} of $O(100)$. Two expressions for f_w were also tested (with the steady-flow-based model for k_s), yielding a difference of 69% ($\Lambda \sim 13$ versus $\Lambda \sim 22$). Intra-wave and wave-averaged observations of sediment flux profiles and transport rates in the lower half of the water column on the

sandbar crest are also presented for 19 different wave and sediment cases. The total sediment transport rate was partitioned into suspended sediment (SS) and sheet flow (SF) components to quantify the relative contributions of SS and SF to the total sediment transport rate. Net suspended sediment transport rates were greater than net sheet flow transport rates for the positive half-cycle in 14 of 19 cases, compared to 100% (19 of 19) for the negative half-cycle. Total net sheet flow transport was greater than net suspended sediment transport for 13 of the 19 wave cases. The dominant mode of transport was determined from the ratio of net SF to net SS transport rate. In general, net total transport rate was negative (offshore) when SS dominated and positive (onshore) when SF dominated. Net SF transport rate correlated well with increasing near-bed third velocity moments ($r^2 = 0.71$), and no trend was observed related to the influence of sediment size.

Chapter 1

INTRODUCTION

1.1 Surf Zone Sandbar Migration

Surf zone sandbars are a nearshore feature present along many coasts around the world, in both sea- and swell-dominated environments (Ruessink et al., 2003). Sandbars tend to exhibit spatial variability in both the cross-shore and longshore, across a wide range of time scales, from several hours to decades (Gallagher et al., 1998; Lippmann & Holman, 1990; Wijnberg, 2002; Wijnberg & Terwindt, 1995; Wright et al., 1985; Wright & Short, 1984). The dynamic interaction between environmental forcing and coastal morphology plays an important role in the spatial and temporal variability of the nearshore region (Pape et al., 2009; Ruessink et al., 2009; Ruggiero et al., 2005). Figure 1.1 depicts four different temporal scales of morphology over which considerable change in sandbar morphometric parameters may be observed (see Ruessink and Kroon, 1994 for a description of important morphometric parameters). Of the four scales, sub-seasonal is further divided into three sub-scales.

On the shortest time scale, during storms, energetic wave breaking over the sandbar serves to suspend sediment, which is carried offshore by strong near-bed, offshore-directed mean flow (undertow). As a result, the sandbar migrates rapidly offshore, at rates up to 1 – 2 m/hr (Gallagher et al., 1998; Sallenger Jr et al., 1985; Thornton et al., 1996). Conversely, onshore bar migration generally occurs at a much slower rate and persists over a longer period of time (days – weeks), during prolonged episodes of more quiescent wave conditions (Gallagher et al., 1998; Sallenger Jr et al.,

1985; Van Maanen et al., 2008). The most pronounced onshore sandbar migration events occur during beach recovery following a storm (Gallagher et al., 1998; Sallenger Jr et al., 1985; van Maanen et al., 2008). In such cases, the sandbar migration rate in the onshore direction typically occurs at a much slower rate compared to offshore migration, at around 1 – 2 m/day, based on observations at numerous barred beaches, in both sea and swell dominated environments (Van Enckevort & Ruessink, 2003).



Figure 1.1: Flow chart outlining several distinct time scales for sandbar evolution.

The fundamental processes behind onshore sandbar migration are a combination of several factors. Ongoing development of beach profile evolution models in the past 15 – 20 years has been critical in helping to gain a deeper understanding of the underlying mechanisms related to onshore migration (Plant et al., 2004; Ruessink & Kuriyama, 2008). Hoefel and Elgar (2003) showed improvements in the prediction of onshore sandbar migration, as well as overall on/offshore sandbar migration spanning 45 days of observations from the Duck94 field campaign (Gallagher et al., 1998), by accounting for acceleration skewness under forward-pitched breaking waves in the surf zone (Drake

& Calantoni, 2001). Using the same Duck94 dataset, Henderson et al. (2004) found boundary layer streaming and Stokes drift to be important during onshore migration. Near-bed pressure gradients observed in the field have been identified as another mechanism for onshore sandbar migration (Foster et al., 2006).

Significant progress has been made in modelling sandbar migration on short-term (hours to days), episodic time scales; however, operational, process-based morphological models generally exhibit lower skill in predicting medium- and longer-term time scales over which onshore migration events are observed (Plant et al., 2004; Roelvink & Brøker, 1993). In cases where beach profile evolution models have demonstrated capabilities to predict onshore sandbar migration (Fernández-Mora et al., 2015; Hoefel & Elgar, 2003; Ruessink et al., 2007), the model parameters are typically tuned to a specific onshore migration event (Gallagher et al., 1998). In addition, modeling studies almost always neglect alongshore variability in bathymetry (Plant et al., 2006), probably lack the inclusion of important physics (Hsu et al., 2006), and tend towards zero skill (i.e., errors in prediction are as large as the observed changes) for onshore migration events exceeding 17 days (Plant et al., 2004). The last decade has also seen efforts to improve upon the deficiencies intrinsic of process-based models with the development of empirical models relating cross-shore sandbar migration to wave forcing (Pape et al., 2010) and recurrent neural networks (Pape et al., 2007).

1.2 Outline

This dissertation is composed of results from two separate laboratory experiments conducted with the aim of providing a better understanding of the interactions between sheet flow and suspended sediment transport processes. State-of-

the-art sensing techniques were utilized in both experiments to collect hydrodynamic and sediment transport data.

Chapter 2 covers detailed measurements of particle concentration and velocity profiles under gravity-current driven sheet flow transport conditions involving two fundamentally different measurement systems. The two systems have been used more frequently in the last decade to quantify sediment transport processes. Therefore, the main focus of the experiments (PARROT) was to provide a comparative data set under controlled conditions. Chapter 2 outlines the capabilities and limitations of the two measurement technologies, one of which was prominently used in the work discussed in the two chapters that follow (Chapter 3 and Chapter 4). The work of Chapter 2 is in preparation to be submitted to *Journal of Geophysical Research: Earth Surface*. The other primary author of the works presented in Chapter 2 was Guillaume Fromant, whose contributions (amounting to about 30%) were related to the collection and processing of data using the acoustic concentration and velocity profiler (ACVP). Some items were re-produced with the permission of Dr. Fromant (statement included in Appendix B).

Ruessink and Kuriyama (2008) identified the need for detailed near-bed measurements of sediment transport on a sandbar in order to improve long-term predictions of coastal morphology. Chapter 3 introduces a novel collaborative, field-scale laboratory experiment (BARSED) that is among the most detailed observations of sediment transport on a sandbar. New and innovative sensors were used to simultaneously measure highly-resolved fluid velocities, sediment concentrations and pore pressures. The findings provided some of the first field-scale experimental evidence, complemented by the work of Anderson et al. (2017), to strongly support

recent conjectures regarding competing mechanisms driving sandbar migration under wave action (Fernández-Mora et al., 2015). This research focuses on the parameterization of several physical quantities that are important in sheet flow sediment transport including bed shear stress, wave friction factor and grain roughness, where sheet flow observations are tested against several empirical formulations. This work is published in *Journal of Geophysical Research: Oceans* (volume 122, issue 6, <https://doi.org/10.1002/2016JC012438>, 2017).

Chapter 4 incorporates suspended sediment observations from the BARSED experiment to evaluate cross-shore sediment transport and bed response over a surf zone sandbar under field-scale wave conditions. The intra-wave components of hydrodynamics and sediment transport quantities is extracted through phase-averaging. Relative contributions of the sheet flow and suspended sediment transport components to the total net transport rate under various wave forcing conditions are quantified. The dominant mode of sediment transport (suspended load versus sheet flow) is identified for each forcing condition as a function of wave phase, as well as for the net transport rate. Further distinctions are made for the positive (crest) and negative (trough) half-cycles of the waves. The work of Chapter 4 is under preparation for submission to *Journal of Geophysical Research: Oceans*.

The hope is that the data sets generated from the two experimental campaigns (PARROT and BARSED) will have an immediate impact on coastal science and engineering, laying the groundwork for future experiments and field investigations, while also serving as a benchmark dataset for modelers aiming to validate and improve nearshore predictive sediment transport models. An overall summary of both experiments and some main conclusions are provided in Chapter 5.

Chapter 2

QUASI-STEADY SHEET FLOW MEASUREMENT PERFORMANCES OF HIGH-RESOLUTION ACOUSTIC AND CONDUCTIVITY PROFILERS

2.1 Introduction

Over the past two decades, considerable research efforts have been dedicated to the understanding and modeling of sediment transport processes under energetic flow forcing conditions for which bed load moves as a sheet flow. In this context, it is widely accepted that the geophysical community suffers from a technological lack of high-resolution flow measurement tools adapted to the study of sediment transport physics in environmental flows (Liu et al., 2016; Roelvink & Brøker, 1993). Whether the sediment transport is driven by gravity, density, tidal currents, surface waves or internal waves in river, estuarine or coastal flows, the ability to profile sediment transport across the entire bottom boundary layer over a mobile sediment bed is currently limited to a few measurement technologies. The limited measurement capabilities has limited advances in process-based modeling of sediment transport in contrast to empirical models commonly implemented in numerical engineering codes applied for long-term predictions of morphological evolution. Such predictions are known to be subject to large uncertainties and errors which is a main research concern in the context of adaptation to climate change.

Two-phase flow modeling has been developed to account for the dynamic interactions between fluid and solid phases (Berzi, 2011; Chiodi et al., 2014; Hsu et al., 2004; Jackson, 1997; Jenkins & Hanes, 1998; Liu et al., 2016; Revil-Baudard &

Chauchat, 2013). This approach considers the detailed fluid momentum and sediment concentration mixing processes occurring in the sheet flow layer, dominated by particle-particle interactions, up to the turbulence driven dilute suspension layer. The theoretical modeling framework include all possible fluid-particle interaction mechanisms; however, validation and optimization require advanced high-resolution measurement tools capable of sediment flux profiling (as the product of concentration and velocity profiles) at turbulent flow scales across both the suspension and sheet flow layers.

High particle concentration ($0.08 < \phi < 0.53$; where ϕ is volumetric concentration) and limited vertical thickness (of the order of the particle size) of the sheet flow layer makes it particularly difficult to accurately measure the particle velocities and concentrations with conventional non-intrusive optical and acoustic flow measuring tools. The difficulty is mainly because light and sound propagation are subject to strong scattering-dominated attenuation. Only several datasets of high-resolution sheet flow measurements are available. Time-averaged volumetric concentration and velocity profiles were measured in small-scale pipe flow experiments using gamma-ray and conductivity techniques, respectively (Daniel, 1965; Horikawa et al., 1982; Nnadi & Wilson, 1992; Pugh & Wilson, 1999). Novel techniques were developed later, aiming at measuring local concentration and streamwise velocity measurements involving the use of point-wise capacitance probes (Horikawa et al., 1982; Ribberink & Al-Salem, 1995; Sumer et al., 1996), borescopic techniques (Cowen et al., 2010), two-component (2C) particle velocity and mean concentration profiles through video imaging (Armanini et al., 2005; Capart & Fraccarollo, 2011; Spinewine et al., 2011) and point-wise intrusive conductivity meters with automated bed level tracking capability (Van der Zanden et al., 2015; Van der Zanden, van der A, Hurther,

Cáceres, O'Donoghue, Hulscher, et al., 2017). Only recently have advanced acoustic and conductivity techniques been developed (Lanckriet et al., 2013; Mieras et al., 2017a) and used (Hurther & Thorne, 2011; Mieras et al., 2017a; Naqshband, Ribberink, Hurther, & Hulscher, 2014; Revil-Baudard et al., 2015) to profile such challenging media at sufficiently high temporal ($O(0.1\text{ s})$) and spatial ($O(0.001\text{ m})$) resolutions to measure the multi-scale sheet flow sediment transport processes.

This chapter reports on detailed measurements of particle concentration and velocity profiles under gravity-current driven sheet flow transport conditions involving two fundamentally different measurement systems: an Acoustic Concentration and Velocity Profiler (ACVP) and Conductivity Concentration Profilers (CCP) at two vertical resolutions (1 mm versus 2 mm). This study marks the first use of the 2 mm CCPs, as well as it is the first time the CCP technology is used with light-weight acrylic particle flows driven by steady, unidirectional gravity currents. i.e., The main objective of this study is to evaluate the performances and limitations of the above mentioned measurement techniques, the ACVP and the CCPs, for (i) measuring time-resolved and average sediment concentration profiles over the entire sediment transport layer, and for (ii) tracking the temporal bed level evolution and sheet flow layer thickness.

2.2 PARROT Experiment

2.2.1 Experimental Facility and Flow Conditions

The experiments were carried out at the Laboratory of Geophysical and Industrial Flows (LEGI) in the LEGI/ENSE3 tilting flume (Figure 2.1). The experimental facility is extensively described in (Revil-Baudard et al., 2015; Revil-Baudard & Chauchat, 2013). The flume is $L = 10\text{ m}$ long and $W = 0.35\text{ m}$ wide, with an

adjustable bed slope S_0 . A particle pit that is $L_p = 3$ m long by $z_p = 0.11$ m deep is mounted at the channel bed 2 m upstream of the channel outlet (Figure 2.1).

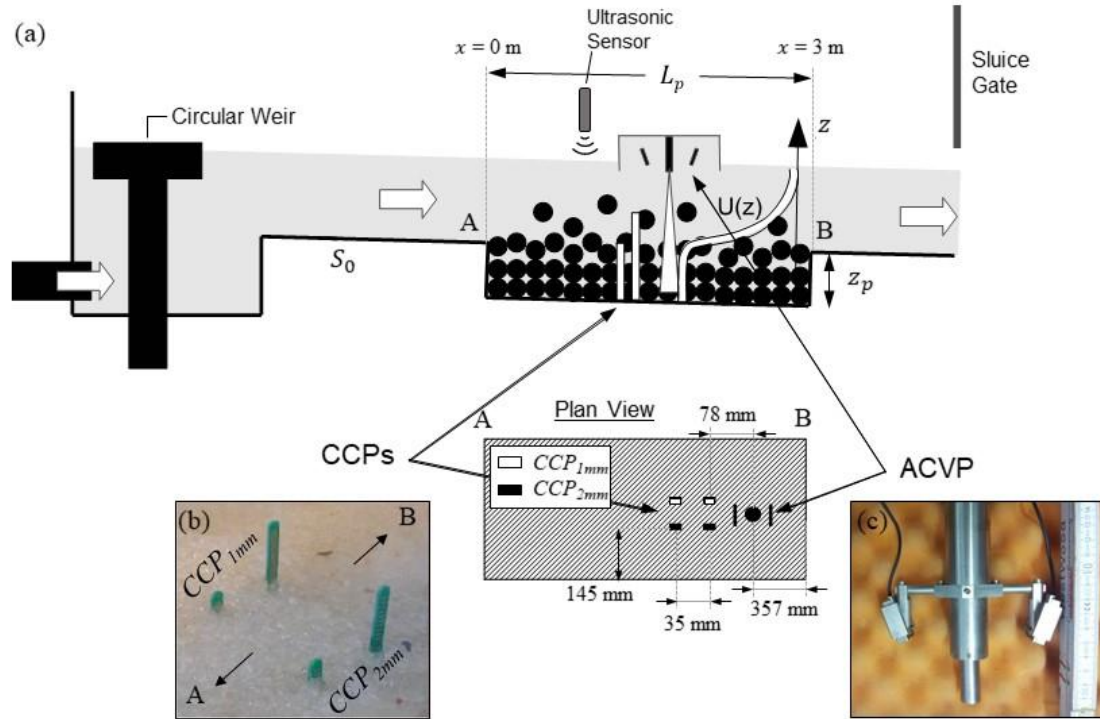


Figure 2.1: (a) Sketch of the experiment under active flow and location of the instruments. A and B delineate the upstream and downstream edges of the sediment pit, at $x = 0$ m and $x = 3$ m, respectively. (b) Picture of the CCP probes deployed before an S3 run. (c) Picture of the ACVP.

Irregularly shaped Poly-Methyl MethAcrylate (PMMA) particles were used with a density of $\rho_p = 1,192$ kg/m³. Two particle sizes were used in separate experiments, the coarse S3 and fine S1 particles with median particle diameters, d_p , of 3.0 and 1.0 mm, respectively. The particle size distribution was well-sorted with a relative standard deviation (Moate & Thorne, 2013), σ_0 , of 0.015 for both particles,

under the assumption of a log-normal distribution. The mean settling velocity w_s was 5.5 cm/s for S3 and 2.0 cm/s for S1 (see Table 2.1). A specific flow condition (i.e., water discharge and bed slope) was set for each particle size to achieve similar Shields' numbers. The bed slope was set to 0.0025 for S3 and to 0.0050 for S1, with an average water discharge flow rate, Q_f , of 0.028 m³/s and 0.021 m³/s for S3 and S1, respectively (Table 2.1).

Table 2.1: Summary of experiments, particle sizes, and flow parameters.

	N	d_p	S_0	w_s	u_*	H_f	Q_f	U	θ	$\frac{w_s}{u_*}$
	(-)	(mm)	(-)	(cm/s)	(cm/s)	(m)	(m ³ /s)	(m/s)	(-)	(-)
S3	6	3.0	0.0050	5.5	4.1	0.14	28	0.57	1.2	1.3
S1	3	1.0	0.0025	2.0	2.1	0.13	21	0.46	1.7	1

2.2.2 Instrumentation Setup

The ACVP was positioned at the downstream end of the particle pit ($x = 2.64$ m) to collect profiles of velocity and sediment concentration along the flow normal z -direction over a distance of 0.15 m above the initial flat bed level (Figure 2.1). Two pairs of CCPs were installed to measure concentration profiles along the flow normal z -direction. The vertical resolution was 1 mm for the pair of CCP_{1mm} probes, and 2 mm for the pair of CCP_{2mm} probes. Each pair of CCPs was aligned in the streamwise direction, 0.145 m away from the flume walls, and 0.035 m apart from each other in the streamwise direction (Figure 2.1b). The two CCPs with the same resolution were

mounted with a vertical offset, overlapping by a few millimeters to increase the total vertical profiling range. The downstream probes of each CCP pair were positioned 0.078 m upstream from the ACVP at $x = 2.56$ m. The streamwise shift avoided acoustic echoes from the CCP probes in the ACVP signal. An ultrasonic limnimeter was mounted on the trolley to measure the instantaneous water surface. The signal of the ultrasonic limnimeter was simultaneously recorded by the ACVP and the CCP systems allowing time referencing of all data in the post-processing phase.

2.2.3 Experiment Protocol

The experimental protocol described in Revil-Baudard et al. (2015) was applied for each experimental run (Figure 2.1). Before the start of each run, the particle pit was filled with sediments, manually compacted and leveled as a flat uniform sediment bed of constant slope. In order to minimize the duration of transient flow until the target discharge was reached, the flume was filled slowly with no particle movement until the still water depth was greater than the desired level. At this stage, the sluice gate at the flume outlet was still closed and a circular weir located at the upstream end of the flume bypassed any additional water discharge, resulting in very low flowrate over the test section. An initial topographic survey of the particle pit was carried out by towing the ACVP mounted on a trolley, along the flume centerline between positions B and A (see Figure 2.1). Survey data were used to estimate the initial sediment volume assuming a spanwise-uniform flat bed with a constant packed bed porosity of 45%. The two downstream CCP probe pairs were then manually raised to the desired vertical positions from beneath the flume. The probes were equipped with a cylindrical collar to ensure identical vertical positioning for each repeated run. The vertical position of each pair of CCPs was sufficient to cover the entire thickness of the mobile sediment layer (i.e., from

the undisturbed flow bed to the top of the dilute suspension layer). The ACVP was positioned at $x = 2.64$ m (Figure 2.1) before starting the experiment. An experimental run was initiated by rapidly opening the sluice gate at the outlet of the channel, provoking a sudden water level drop that deactivated the circular overflow-weir and transferred the entire flow discharge into the flume. The start time (i.e., $t = 0$ s) was defined for each run as the instant the water level – recorded by the ultrasonic sensor – dropped to 95% of its original level.

After a period of transient flow lasting about 30 s (Revil-Baudard et al., 2015), the fluid flow and the particle transport layer became fully developed with a normal flow depth of $H_f = 0.14$ m (0.13 m) and a mean bulk flow velocity of $U = 0.46$ m/s (0.57 m/s) for S3 (S1). After a duration of about two minutes, the sluice gate was closed to end the run and the original still water level, for which the circular weir at the upstream end of the flume bypassed the discharge, was recovered. A post-experiment topographic survey was conducted by traversing the ACVP along the flume from B to A (see Figure 2.1a). The topographic surveys are used to estimate the total transported volume of sediments for each run (using the assumption of spanwise topographic uniformity). After each run, the height of the CCP probes, relative to the bottom of the particle pit, was measured. The experimental protocol was repeated for $N = 6$ runs for the coarse particles (S3) and $N = 3$ runs for the fine particles (S1) which provided a sufficient amount of data to minimize the bias errors of the statistical flow quantities. For each run, $z = 0$ m was defined as the bed elevation at $t = 0$ s.

2.3 High-resolution Measurement Systems

2.3.1 Conductivity Concentration Profiler (CCP)

2.3.1.1 Concentration Measurements

The CCP measures electrical conductivity of a fluid-particle mixture, σ_m , which is related to volumetric particle concentration via Archie's Law (Archie, 1942; Lanckriet et al., 2013),

$$\frac{1}{F} = \frac{\sigma_m}{\sigma_f} = (1 - \phi)^m, \quad (2.1)$$

where F is the form factor, σ_f is the conductivity of the fluid, and m is a calibration factor. Each CCP probe has 32 plate electrodes spaced at either 1 or 2 mm vertical increments, resulting in a vertical profile of volumetric particle concentration, $\phi(z)$, spanning either 29 or 58 mm, respectively. All of the CCPs recorded profiles at 8 Hz. An m -value was determined for each CCP and experiment using in-situ conductivity data and the two-point calibration method outlined by Lanckriet et al. (2013) where $\phi_0 = 0.55 \text{ m}^3/\text{m}^3$ was used as the volumetric concentration of the fully packed bed. The average value of m (\bar{m}) across all experiments was 1.3 (1.5) for CCP_{1mm} (CCP_{2mm}). Values for \bar{m} were smaller for the coarse particles (S3) compared to the fine particles, (S1) (Table 2.2). Standard deviations, σ_{std} , about \bar{m} were larger for S3 compared to S1 (Table 2.2), likely due to lower homogeneity of $\phi(z)$ in the packed bed across experiments for the more irregularly shaped grains of S3. The effect of lower homogeneity with S3 is exacerbated for the 1 mm CCPs (i.e., $\sigma_{std,S3} = 5.5\sigma_{std,S1}$), because the presence of a large void space near a CCP_{1mm} probe influences twice as many measurement bins versus CCP_{2mm} probes.

Table 2.2: CCP calibration parameters.

	CCP_{1mm}		CCP_{2mm}	
	\bar{m}	σ_{std}	\bar{m}	σ_{std}
S3	1.2	0.11	1.5	0.08
S1	1.5	0.02	1.6	0.03

2.3.1.2 Bed Interface Detection and Sheet Layer Thickness

The bed interface, $z_b(t)$, was determined by fitting a composite power law and linear curve to the convolution of each instantaneous CCP concentration profile with a boxcar window (width of 3 measurement bins) to identify the sharp shoulder transition in each sheet flow concentration profile (Lanckriet et al., 2014; Mieras et al., 2017a; O’Donoghue & Wright, 2004a). The top of the sheet flow layer, $z_t(t)$, was determined by locating the 8% volumetric concentration contour ($\phi = 0.08 \text{ m}^3/\text{m}^3$). At concentrations greater than $0.08 \text{ m}^3/\text{m}^3$, the average distance between spherical particles is less than one particle diameter (Bagnold, 1956), and particle-particle interactions become important. The top of the sheet flow layer was obtained from the same convolved instantaneous CCP concentration profiles used to identify the bed interface. The difference in elevation between the top and bottom of the sheet layer yields the so-called “observed” sheet layer thickness, $\delta_{s,sens}(t)$,

$$\delta_{s,sens}(t) = z_t(t) - z_b(t). \quad (2.2)$$

However, the finite nature of the vertical measurement extent for the CCPs means that observed sheet thicknesses may be over-estimated, relative to the true sheet thickness, and a correction formula must be used to account for this. Because this was the first

experiment wherein the 2 mm CCP probes were used, a new correction formula was developed to convert observed sheet layer thickness to “actual” sheet layer thickness, δ_s . The sheet layer thickness correction formula for the 1 mm CCP probes is given in Lanckriet et al. (2014), with details of the 2 mm CCP probe correction formula derivation and evaluation of errors provided in Section 2.3.1.3.

2.3.1.3 Sheet Layer Thickness Correction Formula and Measurement Volume for CCP2mm

The measurement volume for the 1 mm CCPs was evaluated using a numerical model to solve for the electric field around a CCP probe (Lanckriet et al., 2013). The lateral extent of the measurement volume for the 1 mm probes was an ellipsoid with semi-axes lengths of 8.7 mm (x) and 8.4 mm (y). The vertical extent of the overall measurement volume is a function of the sheet flow layer thickness, δ_s . Sheet layer thickness can be over-estimated as a result of profile smoothing due to the finite extent of the measurement volume of the CCP. Consequently, there is a minimum sheet flow thickness that can be reliably observed by the CCP, below which measurements are dominated by smoothing. A correction formula must be used to adjust observed sheet flow thicknesses, $\delta_{s,sens}$, to real sheet flow thicknesses, $\delta_{s,real}$, where the minimum real sheet flow thickness that can be resolved with the 1 mm probe is 5 mm (Lanckriet et al., 2014).

The numerical model developed by Lanckriet et al. (2013) was used to evaluate the lateral extent of the measurement volume and minimum reliable sheet flow thickness for the CCP probe with 2 mm plate spacing. The spatial extent of the computational domain was necessarily doubled, $0 \text{ mm} \leq x \leq 25.4 \text{ mm}$, $0 \text{ mm} \leq y \leq 25.4 \text{ mm}$, and $-16.26 \text{ mm} \leq z \leq 16.26 \text{ mm}$. The same multigrid approach was followed, but due to a

factor 8 increase in computational nodes from doubling the extent of the domain, the finest grid resolution (Grid 3 in Lanckriet et al., 2013) was 0.169 mm in all three dimensions. To ensure that the larger grid resolution was still adequate, the simulation results of the 1 mm CCP from Lanckriet et al. (2013) were re-analyzed on the coarser grid (Grid 3). The lateral extent of the measurement volume decreased by 0.1 mm, which is a difference of just 1%. The lateral measurement extent is defined as the region where the current density, J , has decayed to 1% of its original value (i.e., $J/J_{max} = 0.01$). Following this definition, the lateral extent for the CCP with 2 mm plate spacing extends from $-15.8 \text{ mm} \leq x \leq 15.8 \text{ mm}$ and $-15.6 \text{ mm} \leq y \leq 15.6 \text{ mm}$ (Figure 2.2), containing 86% of the total current (compared to 88% for CCP_{1mm}). Overall, the area of the lateral measurement extent is 3.4 times greater for CCP_{2mm} than for CCP_{1mm} .

The electric field around the 2 mm CCP probe was then simulated following the same piecewise-linear concentration profile approach as in Lanckriet et al. (2013). The conductivity field for each piecewise-linear profile was computed with equation (2.1), using a concentration of $\phi_0 = 0.55$ in the bed and an m -value of 1.5 (average of all 9 experiments with S3 and S1, Table 2.2). Fourteen different prescribed thicknesses of the linear transition from the packed bed to clear water were modeled, ranging from 0 to 20 mm. For each prescribed transition thickness, the conductivity profile was traversed vertically at 1 mm increments (compared to 0.5 mm increments with the CCP_{1mm} model; Lanckriet et al., 2013). Vertically shifting the conductivity profile is equivalent to measuring a fixed conductivity profile with electrodes at different elevations, which is what occurs during an actual CCP measurement cycle (see (Lanckriet et al., 2013) for details). The prescribed (piecewise-linear) and measured

(with the simulated CCP) conductivity profiles were converted to concentration profiles using equation (2.1).

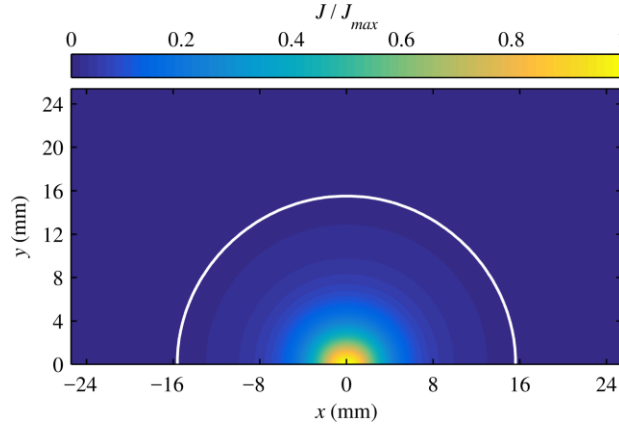


Figure 2.2: Normalized current density field results from the numerical simulations of the electric field around CCP_{2mm} . The region inside the white curve (0.01 contour) contains 86% of the total current.

Sheet layer thickness was computed for each of the 14 prescribed ($\delta_{s,real}$) and measured ($\delta_{s,sens}$) concentration profiles following the definition given by equation (2.2) (Figure 2.3). The measured sheet flow thickness of the modeled concentration profile for a prescribed transition thickness of 6 mm was $\delta_{s,sens} = 6.8$ mm, which is 53% larger than the actual sheet flow thickness $\delta_{s,real} = 4.5$ mm. For prescribed transition thicknesses less than 6 mm, the measured sheet flow thickness is dominated by smoothing (i.e., it is not sensitive to the prescribed transition thickness). Measured sheet flow thickness for the cases with a transition thickness of 6 mm or greater follow the trend of actual sheet flow thickness (Figure 2.3; circles vs. dotted line), but are over-estimated and require a correction formula to convert measured sheet flow thickness to ‘true’ sheet flow thickness.

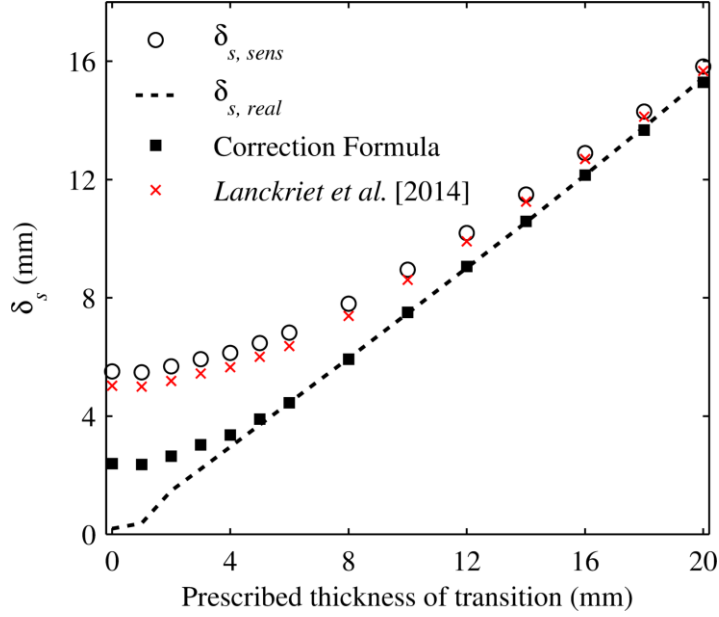


Figure 2.3: Prescribed transition thicknesses versus sheet thickness determined from prescribed concentration profiles (dotted line) and from concentration profiles measured by a simulated 2 mm CCP probe (circles). Solid squares represent corrected sheet thickness values using equation (2.4), while the red markers indicate corrected sheet thickness values using the correction formula for a 1 mm probe (Lanckriet et al., 2014).

Corrected sheet flow thicknesses from the 2 mm CCP model simulations were over-estimated when applying the correction formula for a 1 mm CCP probe (Lanckriet et al., 2014) (Figure 2.3). Therefore, a second, new sheet flow thickness correction formula was developed for the 2 mm CCP probes, using the results of the model simulations and a relationship of the form,

$$\frac{\delta_{s,sens}}{\delta_{s,real}} - 1 = \frac{1}{A(\delta_{s,sens})^2 - B(\delta_{s,sens}) + C}, \quad (2.3)$$

with $\delta_{s,sens}$ and $\delta_{s,real}$ expressed in meters. The term on the left hand side of equation (2.3) is a measure of the magnitude of the smoothing effect, vanishing to zero for no smoothing (i.e., $\delta_{s,sens} = \delta_{s,real}$). Nonlinear least squares regression was carried out to

determine A , B and C using only sheet thickness values for model runs with prescribed transition thicknesses greater than 5 mm (Figure 2.4a; solid black dots), below which, sheet thickness is dominated by smoothing. The smoothing effect is removed by applying the following correction formula to data measured with CCP_{2mm} (Figure 2.3):

$$\delta_s = \delta_{s,sens} * \left(\frac{1}{208 \times 10^3 (\delta_{s,sens})^2 - 1723 (\delta_{s,sens}) + 3.9} + 1 \right)^{-1} \quad (2.4)$$

again, with δ_s and $\delta_{s,sens}$ expressed in meters. The threshold for reliable corrected sheet flow thicknesses with the 2 mm CCP probe was determined by examining the relative error, ε , between corrected (δ_s) and actual ($\delta_{s,real}$) sheet flow thickness values,

$$\varepsilon = \frac{|\delta_s - \delta_{s,real}|}{\delta_{s,real}}. \quad (2.5)$$

The minimum reliable sheet flow thickness that can be resolved with a 2 mm CCP probe was defined where the relative error is 10%, which corresponds to an uncorrected sheet flow thickness of $\delta_{s,sens} = 6.3$ mm (Figure 2.4b). Measurements made with a 2 mm CCP probe with an uncorrected sheet flow thickness less than 6.3 mm (leading to a corrected sheet flow thickness of 3.6 mm) are dominated by smoothing and are deemed unreliable.

The measurement volume for a 1 mm CCP probe is roughly 765 mm^3 , based on the volume approximated by an ellipsoid with semi-axes lengths of $x = 8.7$ mm, $y = 8.4$ mm (Lanckriet et al., 2013), and $z = 2.5$ mm (Lanckriet et al., 2014). In comparison, the measurement volume for the 2 mm CCP, based on an ellipsoid with semi-axes lengths of $x = 15.8$ mm, $y = 15.6$ mm, and $z = 1.8$ mm (half of the smallest sheet flow thickness that is resolved by the 2 mm CCP), was $1,858 \text{ mm}^3$, 2.4 times larger than for a 1 mm probe. Assuming a linear concentration profile from 0.08 to $0.55 \text{ m}^3/\text{m}^3$ and spherical particles, the measurement volume with a 1 mm CCP would contain 17 (460) particles

with diameter of 3.0 mm (1.0 mm). For a 2 mm CCP probe, the number of particles contained within the measurement volume increases to 41 (1,117) for spherical particles with diameter of 3.0 mm (1.0 mm).

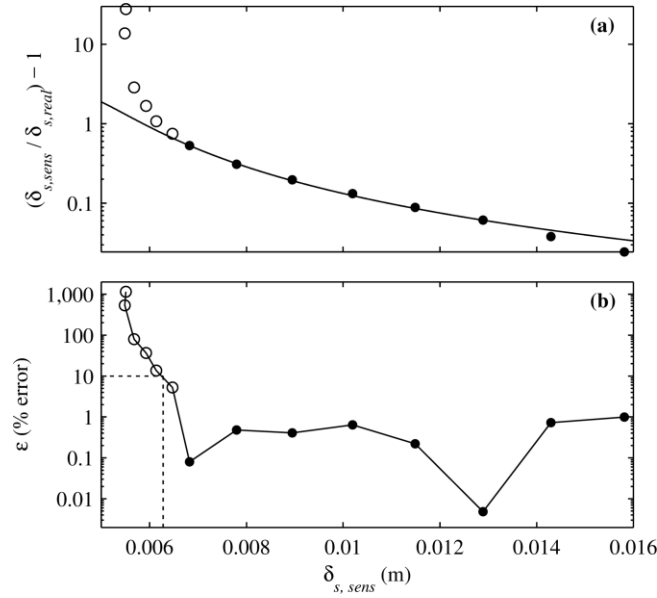


Figure 2.4: (a) Nonlinear least squares regression of the form given by equation (2.3), where the solid line is the best fit to the solid dots. The open circles were excluded from the fit. (b) Relative error between corrected (δ_c) and actual ($\delta_{s,real}$) sheet thickness computed using equation (2.5) for the 2 mm CCP probe, with the 10% error cutoff at $\delta_{s,sens} = 6.3$ mm (dotted line).

2.3.2 Acoustic Concentration and Velocity Profiler (ACVP)

2.3.2.1 Velocity Measurements

The ACVP technology provides time-resolved 1D vertical profiling of the two-component velocity field, u (streamwise) and w (flow normal), respectively, and the volumetric sediment concentration (Revil-Baudard et al., 2016). The latter is obtained from the inversion of acoustic intensity profile observations. Concentration profiles are

combined with the simultaneous and co-located velocity measurements to provide multi-directional particle flux profiles across a range of spatio-temporal turbulent flow scales. The velocity measurement principle relies on the use of multi-bistatic pulse-coherent Doppler technology (Hurther & Lemmin, 2001, 2008). The ACVP is composed of one central transmitter with two bistatic receivers in the streamwise plane. Estimates of the quasi-instantaneous Doppler frequencies using the pulse-pair algorithm at the two receivers are then converted into the desired (u, w) velocity profile considering the transformation matrix associated with sensor geometry and positioning relative to flow orientation. The unique high-resolution sediment flux measurement ability of the ACVP has recently provided new insights into a variety of wave (Chassagneux & Hurther, 2014; Hurther & Thorne, 2011; Van der Zanden et al., 2016) and current driven (Naqshband, Ribberink, Hurther, Barraud, et al., 2014; Naqshband, Ribberink, Hurther, & Hulscher, 2014; Revil-Baudard et al., 2015, 2016) boundary layer sediment transport processes.

2.3.2.2 Concentration Measurements

The ACVP was set to operate at an acoustic frequency of 1 MHz, with a pulse duration of 2 μ s, allowing a vertical resolution of 1.5 mm and temporal resolutions of 78 and 4.9 Hz for the velocity and concentration measurements, respectively. Note that the lower temporal resolution for the concentration measurements comes from the necessity of incoherent scattering conditions implying that the backscattered signal has random phase statistics uniformly distributed over 2π . In our highly turbulent flow conditions, this requirement is typically fulfilled at a maximum temporal rate of about 5 Hz which induces a statistical bias error of less than 20% for the time-resolved concentration data. Because the pressure amplitude realizations are statistically

Rayleigh distributed, the bias error of the concentration moments decreases with population size to the power of -0.5 (Bricault, 2006).

Under incoherent scattering and negligible multiple scattering conditions, the output intensity signal of the ACVP is written as (Hurther et al., 2011):

$$I = A_j A_s \rho_p \phi \exp\left(-4 \int_0^r \zeta_s C dr\right), \quad (2.6)$$

where,

$$A_j = R_0^2 \frac{\tau c}{4} \exp(-4\alpha_w r), \quad (2.7)$$

$$A_s = \frac{3}{4\rho_p} \frac{\{a^2 f^2(\theta = \pi, ka)\}}{\{a^3\}}, \quad (2.8)$$

$$\zeta_s = \frac{3}{4\rho_p} \frac{\{a^2 \chi(\theta = \pi, ka)\}}{\{a^3\}}. \quad (2.9)$$

The term A_j includes the system dependent parameters and the water absorption term along the profile; R_0 is a system constant containing the transducer sensitivity and transfer function of the hardware unit (Bricault, 2006; Hurther et al., 2011); τ is the pulse duration; r the range from the transducer; c is the speed of sound in water; α_w is the water absorption coefficient (Thorne & Hurther, 2014). The term A_s is the particle backscattering constant (Thorne & Hanes, 2002) and ζ_s is the attenuation coefficient. The term ka is the product of the wave number, k , and particle radius, a . The functions f and χ are, respectively, the intrinsic form function in the backscattered direction, describing the backscattering characteristics of the suspended particles, and the total scattering cross-section, describing the scattering attenuation characteristics of the suspension along the acoustic path at a distance r from the emitter.

For spherical PMMA particles of density $\rho_p = 1,992 \text{ kg/m}^3$, compressional and shear velocities $c_p = 2,690 \text{ m/s}$ and $c_s = 1,340 \text{ m/s}$, and assuming a water density and sound velocity of $1,000 \text{ kg/m}^3$ and $1,480 \text{ m/s}$, respectively, the intrinsic form function and total scattering cross-section are expressed as follows (Gaunard & Überall, 1983; Hefner & Marston, 2000; Moate & Thorne, 2013):

$$f_\infty(\theta = \pi, ka) = \left\| \frac{2}{ika} \sum_{i=0}^{\infty} (-1)^n (2n+1) \frac{B_n(ka)}{D_n(ka)} \right\|, \quad (2.10)$$

$$\chi(ka) = \frac{2}{ka} \sum_{i=0}^{\infty} (2n+1) \left\| \frac{B_n(ka)}{D_n(ka)} \right\|. \quad (2.11)$$

The functions $B_n(ka)$ and $D_n(ka)$ are 3×3 determinants, the elements of which are given in (Gaunard & Überall, 1983). Here, $k = 2\pi\nu/c$ is the wave number, function of the acoustic frequency ν and the sound velocity in water c and a is the particle radius. They depend on the sound compressional and shear velocities inside the PMMA spheres, as well as the density contrasts between the water and PMMA densities. The scattering angle θ is set to π corresponding to the backscattered sound. The first 20 terms of the modal series solution exposed equations (2.10), and (2.11) has been computed to ensure complete convergence. Curly brackets $\{ \}$ denote the average over the particle size distribution $n(a)$ in suspension, such that the volumetric concentration can be written as:

$$\phi = N_p \frac{4}{3} \pi \int_0^{\infty} a^3 n(a) da, \quad (2.12)$$

where N_p is the numerical particle density (number/m³) of mean radius $a_s = \{a\} = \int_0^{\infty} an(a)da$. When A_j , f , χ , a_s and $n(a)$ are known a priori, it is possible to evaluate the volumetric concentration profile, $\phi(z)$, by inverting equation (2.6) using a direct

implicit iterative approach, the performances and limitations of which are addressed in (Hurther et al., 2011) and (Bricault, 2006).

2.3.2.3 Bed Interface Detection

The Acoustic Bed Interface Tracking (ABIT) method is applied to ACVP measurements to compute the instantaneous bed interface. It enables the separation of the total acoustic intensity within the same measurement volume (often referred to as a bin) into the intensities scattered by the moving and the non-moving particles, where the non-moving particles are the undisturbed bed. The corresponding acoustic intensity at the elevation of the undisturbed bed is called the bed intensity. The ability to detect the undisturbed bed relies on the use of the frequency de-modulated Doppler signal for the estimation of the acoustic intensity, the Doppler signal being constant when generated by a non-moving target. The localization of the peak intensity in the vertical bed intensity profiles is associated with the position of the undisturbed flow bed. The ABIT method was used to detect the instantaneous undisturbed bed level (bed interface) below which the instantaneous velocity and concentration are forced to zero and to ϕ_0 , respectively. Due to strong acoustic signal loss inside the dense sheet flow layer, the raw intensity profiles were corrected from particle scattering attenuation before the ABIT method is applied.

2.3.3 Validation of Acoustic Transport Rate Measurements

Before looking into the detailed comparison of the conductivity and acoustic measurements, the acoustic sediment transport measurements are validated. The validation relies on a volume balance approach comparing the total volume of transported sediments estimated from the topographic surveys to the transported volume

estimated from the sediment flux profiles provided by the ACVP. In 2.3.3.1, the topographic survey method is first described. Because the S1 particles were measured acoustically for the first time, the determination of the acoustic inversion parameter is explained in 2.3.3.2. In 2.3.3.3, comparison of the topographically and acoustically estimated sediment volumes for all runs is discussed in terms of transport rate measurement accuracy.

2.3.3.1 Topographic Estimation of Transported Particle Volume

For each run, topographic surveys were used to estimate the total transported particle volume following the towing procedure described in Section 2.2.3. The ACVP recorded acoustic intensity and velocity profiles while it was towed over the particle pit. A reference bed level was determined before and after each experiment above the rigid bed ends adjacent to the edges of the particle pit (labeled as points A and B in Figure 2.1a). This reference bed level is common to all initial and final topographic surveys. The bed level based on topography bed scans, $z_b(x)^{topo}$, was defined by the peak value in the acoustic profiles (Figures 2.5b and 2.5d). As the ACVP was towed relative to the bed, the bed velocity measured at the elevation of peak intensity corresponds to the trolley speed. The instantaneous velocities of the towed ACVP trolley relative to the fixed tilted flume (Figures 2.5a and 2.5c) were integrated over time to determine the instantaneous horizontal position of the trolley over the particle pit. Finally, the total transported particle volume, V_{Topo} , was determined by subtracting the topographic elevations before and after each run and integrating over the length of the particle pit,

$$V_{Topo} = W\phi_0 \int_0^{L_p} [(z_b(x)^{topo})_{After} - (z_b(x)^{topo})_{Before}] dx . \quad (2.13)$$

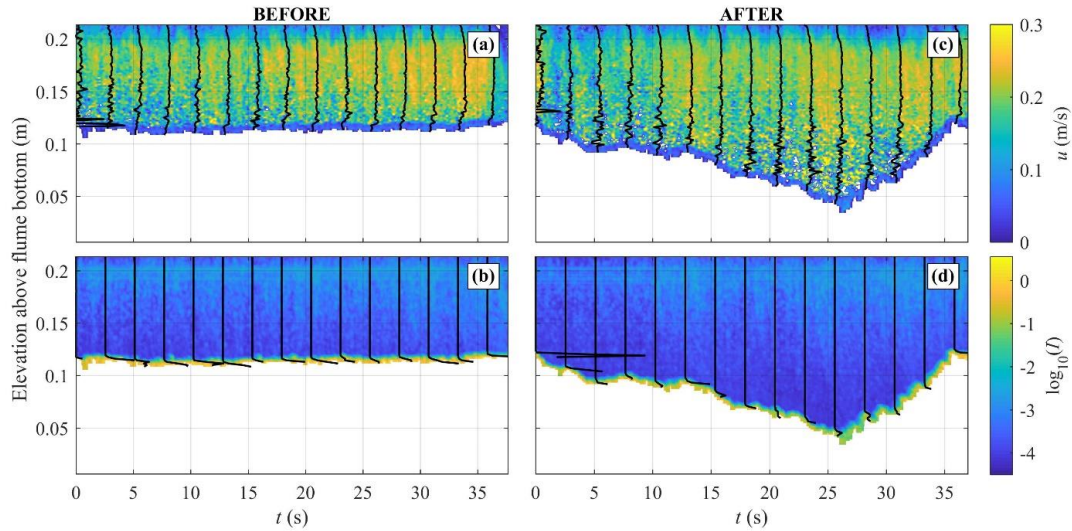


Figure 2.5: Example time-space color plots of (a, c) streamwise velocity and (b, d) logarithm base-10 of the acoustic intensity measurements during a topographic survey conducted (a, b) before and (c, d) after an experimental run. The black lines represent instantaneous profiles at intervals of approximately 3 s, where the time range on the x -axis (i.e., $t = 0 \sim 37$ s) is the duration of time over which the trolley traversed the 3-m long particle pit.

It is assumed in equation (2.13) that the packed bed concentration, ϕ_0 , is spatially homogeneous in the post-run bed and that the bed along the flume centerline is representative of the spanwise averaged bed elevation. The last assumption is strongly supported by the visual inspection of two-dimensional bed topography over the entire length of the sediment pit.

2.3.3.2 Acoustic Inversion Parameters

For the experiments with the coarse S3 particles, the inversion parameters $A_j A_s$ previously determined in Revil-Baudard et al. (2015) and Thorne & Hurther (2014) are used to perform the implicit acoustic inversion as described in (Revil-Baudard et al.,

2016), yielding volumetric concentration profiles. Since no direct calibration of the fine S1 particles is available, the scattering constant, A_s , equation (2.8), as well as the attenuation coefficient ζ_s , equation (2.9), must be evaluated using the theoretical backscattering properties of PMMA particles. No exact backscattering model exists to describe the scattering properties of irregularly shaped PMMA particles, so the S1 particles are assumed to be perfectly spherical. The ensemble-average of f and χ were taken over the total size distribution, following $\{f\} = \left(\frac{\{a\}\{a^2 f^2\}}{\{a^3\}}\right)^{0.5}$ and $\{\chi\} = \frac{\{a\}\{a^2 \chi\}}{\{a^3\}}$.

In order to invert the acoustic signal for the fine particles, the empirically determined constant $A_j A_s$ is thus corrected from the ratio $\frac{\{f_{S1}\}}{\{f_{S3}\}}$

$$(A_j A_s)_{S1} = (A_j A_s)_{S3} \frac{\{f_{S1}\}}{\{f_{S3}\}}, \quad (2.14)$$

and the attenuation coefficient, ζ_s , is calculated from equation (2.9). The inversion of ACVP backscattered intensities to volumetric concentration, ϕ , then follows the same implicit scheme of (Revil-Baudard et al., 2016) as for the S3 particles.

2.3.3.3 Comparison between Topographic and Acoustic Estimations

The temporal evolution of the transported volume of particles at the location of the ACVP was computed for S3 and S1 by cumulatively integrating the vertically-integrated streamwise flux over time (Figures 2.6a – 2.6b),

$$V_{ACVP}(t) = W \int_0^t \int_{z_b(t^*)}^{H_f} u(z, t^*) \phi(z, t^*) dz dt^*. \quad (2.15)$$

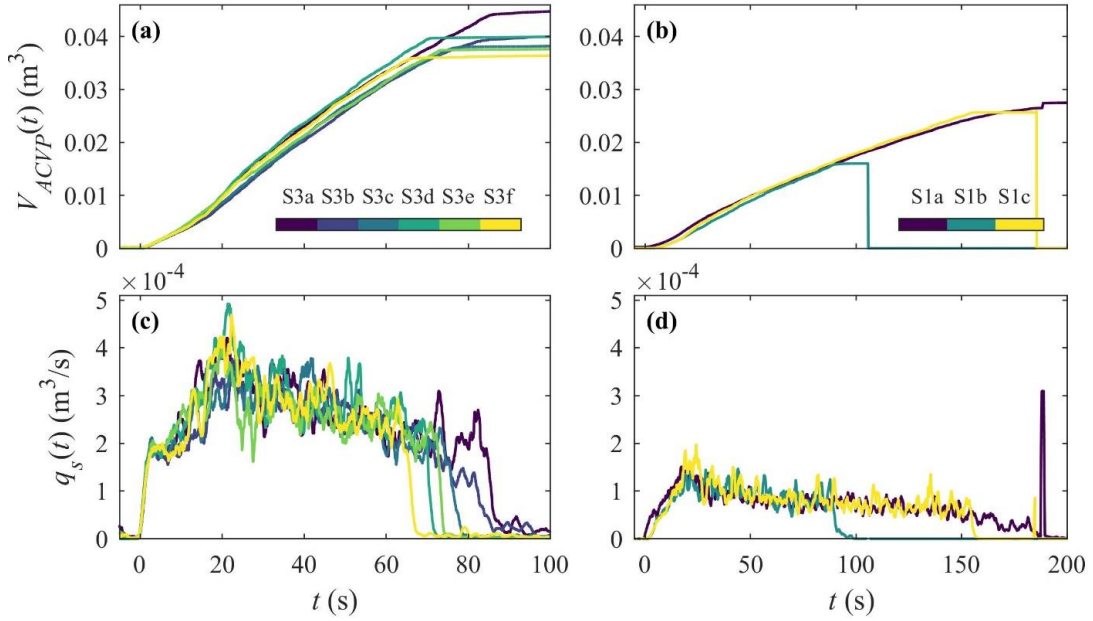


Figure 2.6: Time evolution of (a-b) the cumulative transported particle volume derived from ACVP measurements (Equation (2.15)), and (c-d) particle transport rate (filtered at 1 Hz), for all N runs of the S3 (left column) and S1 (right column) conditions.

First, it can be observed that the runs were reasonably repeatable for both S1 and S3 experiments. The duration of each run, T , was slightly different, where the end of a run (i.e., when the sluice gate was closed) is denoted by the sudden flattening (i.e., plateau) of $V_{ACVP}(t)$, indicating that no additional volume of particles was being transported (Figures 2.6a – 2.6b). The instantaneous transport rate, $q_s(t)$, was computed by taking the time derivative of the cumulative volume transported based on ACVP measurements, $q_s(t) = \frac{dV_{ACVP}(t)}{dt}$ (Figures 2.6c - 2.6d). The transport rate reached a maximum around $t = 20$ s, then remained roughly constant after $t \approx 30$ s ($t \approx 60$ s) for the S3 (S1) condition before sharply decreasing to zero at the end of each run ($t = T$), due to the absence of particle supply from upstream. The accuracy of the ACVP-derived

particle fluxes was evaluated by comparing the total volume of particles transported for each run estimated from the ACVP measurements, with the total transported particle volume estimated from topographic surveys (V_{Topo} ; equation (2.13)) (Figure 2.7). It can be seen that all acoustically estimated volumes are contained within an uncertainty range of 30% (Figure 2.7; dotted lines) which reasonably confirms the transport rate measurement ability of the ACVP technology.

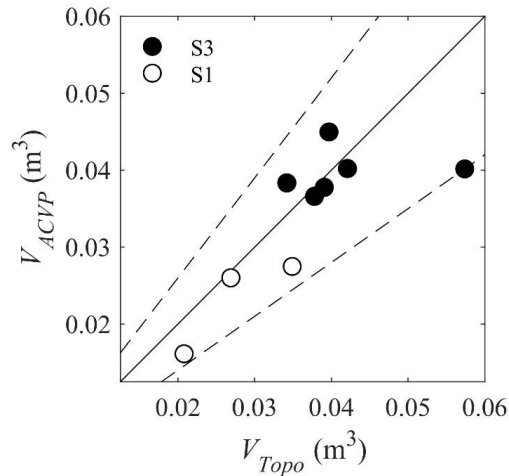


Figure 2.7: Comparison between the total transported particle volume estimates for all runs during the S3 and S1 conditions, from the topographic surveys (V_{Topo} ; Equation (2.13)) and from ACVP measurements (V_{ACVP} ; Equation (2.15)). The solid line represents a 1:1 match, and the dashed lines correspond to an uncertainty of $\pm 30\%$.

2.4 Results

Section 2.4.1 details the inter-comparison of ACVP and CCP measurements. Time-resolved concentration profiles are first analyzed as a function of free-surface elevation and the velocity profiles obtained with the ACVP. The time-resolved detection

of the bed interface are compared and analyzed in 2.4.2. The inter-comparison of averaged velocity, concentration and sediment flux profiles across the sheet flow and suspension layers are investigated in 2.4.3.1. The ensemble-averaged time-varying and time-averaged sheet flow layer thickness estimates are compared in Section 2.4.3.2.

2.4.1 Instantaneous Velocity and Concentration Measurements

Figure 2.8 presents time-space color plots of the time-resolved velocity profiles (ACVP) and concentration profiles (ACVP and CCPs) together with the time series of the bed interface (ACVP and CCPs), for a representative run of the S3 and S1 experiments (named S3b and S1b in Figure 2.8, corresponding to the S3b and S1b experiments in Figure 2.6). Only one run per condition is shown here for brevity, the same figure is available for each run (S3a-S3f and S1a-S1c) in Appendix A.

Consistent with Figure 2.6, the initial phase of the experiments was characterized by a transient phase lasting about 40 s (60 s) for S3 (S1), with rapidly increasing velocities, reaching 1.1 m/s (0.95 m/s) at $t = 20$ s (10 s) for S3 (S1), before decreasing with time until $t = 30$ s (50 s) for the S3 (S1) condition (Figures 2.8a - 2.8b). Concurrently, the color plots of concentration in Figure 2.8 reveal that during the first 20 s of the experiments, the suspension steadily grew in time, reaching higher elevations. After the transient phase, the flow reached a quasi-steady bed erosion phase, where the measured velocities stabilized over a period of time between $t = 30 - 70$ s for S3 and $t = 50 - 80$ s for S1 (Figure 2.8; vertical dashed black lines). This effect can also be visually inferred from the bed level evolution being horizontal for both the ACVP and CCPs over the same time windows (Figures 2.8i and 5j), as well as from the steadiness of the free-surface elevation (black solid lines in the time intervals delimited by the two vertical dashed lines in Figures 2.8a - 2.8b). At the end of each experiment,

the sluice gate was closed, which led to a rapid decrease of the flow rate as the water level rose back to the initial still water level. Note that this instant in time differed for each run (see Figure 2.6), since the sluice gate was lowered manually at the end of each run at different instants.

Qualitatively, both the CCP and ACVP concentrations exhibit highly intermittent concentration variations in the near bed region. These dynamics were shown to be driven by highly intermittent large-scale turbulent flow structures identified as ejection and sweep events (Hurther & Thorne, 2011). However, no direct comparison of these instantaneous events based on observations is possible due to: (i) the horizontal (0.078 m) and lateral (0.03 m) offsets in the ACVP and CCM positioning, and (ii) the fact that the CCP data were merged from a pair of sensors that were offset vertically and horizontally by 0.035 m (Figure 2.1b). At some instants, the ACVP concentration time series was marked with suspiciously low concentrations in the bed (Figures 2.8c - 2.8d). These were attributed to seldom events where the suspended load was so dense that the acoustic signal could not reach the undisturbed bed. However, such events were rare and can be detected easily in the bed level time-series provided by the ABIT method.

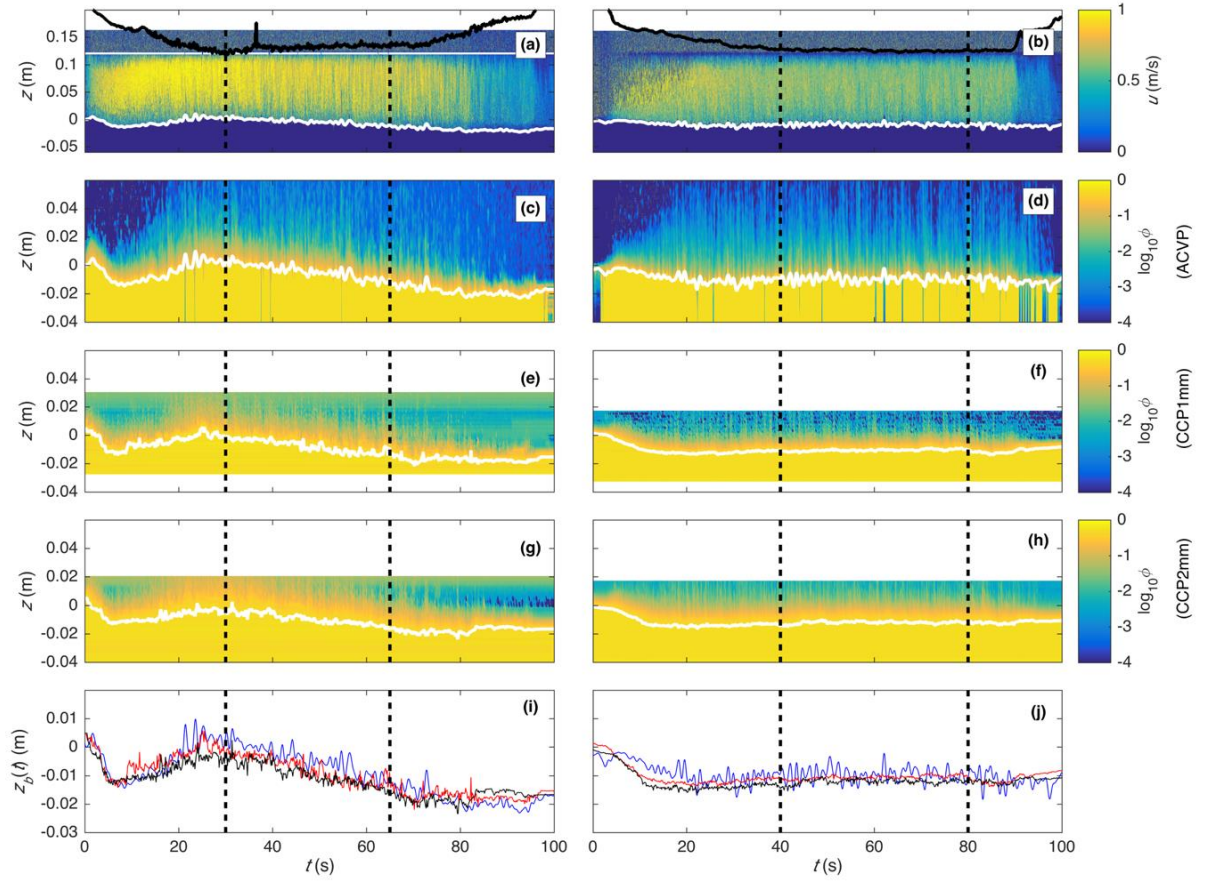


Figure 2.8: Time-space plots of (a, b) streamwise ACVP velocity, (c, d) ACVP-derived concentration, (e, f) CCP_{1mm} -derived concentration, (g, h) CCP_{2mm} -derived concentration; and (i, j) bed interfaces derived from ACVP (blue line), CCP_{1mm} (red line) and CCP_{2mm} (black line) bed interfaces for trials S3b (left panel) and S1b (right panel) experiments. The black lines in (a, b) represent the instantaneous free-surface. The white lines are the bed interfaces estimated from ACVP and CCP data. The vertical dashed black lines denote the quasi-steady time interval over which the data are time-averaged.

2.4.2 Instantaneous Detection of the Bed Interface

The CCP-derived bed levels from both CCP_{1mm} and CCP_{2mm} are in good agreement, only differing by 1 to 2 particle diameters ($d_p = 3.0$ mm), on average for the S3 experiments, during the transient phase of the experiment (up to $t = 40$ s). The agreement is similar for the S1 experiments, during which the interfaces differed by only 2 to 3 particle diameters ($d_p = 1.0$ mm), on average, during the transient phase of the experiment (up to $t = 50$ s).

The overall temporal evolution of the ACVP and CCP measured bed levels was similar during the entire run duration for all nine experiments (see Supplementary figures in Appendix A). During the quasi-steady phase of the flow (delimited by the two vertical dashed lines in Figure 2.8), the agreement between ACVP-based and CCP-based bed interfaces is good for both S3 and S1 with differences of 1 to 2 (4 to 5) particle diameters, on average. During the same period, the average erosion rate (i.e., the drop of the bed interface with time) was faster for the coarse particles (~ 0.5 mm/s from the ensemble-averaged ACVP data) than for the fine particles (~ 0.2 mm/s from the ensemble-averaged ACVP data) (Figures 2.8i and 2.8j).

2.4.3 Averaged Flow Quantities

2.4.3.1 Velocity, Concentration and Sediment Volume Flux Profiles

In order to increase statistical convergence and to minimize the statistical bias errors of measured mean flow quantities, the velocity, concentration and particle volume flux profiles were time-averaged ($\overline{\quad}$) over a portion of the quasi-steady time interval as,

$$\overline{\xi}_n = \frac{1}{t_2 - t_1} \int_{t_1}^{t_2} \xi_n dt, \quad (2.16)$$

where ξ_n represents a measured or computed quantity that varies with time (e.g., bed interface) and sometimes with elevation (e.g., velocity, concentration and particle flux) and n is the run number. The window over which the time-averages were computed (i.e., $[t_1-t_2]$) are $t \in [30 \text{ s}, 65 \text{ s}]$ for the S3 experiments and $t \in [40 \text{ s}, 80 \text{ s}]$ for the S1 experiments. These time intervals are shown by the time in between two vertical dashed black lines in Figure 2.8. Ensemble-averaging, $\langle \xi \rangle$, was carried out following

$$\langle \xi \rangle = \frac{1}{N} \sum_{n=1}^N \xi_n, \quad (2.17)$$

where equation (2.17) is applied separately at every elevation if ξ_n is a function of z (Figure 2.9). Furthermore, ξ_n in equation (2.17) may be an instantaneous or time-averaged quantity. The time-averaged velocity profiles in Figures 2.10a and 2.10d reveal the existence of an inflection point (so-called ‘‘S-shape’’) typical under sheet flow conditions (Revil-Baudard et al., 2015; Revil-Baudard & Chauchat, 2013). The inflection point elevations also correspond well with the 8% volumetric concentration elevation (Figures 2.10b and 2.10e), which separates the sheet flow layer $\langle \bar{\phi} \rangle > 0.08$ from the upper dilute suspension layer $\langle \bar{\phi} \rangle < 0.08$. As demonstrated in Hurther and Thorne (2011), the momentum diffusion processes strongly differ in the two layers; particle-particle collisions and frictional interactions dominate in the sheet flow layer whereas turbulent mixing dominates in the suspension layer.

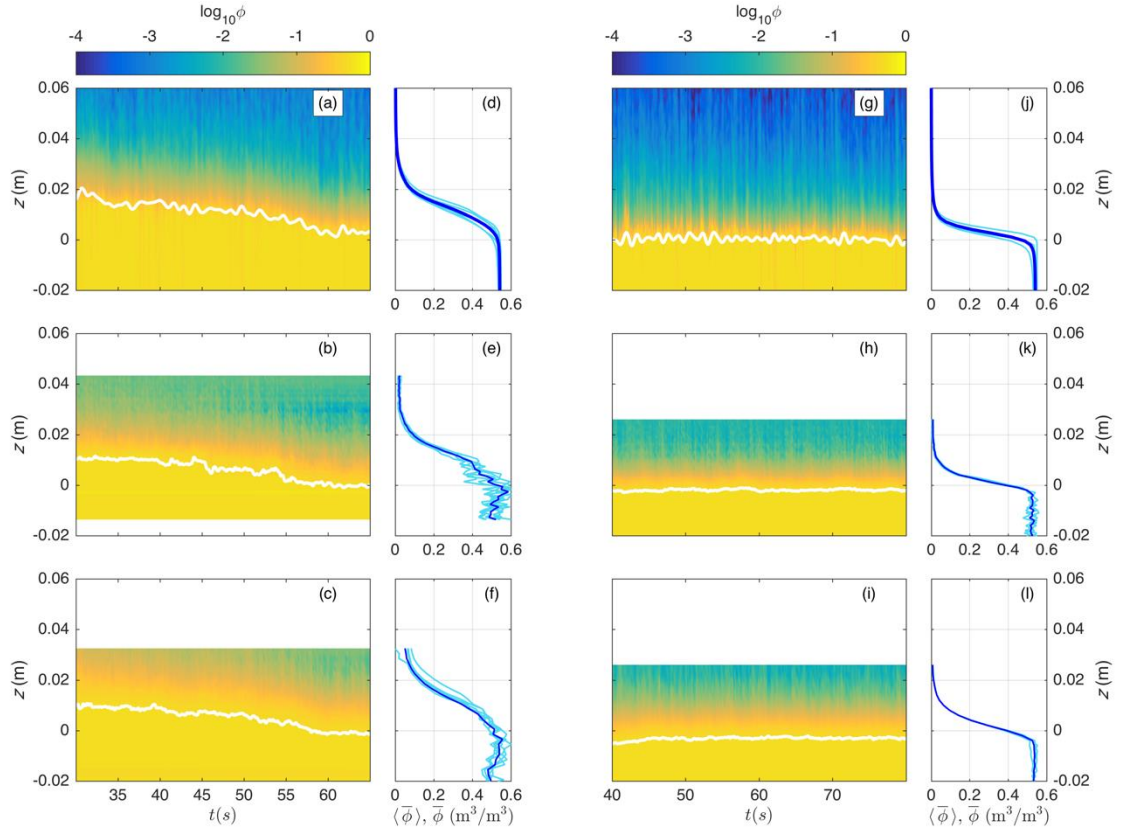


Figure 2.9: Time-space plots of ensemble-averaged (a, g) ACVP-derived concentration, (b, h) CCP_{1mm} -derived concentration, (c, i) CCP_{2mm} -derived concentration; and time-averaged (light blue) and ensemble-time-averaged (dark blue) concentration profiles from (d, j) ACVP, (e, k) CCP_{1mm} , (f, l) CCP_{2mm} for S3 (a-f) and S1 (g-l) conditions. Only the time-span over which time-averages were computed is shown. The white lines outline the bed interfaces estimated from ACVP and CCPs data.

The shapes of the concentration profiles (Figures 2.10b and 2.10e) are also similar to previously observed profiles for sheet flow conditions (O'Donoghue & Wright, 2004a). In the sheet flow layer, the concentration decreases almost linearly with z , whereas in the upper dilute region, an exponential decay typical of the suspension layer is observed (also called Rouse profile). Figures 2.10b and 2.10e present a close-

up of the ensemble-time-averaged concentration profiles, with the same data also shown in figure insets with semi-logarithmic axes. For the sake of comparison, the root-mean-square (RMS) of the relative average concentration differences along the profile between the ACVP and CCPs was computed. Good agreement was observed over the entire profile (see Table 2.3), particularly in the range $0.02 < \langle \bar{\phi} \rangle < 0.35$ for CCP_{1mm} (S3: RMS = $0.018 \text{ m}^3/\text{m}^3$; S1: RMS = $0.014 \text{ m}^3/\text{m}^3$). In the dense region ($\langle \bar{\phi} \rangle > 0.35$), the ACVP measures slightly larger mean concentration values than the CCPs, especially for the S1 condition (RMS = $0.042 \text{ m}^3/\text{m}^3$ for CCP_{1mm} and RMS = $0.031 \text{ m}^3/\text{m}^3$ for CCP_{2mm}), while in the dilute region, the CCPs return higher concentration values (Table 2.3). The over-prediction of concentration in the dilute region by CCP_{2mm} appears closer to the bed ($\langle \bar{\phi} \rangle \lesssim 0.2$) compared to CCP_{1mm} ($\langle \bar{\phi} \rangle \lesssim 0.02$) and is probably related to the larger electrode spacing on the probe.

Table 2.3: Root-mean-square differences between different instruments for different ranges of the ensemble-time-averaged concentration profiles.

RMS (m^3/m^3)	ACVP versus CCP_{1mm}		ACVP versus CCP_{2mm}	
	S3	S1	S3	S1
Entire $\langle \bar{\phi} \rangle$ profile	0.032	0.032	0.030	0.026
$0.02 < \langle \bar{\phi} \rangle < 0.35$	0.018	0.014	-	-
$0.20 < \langle \bar{\phi} \rangle < 0.35$	-	-	0.018	0.056
$\langle \bar{\phi} \rangle > 0.35$	0.049	0.063	0.027	0.051

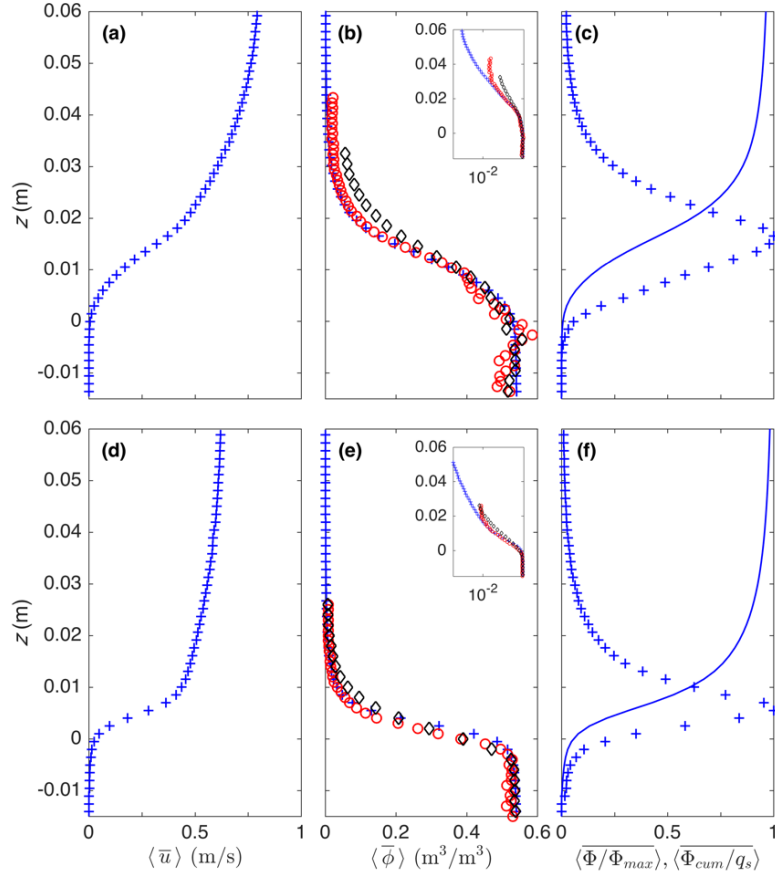


Figure 2.10: Ensemble-time-averaged (a, d) velocity profiles, (b, e) concentration profiles, and (c, f) particle volume flux profiles for S3 (a – c, top row) and S1 (d – f, bottom row). In panels (b, e), the concentration was measured by the ACVP (+, plus), CCP_{1mm} (o, circles) and CCP_{2mm} (diamonds). The same concentration data are plotted in semi-logarithmic scale (insets) to highlight the suspension layer (i.e., $\langle \bar{\phi} \rangle < 0.08$). The blue lines in panels (c, f) are normalized, cumulatively integrated volume flux.

Figures 2.10c and 2.10f show the time-averaged particle volume flux (blue +) and cumulatively integrated time-averaged volume flux profiles (blue line), which were directly estimated from the simultaneous and co-located velocity and concentration measurements provided by the ACVP. The peak of particle volume flux is located close

to the transition between the sheet flow and the suspension layer $\phi \approx 0.08$, which is consistent with previous studies (Revil-Baudard et al., 2015). It reveals that there is a fairly equal partition between the sheet flow and suspended load contributions to the total net sediment transport.

2.4.3.2 Sheet Flow Layer Thickness

The experimental data also enable direct comparison of sheet flow thickness estimates measured with the ACVP and CCPs (Table 2.4). Figures 2.11a and 2.11c present the time-varying, ensemble-averaged sheet flow thicknesses, $\langle \delta_s(t) \rangle$, obtained for both flow conditions S3 and S1 using the ACVP, CCP_{1mm} and CCP_{2mm} probes. Local differences between each pair of instruments can be seen reaching 1 (ACVP vs. CCP_{1mm}) to 4 (ACVP vs. CCP_{2mm}) particle diameters for the S3 experiments (Figure 2.11a) and 3 (ACVP vs. CCP_{1mm}) to 7 (ACVP vs. CCP_{2mm}) particle diameters for S1 (Figure 2.11c). Systematic higher sheet flow thicknesses were obtained with the CCP_{2mm} compared with the other instruments as a result of the lower spatial resolution in z .

Table 2.4: Ensemble-time-averaged sheet flow layer thickness, $\langle \bar{\delta}_s \rangle$, comparison between instruments.

	ACVP	CCP_{1mm}	CCP_{2mm}
S3	15.3 mm	13.4 mm	18.7 mm
S1	7.5 mm	8.6 mm	11.5 mm

Ensemble-time-averaged sheet layer thicknesses, $\langle \bar{\delta}_s \rangle$ (Figures 2.11b and 2.11d), using both measurement systems (ACVP and CCPs) are in good agreement, with a difference of less than 1 and 2 particle diameters for the S3 (Figure 2.11b) and S1 (Figure 2.11d) experiments, respectively. Systematic larger differences are observed with the CCP_{2mm} with relative values of about 4 and 7 particle diameters for the S3 and S1 conditions, respectively.

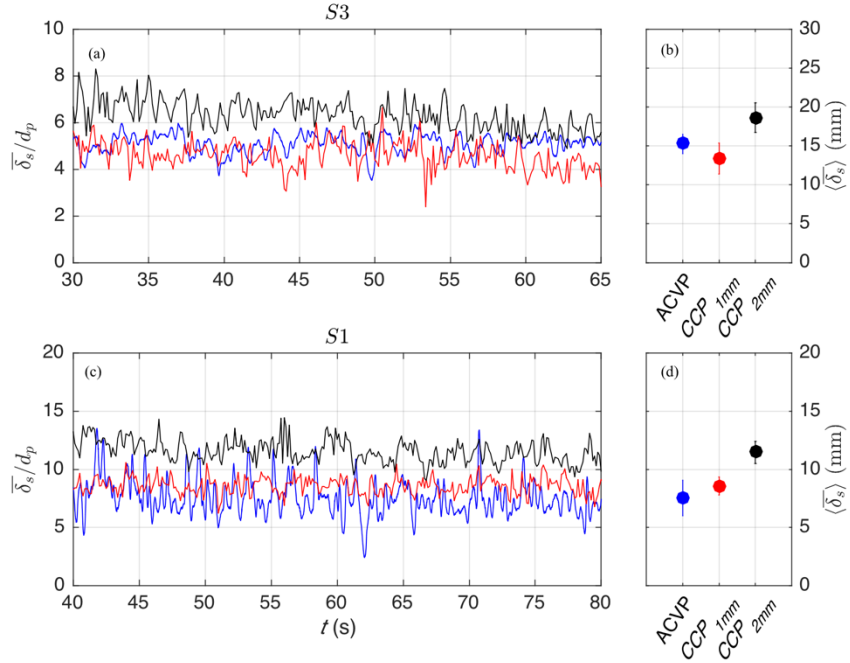


Figure 2.11: (a, c) Time series of ensemble-averaged sheet flow thickness, $\langle \delta_s(t) \rangle$, normalized by particle diameter, and (b, d) time-averages of the ensemble-averaged sheet flow thickness, $\langle \bar{\delta}_s \rangle$, for the ACVP (blue), CCP_{1mm} (red) and CCP_{2mm} (black), with error bars of \pm one standard deviation shown in plots (b) and (d). The top row (a-b) corresponds to the S3 conditions while the bottom row (c-d) corresponds to the S1 condition.

2.5 Conclusions

A detailed comparative analysis of acoustic and conductivity-based measurements was carried out in gravity-current driven sheet flows with two sizes of light-weight acrylic particles with diameters of 1.0 (S1) and 3.0 mm (S3). The measurement performances and limitations of the measurement systems are evaluated for the vertical profiling across the sheet flow and suspension layers of sediment concentration, instantaneous bed level, sheet flow layer thickness and the sediment transport rate provided by the ACVP system.

The ACVP provides reliable non-intrusive concentration estimates across the entire dilute suspension layer with shapes of the mean profiles following the expected Rouse profile (Revil-Baudard et al., 2015, 2016). This confirms the expected validity and applicability of acoustic scattering based technologies in dilute sediment suspension flows. Inside the sheet flow layer, very good agreements with the CCP measurements are found for $\phi \lesssim 0.35$ which covers 75% and 60% of the range of sheet flow layer thicknesses, for the S3 and S1 conditions, respectively. In the lower sheet flow layer associated with the sediment pick-up layer, we observe systematic over-estimations of the acoustic measurements. However, when normalized by the local mean concentrations (given by the CCP measurements as reference values), these relative differences are below 10%. This over-estimation is explained by the presence of rare short duration events during which the undisturbed bed level is incorrectly shifted upwards due to the strong scattering-driven signal attenuation. During these events the bed is detected above the real flow bed position and the corresponding concentration is incorrectly recorded as the packed bed concentration value. The error induces the systematic relative overestimation of the average concentration by less than 10% in the lowest and densest part of the sheet flow layer.

As expected from electric conductivity based measurement principle, the CCP technology provides accurate concentration profiles over the entire dense sheet flow layer associated with $\phi \gtrsim 0.08 \text{ m}^3/\text{m}^3$. More unexpected is the ability to return accurate concentration estimations in the dilute suspension layer down to volumetric concentrations of the order of $0.01 \text{ m}^3/\text{m}^3$ for the CCP_{1mm} and $0.10 \text{ m}^3/\text{m}^3$ for CCP_{2mm} , respectively. This demonstrates that with an appropriate vertical resolution, the CCP technology provides reliable instantaneous profile data outside its conventional range of application previously thought to be restricted to $\phi > 5\text{-}8 \text{ m}^3/\text{m}^3$ for CCP_{1mm} . This experiment marked the first deployment of the CCP_{2mm} instrument.

The observed differences between the two CCPs in terms of lower concentration limit that can be reliably resolved is a consequence of the different measurement volume sizes. In order to reach a representative measurement of the concentration, the latter must be large enough to contain a sufficient number of particles, and small enough to minimize spatial smoothing effects (Lanckriet et al., 2013) in the vertical direction. The larger vertical extent of the measurement volume of CCP_{2mm} leads to increased vertical smoothing of the concentration profiles, hence the observed higher volumetric concentration threshold at which the 2 mm probe becomes unreliable, as well as the overestimated sheet flow layer thickness.

Chapter 3

LARGE-SCALE EXPERIMENTAL OBSERVATIONS OF SHEET FLOW ON A SANDBAR UNDER SKEWED-ASYMMETRIC WAVES

3.1 Introduction

Sandbars represent the largest component of beach profile variability, alter nearshore circulation patterns and dissipate wave energy. During high energy wave events, sandbars undergo rapid offshore migration as suspended sediments entrained through wave-breaking are carried offshore by undertow currents. In contrast, shoreward sandbar migration occurs more slowly during quiescent periods and may be driven by velocity skewness (Hsu et al., 2006; Ruessink et al., 2007), acceleration skewness (Drake & Calantoni, 2001; Foster et al., 2006; Hoefel & Elgar, 2003; Madsen, 1974; Zala Flores & Sleath, 1998) and boundary layer streaming (Henderson et al., 2004; Nielsen, 2006; Trowbridge & Young, 1989).

A 4-day onshore sandbar migration event observed during Duck94 (Gallagher et al., 1998) has served as a benchmark for testing sediment transport formulations and calibrating numerical models. A process-based model (Fernández-Mora et al., 2015) that includes velocity skewness, acceleration skewness, and gravity-driven diffusive transport indicated the morphodynamics in the shoaling zone, seaward of the sandbar, are driven mainly by velocity skewness. Morphodynamics in the inner surf zone were dominated by wave asymmetry. Bottom changes in the vicinity of the sandbar crest, resulting in onshore migration, were attributed to both velocity and acceleration skewness (Fernández-Mora et al., 2015). However, the effect of boundary layer

streaming, which can be similar to the effects of acceleration skewness (Nielsen, 2006), was not included in the Fernández-Mora et al. (2015) model formulation.

Presently available field datasets contain spatially sparse bed level and hydrodynamic observations and rarely contain detailed sediment concentration measurements that may be needed to fully test detailed, process-based numerical models (Conley & Beach, 2003; Gallagher et al., 1998; Kuriyama, 2002; Ruessink et al., 2000; Van Enckevort & Ruessink, 2003). In fact, models are generally calibrated via tunable parameters to maximize skill in predicting cross-shore position of the sandbar crest and/or the cross-shore profile shape (e.g., Henderson et al., 2004; Hoefel & Elgar, 2003; Hsu et al., 2006; Ruessink et al., 2007). High resolution sediment concentration and velocity profile measurements on a sandbar are needed to better understand the relevance and/or contribution of particular physical processes (that may currently be embedded in the tunable parameters) driving onshore/offshore sandbar migration (Ruessink et al., 2007).

Detailed field measurements on a surf zone sandbar are difficult to obtain (e.g., Pape et al., 2010; Van Maanen et al., 2008). This difficulty can be partially circumvented using large wave flume studies (Grasso et al., 2011; Scott et al., 2009; Yoon & Cox, 2012). But nearly all prior field and laboratory efforts were conducted under active morphological adjustment, which complicates the use of ensemble-averaging when separating wave-induced processes from processes occurring over shorter (turbulent) and longer (infragravity) time scales.

The transport component related to sheet flow may be important to net sediment transport associated with sandbar migration. Sheet flow is the transport of a thin, high concentration, near-bed layer of sediment (sheet layer). Conventional bed load models

are inadequate in describing sediment transport in the sheet layer under steep, pitched-forward waves (Plant et al., 2004), which is typically observed under high bed shear stress in steady, unidirectional flow (Wilson, 1987). Strong horizontal pressure gradients during flow reversal under skewed-asymmetric waves may assist in mobilizing sediment, enhancing transport in the sheet layer (Foster et al., 2006; Madsen, 1974; Zala Flores & Sleath, 1998).

Sheet flow concentration measurements have previously been made with conductivity sensors in oscillatory flow tunnels (Horikawa et al., 1982; O'Donoghue & Wright, 2004a; Ribberink & Al-Salem, 1995) and large-scale wave flumes with flat beds without shoaling and breaking waves (Dohmen-Janssen & Hanes, 2002, 2005; Schretlen, 2012). More recently, measurements have been obtained under more energetic conditions in large-scale laboratory (Puleo et al., 2015; Van der Zanden et al., 2015; Van der Zanden, 2016) and natural swash zones (Lanckriet et al., 2013, 2014). This chapter highlights the first known measurements of instantaneous sediment concentration profiles in the sheet layer on a sandbar. High resolution sheet flow concentration profiles are coupled with concurrent near-bed velocity profiles and pore-pressure observations to investigate the roles of bed shear stress and horizontal pressure gradient in wave-driven sheet flow on a sandbar.

3.2 Methodology

3.2.1 Experimental Setup

The sandBAR SEDiment transport experiment (BARSED) was conducted in 2015 in the large wave flume at Oregon State University's O.H. Hinsdale Wave Research Laboratory (HWRL). The flume is 104 m long, 3.7 m wide and 4.6 m deep,

with a programmable piston-type wave maker equipped with active wave absorption. A fixed, barred beach profile was constructed to near-field scale, based on an observed beach profile during the Duck94 experiment (Scott et al., 2005). Concrete slabs (3.66×3.66 m) were fixed to the flume sidewalls, resulting in a piecewise continuous profile (Figure 3.1a). However, in place of a concrete slab on the sandbar crest, a steel sediment pit was installed and filled with sand (Figure 3.1b-c). The pit was designed to reduce the total volume of sediment needed to create a level bed with the top of the two adjacent concrete slabs (Figure 3.1c), which are 0.17 m thick, while still being deep enough to accommodate the burial of sensors. Therefore, in addition to the 0.17 m depth of the entire sediment pit, a secondary square pit ($1.22 \text{ m}^2 \times 0.46$ m deep) was added in the center (Figure 3.1b). The nominal still water depth was 2.448 m, and the still water depth over the sandbar was 1 m. The hybrid beach profile design allowed for the isolation of small-scale bed response to large-scale wave forcing over an immobile sandbar.

Guy-wires were used to anchor the instrument frame to the flume sidewalls at an angle, which helped minimize streamwise and spanwise vibrations of the frame during wave breaking (Figure 3.1d). Trials were limited to 10 regular waves (potential for seiching reduced) but were repeated several times to increase the number of ensembles for averaging. Each wave during each trial represented one potential ensemble. The term “wave case” is used hereafter to refer to all repeated trials conducted using the same wave maker input signal. Each wave case is assigned an ID based on the *prescribed* wave period and wave height. For example, if the prescribed wave period is 7.0 s and wave height is 0.60 m, the Case ID would be T7H60.

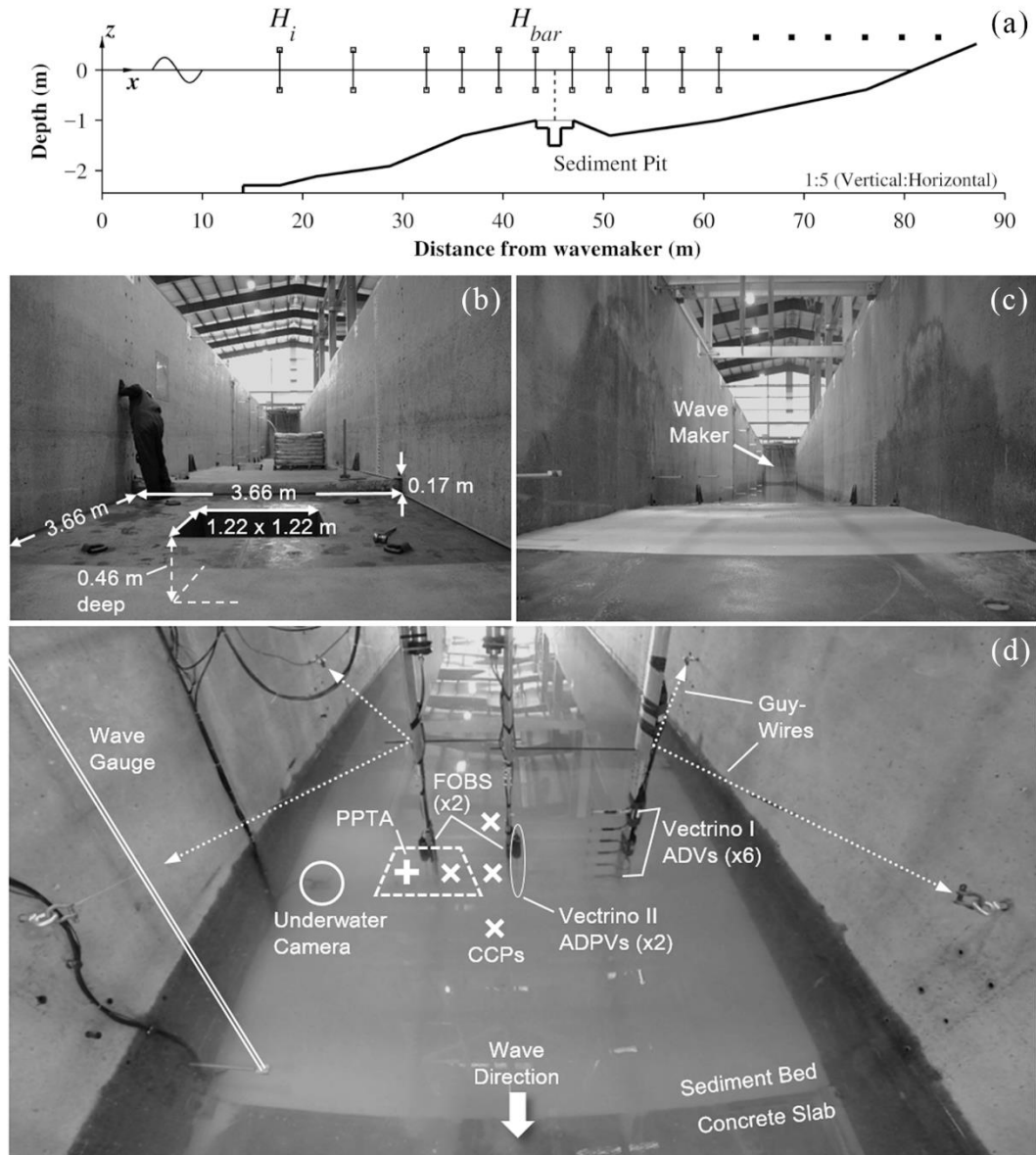


Figure 3.1: (a) Barred beach profile and sediment pit, where the vertical dashed line (--) on the sandbar crest denotes the instrument frame location shown in panel (d). Surface piercing wave gauges are plotted as vertical lines with open squares, and ultrasonic wave gauges are plotted as solid squares. Two wave gauges in particular are labeled for use in Table 3.1 (H_i : $x = 17.7$ m; H_{bar} : $x = 43.3$ m). (b) Sediment pit installed on the sandbar crest, prior to being filled with sand. (c) Sediment pit filled with sand. (d) Instrumentation deployed on/over the sandbar, viewed from above.

Two different sands were used during the experiment (Figure 3.2): the first sand, S1, was well-mixed ($d_{50} = 0.17$ mm, $d_{16} = 0.10$ mm, $d_{84} = 0.26$ mm), and the second sand, S2, was moderately well-mixed ($d_{50} = 0.27$ mm, $d_{16} = 0.16$ mm, $d_{84} = 0.38$ mm), where d_{50} is the median grain diameter (Figure 3.3). When wave cases need to be further distinguished by sediment size, either S1 or S2 is prepended to the Case ID (e.g., S1T7H60). Sand that transported out of the pit and onto the adjacent sandbar flanks was occasionally swept back into the pit and allowed to settle under gravity. Data from the first trial following each re-placement of sand were discarded.

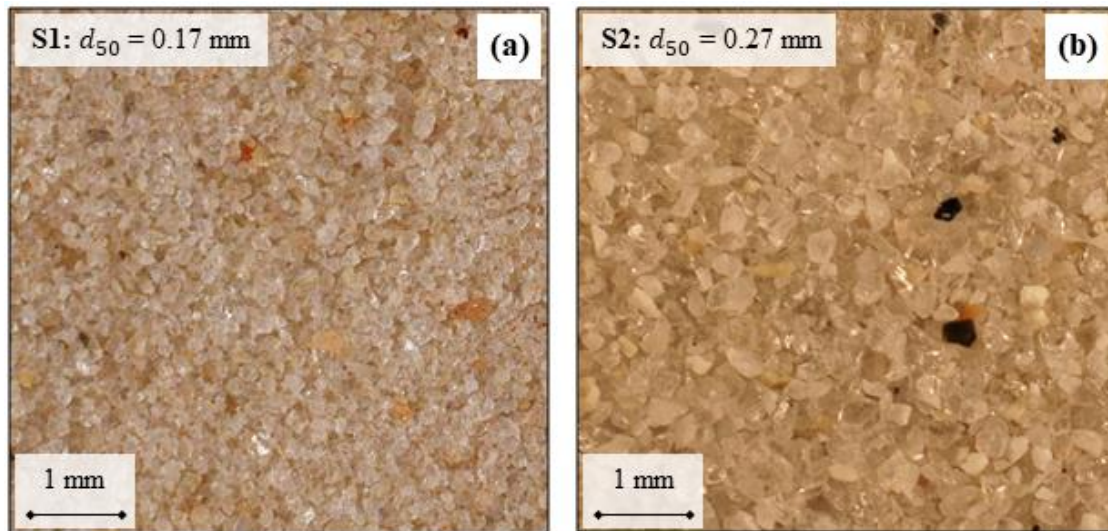


Figure 3.2: Images of samples of the two sediments, (a) S1 and (b) S2, used during the BARSSED experiments.

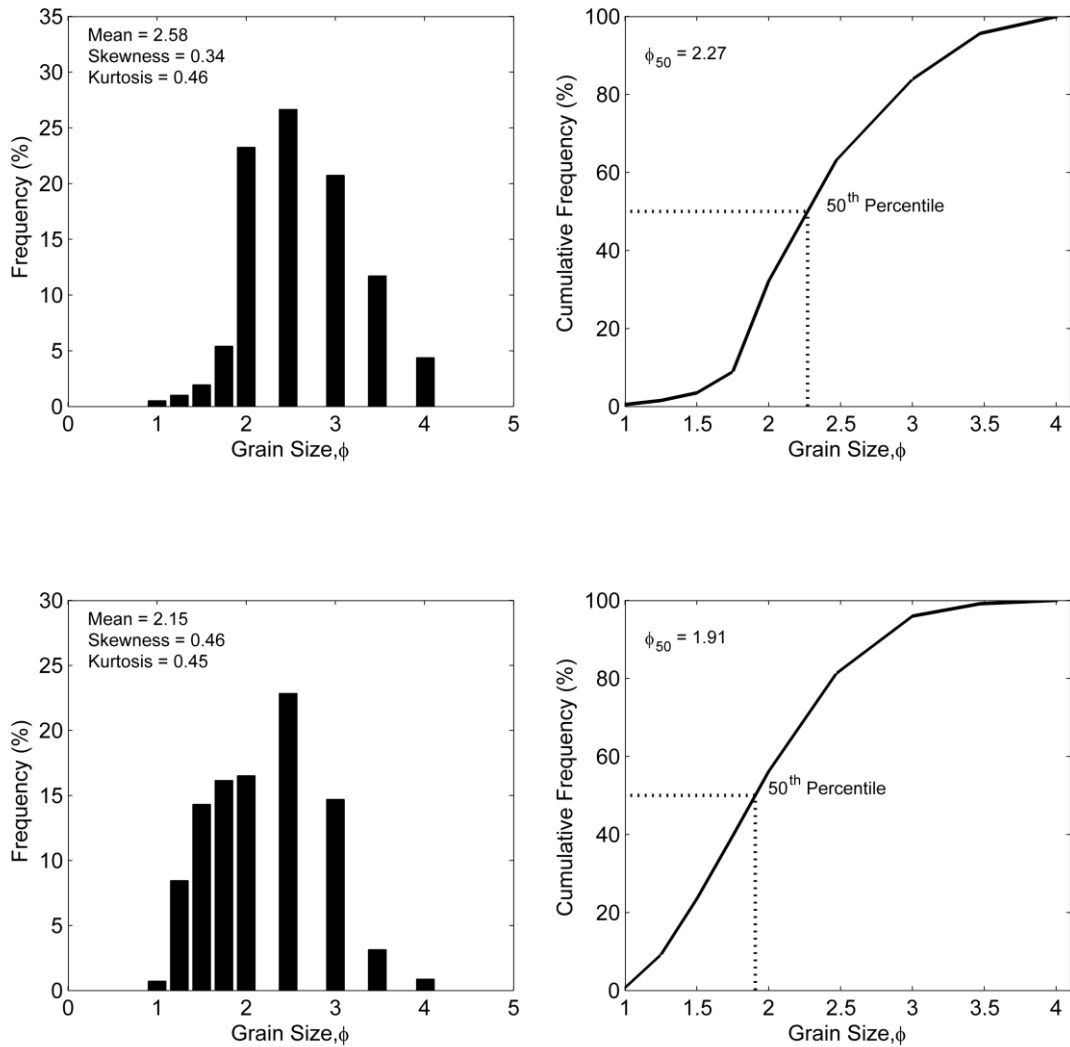


Figure 3.3: Statistics from sieve analysis for the two sediment types used during BARSED: S1 [top row] and S2 [bottom row]. Grain size is presented in phi-scale, where $\phi = -\log_2 D$ and D being grain diameter in units of mm.

A vertical array of 6 Nortek Vectrino Acoustic Doppler Velocimeters (ADV) was used to measure all three components of the fluid velocity in the water column at 100 Hz (Figure 3.1d). The lowest ADV (ADV_1) was deployed at approximately 0.1 m above the initial bed level. The next five ADVs ($ADV_2 - ADV_6$) were spaced evenly

above ADV_1 , at 0.2 m increments, such that ADV_6 was 1.1 m above the initial bed level (i.e., 0.10 m above the still water line). Of the six ADVs in the vertical array, only data from ADV_1 are used in this chapter.

Two pairs of Fiber Optic Backscatter Sensors (FOBS) were used to measure suspended sediment concentration (< 200 g/L) over the sandbar (Figure 3.1d). The FOBS consisted of a pair of probes, each with 10 optical backscatter sensors, that were deployed vertically offset from each other by 0.09 m. The vertical offset between individual sensors on each probe varied from 0.01 m near the bed to 0.07 m higher in the water column. In total, each FOBS resolved 20 points of suspended sediment concentrations within the lower 0.5 meters of the water column. Additional details of the FOBS can be found in Chapter 4.2 but are omitted here as this chapter focuses on sheet flow processes. A small HD underwater camera (DeltaVision Splashcam) was also deployed at the bed next to the flume sidewall to record video images concurrent with hydrodynamic and sediment transport measurements. The camera was aimed in the direction of the near-bed sensors.

Data from all of the sensors were recorded using two standalone acquisition systems, each with a slightly different time stamp. The two separate systems were synchronized in post-processing. Wave gage, pressure and ADV data were acquired on the HWRL data acquisition system, while the remainder of the data was logged on several separate laptop computers. Both systems received time code (NTP) from external GPS antennas with the laptop clocks updating every second. Synchronization across the data acquisition platforms was performed by logging the wave maker signal at 100 Hz (the highest sampling frequency of all the sensors) on both systems. The wave maker output a 5V signal at the start of operations and remained at 5V until after the

paddle was stopped and the signal wound down to 0V. The difference in the timing of the 5V signal between the two systems was used to align the data.

3.2.2 Near-bed Instrumentation

Sediment concentrations in the sheet layer were approximated using Conductivity Concentration Profilers (CCP), which use conductivity of a fluid-sediment mixture as a proxy for volumetric sediment concentration (Lanckriet et al., 2013). The CCP yields an instantaneous 29-point concentration profile at 8 Hz with 1 mm vertical resolution, accurate to within $\pm 0.03 \text{ m}^3/\text{m}^3$. Additionally, CCP data provide the vertical location of the instantaneous bed level (Puleo et al., 2014, 2016). The CCPs were deployed such that the measurement probe (1.6 mm thick \times 5.6 mm wide) intersected the sand-water interface (Figure 3.4). Flow disturbance and scour around the probe are minimal for flow parallel to the sensor (Lanckriet et al., 2013), as was the case during BARSED.

CCPs were deployed at four different locations on the sandbar crest (Figure 3.1d). Two locations were at the same cross-shore location of the instrument frame. The other two deployment locations were 0.5 m seaward and 0.5 m landward of the instrument frame to provide information about the cross-shore variation of near-bed sediment concentration profiles. However, CCP data from these two locations are not used in the analysis in this chapter because the measurements were not co-located with the main instrument frame.

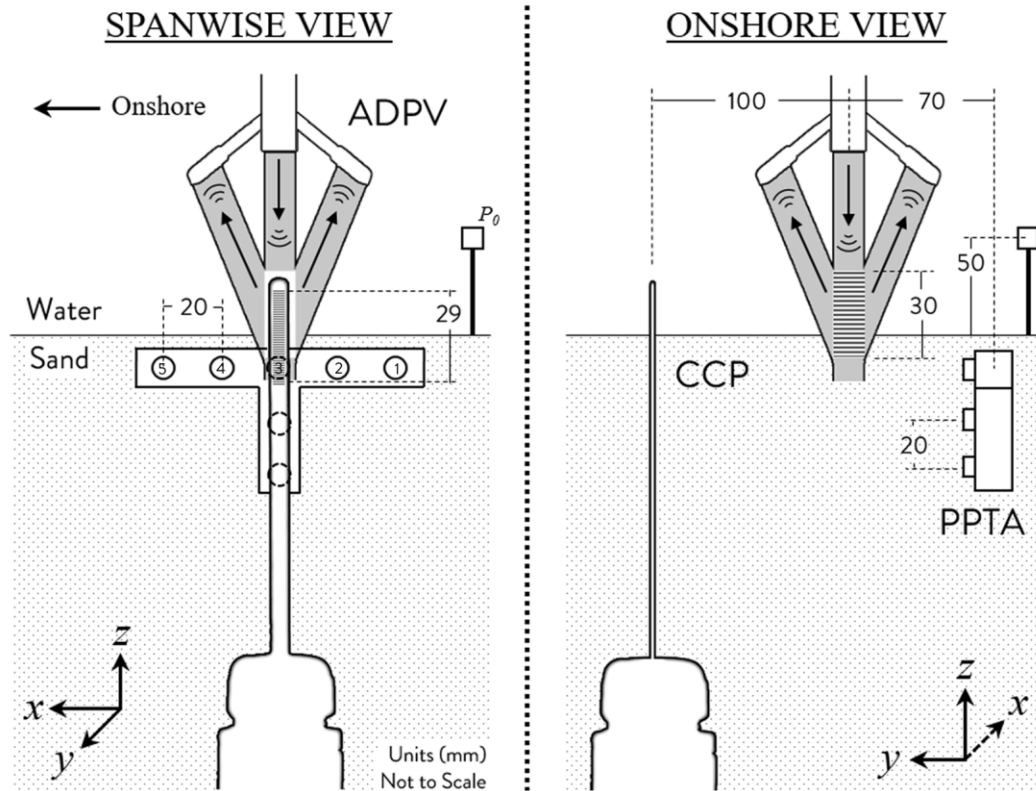


Figure 3.4: Schematic of the near-bed instrumentation outlined by the dashed white box ($x = 45.1$ m) in Fig. 3.1d, viewed looking in the spanwise and onshore directions.

Near-bed velocities (< 30 mm above the bed) were estimated with two Nortek Vectrino Profilers, or Acoustic Doppler Profiling Velocimeters (ADPV) (Craig et al., 2011). The ADPV yields a 31-point vertical profile of the fluid velocity in the streamwise (u), spanwise (v) and vertical (w) directions at 1 mm vertical resolution, sampled at 100 Hz. Each ADPV was positioned so the vertical extent of the measurement volume intersected the initial bed level (Figure 3.4).

A Pore Pressure Transducer Array (PPTA) was used to estimate pore gauge pressure at 100 Hz within the bed. Seven GE Druck PDCR 81 probes (6 mm diameter)

were mounted within a custom molding (Figure 3.4) and attached to a weighted platform (not shown in Figure 3.4) resting on the bottom of the shallower part of the sediment pit, which eliminated movement of the array when the surrounding sediment was mobilized. The horizontal row (5 - 10 mm below initial bed level) was composed of 5 transducers, with a vertical column extending beneath the center transducer (Figure 3.4). The pressure signals were reset to zero before every trial to measure the wave-induced fluctuations from hydrostatic. The spatial extent of the array was sufficiently large enough to observe pressure time lags under the wave train (see Figure 3.5f).

Free surface elevation (Figure 3.5a), $\eta(t)$, at the same cross-shore location as the instrument frame was estimated using another GE Druck PDCR 81 pressure sensor deployed 50 mm above the still bed level, P_o (Figure 3.4).

3.2.3 Test Conditions

Wave heights measured at the seaward toe of the profile (H_i , Figure 3.1a) ranged from 0.38 to 0.66 m and wave periods (T) from 5.0 to 9.0 s for the 12 wave cases analyzed in this chapter (Table 3.1). Wave heights measured at the seaward edge of the sandbar crest (H_{bar} , Figure 3.1a) ranged from 0.55 to 0.94 m. Measured wave period over the sandbar remained constant for each wave within each trial.

The cross-shore location of wave breaking ranged from 1 to 23 m shoreward of the sensors (x_b^* , Table 3.1), where $x_b^* = 0$ m is the cross-shore location of the instrument frame, and positive values correspond to breaking that occurred landward of the instruments. The range of selected wave conditions encompasses shoaling and breaking waves over the sandbar with a variety of skewed and asymmetric wave shapes. Trials were also conducted with smaller wave heights, $0.10 < H_i < 0.35$ m, and the same range

of wave periods but are not used in the analysis of this chapter due to the presence of bed forms, suggesting the absence of sheet flow.

The degree of wave skewness and asymmetry for each case are quantified using the following equations, respectively (Table 3.1),

$$Sk = \frac{\overline{u_{\infty}(t)^3}}{(\overline{u_{\infty}(t)^2})^{3/2}}, \quad (3.1)$$

and

$$As = \frac{\overline{\dot{u}_{\infty}(t)^3}}{(\overline{\dot{u}_{\infty}(t)^2})^{3/2}}, \quad (3.2)$$

where $u_{\infty}(t)$ is the cross-shore (streamwise) free stream velocity, defined here as the streamwise velocity recorded by ADV_1 (~ 0.1 m above the bed); $\dot{u}_{\infty}(t)$ is the time derivative of $u_{\infty}(t)$, computed with a central difference; and the overbar, $\overline{\quad}$, represents wave-averaging. Wave skewness is a measure of the differences in the fluid velocity about the x -axis. A wave with zero skewness has identical velocity magnitudes in the crest and trough (i.e., a perfect sine wave), whereas positive skewness signifies a wave with stronger onshore velocities under the narrow wave crest, relative to the more elongated trough (i.e., Stokes and Cnoidal waves). Wave asymmetry, on the other hand, is a measure of acceleration skewness (Drake & Calantoni, 2001; Hoefel & Elgar, 2003). A wave with zero asymmetry has identical acceleration magnitudes in the forward and backward slopes of the wave. A wave becomes increasingly asymmetric as the crest travels faster than the trough, resulting in a pitched forward, or sawtooth wave shape. Mixed skewed-asymmetric waves (more representative of waves in the surf zone) exhibit non-zero values for both wave skewness and asymmetry.

Table 3.1 lists the values for wave skewness and asymmetry for each wave case and demonstrates the various mixed skewed-asymmetric wave conditions used in the experiments. Skewness for wave periods of 5.0 and 7.0 s was between 0.07 and 0.18. The wave cases with period of 9.0 s were roughly five times more skewed than the shorter periods, with a maximum skewness of 0.57 for both case T9H50 and T9H60. Wave asymmetry tended to increase with wave height (with wave period constant), reaching a maximum of 2.37 for case T7H60.

Table 3.1: Summary of wave cases with select wave conditions, skewness and asymmetry parameters. (Note: the numbers in parentheses correspond to the equation number used to compute each parameter. Data from the Case IDs marked with asterisks are plotted in Figure 3.15.)

Case ID	T (s)	H_i (m)	H_{bar} (m)	x_b^* (m)	Sk (3.1)	As (3.2)
T5H40	5.0	0.41	0.55	7	0.15	1.19
T5H45	5.0	0.46	0.62	4	0.12	1.29
T5H50*	5.0	0.52	0.73	3	0.09	1.37
T5H60*	5.0	0.60	0.87	2	0.07	1.55
T7H40*	7.0	0.44	0.59	20	0.14	1.92
T7H45*	7.0	0.52	0.65	4	0.18	2.17
T7H50	7.0	0.55	0.76	3	0.11	2.20
T7H55*	7.0	0.62	0.82	3	0.15	2.33
T7H60*	7.0	0.66	0.94	1	0.14	2.37
T9H40	9.0	0.38	0.49	23	0.43	1.76
T9H50	9.0	0.46	0.64	14	0.57	1.94
T9H60*	9.0	0.58	0.78	2	0.57	2.07

3.3 Data Analysis

An example time series of data from a single trial within wave case S1T7H60 (maximum asymmetry), is given in Figure 3.5, where a zoomed-in view of two successive waves is provided in the right panel. The time series of the free surface shows the first wave arrived at the sandbar crest after about 13 s, succeeded by 20 s of ramp-up phase (Figure 3.5a). A regular wave train with 10 waves passed the sandbar after ramp-up, followed by 20 s of ramp-down before the wave maker was stopped. Only data contained within the 10 waves between the ramp-up and ramp-down phases were considered for analysis. Figure 3.5b demonstrates the saw-tooth nature of wave case S1T7H60, depicting rapid flow reversal during offshore to onshore, as measured by ADV_1 .

Pressure variations are shown in Figure 3.5c in the form of pressure head difference from hydrostatic in units of meters by dividing the measured pressure, P , by the specific weight of water, γ ($\approx 9,800 \text{ N/m}^3$). The horizontal pressure gradient is shown in Figure 3.5d as the gradient of pressure head. The horizontal pressure gradient, $\partial(P/\gamma)/\partial x$, for each time step was approximated about the central transducer (#3) using a 3rd-order-accurate finite difference formula (Anderson et al., 2017).

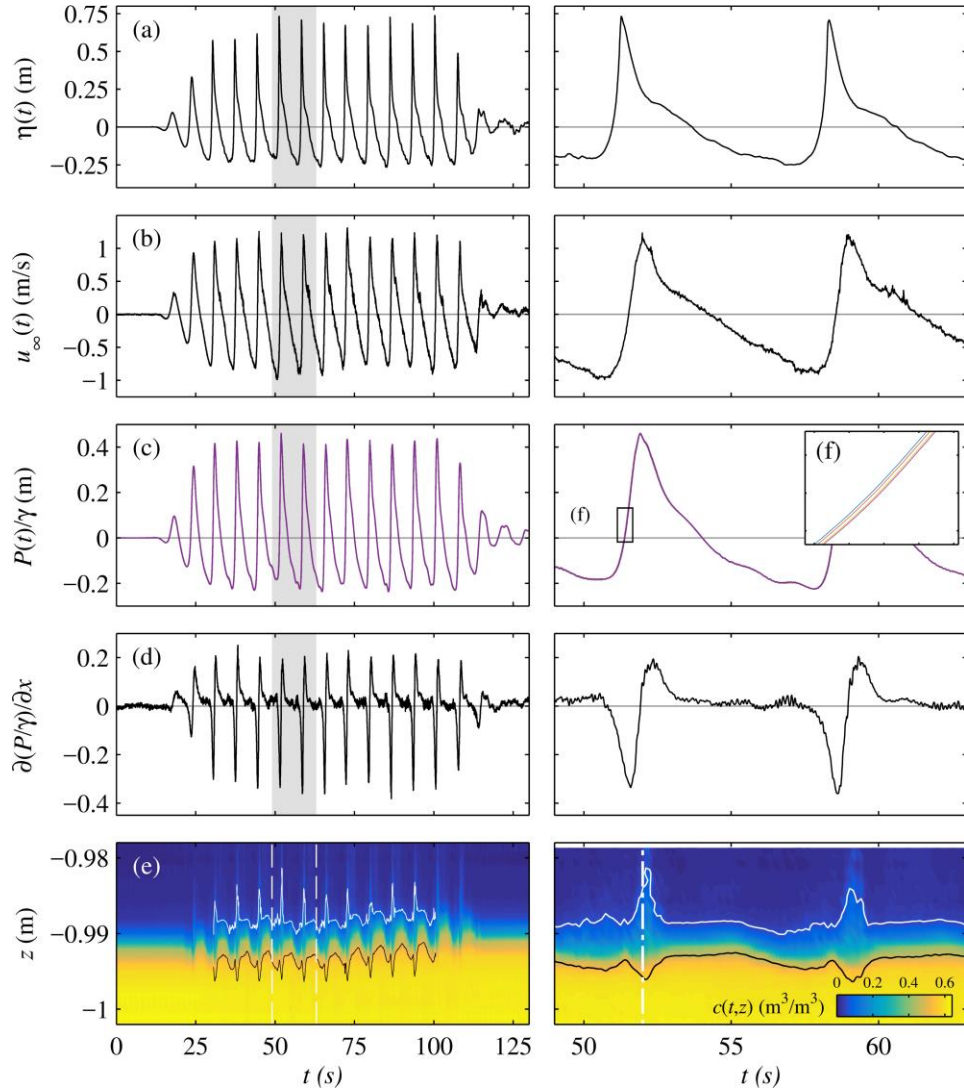


Figure 3.5: Example time series of data from one trial for case S1T7H60. (a) free surface elevation; (b) free stream velocity from ADV_1 ; (c) Pressure head from the horizontal row of transducers 2 – 5 in the PPTA; (d) Horizontal pressure gradient, where negative is onshore directed; (e) volumetric sediment concentration from the CCP, where the solid white line is the top of the sheet layer, z_{top} , and the solid black line is the bottom of the sheet layer, z_{bott} ; (f) inset showing cross-shore variation in pressure head, where P_2 (blue), P_3 (red), P_4 (yellow) and P_5 (purple), where the subscript corresponds to the transducer # in Fig. 3.4. The grey rectangles in (a) – (d) and the dashed white lines in (e) denote the span of data plotted in the panels on the right. The concentration profile marked by the dashed-dot white line in (e) is plotted in Fig. 3.6.

A time-space diagram of sediment concentration data from the CCP is shown in Figure 3.5e (Note the vertical scale is only 25 mm). The fluid-sediment interface is clearly distinguishable before the arrival of the wave train ($t = 0 - 20$ s). Just prior to flow reversal, from offshore to onshore, short-lived concentration peaks were visible (yellow peaks in Figure 3.5e), which demonstrate sudden accretion of the bed. However, immediately following the short-lived accretion events, at flow reversal (e.g., $t \sim 51.5$ s), the bed experienced momentary failure and began eroding at a rate of almost 10 mm/s (Figure 3.5e; black line). Peak onshore-directed horizontal pressure gradients (negative peak) occurred in coincidence with the onset of bed failure. The sheet layer thickness, which is outlined with black and white lines in Figure 3.5e, was minimum at flow reversal. However, after flow reversal, as the flow velocity (Figure 3.5b) increased and the (negative) horizontal pressure gradient (Figure 3.5d) decreased, the sheet layer thickness increased (light blue peaks in Figure 3.5e), as sediment was entrained upward in the sheet layer. The sheet layer reached maximum thickness beneath the backside of the wave crest, coinciding with maximum free stream velocity and near-zero horizontal pressure gradient. The sheet layer thickness then decreased and the bed accreted at roughly the same rate at which it underwent erosion. This rapid accretion/erosion/accretion of the bed is evident in the positive/negative/positive slope of the bottom of the sheet layer, respectively (Figure 3.5e; black line). The rate of bed level accretion decreased as the backside of the wave crest became less steep. Finally, under the wave trough, the bed eroded again, but at a slower rate than under the wave crest following offshore to onshore flow reversal. Although the bed level eroded under the wave trough, a corresponding upward entrainment of sediment was not apparent. In general, the sheet

layer thickness expanded and contracted with a similar phase relationship to free stream velocity.

Small bed level variations (< 5 mm) between the CCP and ADPV were accounted for during analysis, due to sensor separation of ~ 100 mm (Figure 3.4) and/or slight uncertainty (< 5 mm) in the vertical position of the CCP. The maximum curvature in the center beam amplitude return of the ADPV was used to define the bed level prior to each trial. The initial bed level at the CCP location was determined following Lanckriet et al. (2014). The vertical coordinates associated with CCP data for each trial were adjusted up/down to align the CCP-derived bed level with the ADPV-defined bed level.

Time series of pressure, concentration profiles and velocity profiles were separated into ensembles for each trial based on zero up-crossings of $u(t)$ recorded 45 mm below the transducer of each ADPV. Each ensemble was resampled onto a uniform time vector normalized by the period of the ensemble. Due to small time-varying bed levels relative to the fixed sensors over the course of a trial (see black line in Figure 3.5e; left panel), each ensemble of data were assigned a local z^* -coordinate, where $z^* = 0$ is the elevation of the inflection point in the concentration profile at each zero up-crossing (see Figure 3.6). Phase-averaging was carried out for each wave case using

$$\tilde{\xi}(t) = \frac{1}{N} \sum_{n=0}^{N-1} \xi(t + nT), \quad (3.3)$$

where ξ represents some quantity over time at a given z^* elevation and N is the number of ensembles (Table 3.2).

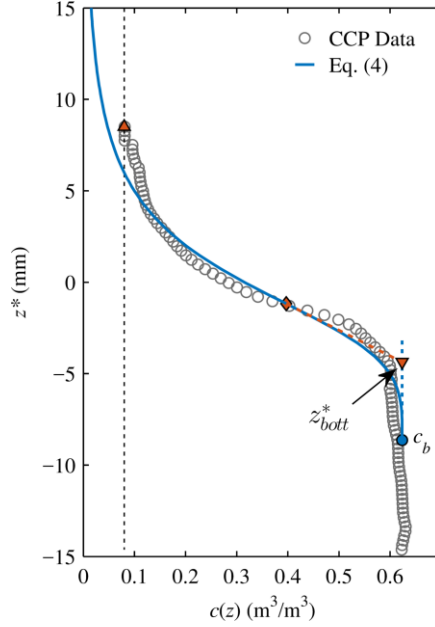


Figure 3.6: Example measured sheet flow concentration profile (Fig. 3.5e; dashed-dot white line) showing the best fit to equation (3.4) (blue curve), with free parameters: $\alpha = 3.68$, $\beta = 0.0087$ m, $c_b = 0.624$ m³/m³ and $z_1 = -8.6$ mm. The vertical dashed line represents the upper sheet layer cutoff value of 0.08 m³/m³.

The top of the sheet layer was defined as the elevation of the 8% (0.08 m³/m³) volumetric concentration contour (z_{top}^*), where grain-grain interactions become important (Bagnold, 1956). The bottom of the sheet layer (z_{bott}^*) is plotted as a black line on top of the time-space diagram of volumetric concentration in Figure 3.5e. It was determined based on the work of O'Donoghue & Wright (2004a) in an oscillatory flow tunnel, and more recently by Lanckriet et al. (2014) in a natural swash zone which fits sheet flow sediment concentration profiles measured with the CCP to the following equation,

$$c(z^*) = c_b \frac{\beta^\alpha}{\beta^\alpha + (z^* - z_1)^\alpha}, \quad (3.4)$$

where c_b is the concentration in the compact bed, determined by fitting (3.4) to each of the instantaneous concentration profiles and z_1 is the vertical location of c_b , with α, β, c_b and z_1 as free parameters. The best fit to (3.4) was determined for each instantaneous profile of sheet layer sediment concentration to determine z_{bott}^* for each time step (Figure 3.6). Then, a straight line (Figure 3.6; dashed red line) was extended outward from the inflection point of the best fit (Figure 3.6; red diamond), down to the bed concentration, c_b (Figure 3.6; blue dot). The intersection between the linear extension (Figure 3.6; dashed red line) and a vertical line through c_b (Figure 3.6; dashed blue line) was used to define the elevation of the bottom of the sheet layer (Figure 3.6; downward-facing triangle).

Sheet thickness can be over-predicted due to vertical profile smoothing resulting from the finite extent of the measurement volume of the CCP. A correction formula was applied to the uncorrected sheet thickness ($\delta_{ccp} = z_{top}^* - z_{bott}^*$) to obtain true sheet thickness, δ_s (Lanckriet et al., 2013), as

$$\frac{\delta_{ccp}}{\delta_s} = \frac{1}{127 \cdot 10^3 (\delta_{ccp})^2 - 94.1 \delta_{ccp} - 2.07} + 1 . \quad (3.5)$$

The minimum sheet thickness that can be resolved by the CCP is 3.1 mm. Small corrected sheet thickness values, $\delta_s < 3.1$ mm, are deemed unreliable (Lanckriet et al., 2013) and removed from the data record.

3.4 Results

3.4.1 Phase-averaged Sediment Concentration Profiles

Phase-averaged streamwise velocities, $\tilde{u}(t, z^* = 15 \text{ mm})$, and sediment concentrations, $\tilde{c}(t, z)$, for nine different wave cases are shown in Figure 3.7. Maximum variability (st. dev. of $0.05 - 0.1 \text{ m}^3/\text{m}^3$) across concentration ensembles (not shown) was observed during onshore to offshore flow reversal ($t/T \sim 0.3 - 0.6$). Variability in phase-averaged concentrations under the crest ($t/T \sim 0 - 0.3$) and trough ($t/T \sim 0.6 - 1$) was less (st. dev. $\sim 0.03 \text{ m}^3/\text{m}^3$) and within the accuracy of the CCP. Similar variability in phase-averaged concentration profiles were observed in a similar study of sheet layer concentration profiles in a large wave flume under surface waves (Dohmen-Janssen & Hanes, 2002).

The phase-averaged velocity time series (Figures 3.7a - 3.7c) steepened under the wave crest and maxima occurred earlier in the wave cycle (increasing asymmetry) for increasing wave height and constant period (Figure 3.7; columns). Additionally, for constant period, the onshore velocity maxima increased with increasing wave height, while the offshore velocity maxima remained similar in magnitude (increasing skewness). The vertical distance between the top of the color shading and the solid black curves identifies the sheet layer (Figures 3.7d - 3.7l). The sheet layer thickness grew at a faster rate for larger wave heights with constant period. Moreover, the maximum sheet layer thickness under the wave crest ($t/T \sim 0 - 0.3$) increased with increasing wave height, while the maximum sheet layer thickness in the offshore phase ($t/T \sim 0.6 - 1.0$) exhibited little variance with wave height for constant wave period (Figures 3.7d - 3.7l), following the same skewed trend as velocity.

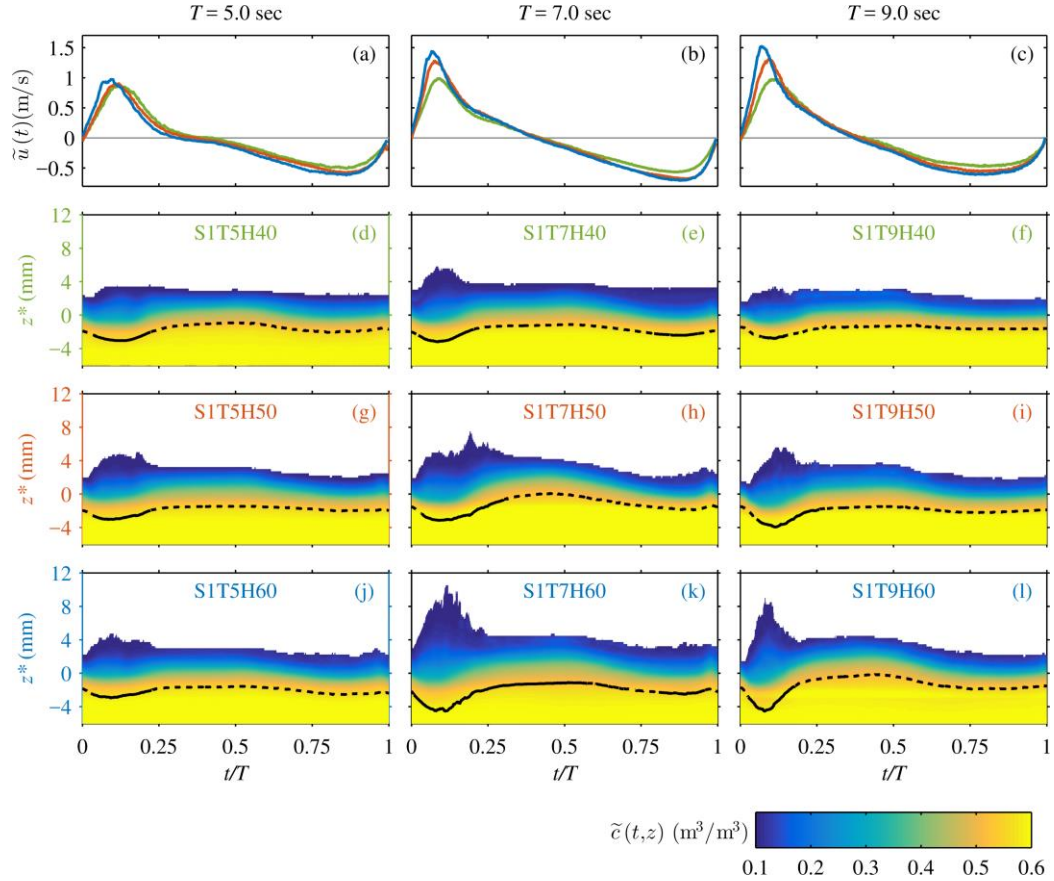


Figure 3.7: Phase-averaged (a) – (c) streamwise near-bed velocity at $z^* = 15$ mm, and (d) – (l) time-space diagrams of sediment concentration, for nine different wave cases with S1 ($d_{50} = 0.17$ mm). The bottom of the sheet layer is marked (solid-dotted black line) in (d) – (l), where the solid black line signifies when phase-averaged sheet thickness was strictly resolvable by the CCP. Columns denote constant T , and the y-axis colors correspond to the line colors in (a) – (c).

3.4.2 Bed Shear Stress and Sheet Thickness

The Shields parameter, $\theta(t)$, is used to identify different modes of sediment transport. It represents dimensionless bed shear stress over a single layer of sediment grains as

$$\theta(t) = \frac{\tau_b(t)}{\rho g (s - 1) d_{50}}, \quad (3.6)$$

where $\tau_b(t)$ is nominal bed shear stress, ρ is fluid density ($= 1000 \text{ kg/m}^3$), g is gravitational acceleration, and s is sediment specific gravity ($= 2.65$). Large values for θ (> 1) indicate the occurrence of sheet flow (Sumer et al., 1996). Bed shear stress is estimated using

$$\tau_b(t) = 0.5 \rho f_w |\tilde{u}(t, z^* = 15 \text{ mm})| \tilde{u}(t, z^* = 15 \text{ mm}), \quad (3.7)$$

where f_w is a wave friction factor and $\tilde{u}(t, z^* = 15 \text{ mm})$ is the phase-averaged streamwise velocity at $z^* = 15 \text{ mm}$, or the velocity from the nearest elevation to $z^* = 15 \text{ mm}$ if no velocities were measured at $z^* = 15 \text{ mm}$, which was necessary for two wave cases (see Table 3.2). Near bed velocities were used in (3.7) rather than from higher in the water column to more closely link the fluid forcing to sediment response. (See §3.5.2 for a discussion on alternative methods for quantifying bed shear stress.) It is worth pointing out that the average phase difference between $\tilde{u}(t, z^* = 15 \text{ mm})$ and $\tilde{u}_\infty(t)$ for all 21 wave cases was only $3.4^\circ \pm 3^\circ$, based on a Hilbert transform analysis. The phase of shear stress varies rapidly with elevation through the sheet layer. In order to resolve the magnitude and phase of shear stress as a function of z^* , τ could be extrapolated into the sheet layer (Nielsen & Guard, 2011).

Table 3.2: Summary of friction parameters and flow parameters, where N is the number of ensembles used during phase-averaging for each wave case and sediment size. All values are reported for $z^* = 15$ mm, unless otherwise noted.

Case ID	N	U_{rms} (m/s)	k_s (m)	f_w	$\delta_{s,max}$ (mm)	u_{min} (m/s)	u_{max} (m/s)	θ_{min}	θ_{max}
S1T5H40	10	0.39	0.0005	0.0075	5.0	-0.50	0.87	-0.54	1.03
S1T5H45	10	0.43	0.0005	0.0075	5.2	-0.57	0.92	-0.69	1.15
S1T5H50	19	0.42	0.0010	0.0091	7.0	-0.57	0.89	-0.81	1.32
S1T5H60	30	0.45	0.0009	0.0086	6.5	-0.61	0.97	-0.87	1.46
S1T7H40	66	0.44	0.0012	0.0087	7.9	-0.56	0.99	-0.72	1.54
S1T7H45 ¹	20	0.49	0.0013	0.0084	8.0	-0.61	1.08	-0.82	1.79
S1T7H50	39	0.54	0.0016	0.0089	9.4	-0.68	1.27	-1.06	2.60
S1T7H55	10	0.52	0.0018	0.0092	9.9	-0.67	1.23	-1.07	2.53
S1T7H60	30	0.57	0.0030	0.0106	14.5	-0.70	1.43	-1.34	3.95
S1T9H40	28	0.43	0.0003	0.0056	4.3	-0.46	0.96	-0.34	0.93
S1T9H50	30	0.52	0.0014	0.0079	8.5	-0.55	1.30	-0.61	2.43
S1T9H60	20	0.56	0.0026	0.0094	13.1	-0.61	1.51	-0.88	3.89
S2T5H40 ²	10	0.32	0.0003	0.0068	3.4	-0.41	0.70	-0.16	0.38
S2T5H50	39	0.41	0.0003	0.0064	5.6	-0.56	0.88	-0.41	0.56
S2T7H40	29	0.45	0.0003	0.0057	4.9	-0.56	0.99	-0.32	0.64
S2T7H45	20	0.49	0.0003	0.0056	5.8	-0.59	1.11	-0.38	0.79
S2T7H50	40	0.51	0.0006	0.0067	7.3	-0.61	1.30	-0.46	1.30
S2T7H55	20	0.50	0.0012	0.0083	9.7	-0.61	1.29	-0.54	1.58
S2T7H60	18	0.50	0.0015	0.0088	10.6	-0.62	1.31	-0.58	1.72
S2T9H40	27	0.40	0.0003	0.0056	4.9	-0.43	0.91	-0.18	0.53
S2T9H50	28	0.45	0.0003	0.0054	5.6	-0.44	1.11	-0.20	0.76

¹ Streamwise velocity taken from $z^* = 12$ mm

² Streamwise velocity taken from $z^* = 19$ mm

The wave friction factor is computed using a slightly modified version of Swart's (1974) formula more suitable for small values of k_s/A (See §3.5.1; Figure 3.13) (Table 3.2) (Nielsen, 1992).

$$f_w = \exp \left[5.5 \left(\frac{k_s}{A} \right)^{0.2} - 6.3 \right]; \quad A = \frac{T\sqrt{2}}{2\pi} U_{rms}, \quad (3.8)$$

where k_s is the grain roughness height, A is the orbital excursion amplitude, and U_{rms} is the root-mean-square of $\tilde{u}(t, z^* = 15 \text{ mm})$. Under intense sheet flow, k_s is not constant, but depends on flow intensity (Carstens et al., 1969) and sheet thickness (Wilson, 1989), which has been shown to depend linearly on the Shields parameter (Wilson, 1987),

$$\frac{(\delta_s)_{max}}{d_{50}} = \Lambda \cdot \theta_{max}, \quad (3.9)$$

where Λ is the slope of the least-square-error regression line forced through the origin when θ_{max} is plotted against maximum dimensionless sheet thickness, $(\delta_s)_{max}/d_{50}$. Ribberink (1998) defines mobile grain roughness as a function of the Shields parameter,

$$k_s = \begin{cases} d_{50}, & \theta \leq 1 \\ d_{50}[1 + 6(\theta - 1)], & \theta > 1 \end{cases}. \quad (3.10)$$

Equation (3.9) can be rearranged and substituted into the expression for k_s given by equation (3.10), leading to the following:

$$k_s = \begin{cases} d_{50}, & \frac{(\delta_s)_{max}}{\Lambda_{pre} \cdot d_{50}} \leq 1 \\ d_{50} \left[1 + 6 \left(\frac{(\delta_s)_{max}}{\Lambda_{pre} \cdot d_{50}} - 1 \right) \right], & \frac{(\delta_s)_{max}}{\Lambda_{pre} \cdot d_{50}} > 1 \end{cases}. \quad (3.11)$$

Equations (3.9) and (3.11) are coupled and depend implicitly on Λ . Rather than use an empirically determined value for Λ from previous studies, Λ was determined using an iterative approach, with $\Lambda_{pre} = 10.6$ in equation (3.11) as an initial value

(Ribberink et al., 2008). Then, k_s , f_w and θ_{max} were computed for each wave case and sediment size. The slope of the least-squares fit of θ_{max} versus $(\delta_s)_{max} / d_{50}$ (forced through the origin) provided Λ_{pre} for each subsequent iteration. This procedure was repeated until the percent error between two successive iterations $\frac{|\Lambda - \Lambda_{pre}|}{\Lambda_{pre}}$ was less than 0.1%, which was satisfied after 10 iterations (Figure 3.8). The analysis yielded values for k_s an order of magnitude larger than d_{50} (Table 3.2).

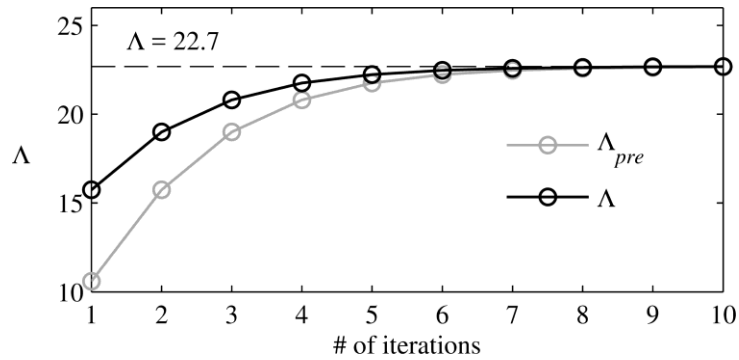


Figure 3.8: Slope of the least-square-error regression, Λ , versus number of iterations, for $z^* = 15$ mm.

Past experiments have been conducted to investigate the relationship between maximum Shields parameter and maximum dimensionless sheet thickness (Figure 3.9), which all employed similar data analysis methodology to the present study. (Ribberink et al., 2008) synthesized results from multiple oscillatory flow studies (with and without superimposed currents) with median grain diameters ranging from $d_{50} = 0.13 - 0.46$ mm and flow periods between $T = 5.0 - 7.5$ s (Figure 3.9; triangles). The best linear fit to the data points was $\Lambda = 10.6$ (Figure 3.9; solid line), with all the data points falling just within a factor of two of the best fit, $5.3 < \Lambda < 21.2$. Experimental results for both

crest and trough phases from large wave flume experiments with uniform waves over a flat sand bottom (Schretlen, 2012) and over a mobile sandbar (Van der Zanden, 2016) are also included in Figure 3.9. Schretlen, (2012) finds a better fit to the data with a power law and observed different relationships for fine sand versus medium sand (Figure 3.9; dotted and dashed lines). Van der Zanden (2016) included the influence of acceleration skewness (wave asymmetry) in the wave friction factor (Da Silva et al., 2006; Van der A et al., 2013), which increased f_w by 30% in the crest phase and decreased f_w by 6% in the trough phase, on average, compared to f_w without accounting for acceleration skewness. Since neither Ribberink et al. (2008) nor Schretlen (2012) included the effect of acceleration skewness in the wave friction factor, Van der Zanden (2016) crest phase data were multiplied by 1/1.3 and trough phase data by 1/0.94, to be more consistent with the other experimental data presented in Figure 3.9.

Least-square-error regression analysis of the data collected in this study (BARSED), using streamwise velocity at $z^* = 15$ mm to compute bed shear stress, yielded $\Lambda_{15 \text{ mm}} = 22.7$ (Figure 3.9; dots). There is less spread about the trend line of $\Lambda_{15 \text{ mm}} = 22.7$ (coefficient of determination, $R^2 = 0.90$) than the prior studies shown in Figure 3.9. When phase-averaged free stream velocity was used to compute bed shear stress in (3.7) instead of $\tilde{u}(t, z^* = 15 \text{ mm})$, and the same procedure for implicitly determining Λ was followed, least-square-regression analysis yielded $\Lambda_\infty = 40$ (Figure 3.9; squares), which is roughly 76% greater than $\Lambda_{15 \text{ mm}}$. There was slightly more spread about the trend line when using free stream velocity ($R^2 = 0.85$).

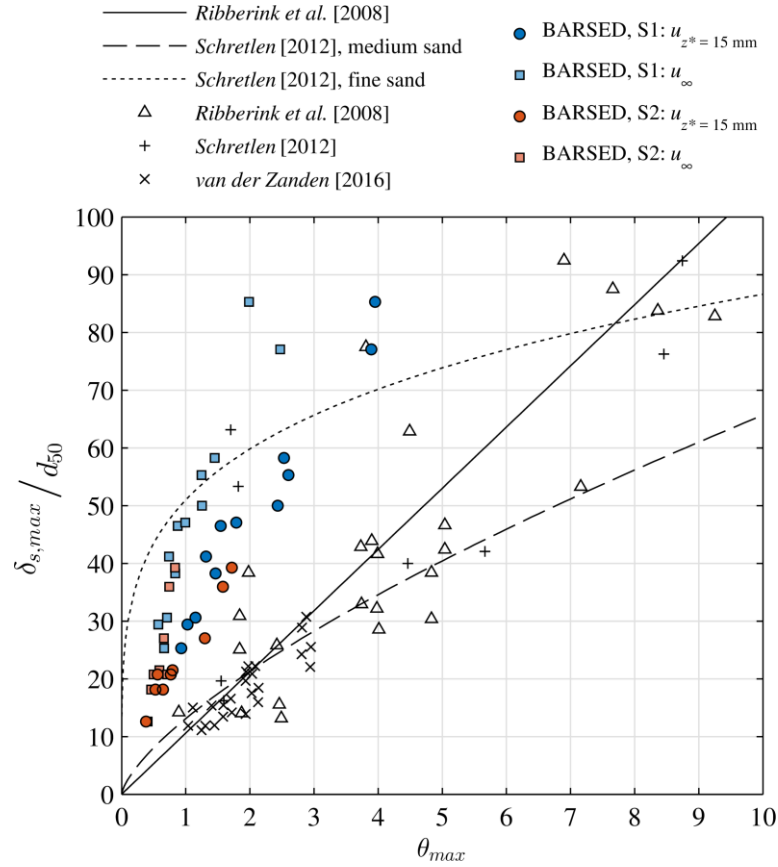


Figure 3.9: Maximum Shields parameter versus maximum non-dimensional sheet thickness. Empirical relationships are given for oscillatory flow tunnel data (Ribberink et al. (2008), solid line) and wave flume data (Schretlen (2012), dashed and dotted lines). Experimental data are provided for a range of oscillatory flow tunnel experiments (with and without a superimposed current) for fine to coarse sand (Δ) (Ribberink et al., 2008), as well as for large wave flume experiments with a flat sediment bed (fine to medium sand) (+) (Schretlen, 2012) and over a mobile sandbar (\times) (Van der Zanden, 2016).

Analysis of the grain roughness was also carried out following the same methodology outlined in Ribberink et al. (2008) for the smaller sediment, S1, so that a direct comparison to the BARSSED data may be made. The effect of acceleration skewness on bed shear stress was included in the formulation of the wave friction factor

(Da Silva et al., 2006; Van der A et al., 2013), and an iterative technique was used to determine the Shields parameter. The slope of the linear fit through the origin using the new analysis decreased from 22.5 (see Table 3.3; Λ_{S1}) to 17.1 due to increased bed shear stress from accounting for acceleration skewness (wave asymmetry). When compared to $\Lambda = 10.6$ (Ribberink et al., 2008), the slope is 62% greater for the results from the small sediment of BARSED. However, acceleration skewness was not accounted for in the wave friction factor formulation used by Ribberink et al. (2008). If the acceleration skewness term in f_w (Da Silva et al., 2006) is neglected in the reanalysis, then Λ increases by 9.4%, from 17.1 to 18.7, which is 76% larger than $\Lambda = 10.6$ (Ribberink et al., 2008).

The results in Figure 3.9 (red versus blue symbols) also indicate similar trends regardless of grain size in contrast to past suggestions that maxima in Shields parameter and dimensionless sheet thickness may differ by a factor of 2 to 3 for different sediment sizes (Dohmen-Janssen et al., 2001; Schretlen, 2012). However, it is worth noting that Λ values in Dohmen-Janssen et al. (2001) and Schretlen (2012) were obtained via best-fits to just two – four data points, whereas the dataset in this study is comprised of 21 points.

Figure 3.10 shows an example phase-averaged event for case T7H60. The left column of subplots shows quantities computed using $\tilde{u}(t, z^* = 15 \text{ mm})$ which are denoted hereafter using the subscript $()_{z^* = 15 \text{ mm}}$. Likewise, the right column in Figure 3.10 shows the same quantities computed with phase-averaged, free stream velocity, and are denoted hereafter with the subscript, $()_{\infty}$. Both streamwise velocity signals exhibited strong asymmetry (Figure 3.10a-b). The maximum value for $\tilde{u}_{z^* = 15 \text{ mm}}$ is 1.40 m/s, whereas the maximum value for \tilde{u}_{∞} is 1.15 m/s, which is 18% smaller (Figure

3.10a-b). On average, across all 12 wave cases, the maximum value for $\tilde{u}_{z^* = 15 \text{ mm}}$ was 12.5% larger than the maximum value for \tilde{u}_∞ . On the contrary, the maximum magnitude of free stream velocity in the trough was 6% larger on average than the maximum magnitude of the near bed (i.e., at $z^* = 15 \text{ mm}$) velocity in the trough. The observed differences in peak crest and trough velocities at different elevations under large-scale wave forcing over a sandbar are on the same order as recent wave flume observations (Van der Zanden et al., 2016).

Maximum sheet thickness was larger by a factor of 1.4 for the finer sediment, S1 (Figure 3.10c-d). A similar trend was observed for the other 11 cases (Table 3.2). Sheet thickness for both sediment sizes grew and decayed beneath the wave crest at roughly the same rate; although, there was a slight phase lag between the initiation in growth of the sheet layer between S1 and S2, because larger bed shear stress is necessary for incipient motion of larger sediments. Sheet thickness also decayed earlier for S2 versus S1; perhaps due to insufficient bed shear stress to maintain transport, and/or because of larger settling velocity (Figure 3.10e-f).

The Sleath parameter quantifies the effects of the horizontal pressure gradient on sediment mobility and is defined as (Sleath, 1999)

$$\tilde{S}_p = \frac{-\partial \widetilde{P} / \partial x}{\rho(s-1)g}, \quad (3.12)$$

where $\partial \widetilde{P} / \partial x$ is the phase-averaged, cross-shore pressure gradient. An example time series of cross-shore pressure gradient observations was given in Figure 3.5d. The Sleath parameter computed with the cross-shore pressure gradient is shown in Figure 3.10g-h. The small standard deviation about the phase-averaged curve (Figure 3.10g-h; shaded grey areas) demonstrates the repeatability of the experimental setup.

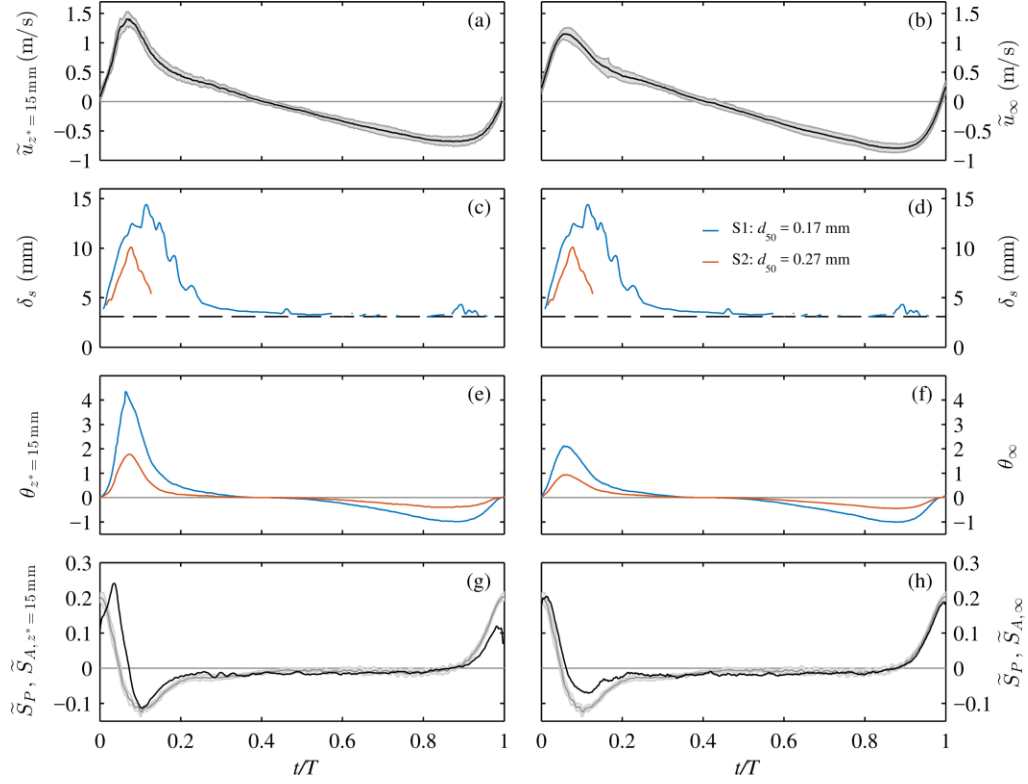


Figure 3.10: Phase-averaged results for case T7H60 with sediments S1 (blue) and S2 (red). (a) streamwise velocity at $z^* = 15$ mm and (b) free stream velocity; (c) – (d) sheet thickness; (e) – (f) Shields parameter; and (g) – (h) Sleath parameter using equations (3.12) (grey) and (3.19) (black). The dashed lines in (b – c) are the minimum reliable δ_s , which was only exceeded under the crest for S2. The standard deviation from the phase-averaged quantities are shown in grey envelopes in (a – b) and (g – h).

Originally, the critical Sleath value corresponding to the onset of bed failure and mobilization of a layer of sediment was 0.29 (Sleath, 1999). However, the onset of bed failure has been observed in the field on a surf zone for Sleath parameter values as low as 0.10 (Foster et al., 2006). For case T7H60, the peak \tilde{S}_P value reached 0.20 during flow reversal (Figure 3.10g-h; grey lines), suggesting the horizontal pressure gradient may have contributed to bed destabilization. The Sleath parameter peaked during

offshore to onshore flow reversal (Figure 3.10g-h), but the phases of \tilde{S}_p maxima correlated poorly with peaks in sheet thickness (Figure 3.10c-d). Although, initiation in growth of the sheet layer immediately following flow reversal occurred when \tilde{S}_p was maximum and θ was nearly zero. The difference in sheet thickness between S1 and S2 (Figure 3.10b) is likely related to variations in bed shear stress (grain size dependency embedded in f_w) rather than \tilde{S}_p (independent of grain size).

3.5 Discussion

3.5.1 Grain Roughness and Friction Factor

Mobile sediment beds under strong shear stresses are not properly represented as either rough or smooth (fixed), which means that using a nominal value for grain roughness (i.e., $k_s = 2.5d_{50}$) is inappropriate. Under steady sheet flow, grain roughness is more closely related to sheet thickness (i.e., $k_s \sim 0.5\delta_s$), based on measurements in a closed conduit tunnel with nylon and sand particles (Wilson, 1989), which gives k_s values an order of magnitude larger than the grain diameter (Figure 3.11; dotted line). Grain roughness values derived via energy dissipation measurements in oscillatory flow tunnels under sheet flow conditions,

$$k_s = 70\sqrt{\theta} d_{50} \quad \text{for } \theta > 0.5, \quad (3.13)$$

are on the order of 100 to 200 grain diameters (Carstens et al., 1969; Nielsen, 1992), which is an order of magnitude larger than roughness values for steady sheet flow observations (Wilson, 1989) (Figure 3.11; dashed line). Equation (3.13) can be expressed in terms of the nominal grain roughness Shields parameter, $\theta_{2.5}$,

$$k_s = 170\sqrt{\theta_{2.5} - 0.05} d_{50} \quad (3.14)$$

where $\theta_{2.5}$ is the Shields parameter computed with $k_s = 2.5d_{50}$. Ribberink (1998) focused specifically on the sand data from (Wilson, 1989) and proposed the formulation for mobile grain roughness as a function of Shields parameter given in equation (3.10) (Figure 3.11; solid line). The grain roughness values computed following the iterative approach outlined in equation (3.11) (Table 3.2) generally follow the empirical formulation in equation (3.10) (Ribberink, 1998) (Figure 3.11; dots). Grain roughness values from (3.14) are 10 – 100 times larger compared to grain roughness computed from equation (3.11) (Figure 3.11).

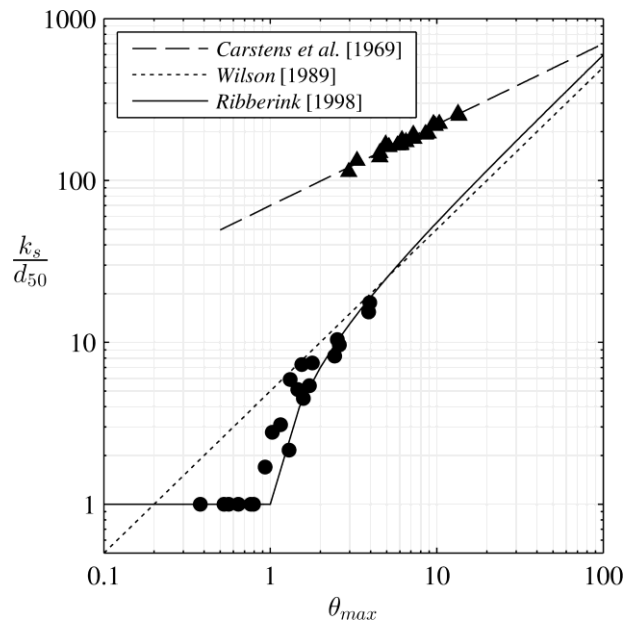


Figure 3.11: Comparison of three different empirical expressions for grain roughness (normalized by median grain diameter) as a function of Shields parameter. Grain roughness values were computed using equation (3.11) (dots, ●) and equation (3.14) (triangles, ▲).

Figure 3.12 demonstrates the differences between using a mobile grain roughness expression versus a nominal expression. The open circles in Figure 3.12 are the same data points as the closed circles in Figure 3.9. Using a constant value for k_s that does not take into account the flow conditions or the bed response leads to an overall slope of $\Lambda = 31.1$. Maximum Shields parameters ranged between $3 < \theta_{max} < 14$ (Figure 3.11; triangles) when equation (3.14) was used to compute grain roughness. These results were not included in Figure 3.12 because doing so compressed the results from the other two methods, rendering them nearly indistinguishable from one another. Instead, the proportionality constants (Λ) resulting from using equation (3.14) are included in Table 3.3, along with the slopes of each line in Figure 3.12, where Λ_{S1} (Λ_{S2}) corresponds to the slope of a least-squares fit to only the data for S1 (S2). For equal dimensionless sheet thickness, maximum Shields parameter (i.e., maximum bed shear stress) was more than four times larger when using roughness values derived from oscillatory sheet flow experiments, equation (3.14) (Carstens et al., 1969), as opposed to using roughness values derived from steady sheet flow experiments, equation (3.11). The Λ values (4.0 – 5.3, Table 3.3) were 100 - 400% smaller than previous observations in oscillatory sheet flow (Dohmen-Janssen & Hanes, 2002, 2005; Ribberink et al., 2008; Schretlen, 2012; Van der Zanden, 2016). The smallest Shields parameter as a result of using (3.14) was 2.96 (S2T5H40), almost three times greater than the typical threshold for sheet flow, suggesting that intense sheet flow was occurring. This contradicted visual observations from the underwater camera (Figure 3.1d), which indicated there was no development of intense sheet flow for case S2T5H40.

Table 3.3: Summary of values for Λ obtained using three different expressions for grain roughness, k_s .

	k_s	Λ	Λ_{S1}	Λ_{S2}
Nominal	$2.5d_{50}$	31.1	33.2	24.6
Ribberink (1998)	Eq. (3.11)	22.7	22.5	24.2
Carstens et al. (1969)	Eq. (3.14)	5.3	5.8	4.0

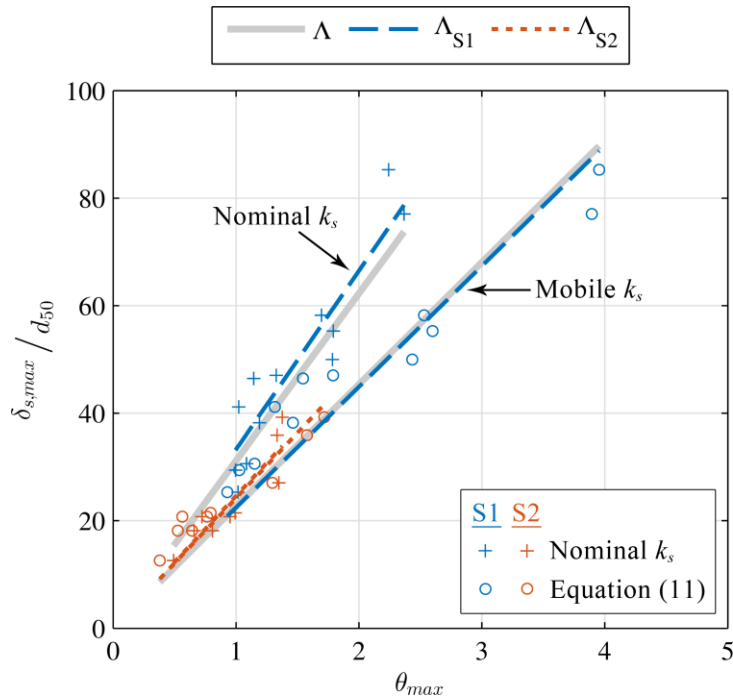


Figure 3.12: Comparison between least-squares-fits to data for both sediment sizes using a constant k_s value as nominal grain roughness ($= 2.5d_{50}$), and mobile grain roughness based on observed sheet thickness and iteration for Λ (Equation (3.11)). Overall fits, Λ , are shown for both methods (grey lines), as well as separately for each grain size, Λ_{S1} (dashed blue lines) and Λ_{S2} (dotted red lines). The Shields parameter for all data points is computed using (3.6) and (3.7).

The near coincidence of all three lines along the same slope for mobile k_s (Figure 3.12) demonstrates the robustness of the variable expression for grain roughness. Conversely, for nominal k_s , there is considerable deviation from the overall fit for Λ when considering each sediment size separately (Figure 3.12; Table 3.3). Using nominal grain roughness, the resulting Λ is even larger than using mobile roughness. Thus, the main finding that Λ is larger under surface waves than for oscillatory flow tunnels and/or steady flow remains. In fact, using mobile roughness and streamwise velocity at $z^* = 15$ mm provides the most conservative estimate of Λ , compared to using free stream velocity and/or nominal grain roughness, to compute bed shear stress. The analysis also supports the notion that a constant k_s based only on the median grain diameter may fail to properly parameterize the bed roughness under sheet flow conditions.

Slightly different formulations for the grain roughness and wave friction factor were used in the present study compared to the data points presented in Figure 3.9. The necessary data required to perform a limited re-analysis were presented in Schretlen (2012). Therefore, the analysis of the relationship between maximum Shields parameter and maximum dimensionless sheet thickness given by equation (3.9) was carried out with data from Schretlen (2012) (experiments Re1575m, Re1565m, Re1575f and Re1565f) using four combinations of k_s and f_w , and compared to the results using the data in the present study (BARSED) and the same four combinations of k_s and f_w (Table 3.4). First, the formulation for wave friction factor given by (3.8) was used to examine the influence of the model for k_s on Λ . Re-analysis of the BARSED data for both sediment sizes, using equations (3.6), (3.8) and (3.10) to iterate for θ_{max} until the percent difference between subsequent iterations was less than 0.1%, yielded $\Lambda = 21.9$,

a difference of less than 4% compared to $\Lambda = 22.7$ (Table 3.4). A larger difference of about 8% was observed for the Schretlen (2012) data ($\Lambda = 16.2$ versus $\Lambda = 17.6$; Table 3.4). The relatively small difference for Λ based on the model for k_s is supported by the cluster of dots, (3.11), about the solid line, (3.10), in Figure 3.11. The correlation was lower when equation (3.10) was used ($R^2 = 0.63, -0.07$) compared to when k_s was computed with equation (3.11) ($R^2 = 0.90, 0.30$; Table 3.4), likely a consequence of the assumption built into (3.11) that the relationship between θ_{max} and $\delta_{s,max}/d_{50}$ follows the linear trend given by (3.9) (Wilson, 1987).

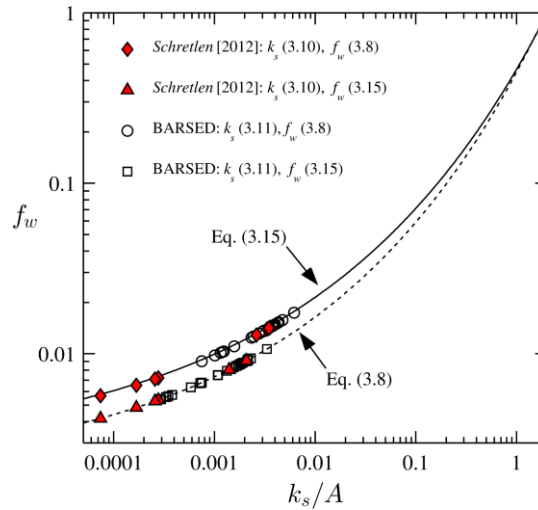


Figure 3.13: Wave friction factor as a function of k_s/A , computed with equations (3.8) and (3.15), using data from BARSED and Schretlen (2012).

Table 3.4: Summary of Λ values and respective coefficients of determination (R^2) for 4 different combinations of expressions for k_s and f_w .^a

k_s	f_w	Schretlen (2012)		BARSED		$\frac{ \Lambda - \Lambda_{Sch12} }{\Lambda_{Sch12}}$
		Λ_{Sch12}	R^2	Λ	R^2	
Eq. (3.10)	Eq. (3.8)	16.2	-0.07	21.9	0.63	35%
Eq. (3.10)	Eq. (3.15)	10.1	0.24	13.3	0.76	32%
Eq. (3.11)	Eq. (3.8)	17.6	0.30	22.7	0.90	29%
Eq. (3.11)	Eq. (3.15)	11.3	0.31	13.6	0.92	20%

^a Bold values correspond to the least-square-error linear regression line (through the origin) to the respective data plotted in Figure 3.9. Data for reanalysis were obtained from Tables 4.1 and 4.2 in Schretlen (2012). BARSED data correspond to $z^* = 15$ mm.

Because the experimental data points to which the BARSED results were compared in Figure 3.9 (Ribberink et al., 2008; Schretlen, 2012; Van der Zanden, 2016) used the original Swart (1974) formula,

$$f_w = \exp \left[5.213 \left(\frac{k_s}{A} \right)^{0.194} - 5.977 \right], \quad (3.15)$$

whereas the BARSED results were computed with a slightly modified version of Swart's (1974) formula, it is important to determine how the model for f_w may affect the result for the proportionality constant Λ so that proper comparisons can be made. The wave friction factor given by equation (3.15) tends to over predict f_w for small values of $k_s/A \lesssim 10^{-2}$ (see Figure 1.2.8, Nielsen 1992), which is why the slightly modified version of (3.15), given by equation (3.8), was used to compute f_w in Section 4.2. When the BARSED data were re-analyzed using equation (3.15) to compute the wave friction factor, Λ decreased by 40% compared to the result using equation (3.8) (Table 3.4). The

same trend (37% decrease in Λ) was observed in the results using the Schretlen (2012) data (Table 3.4). The range of test conditions for BARSED and Schretlen (2012) span $10^{-5} < k_s/A < 10^{-2}$, which appears to suggest that (3.8) is the more appropriate wave friction factor for these data sets (Figure 3.13). While values for Λ (16.2 – 17.6) computed using Schretlen (2012) and equation (3.8) reveal an enhanced sheet thickness relative to $\Lambda = 10.6$ (Ribberink et al., 2008), further analysis of flow tunnel (Ribberink et al., 2008) and large wave flume (Van der Zanden, 2016) observations using the appropriate model for f_w is required before definitive conclusions may be drawn.

Regardless of the apparent robustness of mobile grain roughness versus constant grain roughness, the results for mobile k_s in Figure 3.12 have the same caveat as all previous investigations using equation (3.9). The linear relationship is generally only valid when comparing maxima but tends to break down when considering instantaneous values of dimensionless sheet thickness versus Shields parameter; a consequence of applying steady, unidirectional flow theory (Wilson, 1987) to unsteady, oscillatory flow. In addition, which model to use for grain roughness in oscillatory flow when the Shields parameter is in the range, $0.5 < \theta < 1$, but sediment may still be in motion, is still an open research question (Nielsen, 2016). Another largely open question is which formulation to use to quantify bed shear stress when it is not measured directly.

3.5.2 Quantification of Bed Shear Stress

Bed shear stress is perhaps one of the most difficult forcing mechanisms to measure and/or quantify during oscillatory flow with a mobile sediment layer. Consequently, numerous formulations and empirical relationships exist to estimate bed shear stress with those that require the fewest data points or coefficients often used. Three different formulations for bed shear stress are discussed, as well as the advantages

and drawbacks of each when applied to skewed-asymmetric oscillatory flow under waves, as observed during BARSED. The formulations covered are not meant to be exhaustive, but rather a discussion of more commonly used expressions.

The simplest formulation is the quadratic drag law given in (3.7). It is essentially an adaptation of the drag law formulation for bed shear stress in open channel and/or pipe flow, where a wave friction factor is used in place of a drag coefficient (i.e., Darcy friction factor) and directionality of the bed shear stress is obtained via multiplying velocity by its absolute value. The quadratic drag law formulation has been used so often in the past because velocity was only measured at a single (or a few) location(s) in the water column. The near-bed velocity profile was typically not measured, usually due in part to the difficulty of obtaining such detailed measurements under energetic conditions and/or the non-existence of the necessary technology until recently. The advent of coherent acoustic Doppler profiling velocimeters, such as the ADPV (Craig et al., 2011), has allowed for detailed near-bed velocity profiles to be measured.

In any case, the quadratic drag law was not originally intended for use in oscillatory flow, and assumes the bed shear stress has the same shape as observed velocity. Nevertheless, the drag law formulation has been used in many previous studies focused on the forcing mechanisms in oscillatory sheet flow, including all of the studies whose results are depicted in Figure 3.9. Therefore, quadratic bed shear stress was used in this chapter in order to reasonably draw comparisons with previous studies.

Bed shear stress can also be defined using the friction velocity, u_* , as

$$\tau_b = \rho |u_*| u_* , \quad (3.16)$$

where the friction velocity can be determined by fitting measured near-bed velocity profiles to the law of the wall (or “log-law”) velocity profile. This method is somewhat more robust than the quadratic drag law and has been applied rather successfully in both swash/dambreak (O’Donoghue et al., 2010; Puleo et al., 2012) and oscillatory flow tunnel studies (Van der A et al., 2010). However, the law of the wall logarithmic velocity profile was derived for a fully developed, turbulent boundary layer over a fixed, solid boundary, not for unsteady, oscillatory flows with a mobile sediment layer seen in BARSED. It is not likely that the boundary layer was ever fully developed under the wave cases presented in this manuscript, because of the rapidly changing flow direction. In fact, during offshore to onshore flow reversal (arguably the most important phase of the wave signal where bed shear stress should be properly quantified), the velocity profile is essentially uniform and near zero, which results in a poor fit to a logarithmic profile. This limits the practical applicability of (3.16) to strongly skewed-asymmetric oscillatory flows, as was the case during BARSED. In addition, the law of the wall formula is not easily – and perhaps not even properly – applied above a mobile sediment bed with rapid changes in bed level relative to the fixed sensors, since its original intent was for a solid, non-moving boundary. In the end, the time series for friction velocity based on log-law fits results in too many gaps with no information about bed shear stress; therefore, it is concluded that the log-law is not well suited for approximating u_* under the unsteady flow types used in BARSED.

Nielsen (1992) (Section 2.4.4) and Nielsen & Callaghan, (2003) outline an alternative method to determine friction velocity for use in (3.16), which is suitable for turbulent flow under arbitrary wave shapes:

$$u_* = \sqrt{\frac{1}{2} f_{2.5}} \left[\cos(\varphi_\tau) u_\infty + \sin(\varphi_\tau) \frac{1}{\omega_p} \frac{du_\infty}{dt} \right], \quad (3.17)$$

where $f_{2.5}$ is the wave friction factor, (3.8), with $k_s = 2.5d_{50}$; $\varphi_\tau \in [0^\circ; 90^\circ]$ with $\varphi_\tau = 0^\circ$ corresponding to drag dominant sediment transport, and $\varphi_\tau = 90^\circ$ corresponding to pressure gradient dominant sediment transport (Nielsen, 2006; Nielsen & Callaghan, 2003); and ω_p is the peak angular frequency ($= 2\pi/T$).

The optimal phase angle, φ_τ , is determined by matching measured sediment transport rates with sediment transport rates computed by substituting the Shields parameter, with bed shear stress calculated using (3.16) and (3.17), into a Meyer-Peter and Müller type bed load formula for oscillatory flow (see for example, Nielsen, 1992; Chapter 2.4). Two assumptions would be necessary to apply this method to the BARSED dataset, including extrapolating the fluid velocity profile into the sheet layer (not measured due to attenuation of sound signal from ADPV) and assumptions about the shape of the fluid velocity profile (Pugh & Wilson, 1999; Sumer et al., 1996). There are also numerous forms of the Meyer-Peter and Müller type equations (Meyer-Peter & Müller, 1948), raising the question of which formulation to use in calibration against measured data. Finally, perhaps two individual estimates for φ_τ would be appropriate, corresponding to each half-cycle of the wave because acceleration effects under such skewed-asymmetric waves are more prominent near offshore to onshore flow reversal during crest arrival. Such an analysis would require extensive sensitivity testing and validation and is outside the scope of this chapter.

3.5.3 Free Stream Horizontal Advective Acceleration

Strong horizontal pressure gradients during offshore to onshore flow reversal under strongly asymmetric surface waves may loosen sediment, increase bed

erodibility, and lead to a larger sheet thickness than would develop in oscillatory flow tunnels or unidirectional flow, where non-linear advective acceleration terms are negligible (Calantoni & Puleo, 2006; Hsu & Hanes, 2004). The measured horizontal pressure gradient is preferred for use in (3.12), but such information is rarely available in mobile bed experiments and field studies. The horizontal pressure gradient is related to acceleration via the horizontal momentum equation for inviscid flow (assuming variations in the spanwise direction are negligible, $\partial/\partial y = 0$) which can be written as

$$\frac{\partial u}{\partial t} + u \frac{\partial u}{\partial x} + w \frac{\partial u}{\partial z} = -\frac{1}{\rho} \frac{\partial P}{\partial x} + \frac{\partial \tau}{\partial z}. \quad (3.18)$$

Vertical variations in shear stress become negligible ($\partial\tau/\partial z \sim 0$) away from the bed, outside the bottom boundary layer (i.e., free stream). Furthermore, in oscillatory flow tunnels, the contributions of both advective acceleration terms in (3.18) are negligible. Conversely, the horizontal advection term ($u \frac{\partial u}{\partial x}$) is not necessarily negligible under surface waves propagating over uneven bottoms. But field observations of cross-shore variation in flow velocity ($\frac{\partial u}{\partial x}$) over a spatial scale necessary to resolve these gradients are not typically measured. Therefore, the cross-shore pressure gradient in (3.12) is often approximated using the local fluid acceleration, leading to the following expression for the Sleath parameter,

$$\tilde{S}_A = \frac{\partial \tilde{u}(t)/\partial t}{(s-1)g}. \quad (3.19)$$

The acceleration term in the numerator was computed using both the phase-averaged near bed velocity, $\tilde{S}_{A, z^* = 15 \text{ mm}}$, as well as the free stream velocity, $\tilde{S}_{A, \infty}$, for comparison (Figure 3.10g-h).

If the assumptions that advective acceleration terms are negligible and shear stress does not vary outside the bottom boundary layer are correct, one would expect \tilde{S}_p

to be equal to $\tilde{S}_{A,\infty}$ over an entire wave cycle. Yet, differences in these parameters were observed (Figure 3.10d), suggesting that under strongly asymmetric surface waves, the advective acceleration terms may not be negligible. The $w \frac{\partial u}{\partial z}$ term was evaluated using flow velocity measurements from ADV_1 (0.1 m above the bed) and ADV_2 (0.3 m above the bed) for all 12 wave cases. The vertical velocity was approximated 0.2 m above the bed by averaging $w(t)$ observations from ADV_1 and ADV_2 . Likewise, the derivative, $\frac{\partial u}{\partial z}$, was computed by taking the difference between $u(t)$ observations from ADV_1 and ADV_2 , and dividing by 0.2 m. The analysis demonstrated that, on average, $w \frac{\partial u}{\partial z}$ in the free stream is $O(10^{-3})$, which is 2 – 3 orders of magnitude smaller than the contributions of the local acceleration and horizontal pressure gradient terms, $\frac{\partial u}{\partial t}$ and $-\frac{1}{\rho} \frac{\partial P}{\partial x}$, respectively. Therefore, the $w \frac{\partial u}{\partial z}$ advective term may be neglected. Assuming vertical variations in shear stress remain negligible in the free stream, (3.18) reduces to

$$\overbrace{u_\infty \frac{\partial u_\infty}{\partial x}}^I = \left(\overbrace{-\frac{\partial u_\infty}{\partial t}}^{II} \right) + \left(\overbrace{-\frac{1}{\rho} \frac{\partial P}{\partial x}}^{III} \right), \quad (3.20)$$

where the residual term on the left hand side (I) is the free stream horizontal advective acceleration.

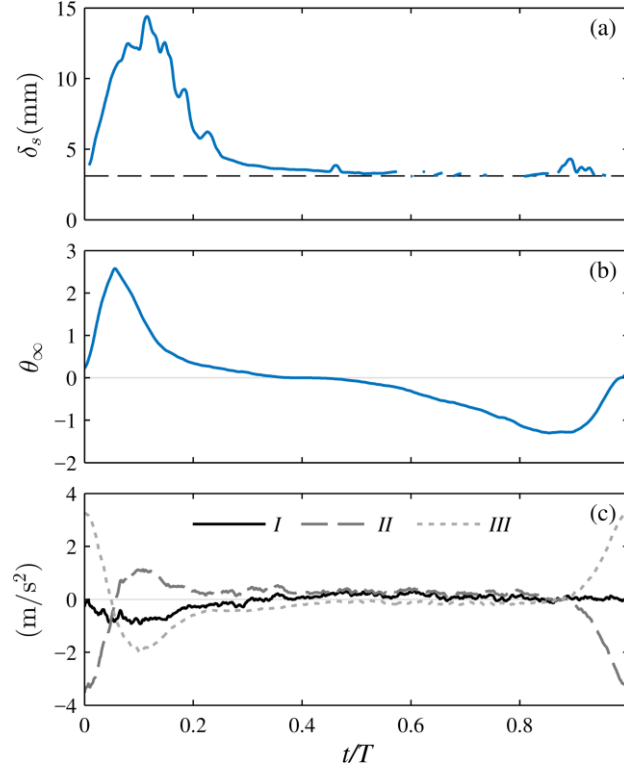


Figure 3.14: (a) Sheet thickness, (b) Shields parameter and (c) cross-shore momentum balance from equation (3.20), for wave case S1T7H60.

The three terms, ($I - III$) in (3.20) are shown along with sheet thickness and Shields parameter, θ_∞ , for the wave case with the largest degree of asymmetry (S1T7H60) in Figure 3.14. Terms II and III were roughly equal in magnitude with opposite sign for the majority of the wave cycle (i.e., $I = 0$). However, in the crest phase ($t/T = 0 - 0.2$), there was a non-zero, negative residual (I), which increased (decreased) in magnitude with increasing (decreasing) sheet thickness (Figure 3.15a,c). This finding is significant because horizontal advective accelerations (I) are only observable under surface waves and are not present in oscillatory flow tunnels. The non-zero residual (I) occurs because the pressure gradient (III) dominates local acceleration (II) beneath the

wave crest for S1T7H60. The sign of (I) depends on the signs of both u_∞ and $\partial u_\infty/\partial x$, where the sign of u_∞ is the same as the sign for θ_∞ (Figure 3.14b). Since u_∞ is positive while (I) is negative under the wave crest, it follows that $\partial u_\infty/\partial x$ must be negative for $0 < t/T < 0.2$ (Figure 3.14b-c).

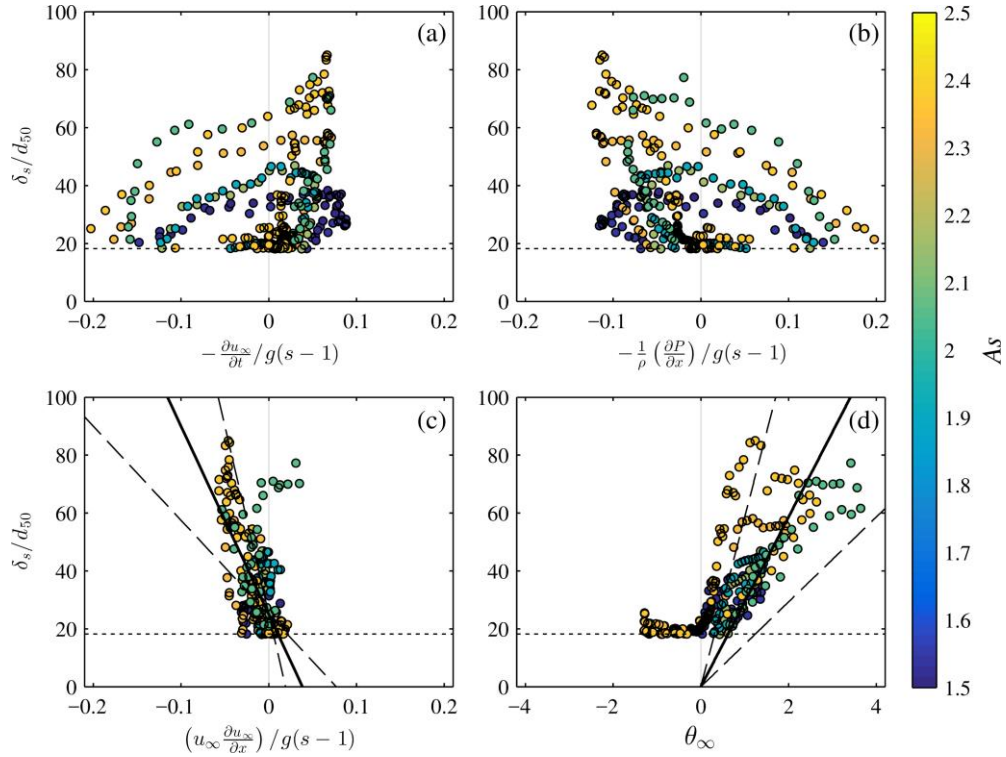


Figure 3.15: Non-dimensional momentum terms ($I - III$) from (3.20) and Shields parameter versus non-dimensional sheet thickness for seven wave cases with sediment S1 (marked with an asterisk, *, in Table 3.1). (a) Local free stream acceleration (II), (b) pressure gradient (III), (c) free stream horizontal advective acceleration (I), (d) Shields parameter. The dot colors denote the magnitude of wave asymmetry, As , for each case (Table 3.1) and the dotted lines are the minimum resolvable sheet thickness by the CCP. The solid lines are a least-square fit with 100% error outlined with the two dashed lines. Note the x -axis limits are different for panel (d).

Data from seven wave cases with sediment S1 (marked with an asterisk, *, in Table 3.1) satisfied the requirements necessary to compare each term in (3.20) to sheet layer thickness (Figure 3.15a-c). The seven different wave cases spanned a wide range of wave periods ($T = 5.0, 7.0$ and 9.0 s), wave heights ($H_{bar} = 0.59 - 0.94$ m), and cross-shore breaking locations ($x_b^* = 1 - 20$ m) (Table 3.1). There is no apparent correlation between sheet thickness and either the local acceleration (*II*) or pressure gradient (*III*) term (Figure 3.15a-b). Only every fourth point in each time series is shown for clarity. Conversely, sheet thickness increases with increasing magnitude of free stream horizontal advective acceleration (*I*), as well as for increasing Shields parameter (Figure 3.15c-d). The general trend in Figure 3.15c indicates that increasing horizontal advective accelerations (*I*), which are present under strongly asymmetric surface waves but absent from oscillatory flow tunnels, may be related to increasing sheet thickness ($R^2 = 0.37$). One of the cases shown (S1T9H60) appears to deviate from the general trend (Figure 3.15; light green dots). Re-performing the least-squares regression, excluding wave case S1T9H60, improved the fit ($R^2 = 0.58$, Figure 3.15; solid black line). Case S1T9H60 was, on average, greater than five times more skewed than the other six cases included in the analysis (Table 3.1), while the asymmetry for case S1T9H60 ($As = 2.07$) was near the middle of asymmetry range for the seven cases ($1.37 < As < 2.37$). The improved correlation following the removal of case S1T9H60 suggests that the free stream horizontal advective acceleration term may not be as directly related to sheet thickness under waves with strong mixed skewness and asymmetry.

One possibility is that the correlation in Figure 3.15c is somewhat fortuitous due to the abscissa's dependence on u_∞ . The relationship between δ_s and u_∞ was deduced

via least-squares regression between non-dimensional sheet thickness and the absolute value of the free stream Shields parameter $|\theta_\infty|$ (Figure 3.15d). When the y-intercept was allowed to be a free parameter in the linear regression, the coefficient of determination was $R^2 = 0.60$ ($y = 15.6x + 19.9$), nearly the same as the correlation with δ_s/d_{50} and $u_\infty \partial u_\infty / \partial x$. However, such a regression curve would yield a sheet layer ~ 20 grain diameters thick for $\theta_\infty = 0$. If the regression is forced through the origin, (i.e., equation (3.9)), the correlation decreases to $R^2 = 0.20$ (Figure 3.15d; solid black line). Nevertheless, a trend of increasing sheet thickness with increasing Shields parameter exists in Figure 3.15d, as well as in Figure 3.9 and Figure 3.12. Therefore, it is not possible to conclude, based solely on the correlation present in Figure 3.15c, that sheet thickness is enhanced under the presence of strong free stream horizontal advective acceleration, and additional experiments over a wider range of skewness and asymmetry parameters are necessary to further verify these observations.

3.6 Conclusions

High resolution measurements in a large wave flume of instantaneous sheet flow concentration profiles, pore pressures and near-bed velocity profiles were obtained on a sandbar for the first time. The intra-wave components were extracted via phase-averaging, leading to the following conclusions:

1. Sheet thickness was larger under wave crests than troughs, suggesting that sediment transport in the sheet layer beneath skewed-asymmetric waves plays an important role in onshore transport over a sandbar. Maximum sheet thickness was also observed to be smaller for larger grain diameter, under similar flow forcing.
2. The magnitude of maximum Shields parameter (and therefore the magnitude of Λ) is sensitive to the elevation of u_{max} , the model for grain roughness and the formulation for wave friction factor, which may partly explain differences in Λ across multiple studies. Comparisons using

- several different combinations of k_s , f_w , and elevation for u_{max} yielded a wide range of Λ values ($5 < \Lambda < 40$).
3. Grain roughness (normalized by d_{50}) varied by two orders of magnitude, $O(1 - 100)$, depending on whether a constant value ($k_s = 2.5d_{50}$) or one of two mobile roughness expressions was used. Grain roughness values computed based on an empirical expression from oscillatory sheet flow experiments were on the order of 100 to 300 grain diameters, leading to excessively large magnitudes for maximum Shields parameter. Values for k_s in this range are unrealistic, suggesting the height of the roughness elements was up to ten times larger than the sheet layer thickness, which ranged from $10 < \delta_s < 85$ grain diameters.
 4. The value for Λ was reduced by 40% using the standard expression for f_w given by (Swart, 1974) ($\Lambda \sim 13$) compared to a slightly modified version ($\Lambda \sim 22$). The modified version for f_w has previously been shown to better fit experimental data with small values of $k_s/A \lesssim 0.01$, where the standard version of f_w over-estimated observed wave friction factors [Nielsen, 1992]. This is important because k_s/A for the BARSSED data were unanimously less than 0.01.
 5. A non-zero residual in the horizontal momentum (i.e., free stream horizontal advective acceleration, $u_\infty \frac{\partial u_\infty}{\partial x}$) was present through a portion of the wave cycle for a sample of seven wave cases, indicating that the pressure gradient term in the horizontal momentum equation is not always equal to the local free stream acceleration under strongly asymmetric surface waves. The free stream horizontal advective accelerations during BARSSED correlated fairly well ($R^2 = 0.56$) with sheet thickness for waves with large asymmetry and near-zero skewness. A smaller correlation existed between sheet thickness and maximum Shields parameter ($R^2 = 0.20$).

Sheet flow sediment concentration profiles were measured in this study using the CCP, while all additional sheet flow data presented in this chapter used the conductivity concentration meter (CCM/CCM⁺) (Ribberink, 1998; Ribberink et al., 2008; Schretlen, 2012; Van der Zanden, 2016). Slight differences in the measurement technologies between the CCP and CCM/CCM⁺ sensors may result in different

quantifications of sheet thickness, which will affect the magnitude of Λ . A controlled comparison study with both sensors would provide insight regarding potential measurement differences in observed sheet thickness. Overall, differences in quantifying bed shear stress, grain roughness, and wave friction factor, as well as the differences in measurement technique make cross-experimental data comparison difficult. For now, the data collected during BARSED will be useful in calibrating and testing numerical models aiming to incorporate the combined effects of bed shear stress and pressure gradients in driving sheet flow.

Chapter 4

RELATIVE CONTRIBUTIONS OF WAVE-INDUCED SHEET FLOW AND SUSPENDED SEDIMENT TRANSPORT ON A SANDBAR

4.1 Introduction

Surf zone sandbars are migratory nearshore features, responding to ever-changing environmental conditions on time scales ranging from hours/days to weeks/months (Van Enckevort & Ruessink, 2003), up to years and decades (Ruessink et al., 2003; Wijnberg, 2002). In general, during high energy wave events, surf zone sandbars undergo rapid offshore migration at rates up to 1 m/hour, as suspended sediments entrained through wave-breaking are carried offshore by undertow currents (Gallagher et al., 1998). In contrast, shoreward sandbar migration events tend to occur more slowly, at rates on the order of 1 m/day (Van Maanen et al., 2008), during periods with more quiescent wave conditions, where a majority of the total net sediment transport is confined within the wave bottom boundary layer (Van der Zanden, van der A, Hurther, Cáceres, O'Donoghue, & Ribberink, 2017). Several wave-induced processes contribute to onshore sandbar migration, including near-bed orbital velocity skewness (Hsu et al., 2006; Ruessink et al., 2007) and velocity asymmetry/acceleration skewness (Drake & Calantoni, 2001; Elgar et al., 2001; Hoefel & Elgar, 2003); strong pressure gradients at off-to-onshore flow reversal (Foster et al., 2006; Madsen, 1974; Zala Flores & Sleath, 1998); and onshore boundary layer streaming under the presence of skewed-asymmetric surface waves (Henderson et al., 2004; Nielsen, 2006; Trowbridge & Young, 1989; Yu et al., 2010).

The total amount of sediment transported by waves and currents (total load) in the surf zone is usually separated into two fundamental components (Bagnold, 1956; Bailard, 1981; Dally & Dean, 1984; Roelvink & Brøker, 1993; Van Rijn, 2007): suspended load and bed load. Suspended load transport is the transport sediment in suspension, supported by turbulent fluid motions. Although suspended sediment concentrations are relatively small ($\phi \sim 0.001 - 0.08 \text{ m}^3/\text{m}^3$), in the surf zone, the suspended load regime spans the majority of the water depth, h . Bed load transport occurs in direct proximity to the sediment bed and may be further separated into two distinct transport modes: (i) the transport of particles by rolling, sliding, and saltating, and (ii) sheet flow. The former bed load component occurs in lower-energy flow conditions and typically results in the development of small scale bed forms (e.g., ripples). Under strong bed shear stress and strong pressure gradients, typical of skewed-asymmetric waves in the surf zone, small-scale bed forms are wiped out with the onset of sheet flow. Sheet flow is the transport of high concentrations of sediment ($\phi^{sf} \sim 0.08 - 0.64 \text{ m}^3/\text{m}^3$) supported by intergranular and pore-pressure interactions within a relatively thin layer near the bed. The sheet flow layer expands and contracts with the passing of each wave, varying in thickness, $\delta_s(t)$, from a few millimeters to several centimeters (Dohmen-Janssen & Hanes, 2002, 2005; Mieras et al., 2017a; O'Donoghue & Wright, 2004a; Ribberink & Al-Salem, 1995). While sheet flow layer thickness is very thin relative to the water depth ($\delta_s \ll h$), average sediment concentrations in the sheet flow layer are 1 – 3 orders of magnitude greater than those in suspension ($\phi^{sf} \gg \phi^{ss}$). Consequently, it is possible that the contribution of sheet flow to the total transport rate is similar in order of magnitude to the contribution of the wave component of

suspended load (Mieras et al., 2017b; O'Donoghue & Wright, 2004b; Van der Zanden, van der A, Hurther, Cáceres, O'Donoghue, Hulscher, et al., 2017).

Prior field studies that were focused on quantifying the mechanisms driving suspended sediment transport in the nearshore followed similar methodology (Aagaard et al., 1998; Aagaard & Greenwood, 1994; Beach & Sternberg, 1988, 1996; Conley & Beach, 2003; Hanes & Huntley, 1986; Mariño-Tapia et al., 2007; Yu et al., 1993). Sensors were deployed at either a single or multiple cross-shore stations (1 – 7) spanning tens to hundreds of meters in the cross-shore direction and spaced anywhere from 2 – 80 m apart. Suspended sediment concentrations were measured using optical backscatter sensors (OBS) and fiber optical backscatter sensors (FOBS) (Beach et al., 1992; Conley & Beach, 2003). With the exception of Conley and Beach (2003), the lowest suspended sediment observations were typically between 0.02 – 0.05 m above the nominal bed, and horizontal flow velocities were measured at only one location in the water column at each station, typically between 0.1 and 0.3 m above the nominal bed. However, to the authors' knowledge, field observations of sediment transport within the sheet flow layer have not been observed.

The majority of cross-shore sandbar migration field studies have been conducted from the morphological standpoint, whereby, (i) bathymetric profiles are collected at temporal intervals ranging from hourly/daily (Gallagher et al., 1998; Kuriyama, 2002; Lippmann & Holman, 1990) to monthly/yearly (Wijnberg, 2002; Wijnberg & Terwindt, 1995), over periods of time ranging from weeks to decades (Ruessink et al., 2003); and (ii) hydrodynamic observations typically consist of far-field wave and environmental conditions. Subsequent process-based modeling efforts have generally focused on tuning individual parameters in the model formulations for suspended load and bed load

to maximize model skill in predicting observed beach profiles over time (Fernández-Mora et al., 2015; Hoefel & Elgar, 2003; Hsu et al., 2006; Plant et al., 2004). However, little emphasis at the operational level has been placed on tuning coastal morphology models to the true relative contributions of the physical processes (e.g., suspended load, bed load and sheet flow) that drive the changing bathymetry. Such a modeling approach can lead to the improper quantification (magnitude and/or direction) of each modeled sediment transport component under skewed and/or asymmetric waves often observed in the surf zone (Thornton et al., 1996; Van Maanen et al., 2008). The fact that models are calibrated to match morphology instead of observations of physical processes is due, in part, to the lack of detailed sediment transport observations (field and lab) under realistic wave forcing conditions and spatially variable bathymetry.

Sheet flow studies carried out in oscillatory flow tunnels (OFT) have significantly improved our understanding of wave-induced sediment transport processes under varying degrees of velocity skewness and asymmetry (Hassan & Ribberink, 2005; O'Donoghue & Wright, 2004b; Ribberink & Al-Salem, 1995; Silva et al., 2011; Van der A et al., 2010; Watanabe & Sato, 2004). However, not all physical processes that contribute to enhanced net onshore sediment transport, e.g., boundary layer streaming (Kranenburg et al., 2013; Yu et al., 2012) and wave-breaking-induced turbulence (Cox & Kobayashi, 2000; Zhou et al., 2014), can be re-produced in OFTs due to the lack of a free-surface. A comprehensive database (SANTOSS) was compiled in 2009 of full scale laboratory experiments (298 in total) focused on wave-induced sediment transport processes (Van der Werf et al., 2009). The number of experiments carried out under full-scale surface wave forcing in large wave flumes made up 7.5% (21 of 298) of the entire database. Moreover, only 8 of the 21 large wave flume studies listed in the

SANTOSS database were conducted in the sheet flow regime ($< 3\%$ of the total). Thus, there is a severe lack of detailed simultaneous observations of suspended sediment and sheet flow processes under realistic wave forcing.

Since 2009, several more small scale (Berni et al., 2013, 2017) and large scale (Brinkkemper et al., 2017; Schretlen, 2012; Van der Zanden, van der A, Hurther, Cáceres, O'Donoghue, Hulscher, et al., 2017; Van der Zanden, van der A, Hurther, Cáceres, O'Donoghue, & Ribberink, 2017; Yoon & Cox, 2012) wave flume studies have contributed significantly to fill the gap in full-scale surface wave experiments in the sheet flow regime. Recent development of a new sensor, the conductivity concentration profiler (Lanckriet et al., 2013), has enabled instantaneous sediment concentration profiles in the sheet flow layer to be measured with high resolution (1 mm vertical bin size, see Chapter 2) in the swash zone (field and large wave flume) (Lanckriet et al., 2014; Puleo et al., 2014, 2016) and surf zone (large wave flume) (Anderson et al., 2017; Mieras et al., 2017a).

This chapter focuses on high-resolution velocity and concentration measurements collected during the BARSED experiment. The main emphasis is to quantify the relative contributions of suspended sediment and sheet flow sediment transport processes over a sandbar under various field-scale wave forcing. Relevant details of the experimental procedure and instrumentation are outlined in Section 4.2. Procedures for processing the data are covered in Section 4.3. Phase-averaged and wave-averaged sediment flux profiles and sediment transport for different transport regimes and wave cycles are presented in Section 4.4. A discussion of potential errors introduced from assumptions and concluding remarks are given in Sections 4.5 and 4.6, respectively.

4.2 Laboratory Experiment

4.2.1 Facilities and Test Conditions

The sandBAR SEDiment transport experiment (BARSED) was conducted in 2015 in the large wave flume at Oregon State University's O.H. Hinsdale Wave Research Laboratory (Anderson et al., 2017; Mieras et al., 2017a). A fixed, barred beach profile was constructed to near-field scale based on observed beach profiles at Duck, NC during the Duck94 experiment (Gallagher et al., 1998; Scott et al., 2005), with a sediment pit installed on the sandbar crest (Figure 4.1a). The still water depth, h , over the sandbar crest was 1 m, such that the still water level was at $z_{SWL} = 2.448$ m. Flume coordinates are defined such that $x = 0$ is the initial location of the wave maker face (positive shoreward), $z = 0$ is the bottom of the wave flume (positive up), and $y = 0$ is the flume centerline in the cross-shore direction (positive following the right-hand-rule). The hybrid profile design minimized the complication of separating the forcing and response under active morphological adjustment, allowing for the isolation of small-scale, wave-induced bed response (and subsequent sediment transport) due to large-scale wave forcing. Moreover, the fixed large-scale beach profile made it possible to conduct repeat trials spanning a multitude of wave conditions typified by erosion and accretion. It was possible to test the influence of grain size on the relative importance of suspended sediment and sheet flow transport rates due to the simplicity of swapping out sediments (i.e., relatively small volume of sediment in the pit, compared to the volume of the entire profile given in the gray area of Figure 4.1a). Two different sediments were used (S1 and S2) in the experiments, with density, ρ_s , of $2,650 \text{ kg/m}^3$ and median grain diameters, d_{50} , of 0.17 mm (S1: $d_{16} = 0.10$ mm, $d_{84} = 0.26$ mm) and 0.27 mm (S2: $d_{16} = 0.16$ mm, $d_{84} = 0.38$ mm).

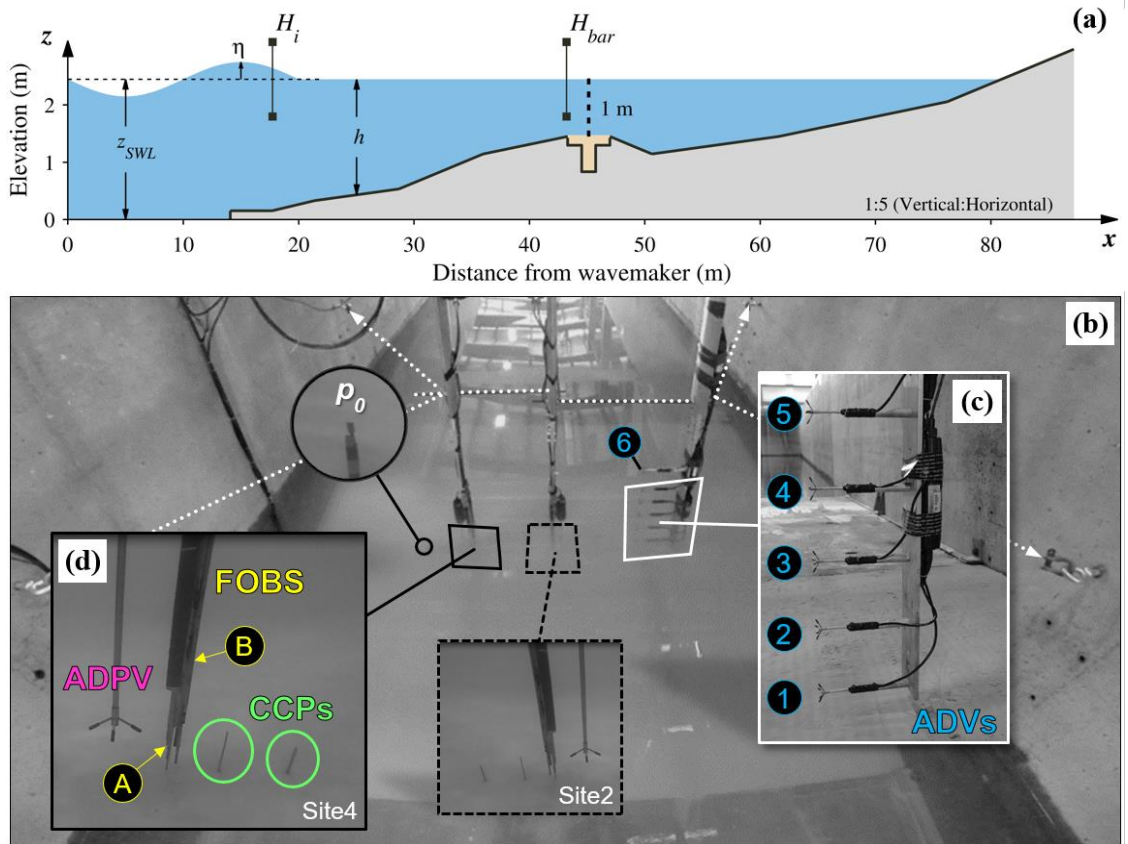


Figure 4.1: (a) Beach profile, sediment pit and two wave gauges, where the vertical dashed line on the sandbar crest indicates the cross-shore deployment location of the sensors. (b) Photo of instrumentation deployed on/over the sandbar. (c) Close-up view of the lower 5 of 6 ADVs ($ADV_1 - ADV_5$), with ADV_6 labeled in (b). (d) Expanded view of the near-bed instrumentation at Site 4.

Table 4.1: Summary of wave cases, trials and number of ensembles.

T (s)	d_{50} (mm)	Case ID	Trial ID ^a	Site ID	N_{trial}	N	N_T	
5.0	0.17	S1T5H40	41, 78	4, 2	10, 40	50		
		S1T5H45	67	2	10	10		
		S1T5H50	48, 49	2, 2	10, 10	20		
		S1T5H60	45, 46, 47	2, 2, 2	10, 10, 10	30		
							<u>110</u>	
	0.27	S2T5H40	120	2	10	10		
		S2T5H50	118, 118 ⁽⁹⁾ , 119, 121	2, 4, 2, 2	10, 9, 10, 10	39		
							<u>49</u>	159
7.0	0.17	S1T7H40	17 ^(6,7) , 18 ⁽⁷⁾ , 74, 79	4, 4, 4, 2	8, 9, 10, 40	67		
		S1T7H45	68, 70	2, 2	10, 10	20		
		S1T7H50	19, 20, 21, 22	4, 4, 4, 4	10, 10, 10, 10	40		
		S1T7H60	14, 51, 80 ⁽⁵⁾	4, 2, 2	10, 10, 9	29		
							<u>156</u>	
	0.27	S2T7H40	123	4	10	10		
		S2T7H45	124 ⁽⁴⁾ , 124	2, 4	9, 10	19		
		S2T7H50	112, 113, 125	4, 4, 2	10, 10, 10	30		
		S2T7H60	127 ⁽¹⁾ , 127	2, 4	9, 10	19		
							<u>78</u>	234
	9.0	0.17	S1T9H40	23, 24 ⁽⁷⁾ , 25	4, 4, 4	10, 9, 10	29	
			S1T9H50	26, 27, 28	4, 4, 4	10, 10, 10	30	
S1T9H60			13, 81	4, 2	10, 10	20		
							<u>79</u>	
0.27		S2T9H40 ^b	115, 115	2, 2	10, 10	20		
		S2T9H50	116, 117, 117	2, 2, 4	10, 10, 10	30		
						<u>50</u>	129	

Note. Additional details on the wave conditions (e.g., measured wave heights, breaking locations and pore-pressure gradients) are provided in Mieras et al. (2017a) and Anderson et al. (2017).

^a Values in parentheses next to trial IDs denote that the (n^{th})_{trial} ensemble(s) was(were) removed from analysis due to spurious peaks of concentration measurements in either CCP or FOBS data.

^b Data from both CCPs at a single site was available within 1 trial, yielding 20 sheet flow concentration ensembles, but only 10 unique ensembles of every other measured parameter.

Wave trials were conducted using a series of 10 monochromatic waves, with 20 s of ramp up and 20 s of ramp down phases. (Note that two trials, 78 & 79 consisted of 40 waves; see Table 4.1.) Trials were repeated multiple times for each sediment size to obtain a synoptic dataset. Each wave within a trial was treated as an individual realization of the same event (i.e., the $(n^{th})_{trial}$ ensemble), where the number of waves in a trial corresponds to the number of ensembles, N_{trial} , for that trial. Trials with the same input wave maker conditions and sediment size (referred to as either “case” or “wave case” hereafter) were collected and analyzed together (Table 4.1). This chapter focuses on 19 (11 with S1; 8 with S2) of the 21 wave cases from Mieras et al. (2017a), typified with either erosive or accretive conditions. Eleven unique wave maker signals comprised the 19 different cases. Wave gauges at the toe of the beach profile (H_i) and the seaward edge of the sandbar crest (H_{bar}) (Figure 4.1a) recorded wave heights ranging from $0.38 \leq H_i \leq 0.66$ m and $0.55 \leq H_{bar} \leq 0.94$ m, respectively, across three different wave periods, T , 5.0, 7.0 and 9.0 s (Table 4.1). Maximum Shields parameters on the sandbar crest were between $0.4 < \theta_{max} < 4.0$ (Mieras et al., 2017a). Bed forms were not present in this range of Shields parameters. For the 19 cases, wave breaking generally occurred between 1 – 7 m landward of the instruments, with a few cases breaking nearer the shoreline.

4.2.2 Instrumentation and Calibration

An array of sensors was positioned over the center of the sandbar crest ($x = 45.1$ m) to measure velocity and sediment concentration profiles (Figures 4.1b - 4.1d). Only sensors relevant to this chapter are discussed here. Details of the entire suite of instrumentation are provided in Mieras et al. (2017a) and Anderson et al. (2017). Free-surface elevation, $\eta(t)$, over the sandbar was captured with a pressure sensor, $p_0(t)$,

deployed just above the sediment bed (Figure 4.1b). The pressure sensor was reset to zero before each trial to measure the wave-induced pressure variations, such that time-varying water depth at the center of the sandbar crest ($x = 45.1$ m) was computed as $h(t) = \eta(t) + z_{SWL}$. The fluid velocity profile ($u(t, z)$, $v(t, z)$, $w(t, z)$; cross-shore, spanwise, vertical) spanning the water column was measured at 100 Hz with a vertical array of six Nortek Vectrino acoustic Doppler velocimeters (ADV; Figure 4.1c) and two Nortek Vectrino acoustic Doppler profiling velocimeters (ADPV; Figure 4.1d) (Craig et al., 2011). Sediment concentration profiles were measured on the sandbar crest at 8 Hz using two dual-probe fiber optic backscatter sensors (FOBS; Figure 4.1d) (Beach et al., 1992) and four conductivity concentration profilers (CCP; Figure 4.1d).

The lowest ADV (ADV_1) was positioned approximately 0.10 m above the bed, with $ADV_2 - ADV_6$ mounted above ADV_1 at 0.20 m increments, such that the highest observation (ADV_6) was 0.10 m above the still water line (Figure 4.2a; squares). In addition, two instrumented stations (Site 2 and Site 4; Figure 4.1d) were installed adjacent to the ADV array, separated by ~ 0.6 m in the y -direction, each containing two CCPs (buried), one ADPV and one FOBS. The CCPs measured sheet flow sediment concentration profiles spanning 29 mm with 1 mm vertical resolution. The conjoined pair of CCPs at each site was deployed with a vertical offset of about 15 mm to increase the vertical sampling range under changing bed levels (Figure 4.2b). The ADPV was positioned such that the sampling volume, located 0.04 to 0.07 m from the transmitter, intersected the sediment bed and measured fluid velocities spanning 30 mm with 1 mm vertical resolution (Figure 4.2b). Each dual-probe FOBS (probes A and B; Figure 4.1d) had ten miniature fiber optic backscatter sensors in a so-called “pipe organ” configuration (i.e., the direction each sensor is “looking” spirals around the central axis).

Sensors 1 – 10 were on probeA, with 11 – 20 on probeB, where the sensors at the tips of probes A and B are defined here as sensor 1 and 11, respectively, labeled in Figure 4.2. The bin spacing between sensors on probeA was 0.01 m, except for between 9 and 10, which were separated by 0.02 m (Figure 4.2; white dots). ProbeB had more variable sensor spacing, where the distance between successive bins was (starting with sensors 11 and 12): 0.02, 0.03, 0.03, 0.04, 0.05, 0.06, 0.06, 0.06, 0.07 m (Figure 4.2; black dots). To fill in the 0.02 m gap between sensors 9 and 10, probeB was installed with a vertical offset of 0.09 m from probeA at Sites 2 and 4. One to three sensors on each FOBS probeA were within the sediment bed during the experiments (Figure 4.2b), yielding FOBS suspended sediment concentration profile observations from the bed to roughly 0.47 m above the bed.

The two FOBS were calibrated for both sediment sizes (S1 and S2) using a recirculating flow chamber. Sediment was added to the chamber with a known volume of water to achieve desired mass concentrations. Then data were recorded with all four FOBS probes for 1 minute. Additional sediment was incrementally added, and the process repeated, until the FOBS backscatter signal became saturated around mass concentrations of 130 g/L (volumetric concentrations, $\phi \sim 0.05 \text{ m}^3/\text{m}^3$). The recorded data were subsequently averaged over the minute of measurement to obtain one characteristic backscatter value for each sensor of the four probes for all 22 mass concentrations. A quadratic calibration curve was obtained for each of the 20 sensors on both FOBS, for both sediment sizes, by performing least-square-error regression analysis.

It is important to note that FOBS backscatter intensity is not a function of ambient light. Every sensor on the FOBS consists of two fibers. One fiber acts as a light

source, which pulsates on/off during a measurement, while the other fiber measures light backscattered from particles in suspension during the on/off conditions (Beach et al., 1992). The ambient (background) light is removed by subtracting the “off” signal from the “on” signal (Puleo et al., 2000).

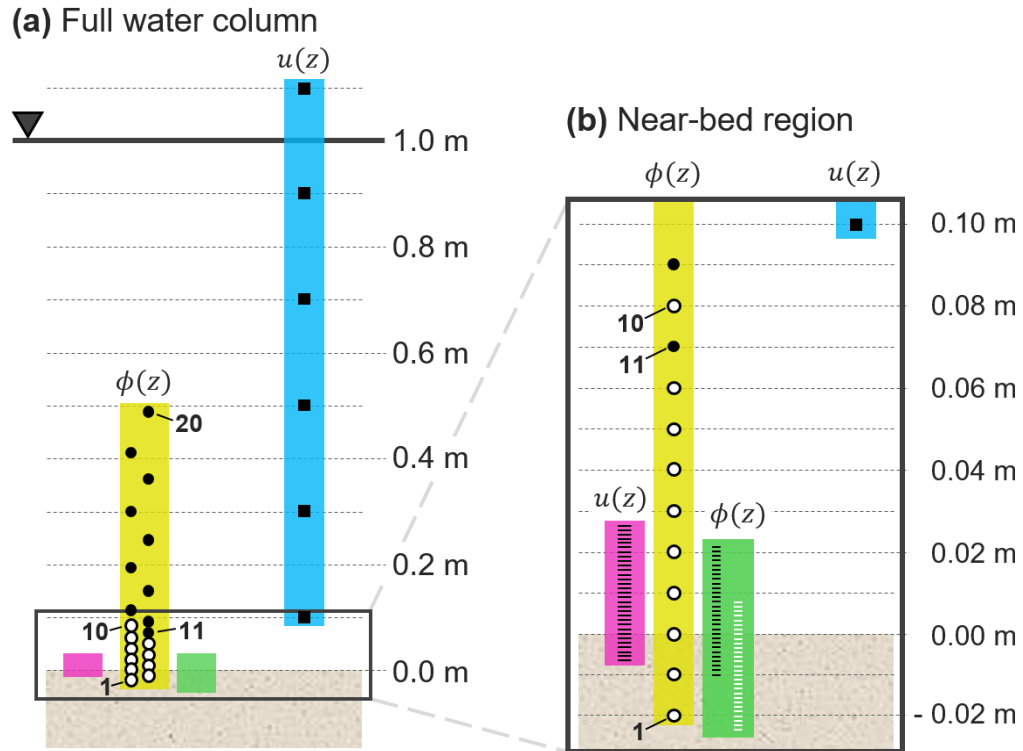


Figure 4.2: Schematic of velocity and concentration measurement bin locations in the (a) entire still water column, and (b) lower 0.10 m of the water column. The shaded regions represent the general range over which measurements were obtained, where the colors correspond to the sensor color scheme in Fig. 4.1. The symbols within the shaded areas represent actual measurement bin locations. Different markers are used to distinguish FOBS probeA (white circles) from probeB (black circles).

4.3 Data Treatment

Prior to processing any data, the trials with suitable data for processing had to be determined. Data were retained if the bed interface was located within the sampling range of either of the two CCPs throughout the duration of the trial. This condition was satisfied once for both CCPs in a pair (Trial 115 at Site 2; Table 4.1). Generally, only one of the two CCPs in a pair captured the bed interface. For five trials, a CCP at both sites (Site 2 & 4) observed the bed interface over the trial duration (Trials 115, 117, 118, 124, and 127; Table 4.1). However, more often than not (always for S1), only one of the two sites had a CCP that captured the bed interface across the trial duration. The limited number of trials with CCPs that captured the bed interface at both sites is due in part to the upper CCP malfunctioning at Site 2 between Trials 15 and 28 (a span containing 41% of the selected trials for S1).

A complete list of Trial and Site IDs (Site 2 and/or 4) from which data were processed for each of the 19 wave cases, as well as the trials from which ensembles were removed, is provided in Table 4.1. Wave cases are grouped by wave period, then grain size, and then from smallest to largest wave height. The number of trials (and sites) with suitable data for a given wave case ranged from 1 to 4. Spurious concentration data appeared in one ensemble for six trials and in two ensembles for one trial (Trial 17), resulting in the removal of eight total ensembles from analysis and leading to seven trials with $N_{trial} < 10$ (Table 4.1). As a result, the number of ensembles, N , for all 19 wave cases ranged from $10 \leq N < 67$. The total number of ensembles (including S1 and S2 together) for cases with 5.0, 7.0 and 9.0 s wave periods, N_T , was 159, 234, and 129, respectively.

4.3.1 Merging Concentration and Velocity Profiles

A time series of volumetric concentration profiles, $\phi(t, z)$, from within the bed to the top of the FOBS (i.e., the 20th sensor, $z_{FOBS,20} \approx 1.92$ m) was constructed for every trial (and site) by merging the instantaneous concentration profiles measured by the FOBS and CCP (Mieras et al., 2017b). FOBS calibrations revealed signal saturation at $\phi \sim 0.05$ m³/m³, whereas CCP measurements become less reliable for $\phi < 0.05$ m³/m³ (Lanckriet et al., 2013). Therefore, when concentrations were observed by both a FOBS and a CCP at a particular elevation, where $\phi_{FOBS} \leq 0.05$ m³/m³ and $\phi_{CCP} \geq 0.05$ m³/m³, precedence was given to CCP data. Linear interpolation was used to approximate concentrations in small gaps between valid FOBS and CCP measurements. The merged sediment concentration profiles were not extrapolated to the free-surface, which may affect net suspended sediment fluxes and relative contributions of suspended and sheet flow sediment transport (see Discussion §4.5.1.1).

Measured ADPV velocities in the top and bottom 5 bins were discarded due to a known bias with the Nortek Vectrino Profiler (Thomas et al., 2017), which reduced the vertical sampling range of the ADPV to 21 mm. A time series of the cross-shore velocity profiles, $u(t, z)$, from the bed ($z \approx 1.46$ m) to the elevation of ADV_6 ($z \approx 2.55$ m) was constructed for each trial (and site) by merging the instantaneous velocity profiles measured by the ADV array and ADPV. With the passage of each wave, ADV_5 and ADV_6 were periodically inundated and exposed in air. The free-surface elevation – derived from near-bed pressure measurements, p_0 (Figure 4.1b) – was used to exclude data when ADVs were exposed to air. Linear interpolation was used to approximate velocities between the elevation of ADV_1 and the top of the ADPV measurement range.

The merged time series of sediment concentration and velocities for every trial (and site) were separated into N_{trial} ensembles based on zero up-crossings of the

pressure, $p_0(t)$. Each time-space ensemble of sediment concentration and velocity were interpolated onto a normalized time vector, $t/T_{n_{trial}}$, from 0 to 1.0 with normalized time intervals of 0.01, where $T_{n_{trial}}$ is the elapsed time between zero up-crossings for the $(n^{th})_{trial}$ ensemble. The average (standard-deviation) percent error between observed wave periods based on zero up-crossings and prescribed wave periods was 1.1% (\pm 1.2%) across all trials presented here. All N data ensembles were then compiled into groups by wave case, where hereafter, the subscript n denotes a single ensemble within a wave case.

4.3.2 Definitions

4.3.2.1 Averaging Operators

Three different averaging operations were used in data processing and analysis: phase-averaging, wave-averaging, and ensemble-averaging. Let ξ be an arbitrary variable representing either a measured or computed quantity. Intra-wave quantities were obtained via phase-averaging across multiple realizations. Phase-averaged quantities are denoted with tildes, $\tilde{\xi}$, and computed as

$$\tilde{\xi} = \frac{1}{N} \sum_{n=1}^N \xi_n, \quad (4.1)$$

where each ensemble of ξ_n varies with time (e.g., $\xi_n \equiv [\eta(t/T)]_n$), but may also vary with elevation (e.g., $\xi_n \equiv [\phi(t/T, z)]_n$, or $\xi_n \equiv [\phi(t/T, z) \cdot u(t/T, z)]_n$). If ensembles of ξ_n are functions of z , then equation (4.1) is applied for each elevation.

An overbar, $\overline{\xi}$, is used to denote wave-averaged quantities that are computed by integrating over the entire normalized wave cycle as

$$\bar{\xi} = \int_0^1 \xi d(t/T), \quad (4.2)$$

where ξ , and thus $\bar{\xi}$, may be functions of z , though it is not required. The integrand, ξ , in equation (4.2) can either be phase-averaged (e.g., $\xi \equiv \tilde{u}(t/T, z)$), or a collection of time-dependent data ensembles as in the examples for ξ_n following equation (4.1). Hereafter, if more than one averaging operator is present over a variable, the order of operations goes from closest to farthest from the variable (i.e., inside-out). For example, $\overline{\bar{\xi}}$, would read “wave-average of phase-averaged ξ .”

Ensemble-averaging is denoted with angled brackets, $\langle \rangle$, and is similar to phase-averaging,

$$\langle \xi \rangle = \frac{1}{N} \sum_{n=1}^N \xi_n, \quad (4.3)$$

though it is reserved for instances where ξ_n is independent of wave phase (i.e., not a function of t/T), but is either a scalar or function of elevation only.

4.3.2.2 Sheet Flow Layer

The time-varying elevation of the top of the sheet flow layer, $[z_{top}(t/T)]_n$, was defined as the $\phi = 0.08 \text{ m}^3/\text{m}^3$ contour (Bagnold, 1956). The time-varying elevation of the bottom of the sheet flow layer, $[z_{bott}(t/T)]_n$, was determined by fitting a composite power law and linear curve to each concentration profile in each ensemble to identify the sharp shoulder transition in the sheet flow concentration profile (Lanckriet et al., 2014; Mieras et al., 2017a; O’Donoghue & Wright, 2004a). The time-varying elevation of the inflection point in each concentration profile, $[z_{ip}(t/T)]_n$, was determined from the curve-fits to the measured concentration profiles (Mieras et al., 2017a). The time-

varying nature, as well as intra-wave variations, of $[z_{top}]_n$, $[z_{ip}]_n$, and $[z_{bott}]_n$ are illustrated for case S1T7H60 in Figures 4.3a – 4.3c.

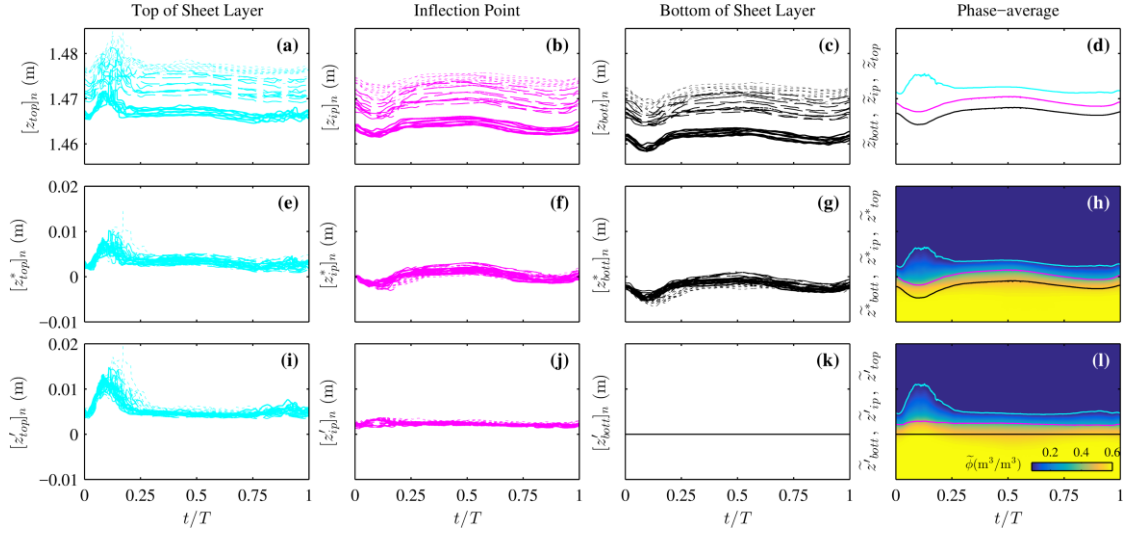


Figure 4.3: Ensembles of sheet flow layer quantities in different vertical coordinate systems for case S1T7H60: Trial 14 (dashed lines), Trial 51 (dotted lines), and Trial 80 (solid lines) in the first three columns. Phase-averaged quantities are shown in the fourth column. (a – d) flume coordinates as in Fig. 4.1, (e – h) z^* -coordinate system, and (i – l) z' -coordinate system. Phase-averaged sediment concentrations are shown in pseudo-color plots in plots (h) and (l).

4.3.2.3 Vertical Coordinate Systems, z^* and z'

Two different ‘local’ vertical coordinate systems are used in this chapter, both of which are different from the fixed, flume coordinate, z . The sediment bed progressively eroded or accreted by a relatively small amount during the course of most trials (Anderson et al., 2017), due to cumulative effects of small intra-wave changes in the bed elevation. In addition, from trial to trial, the initial bed level prior to running waves was never at exactly the same elevation relative to the fixed sensors, especially

for wave cases consisting of trials that were not conducted in chronological succession (e.g., S1T7H60 which consisted of Trials 14, 51 and 80; Table 4.1). Differences in initial and overall bed levels relative to fixed, flume coordinates, for non-successive trials are illustrated in Figures 4.3a - 4.3c, where ensembles within a trial are closely grouped in the vertical, but are noticeably offset in the vertical by up to 0.01 m for different trials. Such differences in bed levels relative to the fixed sensors were taken into account before phase- and/or wave-averaging any data that were a function of distance from the sediment bed by assigning each data ensemble (e.g., h, ϕ, u) a ‘local’ z^* -coordinate, where

$$[z^*]_n = z - [z_{ip}(t/T = 0)]_n, \quad (4.4)$$

and z is the vertical flume coordinate defined in Figure 4.1a. The z^* -coordinate system essentially ensures that each ensemble of data is relative to the same “initial bed level”, $[z^*]_n = 0$, which is the elevation of the inflection point in the sheet flow concentration profile at the n^{th} zero up-crossing of η (Figures 4.3e - 4.3h). The low spread between the ensembles in Figures 4.3e – 4.3g demonstrates the benefit of using the z^* -coordinate system for each ensemble.

Water depth was computed in the z^* -coordinate system using $h(t/T) = \eta(t/T) + z_{SWL} - [z_{ip}(t/T = 0)]_n$, where examples of $[z_{ip}(t/T = 0)]_n$ are shown for all three trials of wave case S1T7H60 in Figure 4.3b. Free-surface elevation, $\eta(t)$, did not change based on choice of coordinate system. The profiles of velocity and volumetric sediment concentration for each ensemble and every trial (and site) were gathered and interpolated onto a universal z^* elevation vector with vertical resolution, $\Delta z^* = 0.00025$ m from $-0.015 \leq z^* < 0.04$ m, $\Delta z^* = 0.01$ m between $0.04 \leq z^* < 0.50$ m, and $\Delta z^* = 0.025$ m from $0.50 \leq z^* \leq 1.12$ m. An example result of phase-

averaged volumetric concentration, $\tilde{\phi}(t/T, z^*)$, in the z^* -coordinate system is provided in Figure 4.3h, with the corresponding phase-averaged top, inflection point, and bottom of the sheet flow layer.

The second ‘local’ vertical coordinate system, z' , relies on the z^* -coordinate system, varies with time, and is defined individually for each ensemble as,

$$[z'(t/T)]_n = z - [z_{bott}^*(t/T)]_n . \quad (4.5)$$

Data in z' -coordinate space are adjusted such that every data ensemble is relative to the instantaneous bottom of the sheet layer (i.e., erosion depth), which is located at $[z']_n = 0$ for all times and ensembles (Figure 4.3k). Such a coordinate system is particularly useful when applying the log-law to obtain bed shear stress so that vertical elevations are always positive, or when a characteristic boundary layer thickness for the entire wave cycle is desired (O’Donoghue & Wright, 2004b). An example result of phase-averaged volumetric concentration, $\tilde{\phi}(t/T, z')$, in the z' -coordinate system is provided in Figure 4.3l, along with the corresponding phase-averaged top, inflection point, and bottom of the sheet flow layer.

For brevity, hereafter, the temporal and/or spatial dependence will be explicitly stated with the introduction of a new variable (measured or computed) and subsequently dropped for all mentions thereafter. In addition, any variable with vertical dependence is to be assumed a function of z^* hereafter, unless explicitly stated otherwise.

4.3.3 Velocity Profiles in the Sheet Flow Layer

The high-frequency (10 MHz) acoustic signal emitted from the ADPV transmitter is quickly attenuated into the dense sheet flow layer. Therefore, ADPV measurements within the sheet flow layer were discarded. Velocity profiles in the sheet flow layer for each ensemble, $[u^{sf}(t/T, z^*)]_n$, were approximated by extrapolating the

measured velocity at the top of the sheet flow layer, $[u(t/T, z^* = z_{top}^*)]_n$, down to zero velocity at the bottom of the sheet flow layer (Pugh & Wilson, 1999; Sumer et al., 1996; Wang & Yu, 2007),

$$[u^{sf}(t/T, z^*)]_n = [u(t/T, z^* = z_{top}^*)]_n \left(\frac{z^* - z_{bott}^*}{z_{top}^* - z_{bott}^*} \right)^\alpha, \quad (4.6)$$

where the exponent, α , is a “profile shape parameter” ($0 < \alpha \leq 1$), with $\alpha = 1$ yielding a linearly decreasing profile through the sheet flow layer. A square-root-shaped velocity profile, $\alpha = 0.50$ (Puleo et al., 2017; Wang & Yu, 2007), was used to estimate the velocity profile in the sheet flow layer for each time step (Figure 4.4a) (Mieras et al., 2017b). The sensitivity of net sheet flow transport rates to the profile shape parameter is explored further in the Discussion (see §4.5.1.1). Bins below the bottom of the sheet flow layer were assigned a velocity magnitude of 0 m/s. Several ensembles with the S1 cases had instances during which velocities were not measured at the top of the sheet flow layer, due to the bed having eroded beyond the measurement range of the ADPV. In such instances, it was not possible to apply equation (4.6) to approximate the velocity profiles in the sheet flow layer.

The ADPVs were positioned slightly higher above the bed for the S2 cases compared with the S1 cases. As a result, velocities were not measured at the top of the sheet flow layer for all time steps in 80% (167 of 207) of the S2 velocity ensembles, making it impossible to apply equation (4.6) to estimate sheet flow layer velocity profiles. Phase-averaged velocity profiles from the corresponding S1 wave cases (Figure 4.4a) were used to fill the spatial and temporal gaps of velocity in the 167 ensembles, from the lowest ADPV observation down to the top of the sheet flow layer,

which is shown between the dashed line and thin solid line in Figure 4.4b. Velocity profiles in the sheet

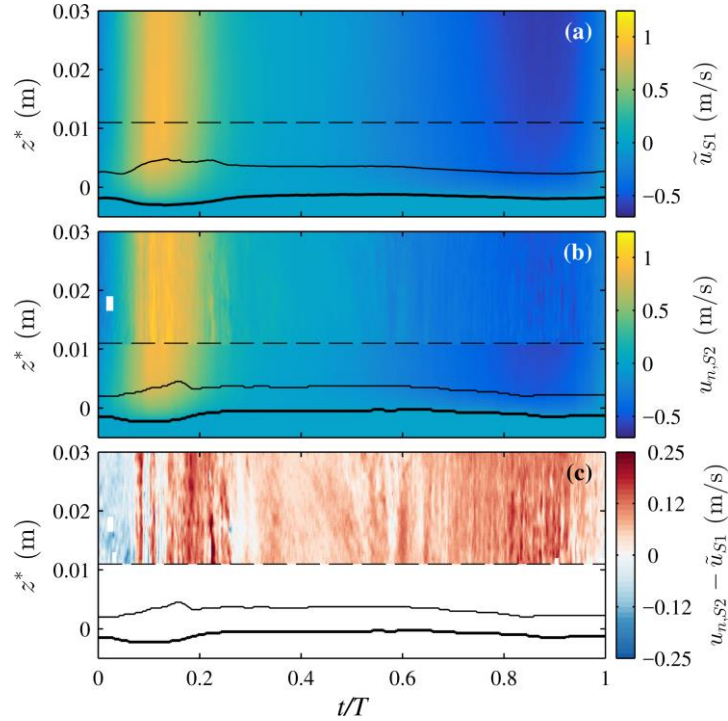


Figure 4.4: (a) Phase-averaged near-bed velocities for S1T5H50. (b) One ensemble of near-bed velocities measured between $0.01 < z^* < 0.03$ m for S2T5H50 (Trial 118, $n_{trial} = 8$). The level of lowest measured velocities by the ADPV for S2T5H50 is shown in (a) and (b) at $z^* = 0.011$ m (dashed black line). (c) Difference between velocities shown in (a) and (b) above the dashed line. Velocity profiles between the bottom (z_{bott}^* , thick black line) and top (z_{top}^* , thin black line) of the sheet flow layer were extrapolated using equation (4.6). The sheet flow layer bounds are phase-averaged in (a) and instantaneous in (b) and (c).

flow layer for the S2 cases were then estimated using equation (4.6), which is shown between the two solid black lines in Figure 4.4b. The difference between the phase-averaged velocities from S1 cases, \tilde{u}_{S1} , and instantaneous velocities for the S2 cases,

$u_{n,S2}$, was computed for each ensemble within a wave case where ADPV measurements overlapped \tilde{u}_{S1} (Figure 4.4c). Any error introduced into the velocity ensembles for the S2 cases was evaluated by phase-averaging the absolute value of the differences in velocity, $|u_{n,S2} - \tilde{u}_{S1}|$, for each case and compiling the phase-averaged data into a single data set. The result contained 455,294 numeric values with a sample mean of 0.03 m/s and standard deviation of 0.045 m/s, where 77% of the data were contained within one standard deviation and 95% fell within two standard deviations (Figure 4.5), supporting the validity of the method for substituting phase-averaged S1 velocity data to fill large spatial and temporal gaps in S2 velocity data.

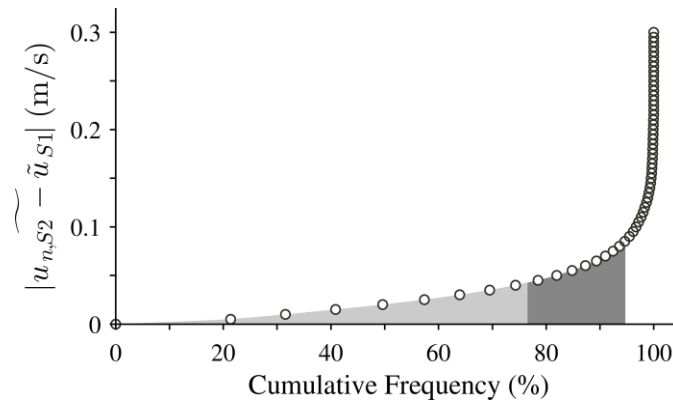


Figure 4.5: Cumulative frequency (%) of the average differences (for all eight S2 cases, 455,294 data points) between measured near-bed ($z^* < 0.04$ m) velocities for each ensemble in an S2 wave case and phase-averaged near-bed velocities for the corresponding S1 wave case (circles, \circ). The shaded areas highlight the percentage of data points contained within one (light grey) and two (dark grey) standard deviations of the sample mean.

4.4 Results

4.4.1 Velocity, Concentration and Sediment Flux

4.4.1.1 Phase-averaged Profiles

Phase-averaged velocity, concentration and horizontal sediment flux profiles are given for wave case S1T7H50 using the z' -coordinate system (Figure 4.6). Phase-averaged free-stream velocity, $\tilde{u}_\infty(t/T)$ (Figure 4.6a), is defined as the velocity at the elevation of the maximum overshoot in the root-mean-square (rms) of the phase-averaged horizontal velocity profiles, $\tilde{u}_{rms}(z')$ (Figure 4.6b). The wave boundary layer thickness, δ , representative for the entire wave cycle is also defined as the elevation of the maximum overshoot in $\tilde{u}_{rms}(z')$, which was 0.2 m for case S1T7H50. Velocity, concentration and sediment flux profiles are shown in Figures 4.6c - 4.6h for phases of zero up-crossing, maximum, zero down-crossing, and minimum free-stream velocity, as well as the temporal midpoints between those phases. Recalling that $t/T = 0$ was defined by zero up-crossings in the free-surface, \tilde{u}_∞ lags η by 10° (Figure 4.6a). Typical sediment concentrations in suspension versus those in the sheet flow layer differ by several orders of magnitude. Therefore, velocity, concentration and sediment flux profiles are shown in separate vertical spans to highlight the processes in each flow regime. Profiles over the entire span of observations (i.e., the bed up to $z' = 1.1$ m) are given in Figures 4.6c - 4.6e. The phase-averaged profiles in the near-bed region (i.e., $z' < 0.10$ m) are provided in Figures 4.6f - 4.6h. The passing of the wave over time is shown by the different vertical spans in the phase-averaged velocity profiles (Figure 4.6c). The magnitudes of suspended sediment concentration (Figure 4.6d) are consistent with observations in other large wave flume studies (Dohmen-Janssen & Hanes, 2002; Van der Zanden, van der A, Hurther, Cáceres, O'Donoghue, & Ribberink, 2017).

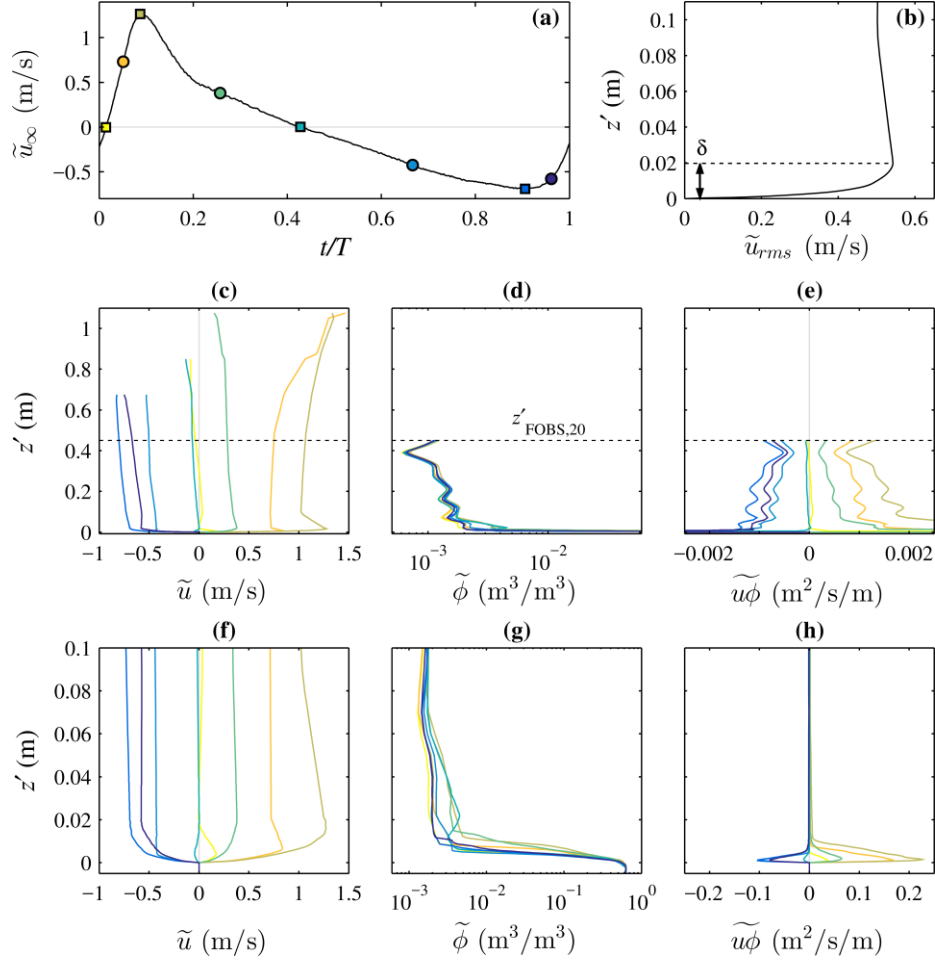


Figure 4.6: Phase-averaged quantities ($N = 40$) for S1T7H50: (a) free-stream velocity, (b) profile of the root-mean-square cross-shore velocity, and boundary layer thickness, δ . Phase-averaged profiles of fluid velocity, sediment concentration, and sediment flux are shown for: (c) – (e) the entire measurement range, and (f) – (h) the lower 0.10 m of the water column. The colors of the curves in (c) – (h) correspond to the wave phase of the marker with the same color in panel (a), where squares (■) denote the phases of maximum, minimum, zero up- and zero down-crossings in the free-stream velocity, while circles (●) denote temporal midpoints between the squares. The elevation of the highest FOBS measurement is shown as a dashed line at $z' = 0.45$ m in plots (c) – (e).

Sediment was suspended near the bed with the passing of the wave crest, where a slight lag was present between the phase of maximum free-stream velocity and entrainment of sediment into suspension (Figure 4.6c). Note that the phase-averaged sediment concentration profiles in Figures 4.6d - 4.6g are shown with different scales. In the example case of S1T7H50, more sediment was suspended under the crest phase compared with the trough (Figures 4.6d and 4.6g). As a result, phase-averaged sediment flux was greater under the wave crest (Figures 4.6e and 4.6h) in both the near-bed region, as well as higher in the water column. Sediment fluxes near the bed versus higher in the water column differed by two orders of magnitude, which is evident by the different horizontal scales required to display the data in Figures 4.6e and 4.6h. In the suspended load region ($z' \gtrsim 0.01$ m), peak flux magnitudes were about 0.002 m^2/s (Figure 4.6e). Near the bed, the maximum magnitude of $\widetilde{u\phi}(t/T, z')$ under the wave crest (~ 0.22 m^2/s) was more than twice as large as compared to the trough (~ -0.1 m^2/s) (Figure 4.6h). In addition, the vertical extent reached by magnitudes of $|\widetilde{u\phi}(t/T, z')| > 0.002$ at the phase of maximum free-stream velocity was higher than during the phase of minimum free-stream velocity (Figures 4.6e and 4.6h), because of larger sheet flow layer thicknesses under the wave crest due to wave skewness and asymmetry (Mieras et al., 2017a). In general, within the wave bottom boundary layer ($z' < \delta$), the shape of $\widetilde{u\phi}(z')$ was characterized by a rapid increase from $z' = 0$, reaching a local maximum after a few millimeters above the instantaneous erosion depth, followed by a rapid decrease towards $\widetilde{u\phi}(t/T, z') \sim 0$ around $z' = 0.01$ m (Figure 4.6h).

4.4.1.2 Wave-averaged Profiles

The effects of wave forcing (height and period) and sediment size on the near-bed ($z^* < 0.03$ m) wave-averaged sediment flux, $\overline{u\phi}(z^*)$, is shown in Figure 4.7. (Note: the z^* -coordinate system will be used for the remainder of the paper.) Profiles of $\overline{u\phi}$ all exhibited the same general shape, consisting of two positive local maxima above and below $z^* = 0$, with a negative local minimum in between. The same general shape of the wave-averaged sediment flux profile was observed in oscillatory flow tunnel experiments with asymmetric flow, for both well-sorted and mixed samples ($0.19 \leq d_{50} \leq 0.28$ mm; M, X1, X2 and X4 experiments) with similar sediment properties to BARSED (O'Donoghue & Wright, 2004b). The lower of the two local sediment flux maxima was always greater in magnitude relative to the upper peak, highlighting that significant amounts of wave-averaged sediment flux occur within the lower few mm of the water column under intense sheet flow conditions. Magnitudes of the three local maxima/minima increased with increasing wave height (period constant) and were greater for smaller sediment size (period constant). In general, maximum erosion depth (i.e., the elevation at which $\overline{u\phi}$ returns to zero) also increased with increasing wave height (period constant), and was greater for smaller sediment size (period constant). The upper local maxima in $\overline{u\phi}$ generally persisted farther from the bed (i.e., returned to zero at higher z^* elevations) with increasing wave height (period constant), with the only exception being case S1T5H60.

Wave-averaged elevations of the top, inflection point, and bottom of the sheet flow layer are plotted along with the flux profiles in Figure 4.7. The elevations of the wave-averaged top (bottom) of the sheet flow layer were located roughly at the same elevations as the upper (lower) local maxima of $\overline{u\phi}$. The differences between the

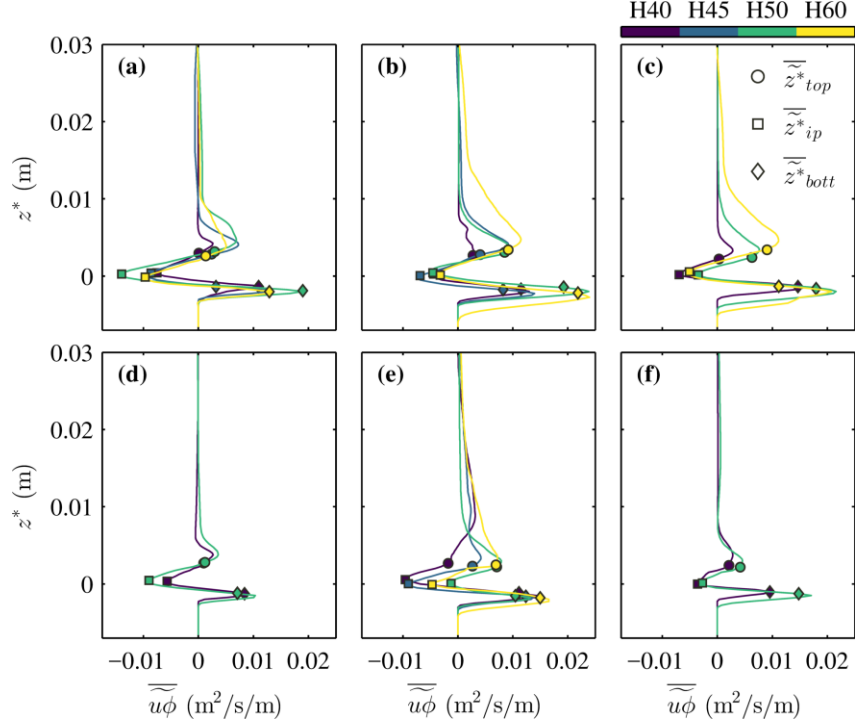


Figure 4.7: Wave-averaged near-bed horizontal sediment flux profiles and sheet flow layer properties for the (a) – (c) S1 and (d) – (e) S2 wave cases. Columns are constant wave period, 5.0, 7.0 and 9.0 s, from left to right. The curves are colored based on the wave maker input signal wave height, given in the Case ID in Table 4.1. Markers represent wave-averaged elevations of the top, inflection point, and bottom of the sheet flow layer for each case.

elevations of \bar{z}_{top}^* (\bar{z}_{bott}^*) and the upper (lower) maxima of $\bar{u}\phi$ were on the order of 1 mm, which is the resolution of observations and of the same order of magnitude as the uncertainty in the vertical location of the sensors. Wave-averaged elevations of the sheet flow layer inflection point, \bar{z}_{ip}^* , corresponded to the elevation of the local minima for every wave case, where the average sediment concentration at the inflection point was usually $\sim 0.30 \text{ m}^3/\text{m}^3$. Models that parametrize pick-up flux with a reference concentration, ϕ_0 , typically specify a value around $\phi_0 = 0.30 \text{ m}^3/\text{m}^3$ for intense flows (Engelund & Fredsøe, 1976; Fredsøe & Deigaard, 1992; Smith & McLean, 1977; Yu et

al., 2012). This supports the idea that the concentration at the elevation of the inflection point in the concentration profile may be a good definition for the pick-up layer for intense flows.

4.4.2 Suspended Sediment and Sheet Flow Transport Rates

For the remainder of the paper, superscripts $()^{ss}$ and $()^{sf}$ will be used to denote quantities pertaining only to the suspended sediment layer and sheet flow layer, respectively. If no superscript is present for a sediment transport quantity, it represents the total quantity (i.e., sum of the suspended sediment and sheet flow components). Time-varying cross-shore suspended sediment and sheet flow transport rates, $[q_s^{ss}(t/T)]_n$ and $[q_s^{sf}(t/T)]_n$, respectively, were computed for each ensemble by integrating sediment flux over the vertical spans of the two layers,

$$[q_s^{ss}(t/T)]_n = \int_{[z_{top}^*]_n}^{[z_{FOBS,20}^*]_n} u_n \phi_n dz^* , \quad (4.7)$$

and

$$[q_s^{sf}(t/T)]_n = \int_{[z_{bott}^*]_n}^{[z_{top}^*]_n} u_n \phi_n dz^* , \quad (4.8)$$

where $[z_{FOBS,20}^*]_n$ is the elevation of the highest (20th) FOBS measurement for each ensemble, typically around $z^* = 0.47$ m. Then, the total time-varying sediment transport rate was computed for each ensemble by adding the contributions from suspended load and sheet flow:

$$[q_s(t/T)]_n = [q_s^{ss}]_n + [q_s^{sf}]_n . \quad (4.9)$$

In every case, the sediment phase was assumed to passively follow the fluid velocity, and all integrals were evaluated with the trapezoidal rule.

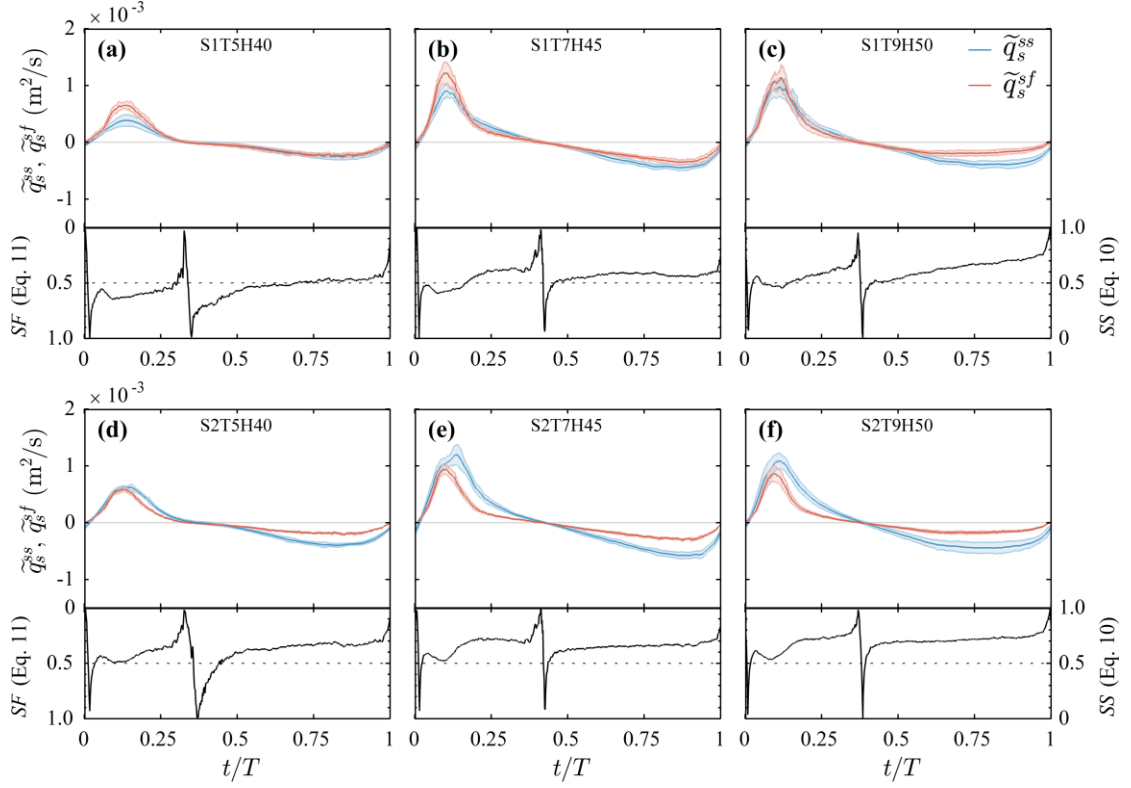


Figure 4.8: Phase-averaged suspended (blue) and sheet flow (red) sediment transport rates for six different wave cases: (a) S1T5H40, (b) S1T7H45, (c) S1T9H50, (d) S2T5H40, (e) S2T7H45 and (f) S2T9H50. The shaded areas represent one standard deviation. The fractional contributions of each component (\tilde{q}_s^{ss} versus \tilde{q}_s^{sf}) to the total transport rate, \tilde{q}_s , given by equations (4.10) and (4.11), are provided in the lower panel of each plot (solid black curves). Equal contribution by both \tilde{q}_s^{ss} and \tilde{q}_s^{sf} is represented with a dotted black line.

Phase-averaged suspended sediment and sheet flow transport rates for three characteristic wave cases with both sediment sizes, S1 and S2, are provided in Figure 4.8, where blue represents suspended sediment transport and red represents sheet flow sediment transport. The smaller standard deviations for the S2 cases relative to S1 are a result of substituting in phase-averaged velocities from the corresponding S1 cases to

fill in spatial gaps of velocity observations near the bed (see §4.3.3). The only variations from the mean were due to differences in the elevation of the top of the sheet flow layer between ensembles. The magnitudes of \tilde{q}_s^{ss} for S2 were larger than for S1, while the opposite was the case for sheet flow, where the magnitudes of \tilde{q}_s^{sf} were larger for S1 than S2. Smaller sheet flow layer thicknesses for the larger S2 sediment (Mieras et al., 2017a) likely led to lower sheet flow transport rates compared with S1. Smaller sheet flow layer thickness led to the suspended load layer covering a larger portion of the water depth than for the S1 cases.

The fractional contributions of suspended sediment and sheet flow to the total transport rate, as a function of wave phase, are obtained through the following ratios, respectively (Figure 4.8; solid black curves):

$$SS(t/T) = \frac{|\tilde{q}_s^{ss}(t/T)|}{|\tilde{q}_s(t/T)|}, \quad (4.10)$$

and

$$SF(t/T) = \frac{|\tilde{q}_s^{sf}(t/T)|}{|\tilde{q}_s(t/T)|}. \quad (4.11)$$

Equal contribution from both suspended sediment and sheet flow to the total transport rate (i.e., $SS = SF$) is marked with a horizontal dashed line at 0.50 for each case. When sheet flow is the dominant transport mode, the black curves drop below the dashed line, whereas the black curves rise above the dashed line when suspended load is the dominant transport mode. For cases S1T5H40 and S1T7H45, sheet flow accounted for 60 – 65% of the total transport rate, \tilde{q}_s , under the wave crest (Figures 4.8a - 4.8b), similar to the 60 – 70% contribution from oscillatory flow tunnel observations under velocity-asymmetric flow (Ruessink et al., 2011). Spikes in SS (SF) with magnitudes of 1.0 (0.0) or 0.0 (1.0) are present around flow reversals due to the temporal differences

in zero crossings of \tilde{q}_s^{SS} and \tilde{q}_s^{SF} . The time difference between when $SF \sim 1$ and when $SS \sim 1$ represents the phase lag between suspended sediment and sheet flow transport rates. Suspended sediment transport rates lagged sheet flow sediment transport rates due to streaming effects from the free-surface.

For the six cases presented in Figure 4.8, SS and SF curves nearly resemble each other in shape. However, it is clear that suspended sediment transport dominated sheet flow in the wave trough more for the S2 cases relative to S1. A similar trend can be observed for sheet flow dominance, where sheet flow dominated suspended sediment transport under the wave crests for the S1 cases but not for the S2 cases. Although, there are notable “dips” in the SS curves under the wave crests for the S2 cases, where for a small portion of the wave, suspended sediment and sheet flow contribute about equally to the overall transport rate (Figures 4.8d - 4.8f). This is also the same portion of the wave cycle where sheet flow layer thickness was maximum (Mieras et al., 2017a).

4.4.3 Net Sediment Transport Rates

4.4.3.1 Suspended Sediment and Sheet Flow

Net suspended sediment and sheet flow transport rates were computed for each ensemble, $[\overline{q}_s^{SS}]_n$ and $[\overline{q}_s^{SF}]_n$ respectively, by wave-averaging equations (4.7) and (4.8) over the entire wave cycle. Total net transport rates were computed for every ensemble, $[\overline{q}_s]_n$, by wave-averaging equation (4.9). The term “net” is loosely used to describe an averaged quantity over either a portion or entirety of the wave cycle using equation (4.2). Ensemble-averaged net transport rates in the sheet flow layer versus in suspension are compared in Figure 4.9, with two one-to-one lines to delineate which transport mode is more dominant. The ensemble-averages are also included in Table

4.2. The major finding is that net suspended sediment transport rates were roughly of the same order of magnitude as net sheet flow sediment transport rates. Ensemble-averaged net sheet flow transport rate was positive (onshore) for all 19 wave cases, whereas ensemble-averaged net suspended sediment transport rate was negative (offshore) for all but two wave cases (S1T7H60 and S1T9H60).

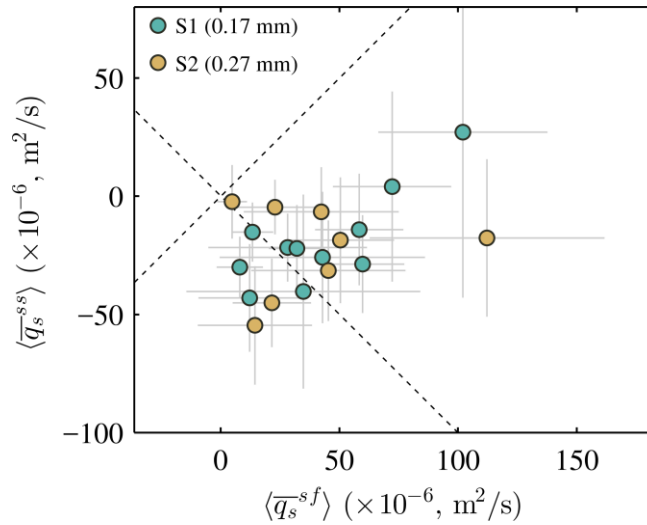


Figure 4.9: Ensemble-averaged net sheet flow versus suspended sediment transport rate. Grey error bars represent one standard deviation from the mean. Positive (negative) values indicate net onshore (offshore) sediment transport.

The net percentage of sediment transported within the sheet flow layer is given by (Table 4.2),

$$\varphi^{sf} = \frac{\varepsilon}{1 + \varepsilon} \times 100, \quad (4.12)$$

where, ε is the ratio of ensemble-averaged net sheet flow transport rate to net suspended sediment transport rate,

$$\varepsilon = \left| \frac{\langle \overline{q_s^{sf}} \rangle}{\langle \overline{q_s^{ss}} \rangle} \right|, \quad (4.13)$$

and

$$\begin{aligned} \varphi^{sf} > 50\% , & \quad \text{Sheet Flow Dominant} \\ \varphi^{sf} < 50\% , & \quad \text{Suspended Load Dominant} \end{aligned}$$

Both the magnitude and direction (onshore/offshore) of the ensemble-averaged total net sediment transport rate, $\langle \overline{q_s} \rangle$, correlate well with φ^{sf} (Figure 4.10). Plots like Figure 4.10 are useful in helping to understand how varying magnitudes of sediment transport in the suspended and sheet flow layers under a wide array of forcing conditions and different sediment sizes contribute to the total transport rate. Equal contribution to the net transport rate by suspended sediment and sheet flow roughly corresponded to zero net transport rate. Increasing offshore transport rates correlated with increasing influence of suspended sediment transport, whereas increasing sheet flow dominance correlated with increasing magnitudes of net onshore sediment transport. Both sediments (S1 and S2) followed the same trend. In general, net transport rate, $\langle \overline{q_s} \rangle$, was negative (offshore) when suspended load dominated ($\varphi^{sf} < 50\%$) and positive (onshore) when sheet flow dominated ($\varphi^{sf} > 50\%$).

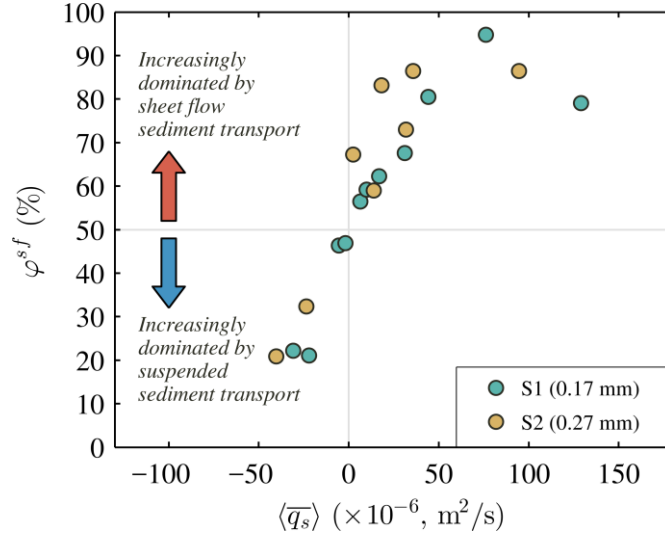


Figure 4.10: Ensemble-averaged net sediment transport rate versus the percentage of the net transport contained within the sheet flow layer, φ^{sf} . Positive (negative) values indicate net onshore (offshore) sediment transport.

4.4.3.2 Positive and Negative Half-Cycles

Net transport rates in suspension and within the sheet flow layer were computed separately for the crest and trough half-cycles. The positive half-cycle (wave crest) was defined for each ensemble as the time span between $t/T = 0$ (zero up-crossing) and the zero down-crossing of the free-surface, and is denoted with superscript $()^+$. Likewise, the duration of the negative half-cycle (wave trough) was defined for each ensemble as the time span between zero down-crossings of η_n and $[\eta(t/T = 1)]_n$ (zero up-crossings), denoted with superscript $()^-$. As in equation (4.9), total transport rates under the wave crest and trough were obtained for every ensemble from the summation of the respective suspended sediment and sheet flow transport components, respectively, as:

$$[q_s^+(t/T_n^+)]_n = [(q_s^+)^{ss}(t/T_n^+)]_n + [(q_s^+)^{sf}(t/T_n^+)]_n, \quad (4.14)$$

$$[\bar{q}_s^-(t/T_n^-)]_n = [(q_s^-)^{ss}(t/T_n^-)]_n + [(q_s^-)^{sf}(t/T_n^-)]_n, \quad (4.15)$$

where T_n^+ and T_n^- are the durations of the positive and negative half-cycles of each ensemble, respectively (Table 4.2), and t/T_n^+ , t/T_n^- both range from 0 to 1. Net transport rates under the crest and trough were obtained by averaging the time-varying transport rate over the respective normalized half-cycle period, equation (4.2), such that the total net transport rate can be expressed for each ensemble by

$$[\bar{q}_s]_n = \frac{1}{T} \left(T_n^+ [\bar{q}_s^+]_n + T_n^- [\bar{q}_s^-]_n \right). \quad (4.16)$$

The same method was applied to the sheet flow and suspended sediment transport rates to obtain the net sheet flow and suspended sediment transport rates in the positive and negative half-cycles for each ensemble.

Table 4.2: Ensemble-averaged net transport rates and half-cycle periods.

Case ID	Crest				Trough						
	$\langle \bar{q}_s \rangle$ ($\times 10^{-6}$ m ² /s)	$\langle \bar{q}_s^{sf} \rangle^a$	$\langle \bar{q}_s^{ss} \rangle^b$	$\langle T^+ \rangle$ (s)	$\langle \bar{q}_s^+ \rangle$ ($\times 10^{-6}$ m ² /s)	$\langle \bar{q}_s^{+sf} \rangle$	$\langle \bar{q}_s^{+ss} \rangle$	$\langle T^- \rangle$ (s)	$\langle \bar{q}_s^- \rangle$ ($\times 10^{-6}$ m ² /s)	$\langle \bar{q}_s^{-sf} \rangle$	$\langle \bar{q}_s^{-ss} \rangle$
S1T5H40	-22.0	8.0	-30.1	1.96	405.4	246.5	158.9	3.04	-299.2	-147.6	-151.6
S1T5H45	-30.8	12.3	-43.0	1.94	558.9	303.8	255.1	3.06	-403.1	-171.6	-231.5
S1T5H50	16.9	42.8	-25.9	1.88	624.8	305.4	319.3	3.12	-374.1	-141.0	-233.1
S1T5H60	-5.5	34.8	-40.4	1.82	510.3	242.3	268.0	3.18	-357.6	-141.8	-215.8
S1T7H40	6.5	28.2	-21.7	2.77	545.4	281.9	263.5	4.23	-364.8	-156.4	-208.4
S1T7H45	9.9	32.1	-22.1	2.72	755.9	395.0	360.9	4.28	-461.1	-197.0	-264.1
S1T7H50	31.1	59.8	-28.7	2.70	805.4	431.5	373.9	4.30	-452.2	-172.3	-280.0
S1T7H60	129.1	102.0	27.1	2.61	1456.7	675.7	781.0	4.39	-660.6	-239.3	-421.4
S1T9H40	-1.8	13.4	-15.2	3.38	476.5	222.1	254.4	5.62	-288.0	-111.5	-176.5
S1T9H50	44.2	58.3	-14.1	3.25	824.7	405.6	419.1	5.75	-397.2	-138.1	-259.1
S1T9H60	76.2	72.2	4.0	3.17	1142.8	563.3	579.5	5.83	-502.6	-194.1	-308.6
S2T5H40	-23.6	21.5	-45.1	1.90	490.7	217.3	273.4	3.10	-337.6	-98.1	-239.5
S2T5H50	-40.2	14.4	-54.6	1.79	557.0	262.6	294.4	3.21	-372.5	-123.8	-248.7
S2T7H40	2.5	4.8	-2.4	2.74	700.8	249.2	451.6	4.26	-446.4	-152.3	-294.1
S2T7H45	35.7	42.4	-6.6	2.71	821.2	313.4	507.7	4.29	-459.7	-129.0	-330.7
S2T7H50	13.8	45.3	-31.5	2.70	756.5	320.0	436.5	4.30	-452.0	-127.7	-324.3
S2T7H60	94.6	112.3	-17.6	2.62	1130.2	462.5	667.7	4.38	-530.0	-102.9	-427.0
S2T9H40	18.2	22.8	-4.6	3.39	458.9	201.4	257.6	5.61	-248.9	-84.8	-164.2
S2T9H50	31.7	50.4	-18.6	3.25	781.9	295.5	486.4	5.75	-391.9	-88.1	-303.9

^a Sheet flow velocity profiles were computed with equation (4.6) and $\alpha = 0.50$.

^b Depth-integrated suspended sediment flux was only computed up to $z_{FOBS,20}^*$, which was $z^* \sim 0.47$ m, on average. See Section 4.5.1.1 for a discussion on extrapolating $\langle \bar{q}_s^{ss} \rangle$ estimates to the free-surface.

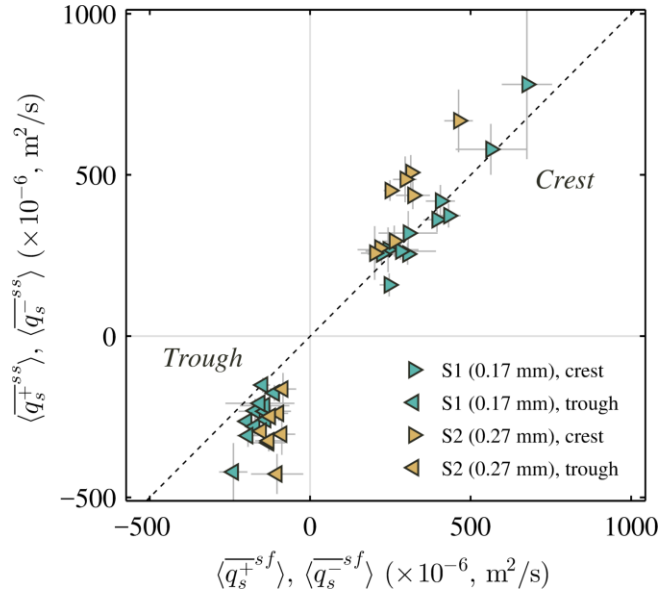


Figure 4.11: Ensemble-averaged net sediment transport rate in the crest and trough half-cycles versus the percentage of the net transport contained within the sheet flow layer for each respective half-cycle. Positive (negative) values indicate net onshore (offshore) sediment transport.

Ensemble-averaged net suspended and sheet flow sediment transport rates under the wave crest and trough are shown in Figure 4.11 and included in Table 4.2. A one-to-one ratio line is shown to delineate whether sheet flow or suspended load was the dominant mode of sediment transport for each half-cycle. Values below the one-to-one line in the upper-right quadrant or above the one-to-one line in the lower-right quadrant indicate sheet flow dominance. Distance increasing from the one-to-one line in either direction indicates increasing dominance of that particular transport mode. Ensemble-averaged net transport rates under the crest are grouped in the upper-right quadrant. Sheet flow net transport slightly dominated net suspended sediment transport under the wave crest for five of the 19 wave cases (all with S1). But in general for S1, suspended load and sheet flow contributed almost equally to the total net transport rate in the

positive half-cycle. However, under the wave crest, where the sheet flow layer is relatively thin, suspended sediment transport was universally the dominant mode. This goes along with the observation that suspended sediment transport dominated sheet flow during the entire negative half-cycle for the six wave cases presented in Figure 4.8. Suspended load was more dominant for the larger sediment size, evident by the farther distance from the one-to-one line for the gold symbols in Figure 4.11.

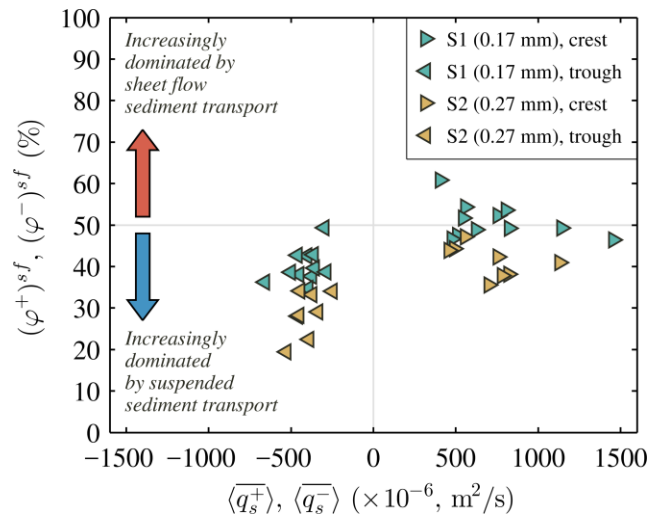


Figure 4.12: Ensemble-averaged net sheet flow versus suspended sediment transport rate within the crest and trough half-cycles. Grey error bars represent one standard deviation from the mean. Positive (negative) values indicate net onshore (offshore) sediment transport.

The net (%) contribution of sheet flow to the total sediment transport rates in the positive and negative half-cycles were computed in a similar fashion as with equation (4.13),

$$(\varphi^+)^{sf} = \frac{\varepsilon^+}{1 + \varepsilon^+} \times 100; (\varphi^-)^{sf} = \frac{\varepsilon^-}{1 + \varepsilon^-} \times 100, \quad (4.17)$$

where,

$$\varepsilon^+ = \left| \frac{\langle \overline{q_s^+}^{sf} \rangle}{\langle \overline{q_s^+}^{ss} \rangle} \right|; \varepsilon^- = \left| \frac{\langle \overline{q_s^-}^{sf} \rangle}{\langle \overline{q_s^-}^{ss} \rangle} \right|. \quad (4.18)$$

The total net transport rate for each half-cycle is compared to the percentage of the respective net sediment that was transported in the sheet flow layer in Figure 4.12. In general, more sediment was transported under the wave crest, compared with the trough, likely due to positive velocity skewness. Suspended sediment transport contributed more to the total net half-cycle transport rates under the wave trough than the wave crest, which is represented by $(\varphi^-)^{sf} < (\varphi^+)^{sf}$. The results in Figure 4.12 follow the observations in Figure 4.8 that suspended sediment transport rates were more dominant in the trough for the S2 cases compared with the same S1 cases, shown by smaller values for $(\varphi^+)^{sf}$ and $(\varphi^-)^{sf}$ with the S2 cases. This is likely related to the smaller sheet thickness for larger sediment size under identical forcing conditions, as discussed in Section 4.4.2. Figure 4.12 also shows that if the crest and trough half-cycles are treated independently, for the majority of the wave cases, suspended sediment transport is the dominant mode. This may lead one to draw the incorrect conclusion that suspended sediment transport is far more important than sheet flow on a sandbar under the range of tested wave conditions and sediment types. However, when the net transport rate is considered over the entire wave cycle, Figure 4.10 demonstrated that sheet flow was the dominant mode of transport for the majority of the wave cases (13 of 19).

4.4.4 Net Sheet Flow Transport Rate and Velocity Skewness

Onshore sandbar migration is often attributed to increased degrees of velocity skewness (Fernández-Mora et al., 2015; Hsu et al., 2006) and/or acceleration skewness (Drake & Calantoni, 2001; Elgar et al., 2001; Hoefel & Elgar, 2003; Watanabe & Sato, 2004) as waves shoal and/or break over the sandbar. Other surface-wave-induced processes like boundary layer streaming (Henderson et al., 2004; Nielsen, 2006; Trowbridge & Young, 1989) and wave-breaking-induced turbulence (Cox & Kobayashi, 2000; Scott et al., 2009; Van der Zanden et al., 2016) may further enhance onshore sediment transport. However, Section 4.4.4 focuses specifically on the effects of velocity skewness on net sheet flow transport rates.

Quasi-steady models for predicting time-varying sediment transport rate are related to either the instantaneous bed shear stress or velocity to some power (Bailard, 1981; Meyer-Peter & Müller, 1948; Ribberink, 1998; Van Rijn, 2007), where those based on velocity are of the form

$$q_s(t) \propto |u(t)|^{n-1}u(t). \quad (4.19)$$

Generally speaking, $n = 3$ for the bed load/sheet flow regime, leading to the net transport rate depending on the third velocity moment, $\overline{q_s} \propto \overline{u^3}$, which is non-zero for skewed waveforms. Ensemble-averaged net sheet flow transport rates correlated fairly well with the third moment of free-stream velocity (coefficient of determination, $r^2 = 0.71$), as indicated by the thick black line in Figure 4.13. The slope of the best fit line (forced through the origin) from linear regression was 450.6. Schretlen (2012) and Dohmen-Janssen & Hanes (2002) observed linear trends with slopes of approximately 435 and 150, respectively, in a large wave flume with similar sediment sizes (d_{50} between 0.21 and 0.245 mm) to BARSED. It is worth pointing out that the third velocity moments in Dohmen-Janssen & Hanes (2002) and Schretlen (2012) were taken from 0.10 m and

0.04 m above the bed, respectively, so a direct comparison is not possible. Oscillatory flow experiments with comparable magnitudes of $\overline{u^3}$ to BARSED performed by Ribberink & Al-Salem (1995) yielded a considerably lower slope around 175, which is likely attributed to boundary layer streaming and increased skewness within the sheet flow layer (Berni et al., 2017; Henderson et al., 2004; Henriquez et al., 2014). The slopes of the best fit linear regression lines to ensemble-averaged net sheet flow transport rates plus (minus) one standard deviation (Figure 4.13; dotted lines) were 676 (250), which are both less than or equal to a factor of two deviation from the best fit line (Figure 4.13; thick grey lines). No clear grain size dependence emerged from Figure 4.13.

A number of prior studies also investigated the relationship between $\overline{q_s}$ and $\overline{u^3}$ (Dohmen-Janssen & Hanes, 2002; Hassan & Ribberink, 2005; Kranenburg et al., 2013; Nielsen, 2006; Schretlen, 2012; Van der Werf et al., 2009), where the total net transport rate was considered, rather than exclusively the sheet flow (or bed load) component. The preceding analysis (not shown) was also carried out for the ensemble-averaged total net transport rate, but the correlation was low ($r^2 = 0.43$), with considerably more spread about the best fit. The fits to plus (minus) one standard deviation were well outside a factor of two from the best fit slope of 321.5. The lower slope (321.5 versus 450.6) is due to the negative net suspended sediment transport rates for 17 of the 19 wave cases, resulting in negative $\langle \overline{q_s} \rangle$ values for small $\overline{u_{\infty}^3}$. Energetics-based models generally relate the net suspended sediment transport rate to $\overline{u(t)^5/w(t)^2}$, which may explain why no trend ($r^2 = 0$) was observed between $\langle \overline{q_s^{ss}} \rangle$ and $\overline{u_{\infty}^3}$.

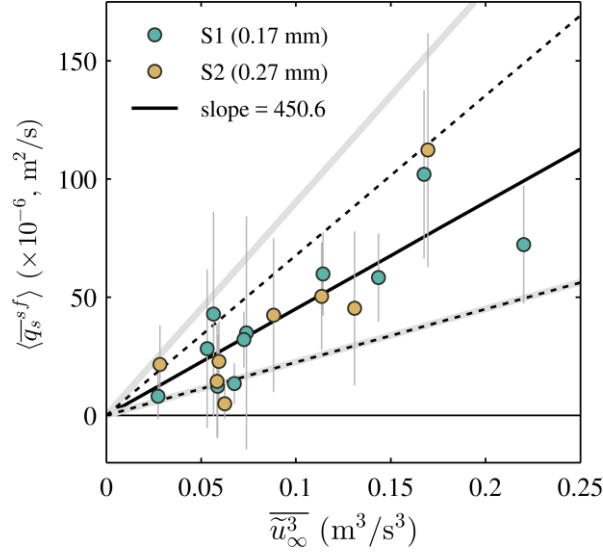


Figure 4.13: Ensemble-averaged net sheet flow sediment transport rates versus the third moment of phase-averaged free-stream velocity (dimensional velocity skewness). Cases with sediment S1 ($d_{50} = 0.17$ mm) are shown with green circles, and S2 cases ($d_{50} = 0.27$ mm) are plotted as gold circles, with grey error bars representing one standard deviation from the mean. Also plotted are the linear regression (forced through origin) best fit to the data points (thick black line), and best fits to the data points plus/minus one standard deviation (dotted lines), along with a factor of two deviation from the best fit (thick grey lines).

4.5 Discussion

Data in this study are among the most highly resolved sediment transport observations (at one cross-shore location) under surface wave in a large wave flume with the concurrent deployment of six ADVs, two ADPVs, four FOBS probes, and four CCPs on a sandbar crest. The detailed dataset collected during the BARSED campaign spans two sediment sizes and eleven unique prototype wave forcing conditions, which should serve as a complement to the recent SINBAD experiments (Van der A et al., 2017; Van der Zanden et al., 2016; Van der Zanden, van der A, Hurther, Cáceres, O'Donoghue, Hulscher, et al., 2017; Van der Zanden, van der A, Hurther, Cáceres,

O'Donoghue, & Ribberink, 2017). Nevertheless, experimental errors and degrees of uncertainty are unavoidable; and, because these data are likely to be used in model validation and improvement in the future, the most likely sources of measurement error and/or uncertainty, as well as the implications of certain assumptions made during data analysis, are discussed in Section 4.5.1.

4.5.1 Net Sediment Transport Rate Estimates

Uncertainty in net transport rate estimates may be attributed to several factors related to the experimental setup and instrument limitations. The sheet flow layer is a very thin layer, but accounted for 20 to 95% of the net total sediment transport rate (Table 4.2). Accurate sheet flow transport rate estimates rely on millimeter precision of the vertical location of each measurement bin. However, precisely knowing the vertical location of every measurement bin is difficult, and it is reasonable to expect errors on the order of 1 mm. This issue was partially circumvented by assigning every ensemble (i.e., realization) a 'local' z^* -coordinate system. Calibration of the FOBS and CCPs may also introduce slight error in concentration estimates, which will bias net sediment transport rates. The experimental protocol, described in more detail in Mieras et al. (2017a), also consisted of occasionally returning transported sediment to the pit (usually after about 10 – 15 consecutive trials). While trials immediately following replacement of sand were excluded from analysis, it was not possible to re-distribute the sand in exactly the same configuration every time. Though, the relatively small standard deviations for phase-averaged quantities presented in Section 4.4 suggest that different initial sediment pit sand configuration did not introduce large variation in the results.

Another potential factor that may have an effect on net sediment transport rates is the linear interpolation between the upper ADPV measurement bin and ADV_1 . Spatial data gaps are a common issue in physical experiments in the laboratory and field (O'Donoghue & Wright, 2004b; Puleo et al., 2016; Van der Zanden, van der A, Hurther, Cáceres, O'Donoghue, Hulscher, et al., 2017). O'Donoghue & Wright, (2004b) had spatial data gaps in the vertical spanning a similar range to the gap between the upper ADPV measurement bin and ADV_1 in this chapter. The gaps were filled by fitting a third-order spline to wave-averaged flux profiles such that the vertically integrated flux profiles matched measured transport rates from sediment traps. In other cases, net sheet flow transport rates are estimated by subtracting the measured suspended sediment transport rate from the total net transport rate, which is obtained through evaluating the Exner equation (Van der Zanden, van der A, Hurther, Cáceres, O'Donoghue, Hulscher, et al., 2017). The validation of net transport rates presented in Section 4.4.3 using the Exner equation was not possible with the BARSED setup, since cross-shore gradients in net sediment transport rate were not observed. Future modeling efforts may help to close the vertical gap in velocity observations (e.g., Kim et al., 2017). For now, Sections 4.5.1.1 and 4.5.1.1 attempt to quantify the range of uncertainty associated with the net sediment transport rates provided in Table 4.2.

4.5.1.1 Sheet Flow Sediment Transport Rates

In Section 4.3.3, the velocity profile in the sheet flow layer, u^{sf} , was approximated by extrapolating measured velocity at the top of the sheet flow layer down to zero at the bottom of the sheet flow layer. The shape of the profile within the sheet flow layer was governed by the profile shape parameter, α , in equation (4.6), where $\alpha = 0.50$ was used. However, prior studies that measured the velocity profile in the sheet

flow layer have observed values for α between 0.25 and 1.0 (Puleo et al., 2017; Sumer et al., 1996; Wang & Yu, 2007; Zala Flores & Sleath, 1998). Studies that require the velocity profile in the sheet flow layer to be approximated tend to assume a linear velocity profile (i.e., $\alpha = 1.0$) (O'Donoghue & Wright, 2004b; Puleo et al., 2016; Zala Flores & Sleath, 1998). The sensitivity of sheet flow transport rates to the profile shape parameter was analyzed by evaluating the velocity profiles in the sheet flow layer using three additional values for α (0.25, 0.75 and 1.0), for every ensemble and wave case. Then, sheet flow sediment transport rates were re-computed for each α -value (Table 4.3).

The factor by which the ensemble-averaged net sheet flow transport rates changed for each value of α is quantified with the following ratio (Table 4.3):

$$\mathbb{F}_\alpha^{sf} = \frac{\langle \overline{q_s}^{sf} \rangle_\alpha}{\langle \overline{q_s}^{sf} \rangle_{50}}, \quad (4.20)$$

where the subscript $\langle \rangle_\alpha$ is either 25, 50, 75 or 100, corresponding to $\alpha = 0.25, 0.50, 0.75$ or 1.0, respectively, and the subscript $\langle \rangle_{50}$ in the denominator corresponds to the ensemble-averaged net sheet flow sediment transport rate with $\alpha = 0.50$. The net sheet flow sediment transport rate was 1.38 ± 0.06 (mean \pm standard deviation) times larger for $\alpha = 0.25$. For larger values of α , the net sheet flow transport rates decreased by a factor of 0.77 ± 0.02 and 0.61 ± 0.02 , on average, for $\alpha = 0.75$ and 1.0, respectively. In other words, using a quadratic ($\alpha = 0.50$) versus linear ($\alpha = 1.0$) velocity profile in the sheet flow layer results in a factor 1.64 increase in the average net sheet flow transport rate.

Regardless of the value for α , the extrapolation method for approximating sheet flow layer velocity profiles makes the assumption that the phase of $u(z^*)$ between

$z_{bott}^* \leq z^* \leq z_{top}^*$ does not vary with elevation. Zala Flores & Sleath (1998) observed rapid phase variation with height of the fundamental component of velocity in the sheet flow layer (10 - 15°). So approximating velocity profiles in the sheet flow layer without accounting for phase variation (i.e., inferring a sort-of “quasi-steady” state) improperly represents the physical processes. Because transport rates are computed from the product of concentration and velocity, net sheet flow transport rates may be sensitive to the phase of velocity with depth. However, Zala Flores & Sleath (1998) also point out that deviations from the quasi-steady assumption were not large and may cancel out in calculations of integral quantities.

The determination of the upper and lower bounds of the sheet flow layer, z_{top}^* and z_{bott}^* (§4.3.2.2) may also affect the results for net sheet flow sediment transport rate. It is a known complication with conductivity sensors used in sheet flow studies (e.g., CCM, CCM⁺ and CCP) that the finite measurement extent results in slight smoothing of the concentration profile. The smoothing effect is larger for the CCP compared with the CCM, due to the vertical extent of the measurement volume with the CCP (see Lanckriet et al., 2013 for more details). Consequently, the top and bottom of the sheet flow layer can be over-predicted for thin sheet flow layers, $z_{top}^* - z_{bott}^* < 0.005$ m, which was nearly always the case under the wave trough for the cases considered (Mieras et al., 2017a). When sheet flow layer thickness is the desired quantity, correction formulas can be applied (Chapter 2) to account for the over-estimated sheet thickness (Lanckriet et al., 2014). However, since z_{top}^* and z_{bott}^* are derived from sediment concentration which is a calibrated, not measured, quantity, it is not presently possible to correct estimates for the top and bottom boundaries of the sheet flow layer.

Table 4.3: Effect of the profile shape parameter on net sheet flow transport rates and corresponding adjustment factors, \mathbb{F}^{sf} .

Case ID	$\langle \bar{q}_s^{sf} \rangle (\times 10^{-6}, \text{m}^2/\text{s})$			$\alpha = 1.00$	\mathbb{F}_{25}^{sf}	\mathbb{F}_{75}^{sf}	\mathbb{F}_{100}^{sf}
	$\alpha = 0.25$	$\alpha = 0.75$	$\alpha = 1.00$				
S1T5H40	10.65	5.65	4.55	1.43	0.76	0.61	
S1T5H45	17.13	8.85	7.03	1.45	0.75	0.59	
S1T5H50	59.74	32.87	25.88	1.38	0.76	0.60	
S1T5H60	48.73	27.41	21.76	1.36	0.77	0.61	
S1T7H40	37.95	21.63	17.37	1.36	0.77	0.62	
S1T7H45	43.36	24.45	19.69	1.37	0.77	0.62	
S1T7H50	81.67	45.98	36.85	1.37	0.77	0.62	
S1T7H60	139.23	79.43	63.81	1.36	0.77	0.62	
S1T9H40	18.66	10.22	8.15	1.39	0.76	0.61	
S1T9H50	78.63	45.02	36.22	1.35	0.77	0.62	
S1T9H60	98.63	56.22	45.37	1.36	0.77	0.63	
S2T5H40	28.63	16.31	13.04	1.35	0.77	0.62	
S2T5H50	19.75	10.98	8.80	1.38	0.77	0.61	
S2T7H40	7.13	3.19	2.48	1.57	0.70	0.55	
S2T7H45	57.37	33.05	26.55	1.35	0.78	0.62	
S2T7H50	60.90	35.21	28.40	1.34	0.78	0.63	
S2T7H60	149.89	87.27	70.14	1.34	0.78	0.63	
S2T9H40	29.99	17.59	14.24	1.33	0.78	0.63	
S2T9H50	67.17	39.56	31.96	1.33	0.78	0.63	
			$\mu \pm \sigma$ ^a	1.38 ± 0.06	0.77 ± 0.02	0.61 ± 0.02	

Note. The last three columns are the ratios of $\langle \bar{q}_s^{sf} \rangle$ computed for each of the three values for α to $\langle \bar{q}_s^{sf} \rangle$ computed with $\alpha = 0.50$ (Table 4.2), given by equation (4.20).

^a mean plus/minus one standard deviation.

4.5.1.2 Suspended Sediment Transport Rates

In Section 4.4.2, suspended sediment transport rates were computed by vertically integrating over the range covered by FOBS measurements (generally, the lower half of the still water column) to avoid the complicated matter of extrapolating suspended sediment concentration profiles to the free-surface – further complicated by the time-varying nature of the free-surface. Any sediment potentially transported in the upper half of the water column above $z_{FOBS,20}^*$ was excluded, with the goal of trying to minimize data extrapolation. A new statistical approach for quantifying the amount of suspended sediment transport that occurred outside the measurement range, and the subsequent net transport rates, are described in this section. The main benefit of the new approach is that only measured quantities are used to infer the magnitude of non-resolved physical processes. No assumptions about the physical processes (e.g., the shape of the suspended sediment concentration profile outside the region of measurements) are required. Essentially, the goal was to determine a baseline factor (with lower and upper bounds) by which suspended sediment transport was potentially under-resolved stemming from sediment concentration observations being contained to the lower 0.47 m of the water column (i.e., “How much more suspended sediment transport would have been observed had the entire suspension layer, $z_{top}^* \leq z^* \leq \eta$, been resolved?”).

For this analysis, data were organized together based on wave period, where an ensemble is denoted with subscript $[]_{n_T}$, and the total number of ensembles for each of the three wave periods, N_T , was 159, 234, and 129 for the cases with wave periods of 5.0, 7.0, and 9.0 s, respectively (Table 4.1). The cumulative time-varying gross suspended sediment transport rate was computed by cumulatively integrating the

absolute value of sediment flux from the top of the sheet flow layer to the highest FOBS measurement,

$$[Q_s^{SS}(t/T, z^*)_{gross}]_{n_T} = \int_{[z_{top}]_{n_T}}^{z^*} |u(t/T, \zeta)_{n_T} \phi(t/T, \zeta)_{n_T}| d\zeta, \quad (4.21)$$

where ζ is a dummy integration variable, upper-case Q represents the cumulatively integrated sediment flux in the vertical, and $[(Q_s^{SS})_{gross}]_{n_T}$ integrated up to $[z_{FOBS,20}^*]_{n_T}$ is the gross suspended sediment transport rate, $[q_s^{SS}(t/T)_{gross}]_{n_T}$ (Figures 4.14a - 4.14c; grey lines). Time-varying, phase-averaged gross suspended sediment transport rates, $\tilde{q}_s^{SS}(t/T)_{gross}$, were computed for all three wave periods (Figures 4.14a - 4.14c; solid black lines), as well as the peak values of $(\tilde{q}_s^{SS})_{gross}$ in the positive (Figures 4.14a - 4.14c; right-facing arrows) and negative (Figures 4.14a - 4.14c; left-facing arrows) half-cycles. Each profile of $[(Q_s^{SS})_{gross}]_{n_T}$ was interpolated onto the z^* -coordinate system normalized by the instantaneous water depth, $[z^*/h(t/T)]_{n_T}$, such that the time-varying free-surface was at a constant elevation of $z^*/h = 1$. The cumulative fraction of the total measured suspended sediment transport rate was computed by normalizing $[(Q_s^{SS})_{gross}]_{n_T}$ by the corresponding gross suspended sediment transport rate,

$$\left[\left(\hat{Q}_s^{SS}(t/T, z^*/h) \right)_{gross} \right]_{n_T} = \left[\frac{(Q_s^{SS})_{gross}}{(q_s^{SS})_{gross}} \right]_{n_T} \quad (4.22)$$

where the hat symbol ($\hat{\quad}$) signifies a normalized quantity. The phase-averaged results, $(\tilde{Q}_s^{SS})_{gross}$, across all N_T ensembles are shown in Figures 4.14d - 4.14f for wave period groups of 5.0, 7.0 and 9.0 s. Profiles of $(\tilde{Q}_s^{SS})_{gross}$ are plotted for the crest and trough phases in Figures 4.14g - 4.14i with right- and left-facing triangles, respectively (only every 6th point is shown in the vertical for clarity).

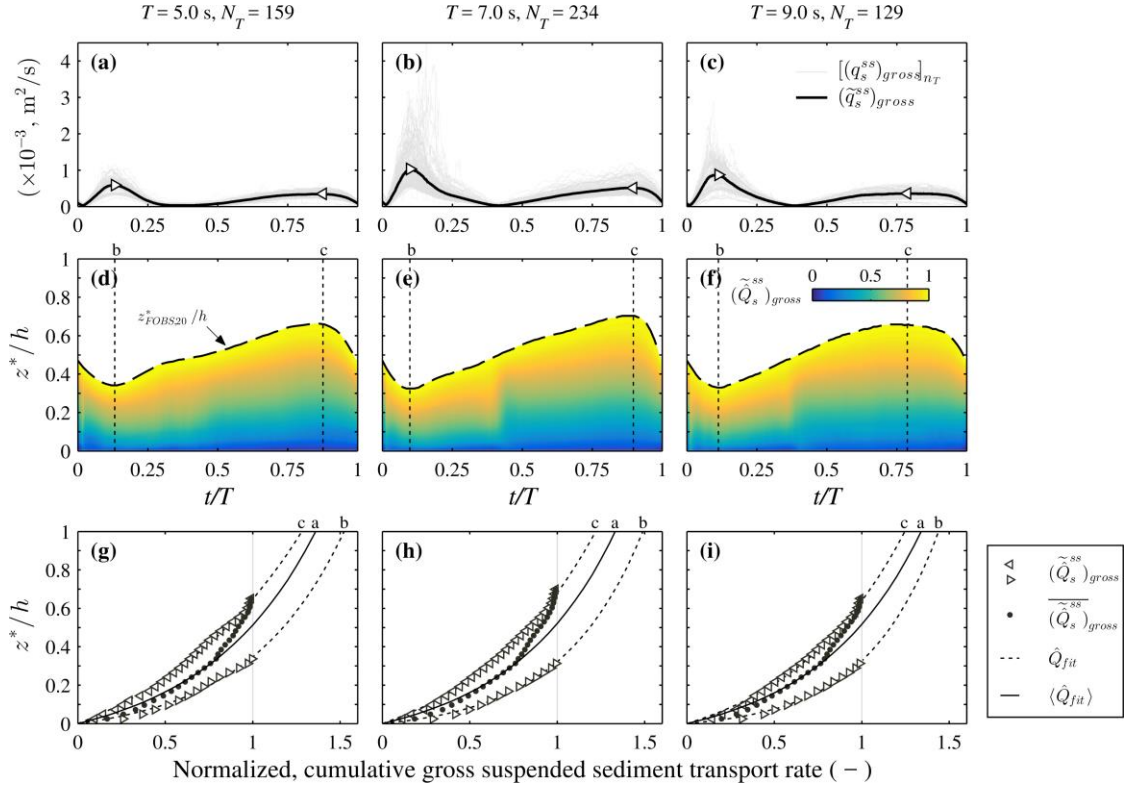


Figure 4.14: [Top row] Gross suspended sediment transport rates for all N_T ensembles (grey lines); phase-averaged gross suspended sediment transport rates (thick black lines), and corresponding peak values under the wave crests (right-triangles) and troughs (left-triangles). [Middle row] Color plots of phase-averaged normalized cumulatively integrated gross suspended sediment transport rates, $(\tilde{Q}_s^{SS})_{gross}$, as a function of relative water depth, z^*/h . The time-varying elevation of $z_{FOBS,20}^*/h$ is shown with dashed lines. [Bottom row] (dots) Wave-averaged profiles of the phase-averaged color plots in (d) – (f). (dotted lines) exponential fits to the profiles of $(\tilde{Q}_s^{SS})_{gross}$, corresponding to the phases of maximum $(\tilde{q}_s^{SS})_{gross}$ in the crests and troughs; the right- and left-facing triangles are the phase-averaged data to which the crest and trough fits were performed, respectively. (solid lines) ensemble-average of all the exponential fits to $(\tilde{Q}_s^{SS})_{gross}$ from $0 \leq t/T \leq 1$. The intersection between the fitted curves labeled ‘a’, ‘b’ and ‘c’ in (g) – (i) and $z^*/h = 1$ are the baseline (F^{SS}), upper (F_U^{SS}), and lower (F_L^{SS}) suspended sediment rate adjustment factors, respectively (see Table 4.4, footnotes).

The time-varying fraction of the water column in which suspended sediment observations were made becomes more clear by tracking the relative elevation of the highest FOBS observation (sensor 20), $z_{FOBS,20}^*/h(t/T)$ (Figures 4.14d - 4.14f; dashed black lines). Using the 5.0 s wave cases as an example, the observed phase-averaged gross sediment transport rate under the wave crest, $(\tilde{Q}_s^{SS})_{gross} \sim 0.6 \times 10^{-3} \text{ m}^2/\text{s}$ (Figure 4.14a; right-facing triangle), only accounts for roughly one-third of the water column (Figure 4.14d). At this phase, nearly two-thirds of the water column is un-resolved; thus, the amount of suspended sediment transport is potentially underestimated. About two-thirds of the water column for the trough phase was resolved, leaving the upper third un-resolved. In either case, suspended sediment transport in portions of the water column were not resolved during the entire wave cycle.

Nonlinear regression was carried out to determine the best fit between profiles of $(\tilde{Q}_s^{SS})_{gross}$ and the following exponential equation (forced through the origin),

$$\left(\frac{z^*}{h}\right) = c_1 \exp(c_2 \hat{Q}_{fit}) - 1, \quad (4.23)$$

which can be rearranged to

$$\hat{Q}_{fit} = \frac{1}{c_2} \ln \left[\frac{1}{c_1} \left(\frac{z^*}{h} + 1 \right) \right], \quad (4.24)$$

where c_1 and c_2 are fitting parameters (Table 4.4). The value of $\hat{Q}_{fit}(z^*/h = 1)$ for any given time (which should always be ≥ 1) is the factor by which suspended sediment transport rate was under-predicted, referred to hereafter as “adjustment factor.” Wave-averaged profiles of $(\tilde{Q}_s^{SS})_{gross}$ are shown for each period as black dots in Figures 4.14g - 4.14i, where the steeper slope beginning at relative water depths $z^*/h > 0.3$ highlights the bias of resolving more of the relative water depth in the wave trough compared with the crest. Fitting equation (4.23) to $(\tilde{Q}_s^{SS})_{gross}$ led to relatively small adjustment factors

of about 1.15, on average. The bias was removed by fitting equation (4.23) to each individual profile of $\left(\tilde{Q}_s^{ss}\right)_{gross}$, and then taking the ensemble-average, $\langle \hat{Q}_{fit} \rangle$ (Figures 4.14g - 4.14i; solid lines). The ensemble-average of all the fits for each wave period group closely follows the profile of $\overline{\left(\tilde{Q}_s^{ss}\right)_{gross}}$ between $0 \leq z^*/h \leq 0.3$, but begins to diverge from $\overline{\left(\tilde{Q}_s^{ss}\right)_{gross}}$ above $z^*/h > 0.3$ (Figures 4.14g - 4.14i; solid dots), demonstrating that the bias introduced by the trough portion of $\left(\tilde{Q}_s^{ss}\right)_{gross}$ led to small adjustment factors.

The intersection of $\langle \hat{Q}_{fit} \rangle$ and $z^*/h = 1$ serves as the baseline suspended sediment adjustment factor, \mathbb{F}_B^{ss} , while the values of $\hat{Q}_{fit}(z^*/h = 1)$ at the crest and trough phases provide lower and upper bounds for the degree to which suspended sediment transport rate was under-estimated, \mathbb{F}_L^{ss} and \mathbb{F}_U^{ss} , respectively (Figure 4.14; dotted lines). The root-mean-square error (*RMSE*) between the crest/trough fits and data, as well as the 95% confidence intervals on the upper (crest) and lower (trough) bounds are listed in Table 4.4. The baseline, lower, and upper bounds for suspended sediment transport adjustment factors are provided for each wave period in Table 4.5. On average, suspended sediment transport rates were under-predicted by a factor of 1.35, with lower and upper bounds of 1.25 and 1.48, respectively.

Adjusted ensemble-averaged net sheet flow and suspended sediment transport rates, $\langle \overline{q_s^{sf}} \rangle^{adj}$ and $\langle \overline{q_s^{ss}} \rangle^{adj}$, respectively, were computed for each wave case by multiplying $\langle \overline{q_s^{sf}} \rangle$ and $\langle \overline{q_s^{ss}} \rangle$ by the proper adjustment factors,

$$\langle \overline{q_s^{sf}} \rangle_i^{adj} = \mathbb{F}_i^{sf} \langle \overline{q_s^{sf}} \rangle, \quad (4.25)$$

$$\langle \overline{q_s^{ss}} \rangle_{jk}^{adj} = \mathbb{F}_{jk}^{ss} \langle \overline{q_s^{ss}} \rangle, \quad (4.26)$$

Table 4.4: Summary of nonlinear regression analysis for all three wave periods.

	Ensemble- average ^a	Crest ^b	Trough ^c
<u>$T = 5.0$ s ($N_T = 159$)</u>			
c_1, c_2	-	0.068, 1.81	0.325, 1.10
t/T ^d	-	0.132	0.876
$\hat{Q}_{fit}(z^*/h = 1)$	1.36	1.52 (1.37, 1.71)	1.28 (1.19, 1.38)
$RMSE$ (%)	2.9%	4.3%	1.8%
<u>$T = 7.0$ s ($N_T = 234$)</u>			
c_1, c_2	-	0.043, 2.14	0.232, 1.37
t/T	-	0.099	0.897
$\hat{Q}_{fit}(z^*/h = 1)$	1.33	1.49 (1.38, 1.61)	1.22 (1.16, 1.29)
$RMSE$ (%)	2.7%	3.8%	1.7%
<u>$T = 9.0$ s ($N_T = 129$)</u>			
c_1, c_2	-	0.032, 2.40	0.190, 1.47
t/T	-	0.112	0.788
$\hat{Q}_{fit}(z^*/h = 1)$	1.34	1.44 (1.35, 1.54)	1.25 (1.17, 1.32)
$RMSE$ (%)	3.1%	3.8%	2.6%

Note. c_1 and c_2 are the nonlinear regression coefficients given by equation (4.23), and $RMSE$ is the root-mean-square error between observed and fit profiles in the range of $z_{top}^*/h \leq z^*/h \leq z_{F0BS,20}^*/h$.

^a Ensemble-average of all fits from $0 \leq t/T \leq 1$ to $(\tilde{Q})_{gross}^{ss}$. The value for $RMSE$ is averaged across all fits.

^b Fit to $(\tilde{Q})_{gross}^{ss}$ associated with the occurrence of maximum \tilde{q}_{gross}^{ss} under the wave crest. Values in parentheses are the 95% confidence lower and upper bounds.

^c Fit to $(\tilde{Q})_{gross}^{ss}$ associated with the occurrence of maximum \tilde{q}_{gross}^{ss} under the wave trough. Values in parentheses are the 95% confidence lower and upper bounds.

^d Phase of $\max((\tilde{q}_s^{ss})^+_{gross})$ and $\max((\tilde{q}_s^{ss})^-_{gross})$, for crest and trough, respectively.

where respectively, $i = 1 - 4$, corresponding to either $\alpha = 0.25, 0.50, 0.75$ or 1.0 ; $j = 1 - 3$, corresponding to either the baseline (B), lower (L) or upper (U) adjustment factor; and $k = 1 - 3$, corresponding to a particular wave period of 5.0, 7.0 or 9.0 s (see Table 4.5) The choice of k was specific to each wave case. The adjusted net (total) transport rate was then computed for each wave case following

$$\langle \overline{q_s} \rangle_{ijk}^{adj} = \langle \overline{q_s}^{sf} \rangle_i^{adj} + \langle \overline{q_s}^{ss} \rangle_{jk}^{adj} . \quad (4.27)$$

Figure 4.15a shows the adjusted net suspended sediment transport rates against a range of sheet flow sediment transport rates described in Section 4.5.1.1. Figure 4.15b shows the adjusted net transport rates versus the adjusted percentages that were transported as sheet flow. Standard deviation error bars are not included with the ensemble-averaged quantities for clarity, but it should be understood that values outside the expected range are possible. Each shaded patch represents the collective net transport rates spanned by the function space of all valid i, j combinations (12 in total) from equations (4.25) - (4.27), with k selectively applied based on the wave period of each case. The black dots within each patch give the baseline results using: $i = 2$ ($\alpha = 0.50$) and $j = 1$ (Table 4.5), with lines connecting each black dot to the corresponding “pre-adjustment” value plotted in Figures 4.9 and 4.10. Two particular patches corresponding to the largest net onshore (dotted) and offshore (solid) transport rates are outlined in Figures 4.15a and 4.15b to highlight how the rectangular patch shapes in Figure 4.15a become distorted into different polygon shapes in Figure 4.15b. Annotations on the left ($\alpha = 1.0$) and right ($\alpha = 0.25$) edges of one of the patches show the influence of α on the ensemble-averaged net sheet flow transport rate (Figure 4.15a), as well as net total transport rate (Figure 4.15b). Several patch areas horizontally span both sides of the one-to-one line, which means that different shapes of the velocity

profile in the sheet flow layer can alter whether sheet flow or suspended load is the dominant transport regime. By accounting for under-resolved suspended load, the baseline number of suspended dominant cases ($\varphi^{sf} < 50\%$) increased from 6 to 7 (Figure 4.15b).

Table 4.5: Summary of net transport rate adjustment factors.

Sheet Flow Transport Rate^a, \mathbb{F}_i^{sf}			
$\mathbb{F}_{25}^{sf} (i = 1)$	$\mathbb{F}_{50}^{sf} (i = 2)$	$\mathbb{F}_{75}^{sf} (i = 3)$	$\mathbb{F}_{100}^{sf} (i = 4)$
1.38	1.00	0.77	0.61

Suspended Sediment Transport Rate, \mathbb{F}_{jk}^{ss}			
T (s)	$\mathbb{F}_B^{ss} (j = 1)$	$\mathbb{F}_L^{ss} (j = 2)$	$\mathbb{F}_U^{ss} (j = 3)$
5.0 ($k = 1$)	1.36	1.28	1.52
7.0 ($k = 2$)	1.33	1.22	1.49
9.0 ($k = 3$)	1.34	1.25	1.44

^a Definition for \mathbb{F}_i^{sf} given in equation (4.20).

Vertically oriented patches in the lower-left corner of Figure 4.15b demonstrate that the net transport rate is more sensitive to the quantification of net suspended sediment transport rates when net sheet flow contribution is low. The two more-horizontally-oriented, yet narrow, patches in the upper-right corner ($\langle \overline{q_s} \rangle^{adj}$ between ~ 50 and $100 \times 10^{-6} \text{ m}^2/\text{s}$) demonstrate that the net transport rate is strongly affected by the shape of the sheet flow layer velocity profile (large patch width), while the net percentage of transport occurring as sheet flow is not as sensitive (small patch height).

Cases corresponding to narrow, or indiscernible patches (generally near zero net transport rate) are not highly sensitive to the quantification of the sheet flow layer velocity profile nor suspended sediment transport rates. However, it is also likely that other factors (e.g., sheet flow layer thickness, skewness, and asymmetry) contribute to the different slopes, widths, and heights of each patch.

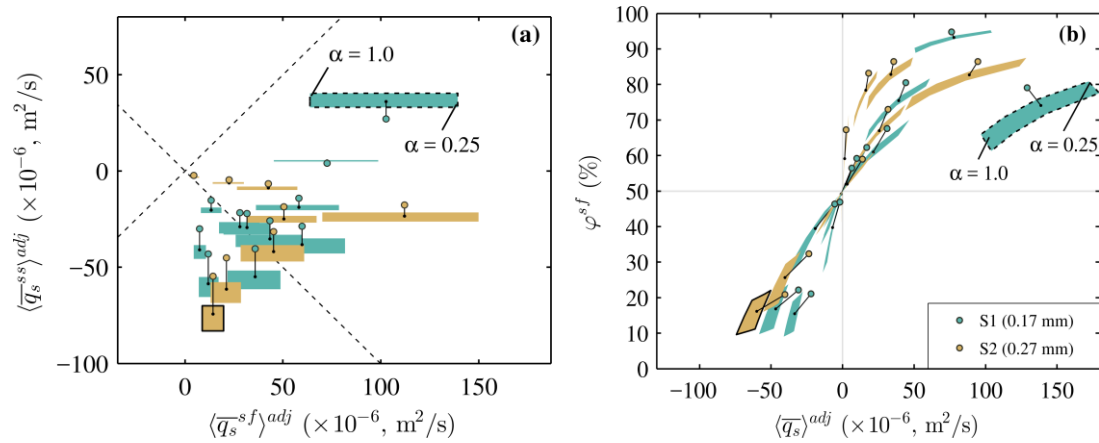


Figure 4.15: Shaded patches represent the range of expected values considering: (i) multiple shapes of the velocity profile in the sheet flow layer ($0.25 \leq \alpha \leq 1$), and (ii) the upper and lower bounds of the suspended sediment transport adjustment factor, \mathbb{F}_U^{SS} and \mathbb{F}_L^{SS} , respectively (see Table 4.5). The black dots inside each patch are the baseline results using: (i) $\alpha = 0.50$, and (ii) the baseline suspended sediment transport adjustment factor, \mathbb{F}_B^{SS} , for the corresponding wave period. The black lines connected to the colored markers show the changes from (a) Fig. 4.9 and (b) Fig. 4.10.

In addition to not resolving suspended sediment concentrations in the upper half of the still water column, another source of bias in the net suspended sediment transport rates may arise from only running ten waves per trial. As a result, it is possible that suspended load was never fully developed. Given the chance to fully develop, suspended load may have been found to contribute more substantially to the total net

transport rate. However, the goal of this study was to investigate the wave-related processes and wave-induced sediment transport components, which are only a part of the total sediment picture under realistic wave forcing. The particular wave conditions and duration of each trial were specifically selected so that strong offshore-directed currents did not develop over the sandbar crest.

4.6 Conclusions

Laboratory measurements of suspended and sheet flow sediment fluxes and transport on a large-scale sandbar were presented. Unprecedented vertical resolution of sediment concentration was achieved through the use of novel conductivity concentration profiling (CCP) sensors alongside unique fiber optic backscatter profilers (FOBS). Velocity profiles near the bed were measured to the same vertical resolution as the CCP with acoustic Doppler profiling velocimeters (ADPV), with the velocity profile in the water column resolved using a vertical array of six acoustic Doppler velocimeters (ADV). The combination of CCPs, FOBSs, ADPVs and ADVs made concurrent profiling of velocities and concentrations possible, which allowed for a synoptic range of forcing conditions and sediment sizes to be tested in a short period of time. Observations of intra-wave, wave-averaged, and ensemble-averaged quantities including cross-shore sediment flux, sediment transport rates, and net transport rates provide strong evidence for the following:

1. Maximum offshore wave-averaged sediment flux coincided with the wave-averaged elevation of the inflection point in sheet flow layer concentration profiles for all 19 wave cases, with wave-averaged volumetric sediment concentrations of $\sim 0.3 \text{ m}^3/\text{m}^3$.
2. Time-varying, phase-averaged suspended sediment transport rates lagged sheet flow transport rates, most likely due to boundary layer streaming surface wave effects. With the exception of short time spans

for a few cases, instantaneous suspended sediment transport rate was generally greater in magnitude than instantaneous sheet flow transport rate.

3. Net suspended sediment transport rates were generally offshore-directed, while net sheet flow sediment transport rates were onshore directed. Total (i.e., sum of sheet flow and suspended components) net transport rate, $\langle \bar{q}_s \rangle$, was negative (offshore) when the fraction of net sediment transport that occurred as sheet flow was less than 50%, and positive (onshore) when the same fraction was greater than 50%. This indicates that net wave-induced onshore sediment transport is strongly related to whether or not sheet flow is the dominant transport regime. In addition, the greater the fraction of the total that was transported as sheet flow, the greater the magnitude of net transport.
4. Net positive half-cycle sheet flow and suspended transport rates were essentially equal in magnitude for the smaller sediment (S1, $d_{50} = 0.17$ mm), whereas suspended sediment transport rates dominated sheet flow under the wave crest for the larger sediment (S2, $d_{50} = 0.27$ mm). Net suspended sediment transport rate dominated sheet flow in the negative half-cycle for every wave case.
5. Ensemble-averaged net sheet flow transport rates, $\langle \bar{q}_s^{sf} \rangle$, were strongly related ($r^2 = 0.71$) to the third free-stream velocity moment, $\overline{\tilde{u}_\infty^3}$, while ensemble-averaged net suspended sediment transport rates showed no correlation with the third velocity moment. The slope of the best fit line (forced through the origin) from linear regression of $\langle \bar{q}_s^{sf} \rangle$ as a function of $\overline{\tilde{u}_\infty^3}$ revealed a proportionality constant of about 450, which was significantly larger than oscillatory flow tunnel observations (Ribberink & Al-Salem, 1995).
6. Net sheet flow transport rates were sensitive to the shape of the velocity profile in the sheet flow layer, which were 1.64 times greater for a quadratic velocity profile shape compared with using a linear sheet flow layer velocity profile. Instantaneous normalized cumulative gross suspended sediment transport observations were extrapolated to the free-surface, revealing that net suspended sediment transport rates may have been under-resolved by roughly 25%.

The implications are that for particular wave conditions, sheet flow has an important role in net onshore sediment transport, and likely for onshore sandbar migration. Neglecting sheet flow in operational morphological models will lead to improperly biasing the magnitude and/or direction of suspended sediment transport in order to compensate for excluding sheet flow sediment transport.

Chapter 5

SUMMARY AND CONCLUSIONS

This chapter provides brief summaries of the findings from the two experimental campaigns (BARSED and PARROT experiments) that were discussed extensively in this dissertation.

5.1 PARROT Experiment

5.1.1 Quasi-steady Sheet Flow High-Resolution Measurement Technologies

Intense sediment transport experiments were performed in gravity driven open-channel flow using two different uniformly distributed, non-spherical acrylic particles with diameters of 1.0 and 3.0 mm, and maximum packing volumetric concentration, $\phi = 0.55 \text{ m}^3/\text{m}^3$. Similar sediment transport regimes were achieved by calibrating the flow conditions to each particle size so the bulk flow Shields number was slightly above unity, ensuring the occurrence of intense sediment transport (sheet flow). The suspension number (i.e., ratio of settling velocity to friction velocity) was near unity for both series of experiments. Instantaneous concentration profiles across the sheet flow and suspension layers were measured with an acoustic scattering based system (Acoustic Concentration and Velocity Profiler; ACVP), and two conductivity-based systems (Conductivity Concentration Profiler; CCP) with vertical sampling resolutions of 1 mm (CCP_{1mm}) and 2 mm (CCP_{2mm}). Measured (instantaneous, time-, and ensemble-averaged) concentration profiles, bed levels, and sheet flow layer thicknesses were compared between the ACVP and CCP systems. A new correction formula was

derived to convert measured sheet layer thickness to true sheet layer thickness for CCP_{2mm} based on prior work with CCP_{1mm} . Numerical simulations with a finite difference model revealed the lateral measurement extent for CCP_{2mm} extended out from the probe center by $-15.8 \text{ mm} \leq x \leq 15.8 \text{ mm}$ and $-15.6 \text{ mm} \leq y \leq 15.6 \text{ mm}$, and contained 86% of the total current (compared to 88% for CCP_{1mm}). Overall, the area of the lateral measurement extent was 3.4 times greater for CCP_{2mm} than for CCP_{1mm} . Ensemble-averaged volumetric sediment concentrations, $\langle \phi(z) \rangle$, were over-estimated by 10% with the ACVP in the dense portion of the sheet flow layer where $\langle \phi(z) \rangle \gtrsim 0.35 \text{ m}^3/\text{m}^3$, and by 100% with the CCPs in the more dilute region where $\langle \phi(z) \rangle \lesssim 0.015 \text{ m}^3/\text{m}^3$ and $\langle \phi(z) \rangle \lesssim 0.20 \text{ m}^3/\text{m}^3$ for CCP_{1mm} and CCP_{2mm} , respectively. Root-mean-square differences between ACVP and CCP ensemble-averaged concentration measurements across the entire vertical sampling range were $0.03 \text{ m}^3/\text{m}^3$, on average. Overall, good agreement was found between the three measurement systems in terms of time-resolved and time-averaged bed levels and sheet flow layer thickness, validating the different bed level detection methods employed by the two separate systems.

5.2 BARSED Experiment

5.2.1 Oscillatory Sheet Flow Dynamics under Skewed-asymmetric Surface Waves

A novel large wave flume experiment was conducted on a fixed, barred beach with a sediment pit on the sandbar, allowing for the isolation of small-scale bed response to large-scale forcing. Concurrent measurements of instantaneous sheet layer sediment concentration profiles and near-bed velocity profiles were obtained on a sandbar for the first time. Two sediment distributions were used with median grain diameters, d_{50} , of 0.17 mm and 0.27 mm. Sheet flow occurred primarily under wave crests, where sheet

thickness increased with increasing wave height. A proportionality constant, Λ , was used to relate maximum Shields parameter to maximum sheet thickness (normalized by d_{50}), with bed shear stress computed using the quadratic drag law. An enhanced sheet layer thickness was apparent for the smaller sediment experiments ($\Lambda = 18.7$), when directly compared to closed-conduit oscillatory flow tunnel data ($\Lambda = 10.6$). However, Λ varied significantly ($5 < \Lambda < 31$) depending on the procedure used to estimate grain roughness, k_s , and wave friction factor, f_w . Three models for k_s were compared (keeping the model for f_w fixed): constant $k_s = 2.5d_{50}$, and two expressions dependent on flow intensity, derived from steady and oscillatory sheet flow experiments. Values of k_s/d_{50} varied by two orders of magnitude and exhibited an inverse relationship with Λ , where $\Lambda \sim 30$ for k_s/d_{50} of $O(1)$ while $\Lambda \sim 5$ for k_s/d_{50} of $O(100)$. Two expressions for f_w were also tested (with the steady-flow-based model for k_s), yielding a difference of 69% ($\Lambda \sim 13$ versus $\Lambda \sim 22$).

5.2.2 Relative Contributions of Suspended Load and Sheet Flow

A large-scale laboratory experiment was conducted to evaluate cross-shore sediment transport and bed response over a surf zone sandbar under a variety of field-scale wave conditions and two sediment sizes, $d_{50} = 0.17$ & 0.27 mm (total of 19 cases). Chapter 4 presented intra-wave and wave-averaged observations of sediment flux profiles and transport rates in the lower half of the water column on the crest of a sandbar. The total sediment transport rate was partitioned into suspended sediment (SS) and sheet flow (SF) components to quantify the relative contributions of SS and SF to the total sediment transport rate. Net suspended sediment transport rates were greater than net sheet flow transport rates for the positive half-cycle in 14 of 19 cases, compared to 100% (19 of 19) for the negative half-cycle. Total net sheet flow transport was greater

than net suspended sediment transport for 13 of the 19 wave cases. The dominant mode of transport was determined from the ratio of net SF to net SS transport rate. In general, net total transport rate was negative (offshore) when SS dominated and positive (onshore) when SF dominated. Net SF transport rate correlated well with increasing near-bed third velocity moments ($r^2 = 0.71$), and no trend was observed related to the influence of sediment size.

REFERENCES

- Aagaard, T., & Greenwood, B. (1994). Suspended sediment transport and the role of infragravity waves in a barred surf zone. *Marine Geology*, *118*(1–2), 23–48. [https://doi.org/10.1016/0025-3227\(94\)90111-2](https://doi.org/10.1016/0025-3227(94)90111-2)
- Aagaard, T., Nielsen, J., & Greenwood, B. (1998). Suspended sediment transport and nearshore bar formation on a shallow intermediate-state beach. *Marine Geology*, *148*(3–4), 203–225. [https://doi.org/10.1016/S0025-3227\(98\)00012-7](https://doi.org/10.1016/S0025-3227(98)00012-7)
- Anderson, D., Cox, D., Mieras, R., Puleo, J. A., & Hsu, T.-J. (2017). Observations of wave-induced pore pressure gradients and bed level response on a surf zone sandbar. *Journal of Geophysical Research: Oceans*, *122*(6), 5169–5193. <https://doi.org/10.1002/2016JC012557>
- Archie, G. E. (1942). The Electrical Resistivity Log as an Aid in Determining Some Reservoir Characteristics. *Transactions of the AIME*, *146*(01), 54–62. <https://doi.org/10.2118/942054-G>
- Armanini, A., Capart, H., Fraccarollo, L., & Larcher, M. (2005). Rheological stratification in experimental free-surface flows of granular-liquid mixtures. *Journal of Fluid Mechanics*, *532*, 269–319. <https://doi.org/10.1017/S0022112005004283>
- Bagnold, R. A. (1956). The Flow of Cohesionless Grains in Fluids. *Philosophical Transactions of the Royal Society of London. Series A, Mathematical and Physical Sciences*, *249*(964), 235. <https://doi.org/10.1098/rsta.1956.0020>
- Bailard, J. A. (1981). An energetics total load sediment transport model for a plane sloping beach. *Journal of Geophysical Research: Oceans*, *86*(C11), 10938–10954. <https://doi.org/10.1029/JC086iC11p10938>

- Beach, R. A., Sternberg, R. W., & Johnson, R. (1992). A fiber optic sensor for monitoring suspended sediment. *Marine Geology*, *103*(1), 513–520. [https://doi.org/10.1016/0025-3227\(92\)90036-H](https://doi.org/10.1016/0025-3227(92)90036-H)
- Beach, R. A., & Sternberg, R. W. (1988). Suspended sediment transport in the surf zone: Response to cross-shore infragravity motion. *Marine Geology*, *80*(1), 61–79. [https://doi.org/10.1016/0025-3227\(88\)90072-2](https://doi.org/10.1016/0025-3227(88)90072-2)
- Beach, R. A., & Sternberg, R. W. (1996). Suspended-sediment transport in the surf zone: response to breaking waves. *Continental Shelf Research*, *16*(15), 1989–2003. [https://doi.org/10.1016/0278-4343\(96\)00029-5](https://doi.org/10.1016/0278-4343(96)00029-5)
- Berni, C., Michallet, H., & Barthélemy, E. (2017). Effects of horizontal pressure gradients on bed destabilization under waves. *Journal of Fluid Mechanics*, *812*, 721–751. <https://doi.org/10.1017/jfm.2016.805>
- Berni, C., Barthélemy, E., & Michallet, H. (2013). Surf zone cross-shore boundary layer velocity asymmetry and skewness: An experimental study on a mobile bed. *Journal of Geophysical Research: Oceans*, *118*(4), 2188–2200. <https://doi.org/10.1002/jgrc.20125>
- Berzi, D. (2011). Analytical Solution of Collisional Sheet Flows. *Journal of Hydraulic Engineering*, *137*(10), 1200–1207.
- Bricault, M. (2006). *Rétrodiffusion acoustique par une suspension en milieu turbulent: application à la mesure de profils de concentration pour l'étude de processus hydrosédimentaires*. Grenoble, INPG.
- Brinkkemper, J. A., de Bakker, A. T. M., & Ruessink, B. G. (2017). Intrawave sand suspension in the shoaling and surf zone of a field-scale laboratory beach. *Journal of Geophysical Research: Earth Surface*, *122*(1), 2016JF004061. <https://doi.org/10.1002/2016JF004061>
- Calantoni, J., & Puleo, J. A. (2006). Role of pressure gradients in sheet flow of coarse sediments under sawtooth waves. *Journal of Geophysical Research: Oceans*, *111*(C1), C01010. <https://doi.org/10.1029/2005JC002875>

- Capart, H., & Fraccarollo, L. (2011). Transport layer structure in intense bed-load. *Geophysical Research Letters*, 38(20), L20402.
<https://doi.org/10.1029/2011GL049408>
- Carstens, M. R., Neilson, F. M., & Altinbilek, H. D. (1969). *Bedforms generated in the laboratory under oscillatory flow* (Technical Memo No. 28). Coastal Engineering Research Center: Fort Belvoir, VA.
- Chassagneux, F. X., & Hurther, D. (2014). Wave bottom boundary layer processes below irregular surfzone breaking waves with light-weight sheet flow particle transport. *Journal of Geophysical Research: Oceans*, 119(3), 1668–1690.
- Chiodi, F., Claudin, P., & Andreotti, B. (2014). A two-phase flow model of sediment transport: transition from bedload to suspended load. *Journal of Fluid Mechanics*, 755, 561–581. <https://doi.org/10.1017/jfm.2014.422>
- Conley, D. C., & Beach, R. A. (2003). Cross-shore sediment transport partitioning in the nearshore during a storm event. *Journal of Geophysical Research: Oceans*, 108(C3), 3065. <https://doi.org/10.1029/2001JC001230>
- Cowen, E. A., Dudley, R. D., Liao, Q., Variano, E. A., & Liu, P. L.-F. (2010). An insitu borescopic quantitative imaging profiler for the measurement of high concentration sediment velocity. *Experiments in Fluids*, 49(1), 77–88.
- Cox, D. T., & Kobayashi, N. (2000). Identification of intense, intermittent coherent motions under shoaling and breaking waves. *Journal of Geophysical Research: Oceans*, 105(C6), 14223–14236. <https://doi.org/10.1029/2000JC900048>
- Craig, R. G. A., Loadman, C., Clement, B., Rusello, P. J., & Siegel, E. (2011). Characterization and testing of a new bistatic profiling acoustic Doppler velocimeter: The Vectrino-II. In *Current, Waves and Turbulence Measurements (CWTM), 2011 IEEE/OES 10th* (pp. 246–252).
<https://doi.org/10.1109/CWTM.2011.5759559>
- Da Silva, P. A., Temperville, A., & Seabra Santos, F. (2006). Sand transport under combined current and wave conditions: A semi-unsteady, practical model.

- Coastal Engineering*, 53(11), 897–913.
<https://doi.org/10.1016/j.coastaleng.2006.06.010>
- Dally, W., & Dean, R. (1984). Suspended Sediment Transport and Beach Profile Evolution. *Journal of Waterway, Port, Coastal, and Ocean Engineering*, 110(1), 15–33. [https://doi.org/10.1061/\(ASCE\)0733-950X\(1984\)110:1\(15\)](https://doi.org/10.1061/(ASCE)0733-950X(1984)110:1(15))
- Daniel, S. M. (1965). *Flow of suspension in a rectangular channel*. University of Saskatchewan, Canada.
- Dohmen-Janssen, C. M., & Hanes, D. M. (2002). Sheet flow dynamics under monochromatic nonbreaking waves. *Journal of Geophysical Research: Oceans*, 107(C10), 3149. <https://doi.org/10.1029/2001JC001045>
- Dohmen-Janssen, C. M., & Hanes, D. M. (2005). Sheet flow and suspended sediment due to wave groups in a large wave flume. *Continental Shelf Research*, 25(3), 333–347. <https://doi.org/10.1016/j.csr.2004.10.009>
- Dohmen-Janssen, C. M., Hassan, W. N., & Ribberink, J. S. (2001). Mobile-bed effects in oscillatory sheet flow. *Journal of Geophysical Research: Oceans*, 106(C11), 27103–27115. <https://doi.org/10.1029/2000JC000513>
- Drake, T. G., & Calantoni, J. (2001). Discrete particle model for sheet flow sediment transport in the nearshore. *Journal of Geophysical Research: Oceans*, 106(C9), 19859–19868. <https://doi.org/10.1029/2000JC000611>
- Elgar, S., Gallagher, E. L., & Guza, R. T. (2001). Nearshore sandbar migration. *Journal of Geophysical Research: Oceans*, 106(C6), 11623–11627. <https://doi.org/10.1029/2000JC000389>
- Engelund, F., & Fredsøe, J. (1976). A Sediment Transport Model for Straight Alluvial Channels. *Hydrology Research*, 7(5), 293–306.
- Fernández-Mora, A., Calvete, D., Falqués, A., & de Swart, H. E. (2015). Onshore sandbar migration in the surf zone: New insights into the wave-induced sediment transport mechanisms. *Geophysical Research Letters*, 42(8), 2014GL063004. <https://doi.org/10.1002/2014GL063004>

- Foster, D. L., Bowen, A. J., Holman, R. A., & Natto, P. (2006). Field evidence of pressure gradient induced incipient motion. *Journal of Geophysical Research: Oceans*, *111*(C5), C05004. <https://doi.org/10.1029/2004JC002863>
- Fredsøe, J., & Deigaard, R. (1992). *Mechanics of coastal sediment transport*. Singapore ; New Jersey: World Scientific.
- Gallagher, E. L., Elgar, S., & Guza, R. T. (1998). Observations of sand bar evolution on a natural beach. *Journal of Geophysical Research: Oceans*, *103*(C2), 3203–3215. <https://doi.org/10.1029/97JC02765>
- Gaunaurd, G., & Überall, H. (1983). RST analysis of monostatic and bistatic acoustic echoes from an elastic sphere. *The Journal of the Acoustical Society of America*, *73*(1), 1–12.
- Grasso, F., Michallet, H., & Barthélemy, E. (2011). Sediment transport associated with morphological beach changes forced by irregular asymmetric, skewed waves. *Journal of Geophysical Research: Oceans*, *116*(C3), C03020. <https://doi.org/10.1029/2010JC006550>
- Hanes, D. M., & Huntley, D. A. (1986). Continuous measurements of suspended sand concentration in a wave dominated nearshore environment. *Continental Shelf Research*, *6*(4), 585–596. [https://doi.org/10.1016/0278-4343\(86\)90024-5](https://doi.org/10.1016/0278-4343(86)90024-5)
- Hassan, W. N., & Ribberink, J. S. (2005). Transport processes of uniform and mixed sands in oscillatory sheet flow. *Coastal Engineering*, *52*(9), 745–770. <https://doi.org/10.1016/j.coastaleng.2005.06.002>
- Hefner, B. T., & Marston, P. L. (2000). Backscattering enhancements associated with subsonic Rayleigh waves on polymer spheres in water: Observation and modeling for acrylic spheres. *The Journal of the Acoustical Society of America*, *107*(4), 1930–1936.
- Henderson, S. M., Allen, J. S., & Newberger, P. A. (2004). Nearshore sandbar migration predicted by an eddy-diffusive boundary layer model. *Journal of Geophysical Research: Oceans*, *109*(C6), C06024. <https://doi.org/10.1029/2003JC002137>

- Henriquez, M., Reniers, A. J. H. M., Ruessink, B. G., & Stive, M. J. F. (2014). PIV measurements of the bottom boundary layer under nonlinear surface waves. *Coastal Engineering*, *94*, 33–46.
<https://doi.org/10.1016/j.coastaleng.2014.08.004>
- Hoefel, F., & Elgar, S. (2003). Wave-Induced Sediment Transport and Sandbar Migration. *Science*, *299*(5614), 1885–1887.
<https://doi.org/10.1126/science.1081448>
- Horikawa, K., Watanabe, A., & Katori, S. (1982). SEDIMENT TRANSPORT UNDER SHEET FLOW CONDITION. *Coastal Engineering Proceedings*, *1*(18). <https://doi.org/10.9753/icce.v18.%p>
- Hsu, T. J., Jenkins, J. T., & Liu, P. L.-F. (2004). On two-phase sediment transport: sheet flow of massive particles. *Proceedings of the Royal Society of London. Series A: Mathematical, Physical and Engineering Sciences*, *460*(2048), 2223–2250. <https://doi.org/10.1098/rspa.2003.1273>
- Hsu, T.-J., Elgar, S., & Guza, R. T. (2006). Wave-induced sediment transport and onshore sandbar migration. *Coastal Engineering*, *53*(10), 817–824.
<https://doi.org/10.1016/j.coastaleng.2006.04.003>
- Hsu, T.-J., & Hanes, D. M. (2004). Effects of wave shape on sheet flow sediment transport. *Journal of Geophysical Research: Oceans*, *109*(C5), C05025.
<https://doi.org/10.1029/2003JC002075>
- Hurther, D., Thorne, P. D., Bricault, M., Lemmin, U., & Barnoud, J.-M. (2011). A multi-frequency Acoustic Concentration and Velocity Profiler (ACVP) for boundary layer measurements of fine-scale flow and sediment transport processes. *Coastal Engineering*, *58*(7), 594–605.
<https://doi.org/10.1016/j.coastaleng.2011.01.006>
- Hurther, D., & Lemmin, U. (2001). Shear stress statistics and wall similarity analysis in turbulent boundary layers using a high resolution 3D ADV. *Journal of Oceanic Engineering*, *25*, 446–457.

- Hurther, D., & Lemmin, U. (2008). Improved Turbulence Profiling with Field-Adapted Acoustic Doppler Velocimeters Using a Bifrequency Doppler Noise Suppression Method. *Journal of Atmospheric and Oceanic Technology*, 25, 452–463.
- Hurther, D., & Thorne, P. D. (2011). Suspension and near-bed load sediment transport processes above a migrating, sand-rippled bed under shoaling waves. *Journal of Geophysical Research: Oceans*, 116(C7), C07001. <https://doi.org/10.1029/2010JC006774>
- Jackson, R. (1997). Locally averaged equations of motion for a mixture of identical spherical particles and a Newtonian fluid. *Chemical Engineering Science*, 52, 2457–2469.
- Jenkins, J. T., & Hanes, D. M. (1998). Collisional sheet flows of sediment driven by a turbulent fluid. *Journal of Fluid Mechanics*, 370, 29–52. <https://doi.org/10.1017/S0022112098001840>
- Kim, Y., Cheng, Z., Hsu, T.-J., Mieras, R. S., & Puleo, J. A. (2017). A NUMERICAL INVESTIGATION OF SHEET FLOW UNDER NON-BREAKING AND BREAKING WAVES. In *Proceedings of the 8th International Conference on Coastal Dynamics* (pp. 1779–1788). Helsingør, Denmark.
- Kranenburg, W. M., Ribberink, J. S., Schretlen, J. J. L. M., & Uittenbogaard, R. E. (2013). Sand transport beneath waves: The role of progressive wave streaming and other free surface effects. *Journal of Geophysical Research: Earth Surface*, 118(1), 122–139. <https://doi.org/10.1029/2012JF002427>
- Kuriyama, Y. (2002). Medium-term bar behavior and associated sediment transport at Hasaki, Japan. *Journal of Geophysical Research: Oceans*, 107(C9), 3132. <https://doi.org/10.1029/2001JC000899>
- Lanckriet, T., Puleo, J., Masselink, G., Turner, I., Conley, D., Blenkinsopp, C., & Russell, P. (2014). Comprehensive Field Study of Swash-Zone Processes. II: Sheet Flow Sediment Concentrations during Quasi-Steady Backwash. *Journal*

- of Waterway, Port, Coastal, and Ocean Engineering*, 140(1), 29–42.
[https://doi.org/10.1061/\(ASCE\)WW.1943-5460.0000209](https://doi.org/10.1061/(ASCE)WW.1943-5460.0000209)
- Lanckriet, T., Puleo, J. A., & Waite, N. (2013). A Conductivity Concentration Profiler for Sheet Flow Sediment Transport. *IEEE Journal of Oceanic Engineering*, 38(1), 55–70. <https://doi.org/10.1109/JOE.2012.2222791>
- Lippmann, T. C., & Holman, R. A. (1990). The spatial and temporal variability of sand bar morphology. *Journal of Geophysical Research: Oceans*, 95(C7), 11575–11590. <https://doi.org/10.1029/JC095iC07p11575>
- Liu, D., Liu, X., Fu, X., & Wang, G. (2016). Quantification of the bed load effects on turbulent open-channel flows. *Journal of Geophysical Research: Earth Surface*, 121(4), 767–789. <https://doi.org/10.1002/2015JF003723>
- Madsen, O. S. (1974). STABILITY OF A SAND BED UNDER BREAKING WAVES. *Coastal Engineering Proceedings*, 1(14).
<https://doi.org/10.9753/icce.v14.%p>
- Mariño-Tapia, I. J., Russell, P. E., O’Hare, T. J., Davidson, M. A., & Huntley, D. A. (2007). Cross-shore sediment transport on natural beaches and its relation to sandbar migration patterns: 1. Field observations and derivation of a transport parameterization. *Journal of Geophysical Research: Oceans*, 112(C3), C03001. <https://doi.org/10.1029/2005JC002893>
- Meyer-Peter, E., & Müller, R. (1948). Formulas for Bed-Load transport. *IAHSR 2nd Meeting, Stockholm, Appendix 2*. Retrieved from
<http://resolver.tudelft.nl/uuid:4fda9b61-be28-4703-ab06-43cdc2a21bd7>
- Mieras, R. S., Puleo, J. A., Anderson, D., Cox, D. T., & Hsu, T.-J. (2017a). Large-scale experimental observations of sheet flow on a sandbar under skewed-asymmetric waves. *Journal of Geophysical Research: Oceans*, 122(6), 5022–5045. <https://doi.org/10.1002/2016JC012438>
- Mieras, R. S., Puleo, J. A., Anderson, D., Cox, D. T., & Hsu, T.-J. (2017b). LARGE-SCALE EXPERIMENTAL OBSERVATIONS OF WAVE-INDUCED SEDIMENT TRANSPORT OVER A SURF ZONE SANDBAR. In

- Proceedings of the 8th International Conference on Coastal Dynamics* (pp. 618–629). Helsingør, Denmark.
- Moate, B. D., & Thorne, P. D. (2013). Scattering from suspended sediments having different and mixed mineralogical compositions: comparison of laboratory measurements and theoretical predictions. *The Journal of the Acoustical Society of America*, *133*(3), 1320–34. <https://doi.org/10.1121/1.4788985>
- Naqshband, S., Ribberink, J. S., Hurther, D., & Hulscher, S. J. M. H. (2014). Bed load and suspended load contributions to migrating sand dunes in equilibrium. *Journal of Geophysical Research: Earth Surface*, *119*(5), 1043–1063. <https://doi.org/10.1002/2013JF003043>
- Naqshband, S., Ribberink, J. S., Hurther, D., Barraud, P. A., & Hulscher, S. J. M. H. (2014). Experimental evidence for turbulent sediment flux constituting a large portion of the total sediment flux along migrating sand dunes. *Geophysical Research Letters*, *41*(24), 2014GL062322. <https://doi.org/10.1002/2014GL062322>
- Nielsen, P. (1992). *Coastal Bottom Boundary Layers and Sediment Transport* (Vol. 4). Singapore: World Scientific.
- Nielsen, P. (2006). Sheet flow sediment transport under waves with acceleration skewness and boundary layer streaming. *Coastal Engineering*, *53*(9), 749–758. <https://doi.org/10.1016/j.coastaleng.2006.03.006>
- Nielsen, P. (2016). 1DV structure of turbulent wave boundary layers. *Coastal Engineering*, *112*, 1–8. <https://doi.org/10.1016/j.coastaleng.2016.02.001>
- Nielsen, P., & Callaghan, D. P. (2003). Shear stress and sediment transport calculations for sheet flow under waves. *Coastal Engineering*, *47*(3), 347–354. [https://doi.org/10.1016/S0378-3839\(02\)00141-2](https://doi.org/10.1016/S0378-3839(02)00141-2)
- Nielsen, P., & Guard, P. A. (2011). VERTICAL SCALES AND SHEAR STRESSES IN WAVE BOUNDARY LAYERS OVER MOVABLE BEDS. *Coastal Engineering Proceedings*, *1*(32), 1. <https://doi.org/10.9753/icce.v32.sediment.1>

- Nnadi, F. N., & Wilson, K. C. (1992). Motion of Contact-Load Particles at High Shear Stress. *Journal of Hydraulic Engineering*, 118(12), 1670–1684.
[https://doi.org/10.1061/\(ASCE\)0733-9429\(1992\)118:12\(1670\)](https://doi.org/10.1061/(ASCE)0733-9429(1992)118:12(1670))
- O'Donoghue, T., Pokrajac, D., & Hondebrink, L. J. (2010). Laboratory and numerical study of dambreak-generated swash on impermeable slopes. *Coastal Engineering*, 57(5), 513–530. <https://doi.org/10.1016/j.coastaleng.2009.12.007>
- O'Donoghue, T., & Wright, S. (2004a). Concentrations in oscillatory sheet flow for well sorted and graded sands. *Coastal Engineering*, 50(3), 117–138.
<https://doi.org/10.1016/j.coastaleng.2003.09.004>
- O'Donoghue, T., & Wright, S. (2004b). Flow tunnel measurements of velocities and sand flux in oscillatory sheet flow for well-sorted and graded sands. *Coastal Engineering*, 51(11–12), 1163–1184.
<https://doi.org/10.1016/j.coastaleng.2004.08.001>
- Pape, L., Plant, N. G., & Ruessink, B. G. (2009). Cross-shore sandbar response to waves. *Journal of Coastal Research*, 1030–1034.
- Pape, L., Kuriyama, Y., & Ruessink, B. G. (2010). Models and scales for cross-shore sandbar migration. *Journal of Geophysical Research: Earth Surface*, 115(F3), F03043. <https://doi.org/10.1029/2009JF001644>
- Pape, L., Ruessink, B. G., Wiering, M. A., & Turner, I. L. (2007). Recurrent neural network modeling of nearshore sandbar behavior. *Neural Networks*, 20(4), 509–518. <https://doi.org/10.1016/j.neunet.2007.04.007>
- Plant, N. G., Holland, K. T., Puleo, J. A., & Gallagher, E. L. (2004). Prediction skill of nearshore profile evolution models. *Journal of Geophysical Research: Oceans*, 109(C1), C01006. <https://doi.org/10.1029/2003JC001995>
- Plant, N. G., Todd Holland, K., & Holman, R. A. (2006). A dynamical attractor governs beach response to storms. *Geophysical Research Letters*, 33(17), L17607. <https://doi.org/10.1029/2006GL027105>

- Pugh, F. J., & Wilson, K. C. (1999). Velocity and Concentration Distributions in Sheet Flow above Plane Beds. *Journal of Hydraulic Engineering*, 125(2), 117–125. [https://doi.org/10.1061/\(ASCE\)0733-9429\(1999\)125:2\(117\)](https://doi.org/10.1061/(ASCE)0733-9429(1999)125:2(117))
- Puleo, J. A., Beach, R. A., Holman, R. A., & Allen, J. S. (2000). Swash zone sediment suspension and transport and the importance of bore-generated turbulence. *Journal of Geophysical Research: Oceans*, 105(C7), 17021–17044. <https://doi.org/10.1029/2000JC900024>
- Puleo, J. A., Lanckriet, T., & Blenkinsopp, C. (2014). Bed level fluctuations in the inner surf and swash zone of a dissipative beach. *Marine Geology*, 349, 99–112. <https://doi.org/10.1016/j.margeo.2014.01.006>
- Puleo, J. A., Krafft, D., Pintado-Patiño, J. C., & Bruder, B. (2017). Video-derived near bed and sheet flow sediment particle velocities in dam-break-driven swash. *Coastal Engineering*, 126, 27–36. <https://doi.org/10.1016/j.coastaleng.2017.04.008>
- Puleo, J. A., Lanckriet, T., Conley, D., & Foster, D. (2015). Sediment transport partitioning in the swash zone of a large-scale laboratory beach. *Coastal Engineering*. <https://doi.org/10.1016/j.coastaleng.2015.11.001>
- Puleo, J. A., Lanckriet, T., Conley, D., & Foster, D. (2016). Sediment transport partitioning in the swash zone of a large-scale laboratory beach. *Coastal Engineering*, 113, 73–87. <https://doi.org/10.1016/j.coastaleng.2015.11.001>
- Puleo, J. A., Lanckriet, T., & Wang, P. (2012). Near bed cross-shore velocity profiles, bed shear stress and friction on the foreshore of a microtidal beach. *Coastal Engineering*, 68, 6–16. <https://doi.org/10.1016/j.coastaleng.2012.04.007>
- Revil-Baudard, T., Chauchat, J., Hurther, D., & Barraud, P.-A. (2015). Investigation of sheet-flow processes based on novel acoustic high-resolution velocity and concentration measurements. *Journal of Fluid Mechanics*, 767, 1–30. <https://doi.org/10.1017/jfm.2015.23>

- Revil-Baudard, T., & Chauchat, J. (2013). A two-phase model for sheet flow regime based on dense granular flow rheology. *Journal of Geophysical Research: Oceans*, *118*(2), 619–634. <https://doi.org/10.1029/2012JC008306>
- Revil-Baudard, T., Chauchat, J., Hurther, D., & Eiff, O. (2016). Turbulence modifications induced by the bed mobility in intense sediment-laden flows. *Journal of Fluid Mechanics*, *808*, 469–484.
- Ribberink, J. S. (1998). Bed-load transport for steady flows and unsteady oscillatory flows. *Coastal Engineering*, *34*(1–2), 59–82. [https://doi.org/10.1016/S0378-3839\(98\)00013-1](https://doi.org/10.1016/S0378-3839(98)00013-1)
- Ribberink, J. S., & Al-Salem, A. A. (1995). Sheet flow and suspension of sand in oscillatory boundary layers. *Coastal Engineering*, *25*(3–4), 205–225. [https://doi.org/10.1016/0378-3839\(95\)00003-T](https://doi.org/10.1016/0378-3839(95)00003-T)
- Ribberink, J. S., van der Werf, J. J., O'Donoghue, T., & Hassan, W. N. M. (2008). Sand motion induced by oscillatory flows: Sheet flow and vortex ripples. *Journal of Turbulence*, *9*, N20. <https://doi.org/10.1080/14685240802220009>
- Roelvink, J. A., & Brøker, I. (1993). Cross-shore profile models. *Coastal Engineering*, *21*(1–3), 163–191. [https://doi.org/10.1016/0378-3839\(93\)90049-E](https://doi.org/10.1016/0378-3839(93)90049-E)
- Ruessink, B. G., van Enckevort, I. M. J., Kingston, K. S., & Davidson, M. A. (2000). Analysis of observed two- and three-dimensional nearshore bar behaviour. *Marine Geology*, *169*(1–2), 161–183. [https://doi.org/10.1016/S0025-3227\(00\)00060-8](https://doi.org/10.1016/S0025-3227(00)00060-8)
- Ruessink, B. G., Wijnberg, K. M., Holman, R. A., Kuriyama, Y., & van Enckevort, I. M. J. (2003). Intersite comparison of interannual nearshore bar behavior. *Journal of Geophysical Research: Oceans*, *108*(C8), 3249. <https://doi.org/10.1029/2002JC001505>
- Ruessink, B. G., & Kuriyama, Y. (2008). Numerical predictability experiments of cross-shore sandbar migration. *Geophysical Research Letters*, *35*(1), L01603. <https://doi.org/10.1029/2007GL032530>

- Ruessink, B. G., Michallet, H., Abreu, T., Sancho, F., Van der A, D. A., Van der Werf, J. J., & Silva, P. A. (2011). Observations of velocities, sand concentrations, and fluxes under velocity-asymmetric oscillatory flows. *Journal of Geophysical Research: Oceans*, *116*(C3), C03004. <https://doi.org/10.1029/2010JC006443>
- Ruessink, B. G., Pape, L., & Turner, I. L. (2009). Daily to interannual cross-shore sandbar migration: Observations from a multiple sandbar system. *Continental Shelf Research*, *29*(14), 1663–1677. <https://doi.org/10.1016/j.csr.2009.05.011>
- Ruessink, B. G., Kuriyama, Y., Reniers, A. J. H. M., Roelvink, J. A., & Walstra, D. J. R. (2007). Modeling cross-shore sandbar behavior on the timescale of weeks. *Journal of Geophysical Research: Earth Surface*, *112*(F3), F03010. <https://doi.org/10.1029/2006JF000730>
- Ruggiero, P., Kaminsky, G. M., Gelfenbaum, G., & Voigt, B. (2005). Seasonal to Interannual Morphodynamics along a High-Energy Dissipative Littoral Cell. *Journal of Coastal Research*, *21*(3), 553–578.
- Sallenger Jr, A. H., Holman, R. A., & Birkemeier, W. A. (1985). Storm-induced response of a nearshore-bar system. *Marine Geology*, *64*(3–4), 237–257. [https://doi.org/10.1016/0025-3227\(85\)90107-0](https://doi.org/10.1016/0025-3227(85)90107-0)
- Schretlen, J. L. M. (2012, June 8). *Sand transport under full-scale progressive surface waves* (info:eu-repo/semantics/doctoralThesis). University of Twente, Enschede. Retrieved from <http://doc.utwente.nl/80884/>
- Scott, C. P., Cox, D. T., Maddux, T. B., & Long, J. W. (2005). Large-scale laboratory observations of turbulence on a fixed barred beach. *Measurement Science and Technology*, *16*(10), 1903.
- Scott, N. V., Hsu, T.-J., & Cox, D. (2009). Steep wave, turbulence, and sediment concentration statistics beneath a breaking wave field and their implications for sediment transport. *Continental Shelf Research*, *29*(20), 2303–2317. <https://doi.org/10.1016/j.csr.2009.09.008>

- Silva, P. A., Abreu, T., A. D. A. van der, Sancho, F., Ruessink, B. G., Werf, J. van der, & Ribberink, J. S. (2011). Sediment transport in nonlinear skewed oscillatory flows: Transkew experiments. *Journal of Hydraulic Research*, 49(sup1), 72–80. <https://doi.org/10.1080/00221686.2011.592681>
- Sleath, J. F. A. (1999). Conditions for plug formation in oscillatory flow. *Continental Shelf Research*, 19(13), 1643–1664. [https://doi.org/10.1016/S0278-4343\(98\)00096-X](https://doi.org/10.1016/S0278-4343(98)00096-X)
- Smith, J. D., & McLean, S. R. (1977). Spatially averaged flow over a wavy surface. *Journal of Geophysical Research*, 82(12), 1735–1746. <https://doi.org/10.1029/JC082i012p01735>
- Spinewine, B., Capart, H., Fraccarollo, L., & Larcher, M. (2011). Laser stripe measurements of near-wall solid fraction in channel flows of liquid-granular mixtures. *Experiments in Fluids*, 50, 1507–1525. <https://doi.org/10.1007/s00348-010-1009-7>
- Sumer, B. M., Kozakiewicz, A., Fredsoe, J., & Deigaard, R. (1996). Velocity and Concentration Profiles in Sheet-Flow Layer of Movable Bed. *Journal of Hydraulic Engineering*, 122(10), 549–558. [https://doi.org/10.1061/\(ASCE\)0733-9429\(1996\)122:10\(549\)](https://doi.org/10.1061/(ASCE)0733-9429(1996)122:10(549))
- Swart, D. H. (1974, December 18). *Offshore sediment transport and equilibrium beach profiles*. T.U. Delft. Retrieved from <http://resolver.tudelft.nl/uuid:057cb136-5f5b-484a-878d-5616fbaeda4e>
- Thomas, R. E., Schindfessel, L., McLelland, S. J., Créëlle, S., & Mulder, T. D. (2017). Bias in mean velocities and noise in variances and covariances measured using a multistatic acoustic profiler: the Nortek Vectrino Profiler. *Measurement Science and Technology*, 28(7), 075302. <https://doi.org/10.1088/1361-6501/aa7273>
- Thorne, P. D., & Hanes, D. M. (2002). A review of acoustic measurement of small-scale sediment processes. *Continental Shelf Research*, 22(4), 603–632. [https://doi.org/10.1016/S0278-4343\(01\)00101-7](https://doi.org/10.1016/S0278-4343(01)00101-7)

- Thorne, P. D., & Hurther, D. (2014). An overview on the use of backscattered sound for measuring suspended particle size and concentration profiles in non-cohesive inorganic sediment transport studies. *Continental Shelf Research*, 73, 97–118.
- Thornton, E. B., Humiston, R. T., & Birkemeier, W. (1996). Bar/trough generation on a natural beach. *Journal of Geophysical Research: Oceans*, 101(C5), 12097–12110. <https://doi.org/10.1029/96JC00209>
- Trowbridge, J., & Young, D. (1989). Sand transport by unbroken water waves under sheet flow conditions. *Journal of Geophysical Research: Oceans*, 94(C8), 10971–10991. <https://doi.org/10.1029/JC094iC08p10971>
- Van der A, D. A., Ribberink, J. S., van der Werf, J. J., O'Donoghue, T., Buijsrogge, R. H., & Kranenburg, W. M. (2013). Practical sand transport formula for non-breaking waves and currents. *Coastal Engineering*, 76, 26–42. <https://doi.org/10.1016/j.coastaleng.2013.01.007>
- Van der A, D. A., O'Donoghue, T., & Ribberink, J. S. (2010). Measurements of sheet flow transport in acceleration-skewed oscillatory flow and comparison with practical formulations. *Coastal Engineering*, 57(3), 331–342. <https://doi.org/10.1016/j.coastaleng.2009.11.006>
- Van der A, D. A., van der Zanden, J., O'Donoghue, T., Hurther, D., Cáceres, I., McLelland, S. J., & Ribberink, J. S. (2017). Large-scale laboratory study of breaking wave hydrodynamics over a fixed bar. *Journal of Geophysical Research: Oceans*, 122(4), 3287–3310. <https://doi.org/10.1002/2016JC012072>
- Van der Werf, J. J., Schretlen, J. J. L. M., Ribberink, J. S., & O'Donoghue, T. (2009). Database of full-scale laboratory experiments on wave-driven sand transport processes. *Coastal Engineering*, 56(7), 726–732. <https://doi.org/10.1016/j.coastaleng.2009.01.008>
- Van der Zanden, J. (2016, December 9). *Sand Transport Processes in the Surf and Swash Zones*. Retrieved from

https://www.researchgate.net/publication/311563590_Sand_Transport_Processes_in_the_Surf_and_Swash_Zones

- Van der Zanden, J., Alsina, J. M., Cáceres, I., Buijsrogge, R. H., & Ribberink, J. S. (2015). Bed level motions and sheet flow processes in the swash zone: Observations with a new conductivity-based concentration measuring technique (CCM+). *Coastal Engineering*, *105*, 47–65. <https://doi.org/10.1016/j.coastaleng.2015.08.009>
- Van der Zanden, J., van der A, D. A., Hurther, D., Cáceres, I., O'Donoghue, T., & Ribberink, J. S. (2016). Near-bed hydrodynamics and turbulence below a large-scale plunging breaking wave over a mobile barred bed profile. *Journal of Geophysical Research: Oceans*, *121*(8), 6482–6506. <https://doi.org/10.1002/2016JC011909>
- Van der Zanden, J., van der A, D. A., Hurther, D., Cáceres, I., O'Donoghue, T., Hulscher, S. J. M. H., & Ribberink, J. S. (2017). Bedload and suspended load contributions to breaker bar morphodynamics. *Coastal Engineering*, *129*, 74–92. <https://doi.org/10.1016/j.coastaleng.2017.09.005>
- Van der Zanden, J., van der A, D. A., Hurther, D., Cáceres, I., O'Donoghue, T., & Ribberink, J. S. (2017). Suspended sediment transport around a large-scale laboratory breaker bar. *Coastal Engineering*, *125*, 51–69. <https://doi.org/10.1016/j.coastaleng.2017.03.007>
- Van Enckevort, I. M. J., & Ruessink, B. G. (2003). Video observations of nearshore bar behaviour. Part 1: alongshore uniform variability. *Continental Shelf Research*, *23*(5), 501–512. [https://doi.org/10.1016/S0278-4343\(02\)00234-0](https://doi.org/10.1016/S0278-4343(02)00234-0)
- Van Maanen, B., de Ruiter, P. J., Coco, G., Bryan, K. R., & Ruessink, B. G. (2008). Onshore sandbar migration at Tairua Beach (New Zealand): Numerical simulations and field measurements. *Marine Geology*, *253*(3–4), 99–106. <https://doi.org/10.1016/j.margeo.2008.05.007>
- Van Rijn, L. C. (2007). Unified View of Sediment Transport by Currents and Waves. I: Initiation of Motion, Bed Roughness, and Bed-Load Transport. *Journal of*

- Hydraulic Engineering*, 133(6), 649–667.
[https://doi.org/10.1061/\(ASCE\)0733-9429\(2007\)133:6\(649\)](https://doi.org/10.1061/(ASCE)0733-9429(2007)133:6(649))
- Wang, Y.-H., & Yu, G.-H. (2007). Velocity and concentration profiles of particle movement in sheet flows. *Advances in Water Resources*, 30(5), 1355–1359.
<https://doi.org/10.1016/j.advwatres.2006.11.012>
- Watanabe, A., & Sato, S. (2004). A sheet-flow transport rate formula for asymmetric, forward-leaning waves and currents. In *Coastal Engineering 2004* (pp. 1703–1714). New York: ASCE.
- Wijnberg, K. M. (2002). Environmental controls on decadal morphologic behaviour of the Holland coast. *Marine Geology*, 189(3–4), 227–247.
[https://doi.org/10.1016/S0025-3227\(02\)00480-2](https://doi.org/10.1016/S0025-3227(02)00480-2)
- Wijnberg, K. M., & Terwindt, J. H. J. (1995). Extracting decadal morphological behaviour from high-resolution, long-term bathymetric surveys along the Holland coast using eigenfunction analysis. *Marine Geology*, 126(1–4), 301–330. [https://doi.org/10.1016/0025-3227\(95\)00084-C](https://doi.org/10.1016/0025-3227(95)00084-C)
- Wilson, K. C. (1987). Analysis of Bed-Load Motion at High Shear Stress. *Journal of Hydraulic Engineering*, 113(1), 97–103. [https://doi.org/10.1061/\(ASCE\)0733-9429\(1987\)113:1\(97\)](https://doi.org/10.1061/(ASCE)0733-9429(1987)113:1(97))
- Wilson, K. C. (1989). Friction of wave-induced sheet flow. *Coastal Engineering*, 12(4), 371–379. [https://doi.org/10.1016/0378-3839\(89\)90013-6](https://doi.org/10.1016/0378-3839(89)90013-6)
- Wright, L. D., Short, A. D., & Green, M. O. (1985). Short-term changes in the morphodynamic states of beaches and surf zones: An empirical predictive model. *Marine Geology*, 62(3–4), 339–364. [https://doi.org/10.1016/0025-3227\(85\)90123-9](https://doi.org/10.1016/0025-3227(85)90123-9)
- Wright, L. D., & Short, A. D. (1984). Morphodynamic variability of surf zones and beaches: A synthesis. *Marine Geology*, 56(1–4), 93–118.
[https://doi.org/10.1016/0025-3227\(84\)90008-2](https://doi.org/10.1016/0025-3227(84)90008-2)
- Yoon, H.-D., & Cox, D. T. (2012). Cross-shore variation of intermittent sediment suspension and turbulence induced by depth-limited wave breaking.

- Continental Shelf Research*, 47, 93–106.
<https://doi.org/10.1016/j.csr.2012.07.001>
- Yu, X., Hsu, T.-J., & Hanes, D. M. (2010). Sediment transport under wave groups: Relative importance between nonlinear wavelike and nonlinear boundary layer streaming. *Journal of Geophysical Research: Oceans*, 115(C2), C02013.
<https://doi.org/10.1029/2009JC005348>
- Yu, X., Hsu, T.-J., Jenkins, J. T., & Liu, P. L.-F. (2012). Predictions of vertical sediment flux in oscillatory flows using a two-phase, sheet-flow model. *Advances in Water Resources*, 48(Supplement C), 2–17.
<https://doi.org/10.1016/j.advwatres.2012.05.012>
- Yu, Y., Sternberg, R. W., & Beach, R. A. (1993). Kinematics of breaking waves and associated suspended sediment in the nearshore zone. *Continental Shelf Research*, 13(11), 1219–1242. [https://doi.org/10.1016/0278-4343\(93\)90050-8](https://doi.org/10.1016/0278-4343(93)90050-8)
- Zala Flores, N., & Sleath, J. F. A. (1998). Mobile layer in oscillatory sheet flow. *Journal of Geophysical Research: Oceans*, 103(C6), 12783–12793.
<https://doi.org/10.1029/98JC00691>
- Zhou, Z., Sangermano, J., Hsu, T.-J., & Ting, F. C. K. (2014). A numerical investigation of wave-breaking-induced turbulent coherent structure under a solitary wave. *Journal of Geophysical Research: Oceans*, 119(10), 6952–6973.
<https://doi.org/10.1002/2014JC009854>

Appendix A

SUPPLEMENTAL FIGURES FOR PARROT EXPERIMENTS

The supplementary figures provided in this Appendix are instantaneous observations of velocity, concentration and bed interface for the seven experiments not shown in Chapter 2.

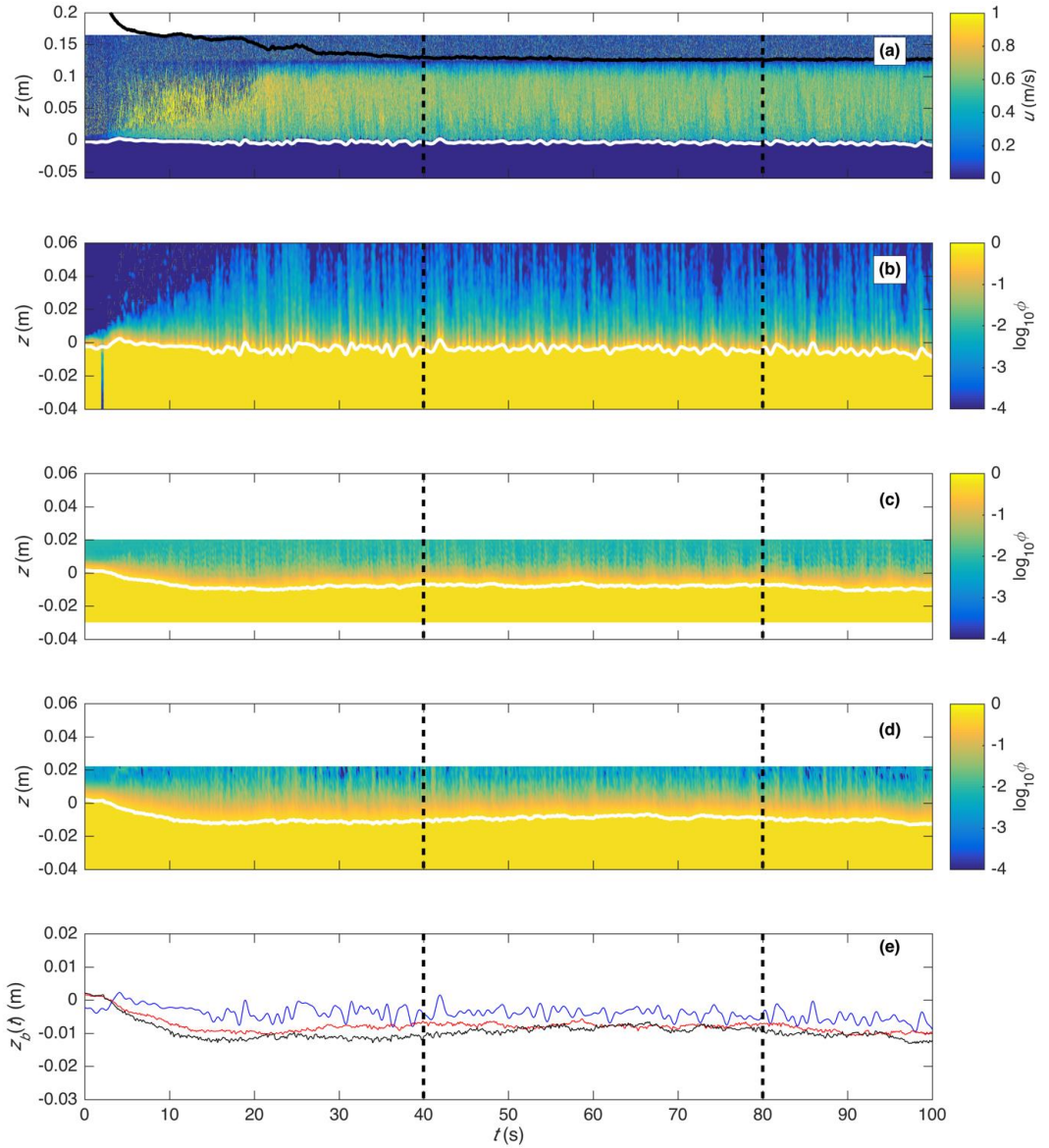


Figure A.1: Time-space plots of (a) streamwise velocity, (b) ACVP-derived concentration, (c) CCP_{1mm} -derived concentration, (d) CCP_{2mm} -derived concentration; and (e) bed interfaces derived from ACVP (blue line), CCP_{1mm} (red line) and CCP_{2mm} (black line) bed interfaces for experiment S3a. The black dashed lines represent the instantaneous free-surface. The white lines outline the bed interfaces estimated from ACVP and CCP data. The vertical dashed black lines signify the time spans over which time-averages were computed.

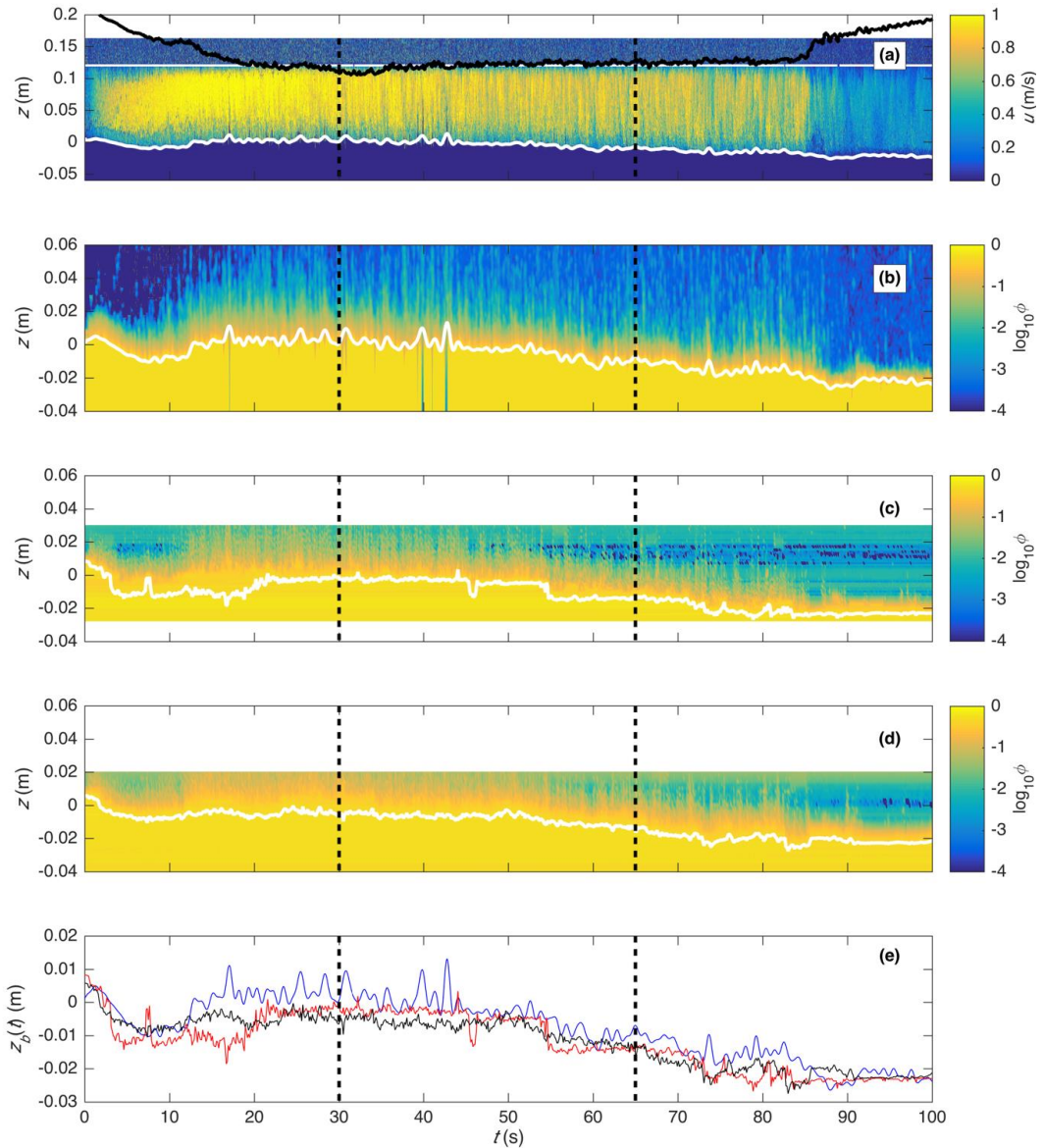


Figure A.2: Time-space plots of (a) streamwise velocity, (b) ACVP-derived concentration, (c) CCP_{1mm} -derived concentration, (d) CCP_{2mm} -derived concentration; and (e) bed interfaces derived from ACVP (blue line), CCP_{1mm} (red line) and CCP_{2mm} (black line) bed interfaces for experiment S3c. The black dashed lines represent the instantaneous free-surface. The white lines outline the bed interfaces estimated from ACVP and CCP data. The vertical dashed black lines signify the time spans over which time-averages were computed.

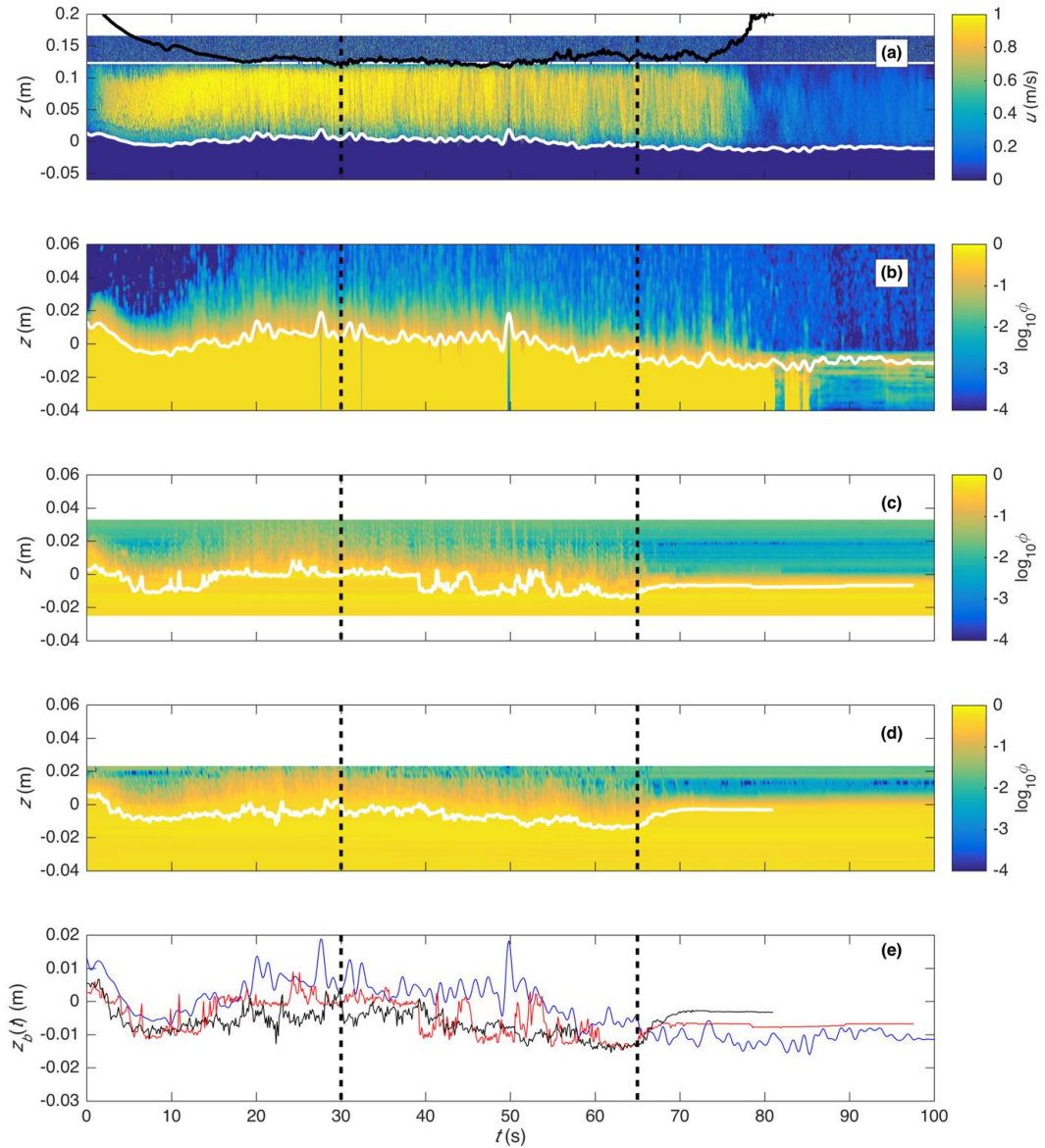


Figure A.3: Time-space plots of (a) streamwise velocity, (b) ACVP-derived concentration, (c) CCP_{1mm} -derived concentration, (d) CCP_{2mm} -derived concentration; and (e) bed interfaces derived from ACVP (blue line), CCP_{1mm} (red line) and CCP_{2mm} (black line) bed interfaces for experiment S3d. The black dashed lines represent the instantaneous free-surface. The white lines outline the bed interfaces estimated from ACVP and CCP data. The vertical dashed black lines signify the time spans over which time-averages were computed.

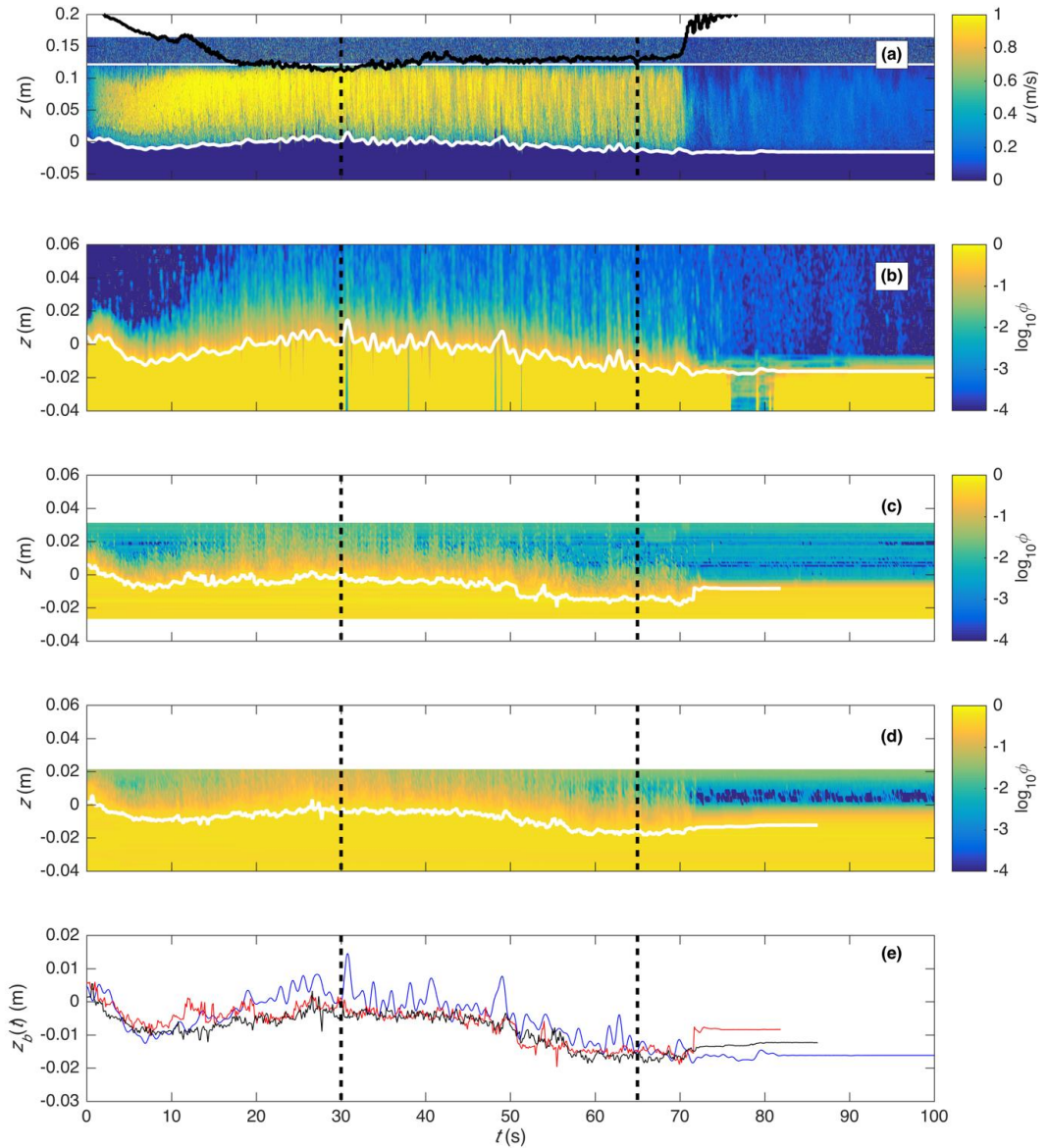


Figure A.4: Time-space plots of (a) streamwise velocity, (b) ACVP-derived concentration, (c) CCP_{1mm} -derived concentration, (d) CCP_{2mm} -derived concentration; and (e) bed interfaces derived from ACVP (blue line), CCP_{1mm} (red line) and CCP_{2mm} (black line) bed interfaces for experiment S3e. The black dashed lines represent the instantaneous free-surface. The white lines outline the bed interfaces estimated from ACVP and CCP data. The vertical dashed black lines signify the time spans over which time-averages were computed.

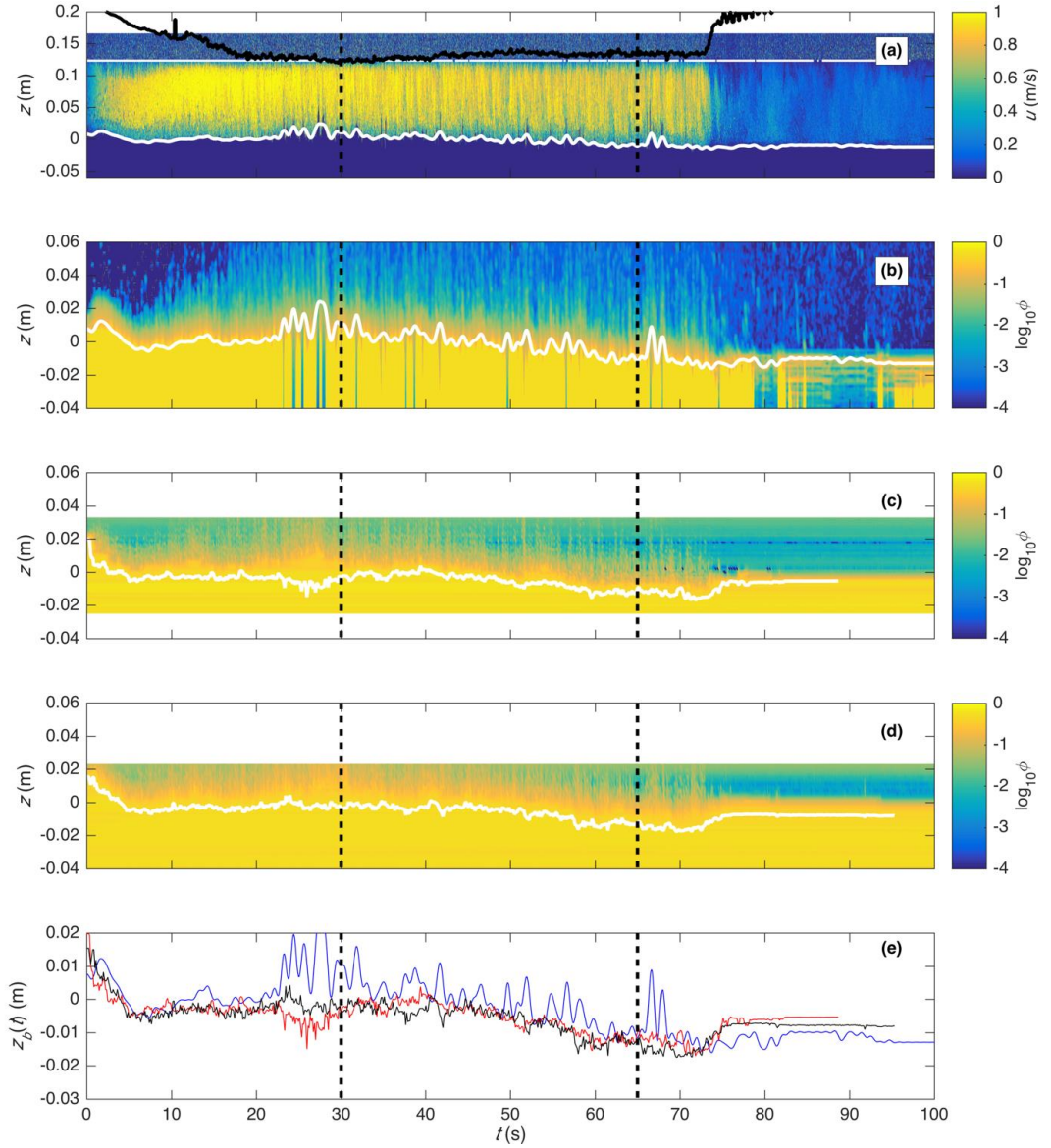


Figure A.5: Time-space plots of (a) streamwise velocity, (b) ACVP-derived concentration, (c) CCP_{1mm} -derived concentration, (d) CCP_{2mm} -derived concentration; and (e) bed interfaces derived from ACVP (blue line), CCP_{1mm} (red line) and CCP_{2mm} (black line) bed interfaces for experiment S3f. The black dashed lines represent the instantaneous free-surface. The white lines outline the bed interfaces estimated from ACVP and CCP data. The vertical dashed black lines signify the time spans over which time-averages were computed.

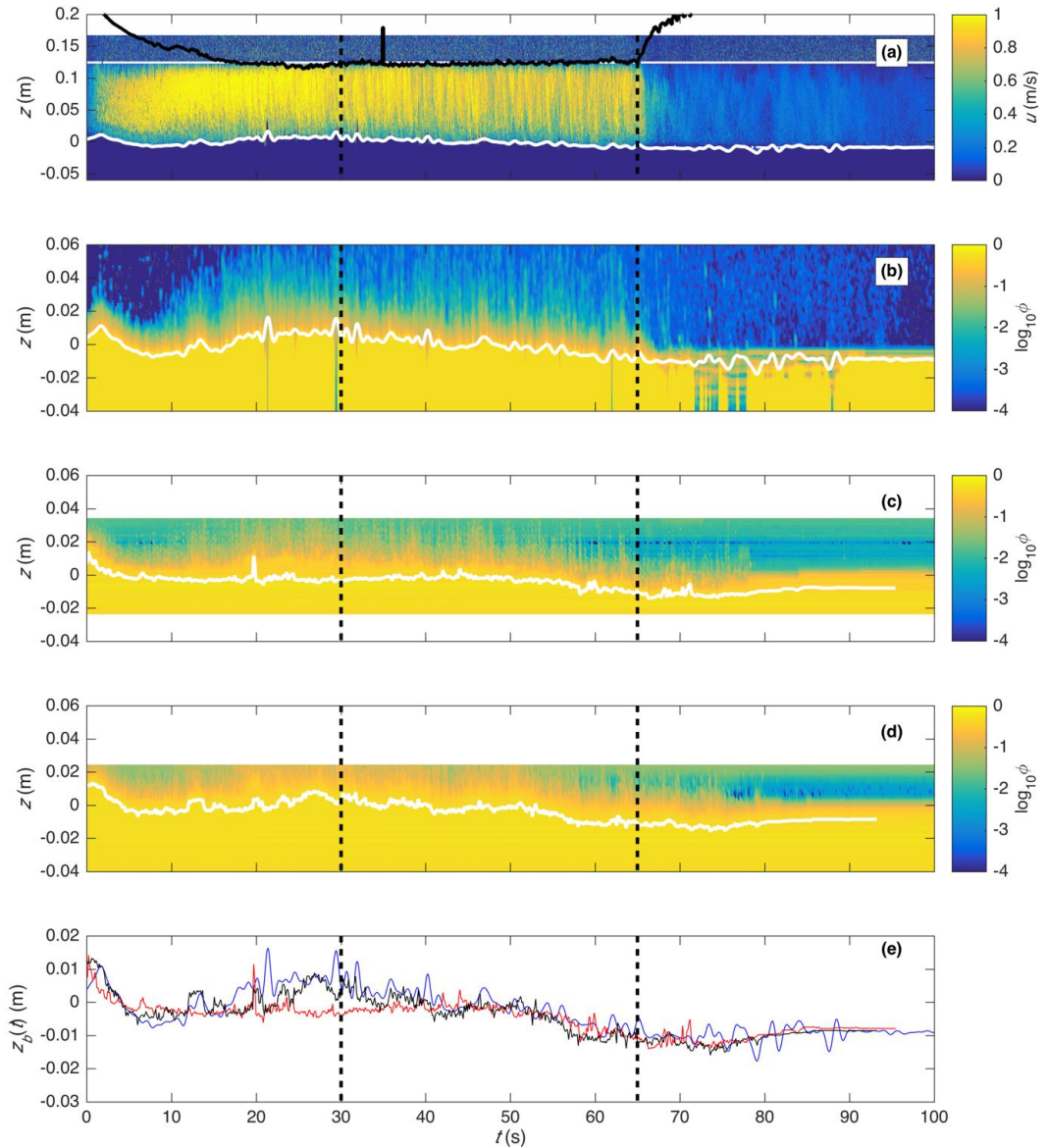


Figure A.6: Time-space plots of (a) streamwise velocity, (b) ACVP-derived concentration, (c) CCP_{1mm} -derived concentration, (d) CCP_{2mm} -derived concentration; and (e) bed interfaces derived from ACVP (blue line), CCP_{1mm} (red line) and CCP_{2mm} (black line) bed interfaces for experiment S1a. The black dashed lines represent the instantaneous free-surface. The white lines outline the bed interfaces estimated from ACVP and CCP data. The vertical dashed black lines signify the time spans over which time-averages were computed.

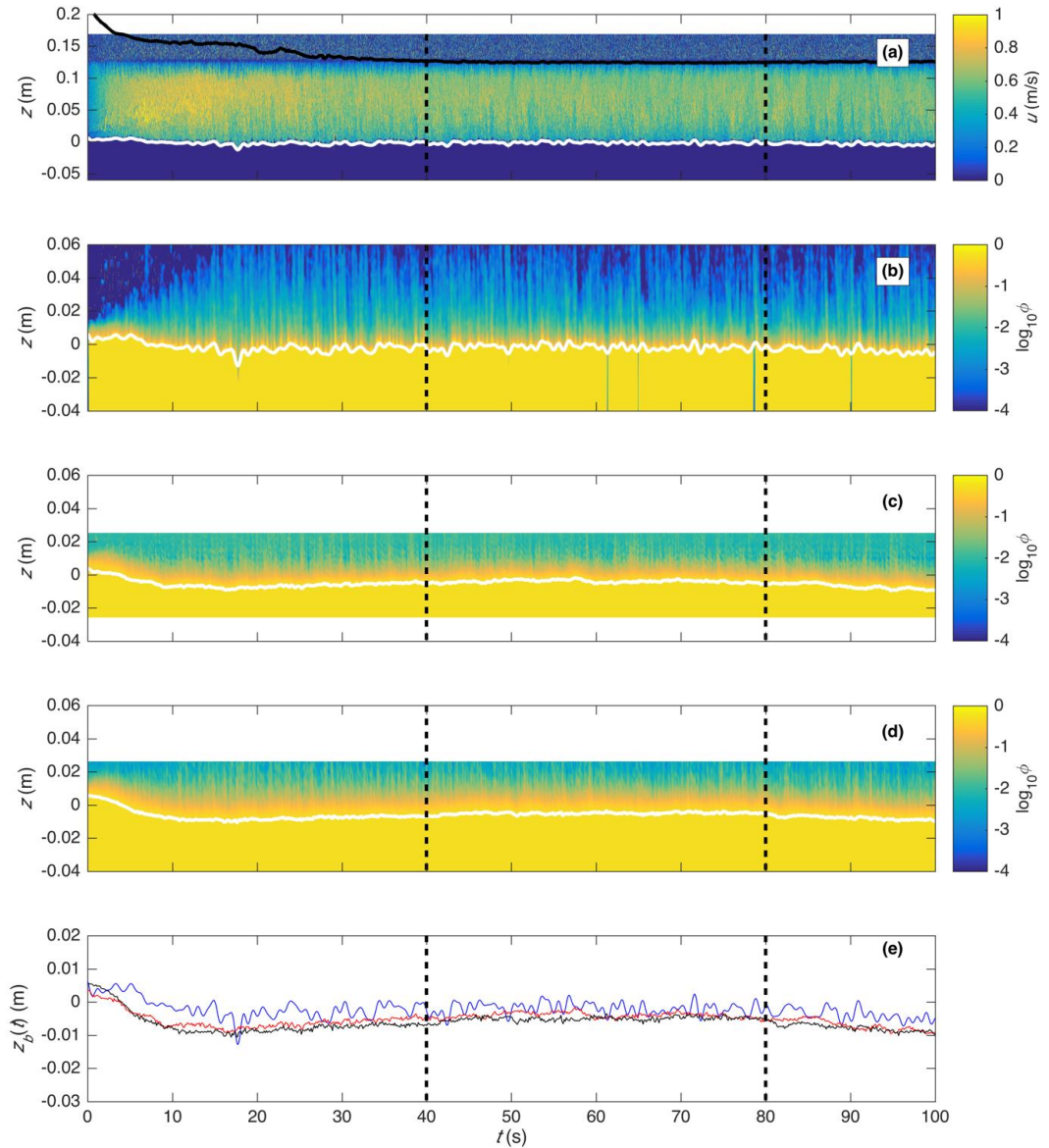


Figure A.7: Time-space plots of (a) streamwise velocity, (b) ACVP-derived concentration, (c) CCP_{1mm} -derived concentration, (d) CCP_{2mm} -derived concentration; and (e) bed interfaces derived from ACVP (blue line), CCP_{1mm} (red line) and CCP_{2mm} (black line) bed interfaces for experiment S1c. The black dashed lines represent the instantaneous free-surface. The white lines outline the bed interfaces estimated from ACVP and CCP data. The vertical dashed black lines signify the time spans over which time-averages were computed.

Appendix B
COPYRIGHT NOTES

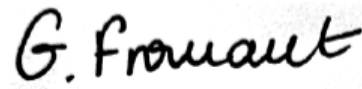
Portions of Chapter 2 pertaining to the ACVP were reproduced with the permission of Dr. Guillaume Fromant.

To whom it may concern,

I, Guillaume Fromant, grant permission to Ryan Mieras to re-print materials to be published in “Sheet flow measurement performances of high-resolution acoustic and conductivity profilers” in his Thesis required by the University of Delaware for the completion of a Ph.D.

I am also aware that the Thesis is to be “published” in its entirety through University Microfilms Inc.’s doctoral dissertation program.

Sincerely,

A handwritten signature in black ink that reads "G. Fromant". The signature is written in a cursive, slightly slanted style.

Guillaume Fromant

October 16, 2017

Chapter 3 is reproduced with permission from John Wiley and Sons, from Mieras, R. S., Puleo, J. A., Anderson, D., Cox, D. T., & Hsu, T.-J. (2017a). Large-scale experimental observations of sheet flow on a sandbar under skewed-asymmetric waves.

JOHN WILEY AND SONS LICENSE
TERMS AND CONDITIONS

Oct 07, 2017

This Agreement between University of Delaware -- Ryan Mieras ("You") and John Wiley and Sons ("John Wiley and Sons") consists of your license details and the terms and conditions provided by John Wiley and Sons and Copyright Clearance Center.

License Number	4203780203557
License date	Oct 07, 2017
Licensed Content Publisher	John Wiley and Sons
Licensed Content Publication	Journal of Geophysical Research: Oceans
Licensed Content Title	Large-scale experimental observations of sheet flow on a sandbar under skewed-asymmetric waves
Licensed Content Author	Ryan S. Mieras, Jack A. Puleo, Dylan Anderson, Daniel T. Cox, Tian-Jian Hsu
Licensed Content Date	Jun 22, 2017
Licensed Content Pages	24
Type of use	Dissertation/Thesis
Requestor type	Author of this Wiley article
Format	Print and electronic
Portion	Full article
Will you be translating?	No
Title of your thesis / dissertation	SHEET FLOW AND SUSPENDED SEDIMENT TRANSPORT PROCESSES ON A SURF ZONE SANDBAR
Expected completion date	Nov 2017
Expected size (number of pages)	250
Requestor Location	University of Delaware 259 Academy St. NEWARK, DE 19716 United States Attn: Ryan Mieras
Publisher Tax ID	EU826007151
Billing Type	Invoice
Billing Address	University of Delaware 259 Academy St. NEWARK, DE 19716 United States Attn: Ryan Mieras
Total	0.00 USD